THREE DIMENSIONAL MIXED MODE FRACTURE ANALYSIS OF FUNCTIONALLY GRADED MATERIALS

A THESIS SUBMITTED TO
THE GRADUATE SCHOOL OF NATURAL AND APPLIED SCIENCES
OF
MIDDLE EAST TECHNICAL UNIVERSITY

BY

SADIK KÖŞKER

IN PARTIAL FULFILLMENT OF THE REQUIREMENTS
FOR
THE DEGREE OF MASTER OF SCIENCE
IN
MECHANICAL ENGINEERING

SEPTEMBER 2007

Approval of the thesis:

THREE DIMENSIONAL MIXED MODE FRACTURE ANALYSIS OF FUNCTIONALLY GRADED MATERIALS

submitted by **SADIK KÖŞKER** in partial fulfillment of the requirements for the degree of **Master of Science in Mechanical Engineering Department, Middle East Technical University** by,

Prof. Dr. Canan Özgen _____
Dean, Graduate School of **Natural and Applied Sciences**

Prof. Dr. S. Kemal İder _____
Head of Department, **Mechanical Engineering**

Asst. Prof. Dr. Serkan Dağ
Supervisor, **Mechanical Engineering Dept., METU** _____

Assoc. Prof. Dr. Bora Yıldırım
Co-Supervisor, **Mechanical Engineering Dept., HÜ** _____

Examining Committee Members:

Prof. Dr. Bülent Doyum
Mechanical Engineering Dept., METU _____

Asst. Prof. Dr. Serkan Dağ
Mechanical Engineering Dept., METU _____

Assoc. Prof. Dr. Bora Yıldırım
Mechanical Engineering Dept., HÜ _____

Prof. Dr. Haluk Darendeliler
Mechanical Engineering Dept., METU _____

Prof. Dr. Suat Kadıoğlu
Mechanical Engineering Dept., METU _____

Date: September 6, 2007

I hereby declare that all information in this document has been obtained and presented in accordance with academic rules and ethical conduct. I also declare that, as required by these rules and conduct, I have fully cited and referenced all material and results that are not original to this work.

Name, Last name: Sadık KÖŞKER

Signature :

ABSTRACT

THREE DIMENSIONAL MIXED MODE FRACTURE ANALYSIS OF FUNCTIONALLY GRADED MATERIALS

KÖŞKER, Sadık

M.S., Department of Mechanical Engineering

Supervisor : Asst. Prof. Dr. Serkan Dağ

Co-Supervisor: Assoc. Prof. Dr. Bora Yıldırım

September 2007, 198 pages

The main objective of this study is to model and analyze a three dimensional inclined semi-elliptic surface crack in a Functionally Graded Material (FGM) coating bonded to a homogeneous substrate with a bond coat. The parametric analyses on FGMs are based upon zirconia-yttria (ZrO2-8wt%-Y_2O_3) FGM coating bonded to a substrate made of a nickel-based superalloy. It is assumed that there is a nickel-chromium–aluminum–zirconium (NiCrAlY) bond coat between the FGM coating and substrate. Metal-rich, linear variation, ceramic-rich and homogeneous ceramic FGM coating types are considered in the analyses. The inclined semi-elliptic surface crack problem in the FGM coating-bond coat-substrate system is analyzed under transient thermal loading. This problem is modeled and analyzed by utilizing three dimensional finite elements. Strain singularity around the crack front is simulated using collapsed 20 – node quarter – point brick elements. Three – dimensional displacement correlation technique is utilized to extract the mixed mode stress intensity factors around the crack front

for different inclination angles of the semi-elliptic surface crack. The energy release rates around the crack front are also calculated by using the evaluated mixed mode stress intensity factors. The results obtained in this study are the peak values of mixed mode stress intensity factors and energy release rates around the crack front for various inclination angles of the semi-elliptic surface crack embedded in the FGM coating of the composite structure subjected to transient thermal loading.

Keywords: FGM coatings, semi–elliptical inclined surface crack, displacement correlation technique, mixed mode stress intensity factors, energy release rate.

ÖZ

FONKSİYONEL DERECELENDİRİLMİŞ KAPLAMALARIN ÜÇ BOYUTLU KARIŞIK MOD KIRILMA ANALİZİ

KÖŞKER, Sadık
Yüksek Lisans, Makina Mühendisliği Bölümü
Tez Yöneticisi : Y. Doç. Dr. Serkan DAĞ
Ortak Tez Yöneticisi : Doç. Dr. Bora YILDIRIM

Eylül 2007, 198 Sayfa

Bu çalışmanın başlıca amacı, homojen taban malzemesine bir birleştirici kaplama malzemesiyle bağlı olan Fonksiyonel Derecelendirilmiş Malzeme (FDM) kaplamasındaki üç boyutlu eğik yarı-eliptik yüzey çatlağının modellenmesi ve incelenmesidir. FDM kaplamasındaki parametrik analizler, nikel tabanlı süper alaşıma bağlı bulunan FDM kaplamasının bir ZrO2-%8 ağ.-Y_2O_3 tabakası olduğu esas alınarak gerçekleştirilmiştir. FDM kaplaması ve taban malzemesi arasında nikel-krominyum-aluminyum-zirkonyum (NiCrAlY) birleştirici kaplamanın olduğu varsayılmıştır. Analizlerde zengin metal, doğrusal değişimli, zengin seramik ve homojen seramik FDM kaplama tipleri dikkate alınmıştır. FDM kaplaması- birleştirici kaplama- taban malzemesi sisteminde bulunan eğik yarı-eliptik yüzey çatlağı problemi, zamana bağlı ısıl yükleme altında incelenmiştir. Bu problem, üç boyutlu sonlu elemanlar kullanılarak modellenmiş ve incelenmiştir. 20 düğümlü çeyrek noktalı elemanlar kullanılarak çatlak çevresindeki gerinim tekilliği benzetilmiştir. Üç boyutlu yer değiştirme korelasyon tekniği kullanılarak

çatlak çevresindeki karışık mod gerilme şiddeti çarpanları, yarı-eliptik yüzey çatlağının değişik eğik açıları için elde edilmiştir. Elde edilen karışık mod gerilme şiddeti çarpanları kullanılarak, çatlak çevresindeki enerji salınım oranları da hesaplanmıştır. Bu çalışmada elde edilen sonuçlar, zamana bağlı ısıl yüklemeye maruz bırakılmış olan kompozit malzemedeki FDM kaplamasında bulunan yarı-eliptik yüzey çatlağının değişik eğik açıları için çatlak çevresindeki karışık mod gerilme şiddeti çarpanları ve enerji salınım oranlarının aldığı en yüksek değerlerdir.

Anahtar Kelimeler: FDM kaplamalar, yarı-eliptik eğik yüzey çatlağı, yer değiştirme korelasyon tekniği, karışık mod gerilme şiddeti çarpanları, enerji salınım oranı.

To My Family with Love and Gratitude

ACKNOWLEDGMENTS

I would like to thank to my supervisor Asst. Prof. Dr. Serkan Dağ, for his guidance, advices and criticism throughout this study.

I am also grateful to my co-supervisor Assoc. Prof. Dr. Bora Yıldırım, for his invaluable helps especially in finite element modeling and APDL programming. It could have been rather difficult for me without his supports on APDL programming.

The permission and supports given by my company ASELSAN Inc. for completing this M.S. study are also greatly acknowledged.

I would finally like to express my deepest love and gratitude to my family for their love, understanding and patience they showed during the completion of this study. My very special thanks are to my mother for giving me endless moral supports and encouragement throughout the preparation of this thesis.

TABLE OF CONTENTS

ABSTRACT iv
ÖZ vi
ACKNOWLEDGMENTS ix
TABLE OF CONTENTS x
LIST OF TABLES xiv
LIST OF FIGURES xv
LIST OF SYMBOLS xxx

CHAPTERS
1. INTRODUCTION 1
1.1 Literature Survey 4
1.2 Scope of the Study 12

2. PROBLEM DEFINITION 14
2.1 Fracture Mechanics 14
2.2 Stress Intensity Factors 19
2.2.1 Modes of Stress Intensity Factors (SIFs) 20
2.2.1.1 Mode I Stress Intensity Factor 21
2.2.1.2 Mode II Stress Intensity Factor 22
2.2.1.3 Mode III Stress Intensity Factor 24
2.3 Geometry of the Problem 25
2.4 Material Property Variations and FGM Coating Types 27
2.5 Model Validation and Types of Loading 30
2.5.1 The Validation of the Model 30

2.5.1.1 First Analysis for Model Validation 30
2.5.1.2 Second Analysis for Model Validation 32
2.5.2 Transient Thermal Loading 34

3. FINITE ELEMENT MODELING AND ANALYSIS OF FUNCTIONALLY GRADED MATERIALS 38
3.1 The Finite Element Models 38
3.1.1 Finite Element Modeling and Analysis of Solid under Uniform Tension 38
3.1.2 Finite Element Modeling and Analysis of the FGM Coating-Bond Coat-Substrate Structure under Transient Thermal Load 46

4. STRESS INTENSITY FACTORS AND ENERGY RELEASE RATE CALCULATIONS 55
4.1 The Displacement Correlation Technique (DCT) 55
4.2 Mode I (K_I) SIF Calculations 56
4.3 Mode II (K_{II}) SIF Calculations 61
4.4 Mode III (K_{III}) SIF Calculations 63
4.5 Energy Release Rate (G) Calculations 65

5. NUMERICAL RESULTS AND DISCUSSION 67
5.1 Introduction 67
5.2 Comparisons to Results of Ayhan et al. [11] 67
5.3 Comparisons to Results of Isida et al. [9] 77
5.4 Transient Thermal Loading 82
5.4.1 SIFs, G and Temperature Distributions around the Crack Front for $\alpha=0^o$ 83
5.4.2 SIFs, G and Temperature Distributions around the Crack Front for $\alpha=15^o$ 87

5.4.3 SIFs, G and Temperature Distributions around the Crack Front for α=30^o 94
5.4.4 SIFs, G and Temperature Distributions around the Crack Front for α=45^o 100
5.4.5 SIFs, G and Temperature Distributions around the Crack Front for α=60^o 106
5.4.6 Peak Values of Normalized SIFs and G Obtained at Various Inclination Angles for 30^o Crack Front Angle 112
5.4.7 Peak Values of Normalized SIFs and G Obtained at Various Inclination Angles for 45^o Crack Front Angle 117
5.4.8 Peak Values of Normalized SIFs and G Obtained at Various Inclination Angles for 60^o Crack Front Angle 123
5.4.9 Peak Values of Normalized SIFs and G Obtained at Various Inclination Angles for 90^o Crack Front Angle 128
5.4.10 Normalized SIFs and G Distributions with respect to Normalized Time for ϕ=45^o and α=0^o 134
5.4.11 Normalized SIFs and G Distributions with respect to Normalized Time for ϕ=45^o and α=15^o 137
5.4.12 Normalized SIFs and G Distributions with respect to Normalized Time for ϕ=45^o and α=30^o 143
5.4.13 Normalized SIFs and G Distributions with respect to Normalized Time for ϕ=45^o and α=45^o 149
5.4.14 Normalized SIFs and G Distributions with respect to Normalized Time for ϕ=45^o and α=60^o 155
5.4.15 Normalized SIFs and G Distributions with respect to Normalized Time for ϕ=90^o and α=0^o 161
5.4.16 Normalized SIFs and G Distributions with respect to Normalized Time for ϕ=90^o and α=15^o 165
5.4.17 Normalized SIFs and G Distributions with respect to Normalized Time for ϕ=90^o and α=30^o 171

5.4.18 Normalized SIFs and G Distributions with respect to Normalized Time for ϕ=90^o and α=45^o 177
5.4.19 Normalized SIFs and G Distributions with respect to Normalized Time for ϕ=90^o and α=60^o 183

6. CONCLUDING REMARKS 189
REFERENCES 194

LIST OF TABLES

Table 2.1 Thermomechanical properties of the material components used in the FGM coating-bond coat-substrate structure 28

Table 2.2 The values of the exponent p for the corresponding coating types 30

Table 5.1 Calculated normalized mixed mode stress intensity factors K_{In} ,K_{IIn} ,K_{IIIn} for a homogeneous plate subjected to uniform tension, α=0^{o}. 68

Table 5.2 Calculated normalized mixed mode stress intensity factors K_{In} ,K_{IIn} ,K_{IIIn} for a homogeneous plate subjected to uniform tension, α=15^{o}. 69

Table 5.3 Calculated normalized mixed mode stress intensity factors K_{In} ,K_{IIn} ,K_{IIIn} for a homogeneous plate subjected to uniform tension, α=30^{o}. 69

Table 5.4 Calculated normalized mixed mode stress intensity factors K_{In} ,K_{IIn} ,K_{IIIn} for a homogeneous plate subjected to uniform tension, α=45^{o}. 70

Table 5.5 Calculated normalized mixed mode stress intensity factors K_{In} ,K_{IIn} ,K_{IIIn} for a homogeneous plate subjected to uniform tension, α=60^{o}. 71

Table 5.6 Calculated normalized mixed mode stress intensity factors K_{In} ,K_{IIn} ,K_{IIIn} for a homogeneous plate subjected to uniform tension, α=75^{o}. 71

Table 5.7 Calculated dimensionless mixed mode stress intensity factors F_I ,F_{II} and F_{III} for a semi-infinite solid subjected to uniform tension, α=15^{o} 78

Table 5.8 Calculated dimensionless mixed mode stress intensity factors F_I ,F_{II} and F_{III} for a semi-infinite solid subjected to uniform tension, α=30^{o} 79

Table 5.9 Calculated dimensionless mixed mode stress intensity factors F_I ,F_{II} and F_{III} for a semi-infinite solid subjected to uniform tension, α=45^{o} 80

LIST OF FIGURES

Figure 2.1 Variation of stress in front of a crack tip 17

Figure 2.2 Change of energy as crack propagation occurs (specimen fixed on its both ends) 18

Figure 2.3 Change of energy as crack propagation occurs (specimen under fixed load)..... 19

Figure 2.4 Distribution of stresses around the crack tip..... 20

Figure 2.5 Modes of stress intensity factors (SIFs) [25] 21

Figure 2.6 An illustration of mode I stress intensity factor [26] 21

Figure 2.7 An illustration of mode II stress intensity factor [26]..... 23

Figure 2.8 An illustration of mode III stress intensity factor [26] 24

Figure 2.9 The geometry of the FGM coating, bond coat and substrate structure (front view)..... 26

Figure 2.10 The geometry of the FGM coating, bond coat and substrate structure (side view) 26

Figure 2.11 A point *P* located on the crack front by the parametric angle, ϕ..... 27

Figure 2.12 A semi-elliptic inclined surface crack in a plate under uniform tensile remote stresses..... 31

Figure 2.13 A semi-elliptic inclined surface crack in a semi-infinite solid under uniform tensile remote stresses 33

Figure 2.14 Thermal boundary conditions for the FGM coating, bond coat and substrate structure..... 35

Figure 3.1 Global view of the plate containing semi-elliptic crack for 45^{o} inclination angle 40

Figure 3.2 A close-up view of the crack for 45^{o} inclination angle..... 40

Figure 3.3 The SOLID92 element [30] 41

Figure 3.4 The SOLID95 element [30] 41

Figure 3.5 Node numbering of a 20-node isoparametric brick element [20] 42

Figure 3.6 Collapsed 20-node isoparametric brick element [20] 42

Figure 3.7 The elements around the crack-front of a semi-elliptic surface crack . 43

Figure 3.8 Meshes with singular elements at $\pi/2$ crack front angle 43

Figure 3.9 Singular elements around the crack front 44

Figure 3.10 Finite element mesh of the FGM coating-bond coat-substrate structure 47

Figure 3.11 Initial finite element mesh of the FGM coating-bond coat-substrate structure 47

Figure 3.12 New volumes around the “crack tunnel” 49

Figure 3.13 An enlarged view of the fine meshes around the crack front 49

Figure 3.14 The SOLID90 element [30] 50

Figure 4.1 Crack front and the local coordinate system at a point *P* 56

Figure 4.2 Deformed shape of the crack surface (symmetric) 56

Figure 4.3 Deformed shape of the crack surface (non-symmetric)..... 59

Figure 5.1 Comparisons of normalized mixed mode stress intensity factors for 0^{o} inclination angle 74

Figure 5.2 Comparisons of normalized mixed mode stress intensity factors for 15^{o} inclination angle 74

Figure 5.3 Comparisons of normalized mixed mode stress intensity factors for 30^{o} inclination angle 75

Figure 5.4 Comparisons of normalized mixed mode stress intensity factors for 45^o inclination angle 75

Figure 5.5 Comparisons of normalized mixed mode stress intensity factors for 60^o inclination angle 76

Figure 5.6 Comparisons of normalized mixed mode stress intensity factors for 75^o inclination angle 76

Figure 5.7 Comparisons of dimensionless mixed mode stress intensity factors for 15^o inclination angle 81

Figure 5.8 Comparisons of dimensionless mixed mode stress intensity factors for 30^o inclination angle 81

Figure 5.9 Comparisons of dimensionless mixed mode stress intensity factors for 45^o inclination angle 82

Figure 5.10 Distribution of normalized mode I stress intensity factors around crack front for 0^o inclination angle and a/t_1=0.2 84

Figure 5.11 Distribution of normalized mode I stress intensity factors around crack front for 0^o inclination angle and a/t_1=0.4 85

Figure 5.12 Distribution of normalized energy release rates around crack front for 0^o inclination angle and a/t_1=0.2 85

Figure 5.13 Distribution of normalized energy release rates around crack front for 0^o inclination angle and a/t_1=0.4 86

Figure 5.14 Distribution of temperature around crack front for 0^o inclination angle and a/t_1=0.2 86

Figure 5.15 Distribution of temperature around crack front for 0^o inclination angle and a/t_1=0.4 87

Figure 5.16 Distribution of normalized mode I stress intensity factors around crack front for 15^o inclination angle and a/t_1=0.2 89

Figure 5.17 Distribution of normalized mode I stress intensity factors around crack front for 15^o inclination angle and a/t_1=0.4 89

Figure 5.18 Distribution of normalized mode II stress intensity factors around crack front for 15^o inclination angle and a/t_1=0.2 90

Figure 5.19 Distribution of normalized mode II stress intensity factors around crack front for 15^o inclination angle and a/t_1=0.4 90

Figure 5.20 Distribution of normalized mode III stress intensity factors around crack front for 15^o inclination angle and a/t_1=0.2 91

Figure 5.21 Distribution of normalized mode III stress intensity factors around crack front for 15^o inclination angle and a/t_1=0.4 91

Figure 5.22 Distribution of normalized energy release rates around the crack front for 15^o inclination angle and a/t_1=0.2 92

Figure 5.23 Distribution of normalized energy release rates around crack front for 15^o inclination angle and a/t_1=0.4 92

Figure 5.24 Distribution of temperature around crack front for 15^o inclination angle and a/t_1=0.2 93

Figure 5.25 Distribution of temperature around crack front for 15^o inclination angle and a/t_1=0.4 93

Figure 5.26 Distribution of normalized mode I stress intensity factors around crack front for 30^o inclination angle and a/t_1=0.2 95

Figure 5.27 Distribution of normalized mode I stress intensity factors around crack front for 30^o inclination angle and a/t_1=0.4 95

Figure 5.28 Distribution of normalized mode II stress intensity factors around crack front for 30^o inclination angle and a/t_1=0.2 96

Figure 5.29 Distribution of normalized mode II stress intensity factors around crack front for 30^o inclination angle and a/t_1=0.4 96

Figure 5.30 Distribution of normalized mode III stress intensity factors around crack front for 30^o inclination angle and a/t_1=0.2 97

Figure 5.31 Distribution of normalized mode III stress intensity factors around crack front for 30^o inclination angle and a/t_1=0.4 97

Figure 5.32 Distribution of normalized energy release rates around crack front for 30^o inclination angle and a/t_1=0.2 98

Figure 5.33 Distribution of normalized energy release rates around crack front for 30^o inclination angle and a/t_1=0.4 98

Figure 5.34 Distribution of temperature around crack front for 30^o inclination angle and a/t_1=0.2 99

Figure 5.35 Distribution of temperature around crack front for 30^o inclination angle and a/t_1=0.4 99

Figure 5.36 Distribution of normalized mode I stress intensity factors around crack front for 45^o inclination angle and a/t_1=0.2 101

Figure 5.37 Distribution of normalized mode I stress intensity factors around crack front for 45^o inclination angle and a/t_1=0.4 101

Figure 5.38 Distribution of normalized mode II stress intensity factors around crack front for 45^o inclination angle and a/t_1=0.2 102

Figure 5.39 Distribution of normalized mode II stress intensity factors around crack front for 45^o inclination angle and a/t_1=0.4 102

Figure 5.40 Distribution of normalized mode III stress intensity factors around crack front for 45^o inclination angle and a/t_1=0.2 103

Figure 5.41 Distribution of normalized mode III stress intensity factors around crack front for 45^o inclination angle and a/t_1=0.4 103

Figure 5.42 Distribution of normalized energy release rates around crack front for 45^o inclination angle and a/t_1=0.2 104

Figure 5.43 Distribution of normalized energy release rates around crack front for 45^o inclination angle and a/t_1=0.4 104

Figure 5.44 Distribution of temperature around crack front for 45^o inclination angle and a/t_1=0.2 105

Figure 5.45 Distribution of temperature around crack front for 45^o inclination angle and a/t_1=0.4 105

Figure 5.46 Distribution of normalized mode I stress intensity factors around crack front for 60^o inclination angle and a/t_1=0.2 107

Figure 5.47 Distribution of normalized mode I stress intensity factors around crack front for 60^o inclination angle and a/t_1=0.4 107

Figure 5.48 Distribution of normalized mode II stress intensity factors around crack front for 60^o inclination angle and a/t_1=0.2 108

Figure 5.49 Distribution of normalized mode II stress intensity factors around crack front for 60^o inclination angle and a/t_1=0.4 108

Figure 5.50 Distribution of normalized mode III stress intensity factors around crack front for 60^o inclination angle and a/t_1=0.2 109

Figure 5.51 Distribution of normalized mode III stress intensity factors around crack front for 60^o inclination angle and a/t_1=0.4 109

Figure 5.52 Distribution of normalized energy release rates around crack front for 60^o inclination angle and a/t_1=0.2 110

Figure 5.53 Distribution of normalized energy release rates around crack front for 60^o inclination angle and a/t_1=0.4 110

Figure 5.54 Distribution of temperature around crack front for 60^o inclination angle and a/t_1=0.2 111

Figure 5.55 Distribution of temperature around crack front for 60^o inclination angle and a/t_1=0.4 111

Figure 5.56 Peak values of normalized mode I stress intensity factors obtained at various inclination angles for 30^o crack front angle and a/t_1=0.2 113

Figure 5.57 Peak values of normalized mode I stress intensity factors obtained at various inclination angles for 30^o crack front angle and a/t_1=0.4 114

Figure 5.58 Peak values of normalized mode II stress intensity factors obtained at various inclination angles for 30^o crack front angle and a/t_1=0.2 114

Figure 5.59 Peak values of normalized mode II stress intensity factors obtained at various inclination angles for 30^o crack front angle and a/t_1=0.4 115

Figure 5.60 Peak values of normalized mode III stress intensity factors obtained at various inclination angles for 30^o crack front angle and a/t_1=0.2 115

Figure 5.61 Peak values of normalized mode III stress intensity factors obtained at various inclination angles for 30^o crack front angle and a/t_1=0.4 116

Figure 5.62 Peak values of normalized energy release rates obtained at various inclination angles for 30^o crack front angle and a/t_1=0.2 116

Figure 5.63 Peak values of normalized energy release rates obtained at various inclination angles for 30^o crack front angle and a/t_1=0.4 117

Figure 5.64 Peak values of normalized mode I stress intensity factors obtained at various inclination angles for 45^o crack front angle and a/t_1=0.2 119

Figure 5.65 Peak values of normalized mode I stress intensity factors obtained at various inclination angles for 45^o crack front angle and a/t_1=0.4 119

Figure 5.66 Peak values of normalized mode II stress intensity factors obtained at various inclination angles for 45^o crack front angle and a/t_1=0.2 120

Figure 5.67 Peak values of normalized mode II stress intensity factors obtained at various inclination angles for 45^o crack front angle and a/t_1=0.4 120

Figure 5.68 Peak values of normalized mode III stress intensity factors obtained at various inclination angles for 45^o crack front angle and a/t_1=0.2 121

Figure 5.69 Peak values of normalized mode III stress intensity factors obtained at various inclination angles for 45^o crack front angle and a/t_1=0.4 121

Figure 5.70 Peak values of normalized energy release rates obtained at various inclination angles for 45^o crack front angle and a/t_1=0.2 122

Figure 5.71 Peak values of normalized energy release rates obtained at various inclination angles for 45^o crack front angle and a/t_1=0.4 122

Figure 5.72 Peak values of normalized mode I stress intensity factors obtained at various inclination angles for 60^o crack front angle and a/t_1=0.2 124

Figure 5.73 Peak values of normalized mode I stress intensity factors obtained at various inclination angles for 60^o crack front angle and a/t_1=0.4 125

Figure 5.74 Peak values of normalized mode II stress intensity factors obtained at various inclination angles for 60^o crack front angle and a/t_1=0.2 125

Figure 5.75 Peak values of normalized mode II stress intensity factors obtained at various inclination angles for 60^o crack front angle and a/t_1=0.4 126

Figure 5.76 Peak values of normalized mode III stress intensity factors obtained at various inclination angles for 60^o crack front angle and a/t_1=0.2 126

Figure 5.77 Peak values of normalized mode III stress intensity factors obtained at various inclination angles for 60^o crack front angle and a/t_1=0.4 127

Figure 5.78 Peak values of normalized energy release rates obtained at various inclination angles for 60^o crack front angle and a/t_1=0.2 127

Figure 5.79 Peak values of normalized energy release rates obtained at various inclination angles for 60^o crack front angle and a/t_1=0.4 128

Figure 5.80 Peak values of normalized mode I stress intensity factors obtained at various inclination angles for 90^o crack front angle and a/t_1=0.2 130

Figure 5.81 Peak values of normalized mode I stress intensity factors obtained at various inclination angles for 90^o crack front angle and a/t_1=0.4 130

Figure 5.82 Peak values of normalized mode II stress intensity factors obtained at various inclination angles for 90^o crack front angle and a/t_1=0.2 131

Figure 5.83 Peak values of normalized mode II stress intensity factors obtained at various inclination angles for 90^o crack front angle and a/t_1=0.4 131

Figure 5.84 Peak values of normalized mode III stress intensity factors obtained at various inclination angles for 90^o crack front angle and a/t_1=0.2 132

Figure 5.85 Peak values of normalized mode III stress intensity factors obtained at various inclination angles for 90^o crack front angle and a/t_1=0.4 132

Figure 5.86 Peak values of normalized energy release rates obtained at various inclination angles for 90^o crack front angle and a/t_1=0.2 133

Figure 5.87 Peak values of normalized energy release rates obtained at various inclination angles for 90^o crack front angle and a/t_1=0.4 133

Figure 5.88 Normalized mode I stress intensity factors at 45^o crack front angle with respect to normalized time, a/t_1=0.2 and α=0^o 135

Figure 5.89 Normalized mode I stress intensity factors at 45^o crack front angle with respect to normalized time, a/t_1=0.4 and α=0^o 135

Figure 5.90 Normalized energy release rate at 45^o crack front angle with respect to normalized time, a/t_1=0.2 and α=0^o 136

Figure 5.91 Normalized energy release rate at 45^o crack front angle with respect to normalized time, a/t_1=0.4 and α=0^o 136

Figure 5.92 Normalized temperature at 45^o crack front angle with respect to normalized time, a/t_1=0.4 and α=0^o 137

Figure 5.93 Normalized mode I stress intensity factors at 45^o crack front angle with respect to normalized time, a/t_1=0.2 and α=15^o 139

Figure 5.94 Normalized mode I stress intensity factors at 45^o crack front angle with respect to normalized time, a/t_1=0.4 and α=15^o 139

Figure 5.95 Normalized mode II stress intensity factors at 45^o crack front angle with respect to normalized time, a/t_1=0.2 and α=15^o 140

Figure 5.96 Normalized mode II stress intensity factors at 45^o crack front angle with respect to normalized time, a/t_1=0.4 and α=15^o 140

Figure 5.97 Normalized mode III stress intensity factors at 45^o crack front angle with respect to normalized time, a/t_1=0.2 and α=15^o 141

Figure 5.98 Normalized mode III stress intensity factors at 45^o crack front angle with respect to normalized time, a/t_1=0.4 and α=15^o 141

Figure 5.99 Normalized energy release rate at 45^o crack front angle with respect to normalized time, a/t_1=0.2 and α=15^o 142

Figure 5.100 Normalized energy release rate at 45^o crack front angle with respect to normalized time, a/t_1=0.4 and α=15^o 142

Figure 5.101 Normalized temperature at 45^o crack front angle with respect to normalized time, a/t_1=0.4 and α=15^o 143

Figure 5.102 Normalized mode I stress intensity factors at 45^o crack front angle with respect to normalized time, a/t_1=0.2 and α=30^o 145

Figure 5.103 Normalized mode I stress intensity factors at 45^o crack front angle with respect to normalized time, a/t_1=0.4 and α=30^o 145

Figure 5.104 Normalized mode II stress intensity factors at 45^o crack front angle with respect to normalized time, a/t_1=0.2 and α=30^o 146

Figure 5.105 Normalized mode II stress intensity factors at 45^o crack front angle with respect to normalized time, a/t_1=0.4 and α=30^o 146

Figure 5.106 Normalized mode III stress intensity factors at 45^o crack front angle with respect to normalized time, a/t_1=0.2 and α=30^o 147

Figure 5.107 Normalized mode III stress intensity factors at 45^o crack front angle with respect to normalized time, a/t_1=0.4 and α=30^o 147

Figure 5.108 Normalized energy release rate at 45^o crack front angle with respect to normalized time, a/t_1=0.2 and α=30^o 148

Figure 5.109 Normalized energy release rate at 45^o crack front angle with respect to normalized time, a/t_1=0.4 and α=30^o 148

Figure 5.110 Normalized temperature at 45^o crack front angle with respect to normalized time, a/t_1=0.4 and α=30^o 149

Figure 5.111 Normalized mode I stress intensity factors at 45^o crack front angle with respect to normalized time, a/t_1=0.2 and α=45^o 151

Figure 5.112 Normalized mode I stress intensity factors at 45^o crack front angle with respect to normalized time, a/t_1=0.4 and α=45^o 151

Figure 5.113 Normalized mode II stress intensity factors at 45^o crack front angle with respect to normalized time, a/t_1=0.2 and α=45^o 152

Figure 5.114 Normalized mode II stress intensity factors at 45^o crack front angle with respect to normalized time, a/t_1=0.4 and α=45^o 152

Figure 5.115 Normalized mode III stress intensity factors at 45^o crack front angle with respect to normalized time, a/t_1=0.2 and α=45^o 153

Figure 5.116 Normalized mode III stress intensity factors at 45^o crack front angle with respect to normalized time, a/t_1=0.4 and α=45^o 153

Figure 5.117 Normalized energy release rate at 45^o crack front angle with respect to normalized time, a/t_1=0.2 and α=45^o 154

Figure 5.118 Normalized energy release rate at 45^o crack front angle with respect to normalized time, a/t_1=0.4 and α=45^o 154

Figure 5.119 Normalized temperature at 45^o crack front angle with respect to normalized time, a/t_1=0.4 and α=45^o 155

Figure 5.120 Normalized mode I stress intensity factors at 45^o crack front angle with respect to normalized time, a/t_1=0.2 and α=60^o 157

Figure 5.121 Normalized mode I stress intensity factors at 45^o crack front angle with respect to normalized time, a/t_1=0.4 and α=60^o 157

Figure 5.122 Normalized mode II stress intensity factors at 45^o crack front angle with respect to normalized time, a/t_1=0.2 and α=60^o 158

Figure 5.123 Normalized mode II stress intensity factors at 45^o crack front angle with respect to normalized time, a/t_1=0.4 and α=60^o 158

Figure 5.124 Normalized mode III stress intensity factors at 45^o crack front angle with respect to normalized time, a/t_1=0.2 and α=60^o 159

Figure 5.125 Normalized mode III stress intensity factors at 45^o crack front angle with respect to normalized time, a/t_1=0.4 and α=60^o 159

Figure 5.126 Normalized energy release rate at 45^o crack front angle with respect to normalized time, a/t_1=0.2 and α=60^o 160

Figure 5.127 Normalized energy release rate at 45^o crack front angle with respect to normalized time, a/t_1=0.4 and α=60^o 160

Figure 5.128 Normalized temperature at 45^o crack front angle with respect to normalized time, a/t_1=0.4 and α=60^o 161

Figure 5.129 Normalized mode I stress intensity factors at 90^o crack front angle with respect to normalized time, a/t_1=0.2 and α=0^o 162

Figure 5.130 Normalized mode I stress intensity factors at 90^o crack front angle with respect to normalized time, a/t_1=0.4 and α=0^o 163

Figure 5.131 Normalized energy release rate at 90^o crack front angle with respect to normalized time, a/t_1=0.2 and α=0^o 163

Figure 5.132 Normalized energy release rate at 90^o crack front angle with respect to normalized time, a/t_1=0.4 and α=0^o 164

Figure 5.133 Normalized temperature at 90^o crack front angle with respect to normalized time, a/t_1=0.4 and α=0^o 164

Figure 5.134 Normalized mode I stress intensity factors at 90^o crack front angle with respect to normalized time, a/t_1=0.2 and α=15^o 166

Figure 5.135 Normalized mode I stress intensity factors at 90^o crack front angle with respect to normalized time, a/t_1=0.4 and α=15^o 167

Figure 5.136 Normalized mode II stress intensity factors at 90^o crack front angle with respect to normalized time, a/t_1=0.2 and α=15^o 167

Figure 5.137 Normalized mode II stress intensity factors at 90^o crack front angle with respect to normalized time, a/t_1=0.4 and α=15^o 168

Figure 5.138 Normalized mode III stress intensity factors at 90^o crack front angle with respect to normalized time, a/t_1=0.2 and α=15^o 168

Figure 5.139 Normalized mode III stress intensity factors at 90^o crack front angle with respect to normalized time, a/t_1=0.4 and α=15^o 169

Figure 5.140 Normalized energy release rate at 90^o crack front angle with respect to normalized time, a/t_1=0.2 and α=15^o 169

Figure 5.141 Normalized energy release rate at 90^o crack front angle with respect to normalized time, a/t_1=0.4 and α=15^o 170

Figure 5.142 Normalized temperature at 90^o crack front angle with respect to normalized time, a/t_1=0.4 and α=15^o 170

Figure 5.143 Normalized mode I stress intensity factors at 90^o crack front angle with respect to normalized time, a/t_1=0.2 and α=30^o 172

Figure 5.144 Normalized mode I stress intensity factors at 90^o crack front angle with respect to normalized time, a/t_1=0.4 and α=30^o 173

Figure 5.145 Normalized mode II stress intensity factors at 90^o crack front angle with respect to normalized time, a/t_1=0.2 and α=30^o 173

Figure 5.146 Normalized mode II stress intensity factors at 90^o crack front angle with respect to normalized time, a/t_1=0.4 and α=30^o 174

Figure 5.147 Normalized mode III stress intensity factors at 90^o crack front angle with respect to normalized time, a/t_1=0.2 and α=30^o 174

Figure 5.148 Normalized mode III stress intensity factors at 90^o crack front angle with respect to normalized time, a/t_1=0.4 and α=30^o 175

Figure 5.149 Normalized energy release rate at 90^o crack front angle with respect to normalized time, a/t_1=0.2 and α=30^o 175

Figure 5.150 Normalized energy release rate at 90^o crack front angle with respect to normalized time, a/t_1=0.4 and α=30^o 176

Figure 5.151 Normalized temperature at 90^o crack front angle with respect to normalized time, a/t_1=0.4 and α=30^o 176

Figure 5.152 Normalized mode I stress intensity factors at 90^o crack front angle with respect to normalized time, a/t_1=0.2 and α=45^o 178

Figure 5.153 Normalized mode I stress intensity factors at 90^o crack front angle with respect to normalized time, a/t_1=0.4 and α=45^o 179

Figure 5.154 Normalized mode II stress intensity factors at 90^o crack front angle with respect to normalized time, a/t_1=0.2 and α=45^o 179

Figure 5.155 Normalized mode II stress intensity factors at 90^o crack front angle with respect to normalized time, a/t_1=0.4 and α=45^o 180

Figure 5.156 Normalized mode III stress intensity factors at 90^o crack front angle with respect to normalized time, a/t_1=0.2 and α=45^o 180

Figure 5.157 Normalized mode III stress intensity factors at 90^o crack front angle with respect to normalized time, a/t_1=0.4 and α=45^o 181

Figure 5.158 Normalized energy release rate at 90^o crack front angle with respect to normalized time, a/t_1=0.2 and α=45^o 181

Figure 5.159 Normalized energy release rate at 90^o crack front angle with respect to normalized time, a/t_1=0.4 and α=45^o 182

Figure 5.160 Normalized temperature at 90^o crack front angle with respect to normalized time, a/t_1=0.4 and α=45^o 182

Figure 5.161 Normalized mode I stress intensity factors at 90^o crack front angle with respect to normalized time, a/t_1=0.2 and α=60^o 184

Figure 5.162 Normalized mode I stress intensity factors at 90^o crack front angle with respect to normalized time, a/t_1=0.4 and α=60^o 185

Figure 5.163 Normalized mode II stress intensity factors at 90^o crack front angle with respect to normalized time, a/t_1=0.2 and α=60^o 185

Figure 5.164 Normalized mode II stress intensity factors at 90^o crack front angle with respect to normalized time, a/t_1=0.4 and α=60^o 186

Figure 5.165 Normalized mode III stress intensity factors at 90^o crack front angle with respect to normalized time, a/t_1=0.2 and α=60^o 186

Figure 5.166 Normalized mode III stress intensity factors at 90^o crack front angle with respect to normalized time, a/t_1=0.4 and α=60^o 187

Figure 5.167 Normalized energy release rate at 90^o crack front angle with respect to normalized time, a/t_1=0.2 and α=60^o 187

Figure 5.168 Normalized energy release rate at 90^o crack front angle with respect to normalized time, a/t_1=0.4 and α=60^o 188

Figure 5.169 Normalized temperature at 90^o crack front angle with respect to normalized time, a/t_1=0.4 and α=60^o 188

LIST OF SYMBOLS

a	Crack Depth
W	Work Done by External Forces
P	Potential Energy Supplied by the Internal Strain Energy and External Forces
G	Strain Energy Release Rate
G_c	Critical Strain Energy Release Rate
U	Strain Energy Stored in the Body per Unit Thickness
K	Stress Intensity Factor
K_c	Critical Stress Intensity Factor
E	Modulus of Elasticity
σ	Tensile Stress
r	Distance from the Crack Tip
σ_{ij}	Stress Components
u_i	Displacement Components
θ	Angle from the Crack Plane
κ	3-4v
μ	Shear Modulus
t_1	Thickness of the FGM Coating
t_2	Thickness of the Bond Coat
t_3	Thickness of the Substrate
c	Crack Length
α	Crack Inclination Angle
ϕ	Parametric Angle
b	Half Width of the Composite Structure
h	Half Length of the Composite Structure

v	Poisson's Ratio
α_t	Thermal Expansion Coefficient
k	Thermal Conductivity
ρ	Density
c_t	Specific Heat
D	Thermal Diffusivity
Q	Shape Factor for Elliptical Crack
K_R	Normalization factor for Stress Intensity Factors
K_I	Mode I Stress Intensity Factor
K_{II}	Mode II Stress Intensity Factor
K_{III}	Mode III Stress Intensity Factor
K_{In}	Normalized Mode I Stress Intensity Factor
K_{IIn}	Normalized Mode II Stress Intensity Factor
K_{IIIn}	Normalized Mode III Stress Intensity Factor
F_I	Dimensionless Mode I Stress Intensity Factor
F_{II}	Dimensionless Mode II Stress Intensity Factor
F_{III}	Dimensionless Mode III Stress Intensity Factor
T_i	Initial Temperature of the Composite Medium
T_o	Temperature of the Environment
h_c	Convection Coefficient
S	The Normalization Stress
G_n	Normalized Energy Release Rate
t	Time
τ	Normalized Time

CHAPTER 1

INTRODUCTION

Metals and their alloys have been widely used in various applications because of their mechanical properties like high fracture toughness and excellent resistance to thermal shocks. From the beginning of the human history, people have been using metals such as copper and iron to make weapons, vehicles and everyday objects. However, the use of metals and their alloys has always been limited, due to their poor strength related properties at high temperatures. This restriction necessitated the use of advanced materials like Functionally Graded Materials, or FGMs, which are made from a mixture of ceramics and metals.

Researches focusing on the processing of structural metals, ceramics, intermetallics and composites have contributed to development in the properties and performance of these materials. Advanced ceramics, ceramic-metal composites, and intermetallics are destined to become base for complex monomaterial or multimaterial structures exhibiting improved or novel functionality [1]. FGMs, which are first developed in the late 1980s, are special types of composite materials characterized by continuously changing material properties due to graded compositions from one surface to the other [2].

FGMs are needed for advanced high temperature structural applications and required to have strength at high temperature, creep resistance, adequate toughness and thermal shock resistance. Joining ceramics to metals, to combine

inherent advantages of these two kinds of materials, has been pursued to meet the material requirements in many applications [3].

The ceramic constituents of the FGMs are able to withstand high-temperature environments due to their better high heat resistance, high temperature strength and creep resistance, and they possess advance properties such as low density. Metal constituents, on the other hand, provide stronger mechanical performance, reduce the possibility of catastrophic fracture and possess excellent thermal shock resistance. Due to their superior thermo-mechanical properties, FGMs have found extensive use in high-performance structural components employed in high temperature environments [4]. Although they have great potential for applications in safety-critical structures such as nuclear fusion reactors, aircraft fuselages, microelectronic devices and biomaterials, the greatest area of usage appears to be the thermal barrier protection of turbines engines, which operates at high temperatures. FGMs are mainly used to protect metallic parts against excessive heat in high temperature aerospace applications, such as aircraft engines, stationary gas turbines and combustion chambers [5]. For instance, the engine components of a gas turbine are subject to rigorous mechanical loadings, high temperatures, and corrosive or erosive media [6]. In such severe environments, FGMs are widely used as thermal barriers.

FGMs are basically inhomogeneous particulate composites in which the volume fractions of the constituents and possibly the microstructure of the medium are varied continuously in the thickness direction [7]. They are essentially two-phase particulate composites whose composition, microstructure and properties vary gradually. Continuous changes in their microstructure distinguish FGMs from conventional composite materials. This continuous change in composition results in gradients in the properties of FGMs. The volume fractions of the constituents in an FGM usually vary continuously from 100% ceramic at the surface to 0% at the interface [5]. Therefore, a typical FGM structure, varying in volume fraction with distance, consists of a change from fully ceramic on one side to fully metal on the

other side, with the intermediate region composed of a mixture of both constituents.

Because of the special composition of the FGMs, the conditions for both high temperature and high toughness can be fulfilled simultaneously. The application of FGMs as coatings reduces the magnitude of residual stresses and increases the bonding strength. In FGM coatings, due to the existence of the gradual increase of the metal content in thickness direction, the toughness of the material also increases.

Since FGMs are mainly used at high temperatures and are opposed to high heating rates, the determination of transient temperature fields of these materials are rather important. However, it is rather difficult to evaluate the temperature distribution because of the arbitrarily distributed and continuously varied material properties of FGMs. Since most of FGMs show one-dimensional non-homogeneity, the temperature field can be readily obtained by composite laminated plate model for simple one dimensional heat conduction [8].

The fracture initiation of FGM coatings is in the form of part-through surface crack because of the fact that they are brittle materials. The reason of the surface cracking of FGMs may both be due to mechanical or thermal loading. For instance, if an FGM - substrate structure is cooled down from an initially high processing temperature; part-through surface cracks at the FGM side can be initiated as a result of the high transient tensile residual stresses. The complex behavior of this crack initiation requires a three dimensional analysis of the surface cracks in FGMs.

In this study, a three dimensional semi-elliptic inclined surface crack in an FGM coating, bond coat and substrate system is considered. The behavior of the surface crack in this structure is analyzed under transient thermal loading with the help of three dimensional finite element analyses.

1.1 Literature Survey

There have been too many studies dealing with the concept of fracture mechanics since the beginning of the 20th century. Surface crack problems in homogeneous and functionally graded materials are also considered by various researchers in the past. However, in most of the previous studies in the literature, the crack problems studied are limited to either two dimensional or axisymmetric geometries. Furthermore, most of these studies are concentrated on only mode I loading where mode II and mode III stress intensity factors are zero along the crack front. Moreover, the loading type considered in those studies is just the mechanical loading.

Because of the information given above and to the author's best knowledge, the present study can be considered as one of the first in the literature dealing with three dimensional cracks in FGMs under mixed-mode thermomechanical loading.

A semi-elliptical surface crack arbitrarily inclined to the free surface of a semi-infinite solid subjected to tension is analyzed in the study of Isida, Tokumoto and Noguchi [9]. Since the semi-elliptical surface crack is obliquely inclined to the solid surface, mixed mode deformation is seen within the semi-infinite solid. In this paper, the analysis is carried out by body force method. The crack domain is divided into fan-wise elements, and general types of body forces, whose densities are assumed as step functions having constant weights in each of the elements, are distributed. The unknown weights of the body force densities are determined from the traction-free conditions, which are replaced by those at the central points of all the crack elements, on the crack surface. The numerical calculations are carried out for all possible combinations of 0^o, 15^o, 30^o and 45^o inclination angles and ten values of crack aspect ratios (crack depth/crack length). In addition, the Poisson's ratio of the material is taken as 0.3. The dimensionless mode I, II and III stress intensity factors (SIFs) are fitted to reliable polynomials in several figures for 15^o, 30^o and 45^o inclination angles for different crack front position angles and crack aspect ratios. Furthermore, dimensionless mode I and II SIFs values are tabulated

for 90^o crack front position angle for various shapes and inclination angles of the crack.

Noda et al. [10] developed a singular integral equation method in order to calculate the stress intensity factor along crack front of a 3D inclined semi-elliptical surface crack in a semi-infinite body under tension. In this study, the solution is obtained via the stress field induced by displacement discontinuities in a semi-infinite body. In the numerical calculation, the unknown body force densities are approximated by using the product of fundamental density functions and polynomials. In the analyses carried out, the effects of inclination angle, crack aspect ratios (crack depth/crack length), and Poisson's ratio are taken into account. In this paper, it is concluded that the analysis of mixed mode 3D cracks is more difficult than that of mode I 3D cracks due to triple number of unknown functions and boundary conditions. Additionally, it is stated that obtaining accurate stress intensity factors near the free surface for inclination angles greater than 45^o is difficult since the effect of free surface on the results is complicated.

Finite element based mixed mode stress intensity factor solutions are presented for deflected and inclined surface cracks in finite-thickness plates under uniform tensile remote loading in the paper by Ayhan [11]. The effects of deflection and inclination angles ranging from 0^o to 75^o and crack length/plate thickness ratio ranging from 0.2 to 0.8 on the mixed mode stress intensity factors are analyzed. For the numerical calculations, FRAC3D, a general-purpose finite element based 3-D fracture analysis program, is used. It is demonstrated that the enriched finite element technique provides fracture solutions for these types of problems in a very direct and convenient manner. It is shown that decreasing the plate thickness results in magnification of mixed mode stress intensity factors along the crack front. By using the computed mixed mode stress intensity factors, crack propagation angles along the deflected and inclined crack fronts are also determined.

In the study by Kadıoğlu, Dağ and Yahşi [12], internal and edge crack problems for an FGM layer attached to an elastic foundation are considered. It is assumed that in the thickness direction, the mechanical properties are not constant. The crack in the FGM layer is assumed to be perpendicular to the surfaces. In this paper, for different crack surface tractions, stress intensity factors are calculated.

In the paper by Jin and Paulino [13], an edge crack in a strip of a functionally graded material is studied under transient thermal loading conditions. Since it is assumed that the FGM has constant Young's modulus and Poisson's ratio, but the thermal properties of the material vary along the thickness direction of the strip, it is concluded that the material is elastically homogeneous but thermally nonhomogeneous. In order to solve the temperature field, a multi-layered material model is used. An analytical first order temperature solution for short times is obtained with the help of the Laplace transform and an asymptotic analysis. Thermal stress intensity factors (TSIFs) are calculated for a TiC/SiC FGM, and the effect of the volume fraction profiles of the constituent materials on thermal stresses and TSIFs is discussed. It is concluded that the TSIF could be reduced if the thermally shocked cracked edge of the FGM strip is pure TiC, whereas the TSIF is increased if the thermally shocked edge is pure SiC.

Wang et al. [14] investigated an embedded or a surface crack in a functionally graded material, which is considered to have arbitrarily distributed material properties in the through-thickness direction. The graded region is assumed to be consisted of a large number of single layers, with each layer being homogeneous material. The problem is reduced to an integral equation and is solved numerically. Two analyses are carried out in this paper. First one is the case of applying a uniform mechanical pressure σ on the crack surfaces. Secondly, the fracture of the FGM caused by a non-uniform thermal stress distribution is considered. For both cases, mode I stress intensity factor is calculated for different crack lengths and property distributions.

In the study of Wang et al. [15], a method for the mode II in plane and mode III anti-plane elastic crack problems for an FGM strip containing a crack along the gradient direction is analyzed. In the analysis, the FGM region is divided into some homogeneous sub-layers along the direction of the thickness. It is assumed that the properties of the strip vary along its thickness direction. [14] and [15] completes the analysis of the mixed-mode crack problem for an infinite length FGM strip with a crack parallel the gradient direction. By using the models developed in this paper and that developed in [14], it is possible to optimize the property distributions of FGMs.

Guo et al. [16] investigated the static crack problem of a functionally graded coating-substrate structure with an internal or edge crack perpendicular to the interface under an in-plane load. It is assumed that the material properties are varying continuously from the coating to the substrate. In order to solve the problem numerically, the mixed boundary value problem is reduced to a singular integral equation with the help of integral transform methods. The influences of material constants and the geometry parameters on the stress intensity factors (SIFs) are analyzed.

The transient response of the functionally graded coating-substrate system with an internal or edge crack perpendicular to the interface under an in-plane impact is additionally analyzed by Guo et al [17]. In this paper, the normalized dynamic stress intensity factors (DSIFs) in the real time domain are obtained by the numerical inversion formula of the Laplace transform. Additionally, the influences of parameters such as the nonhomogeneity constant, crack length and thickness ratio on the DSIFs are studied. It is found that the DSIFs for an internal crack rise rapidly to a peak and then go to the steady value without obvious oscillations, whereas the DSIFs for an edge crack have more obvious oscillations after rising to a peak with the increasing of the nonhomogeneity constant.

In the study of Chi and Chung [18], the stress intensity factors (SIFs) of cracked multi-layered and functionally graded material (FGM) coatings of a coating–

substrate composite, due to the action of uniform normal stress on the crack surfaces are investigated. It is assumed that the substrate is a homogeneous material, whereas the coating consists of multi-layered media or sigmoid FGMs. In this study, for the multi-layered coatings, one, two, and four-layered homogeneous coatings with stepwise changing volume fractions are considered. The appearance of a crack in the coating surface and its growth into the substrate along the direction perpendicular to the interface between the coating and the substrate is analyzed. The results of this paper show that if the coating is stiffer than the substrate, a crack in a one-layered coating is much more susceptible to propagation into the substrate than a crack in the two- or four-layered coating. It is concluded that the crack growth can be effectively prevented by using an S-FGM coating. However, if the coating is softer than the substrate, the S-FGM coating helps the expansion of the crack into the substrate. Whereas it is shown that the one-layered coating can more effectively prevent the crack from propagating into the substrate than two- or four-layered coating. The investigation also indicates that the material gradations of S-FGMs influence SIFs obviously only when the crack tip is inside the coating that is stiffer than the substrate. As the crack extends through the coating and into the substrate, the material gradation of the S-FGM coating and the material mismatch of the multi-layered coating slightly resist on the values of SIFs.

In the paper by Lee and Erdoğan [19], the plane strain thermal stress problem for an interface crack in a homogeneous substrate with a graded coating is considered. The substrate is taken as a superalloy and the graded coating is also taken as a superalloy and partially stabilized zirconia. It is assumed that the proportion of the zirconia varies continuously from 0% at the interface to 100% at the surface. The surface of the coating is exposed to a high-temperature environment, whereas the surface of the substrate is forced-cooled. The ends of the specimen are subjected to natural convection and the surfaces of the crack are assumed to be partially insulated. Therefore, the structure is under steady-state heat conduction with convective boundary conditions. The thermal stress problem is solved for various composition profiles in the coating, including 100% ceramic.

For various values of the heat conductivity index, which describes the insulation condition on the crack surface, the temperature distribution on the surfaces of the substrate and coating are shown. The sample results presented in this paper covers the temperature distribution on the surfaces of the substrate and coating, along the interface and on the crack surfaces and the total heat flow across the substrate surface. For different types of FGM coatings, mode I and mode II SIFs and the strain energy release rate are also presented.

In the study of Yıldırım, Dağ and Erdoğan [20], the three dimensional surface crack problems in functionally graded coatings subjected to mode I mechanical or transient thermal loading are investigated. The behavior of a semi-elliptical surface crack in an FGM coating bonded to a homogeneous substrate is analyzed. The coating-substrate structure is assumed to be subjected to mode I thermomechanical loading. A three dimensional finite element technique is used to examine the behavior of semi-elliptical surface cracks of arbitrary aspect ratio in FGM coatings. The mode I stress intensity factors are computed for FGM coatings subjected to thermomechanical loading with the help of displacement correlation technique (DCT). Four different coating types are examined in the analyses: a homogeneous ceramic coating (H), a ceramic rich coating (CR), a metallic rich coating (MR) and a coating with linear variation (LN). The considered loading types are fixed-grip tension, three point bending and transient thermal loading. Parametric analyses are carried out to examine the effects of the coating type, crack length and semi-ellipse aspect ratio on the mode I stress intensity factors. In the transient thermal loading, temperature and stress intensity factor distributions around the crack front are computed as functions of time.

Yıldırım et al. [21] developed a new method based on the J-integral for fracture analysis of functionally graded materials (FGMs) under thermal stresses. In this study, with the help of equivalent domain integral, line integral definition of J is converted to an area integral around the crack tip for both plane stress and plane strain problems of thermoelasticity. Using the fracture mechanics analysis program FRAC2D by integrating the developed formulation, stress intensity

factors at the tips of mode I cracks are calculated by graded and cubic finite elements. Steady-state and transient thermal loading problems are analyzed numerically in order to investigate the accuracy and reliability of the developed method. The results calculated by an enriched finite element method are compared with those in the literature. The comparisons reveal that the equivalent domain integral approach used in this study produces highly accurate results. Moreover, it is seen that the computed results are independent of the size of the area used in the computation of the domain integral. Therefore, it is concluded that the developed technique possesses the required domain independence.

In the paper by Long and Delale [22], the plane elasticity problem of an arbitrarily oriented crack in an FGM layer bonded to a homogeneous half plane is studied. The problem considered in this paper is modeled by assuming that the elastic properties of the FGM layer are exponential functions of the thickness coordinate. It is further assumed that, these elastic properties are continuous at the interface of the FGM layer and the half-plane. By using the Fourier transform technique, the problem is formulated in terms of a system of Cauchy-type singular integral equations. Then, these equations are solved numerically to obtain the stress intensity factors at the crack tips of various crack orientations. In this paper, the Poisson's ratio is taken to be constant. The results obtained in this paper show that crack length, crack orientation and the nonhomogeneity parameter of the strip material have significant effect on the fracture of the FGM layer.

Shabana and Noda [23] investigated the thermo-elastoplastic stresses in an FGM structure, which is consisted of an FGM bonded to a homogeneous coating layer and a metal substrate, by using finite element method. In order to obtain more accurate thermal stresses in the FGM structure, a microscopic elasto-plastic constitutive equation of particle- reinforced composite is considered with the temperature-dependent properties of the constituent materials. Since the coating layer increases the protection from heat but decreases the thermal shock resistance and the substrate layer increases the rigidity of the structure and decreases strength related properties at high temperature, different values of the substrate

and coating thickness are studied in order to evaluate their effects on the thermal stress response of the FGM structure so as to compromise the thickness of both the coating and substrate layers. Additionally, the effects of the functional form of gradation including the presence and structural arrangement of monolithic ceramic-metal regions in combination with the graded region on the different stress components are examined. First, the FGM structure is cooled down from the production temperature to the room temperature. Then, the structure is heated to its operating temperature after it has reached the steady state temperature. By this sequence, the thermo-elasto-plastic stresses are evaluated by considering the residual stresses coming out due to the heating process faced during the manufacturing of the FGM structure. In order to investigate the importance of the consideration of the residual stresses arising from the production process, an FGM structure with stress-free conditions is also heated to the operating temperature. Then, its thermal stress response is compared with that of an FGM structure having residual stresses. Moreover, several functional forms of gradation of the constituents in the FGM layer are examined, so as to find the optimum profile, which gives the minimum stress level for the FGM structure under thermo-elasto-plastic behavior.

The formulation, solution and investigation of a semi-infinite edge cracked FGM plate with a bi-directional coefficient of thermal expansion under two-dimensional thermal loading is analyzed by Nemat-Alla and Noda [24]. In this study, it is shown that the solution of the boundary value problem, which can be obtained from the mathematical formulation of the crack problem considered in this paper under thermal loading, can be reduced to an integral equation with a generalized Cauchy kernel. This integral equation contains many two-dimensional double singular integrals, which can be solved numerically. In order to separate the singular terms and to avoid the divergence of the integrals, an asymptotic analysis is carried out for the singular parts in the obtained integral equation. In addition, the exact solution for many singular integrals is obtained. The obtained numerical results are used to represent the thermal stress intensity factor versus the thermal/mechanical nonhomogeneous parameters. The numerical results obtained

in this paper show that it is possible to reduce and control the thermal stress intensity factor.

1.2 Scope of the Study

The main objective of this study is to investigate three dimensional semi-elliptic inclined surface cracks in functionally graded materials (FGMs) subjected to transient thermal loading. The surface cracks are assumed to have semi-elliptic crack front profile. The cracks are embedded in the FGM coating which is perfectly bonded to a homogeneous substrate with a bond coat. FGM coating is 100% zirconia-yttria (ZrO2-8wt%-Y_2O_3) at x=0 and 100% NiCrAlY at x=t_1 (Figure 2.10). Substrate is assumed to be made of a nickel-based superalloy. There is a nickel chromium–aluminum–zirconium (NiCrAlY) bond coat between the coating and substrate.

A three dimensional finite element model containing a semi-elliptic inclined surface crack in FGM, which is bonded to a nickel-based superalloy substrate with a nickel chromium–aluminum–zirconium (NiCrAlY) bond coat, is generated with the help of commercial finite element program ANSYS [29]. In order to model the crack tip singularity, quarter point three dimensional finite elements are used around the crack front. After the displacement field is obtained from the commercial finite element code, displacement correlation technique is utilized to evaluate mode I, mode II and mode III stress intensity factors (SIFs). After the calculation of the mixed-mode SIFs, energy release rate (G) is obtained.

Since the material parameters in the asymptotic displacement expressions in FGMs are functions of the spatial coordinates, it is not possible to use standard SIFs computation functions existing in ANSYS library. As a consequence of this reason, new ANSYS Parametric Design Language (APDL) subroutines are generated in order to evaluate the mixed-mode SIFs under thermomechanical loading. The accuracy of the model used for the analysis of FGM-bond coat-substrate structure is validated by comparing calculated mixed-mode stress

intensity factors, which are obtained under tensile remote loading, with those given in the papers of Ayhan et al. [11] and Isida et al. [9].

In the fracture analysis of the semi-elliptical surface cracks in FGM coatings, material property variations are appointed by specifying the thermomechanical properties of each finite element at its centroid. The mixed-mode stress intensity factors are computed for FGM coating-bond coat- substrate system under transient thermal analysis. In the transient thermal analysis, four different types of coatings are considered: homogeneous ceramic (H), ceramic-rich (CR), linear variation (LN) and metal-rich (MR) FGM coatings. The behavior of these four FGM coating types are compared by evaluating mode I, mode II, mode III stress intensity factors (SIFs) and energy release rates (G) around the crack front under transient thermal analysis.

This thesis is composed of six chapters. Introduction, literature survey and scope of the study are given in the present chapter. The problem definition, geometry of the problem and the types of loading are given in Chapter 2. The details of finite element modeling and analysis of Functionally Graded Materials are presented in Chapter 3. Chapter 4 gives information about stress intensity factors and energy release rate calculations. Numerical results and discussion can be found in Chapter 5. Finally, the concluding remarks are given in Chapter 6.

CHAPTER 2

PROBLEM DEFINITION

2.1 Fracture Mechanics

Fracture mechanics is relatively a new branch of applied mechanics which is being applied to assess the safety of engineering structures containing defects like cracks. Fracture is the failure of materials due to the propagation of a crack. Failure of many materials occurs by fast fracture. When the loading is increased, the material (and therefore the structure) behaves in an elastic manner. Then, fracture suddenly occurs without giving any warning. This failure mode, which is known as brittle fracture, is exhibited by many common materials like glass, rock and plain concrete. Furthermore, even for materials that normally behave in a ductile manner (e.g., high strength steel), fast failure may occur under some circumstances. Indeed, the unexpected fracture failure of turbine blades, machine elements, bridges and ships earlier in this century has resulted in a series of investigations leading to the present day understanding of fracture processes.

Fast fracture is due to the sudden propagation of a crack inside a structural component at a load level below that of required for yielding of a complete cross section. Cracks pre-exist in many materials due to a number of reasons. When solid materials are formed, the densification may not be perfect. Trapped air in the molten or liquid state can turn into pores and cracks in the solidified material. During handling of materials, such as transportation of structural components and their installation, surface damages can be introduced. One common example is the

scratch on the surface of window glass. When members are welded together, cracks may form around the weld due to residual stresses and phase changes in the material. Additionally, under repeated loadings, cracks may nucleate in materials and grow larger with each loading cycle. The slow growth of crack in this manner is referred to as fatigue crack growth.

When loading is applied to a material, the stress at the tip of a sharp crack is infinite if elastic behavior is assumed. Since no real material can stay elastic at very high stress levels, an inelastic zone will always be present in front of the crack tip. In metals, inelastic behavior is due to material yielding. For concrete, this is due to the formation of micro-cracks in front of the main crack. When the load is increased, the inelastic zone grows in size. Ultimately, the crack will propagate suddenly at a very high speed.

Crack propagation requires energy. The theory of Griffith suggests that a crack in an ideally brittle component will propagate if the total energy of the system is lowered with crack propagation. In other words, if the change in elastic strain energy due to crack extension is larger than the energy required creating new crack surfaces, the crack will propagate. The Griffith theory in equation form is

$$-\mathrm{d}P/\mathrm{d}a = \mathrm{d}W/\mathrm{d}a \qquad (2.1)$$

where a is the crack length, W is the work done by external forces per unit thickness, and P is the potential energy supplied by the internal strain energy and external forces. The crack will propagate if $-\mathrm{d}P/\mathrm{d}a$ is greater than or equal to $\mathrm{d}W/\mathrm{d}a$.

Irwin's theory extends Griffith's theory to ductile materials by including the energy dissipated by local plastic flow. This theory assumes that the energy due to plastic deformation must be added to the surface energy associated with the creation of new crack surfaces. For ductile materials, the surface energy term is often negligible compared to the energy associated with plastic deformation. In

this theory, a new quantity, G, the strain energy release rate, which is also called the crack extension force or the crack driving force, is defined. The strain energy release rate for a linear elastic material is described as the total energy absorbed during cracking per unit increase in the crack length and per unit thickness. The crack will propagate when a critical strain energy release rate, G_c, is achieved; that is when G is greater than or equal to the crack resistance energy, G_c. The equation below shows Irwin's modification to the Griffith theory, where U is the strain energy stored in the body per unit thickness.

$$G = -dP/da = dW/da - dU/da \tag{2.2}$$

Under general conditions, the mathematical modeling of the fracture process is very difficult. However, if the inelastic zone is much smaller in size than the specimen, critical strain energy release rate (G_c) can be evaluated. In many cases, however, instead of calculating G, a parameter called stress intensity factor, K, is calculated from the equation $K = \sqrt{G.E}$.

The propagation criterion is then given by the stress intensity factor reaching a critical value (K_C) representing the resistance to crack propagation. Therefore, the fracture criterion can then be converted into the form

$$K = K_c = \sqrt{G_c.E} \text{ (at the onset of the fracture)} \tag{2.3}$$

K is a parameter of physical significance because it characterizes the stress concentration in front of the crack tip. K_c is called the critical stress intensity factor or simply the fracture toughness of the material at which the cracks begins to propagate. Along the crack direction, the tensile stress (acting perpendicular to the crack) is given by

$$\sigma = \frac{K}{\sqrt{2\pi r}} \tag{2.4}$$

where r is the distance from the crack tip. As it can be seen from Figure 2.1, the stress concentration is relatively high near the tip of the crack.

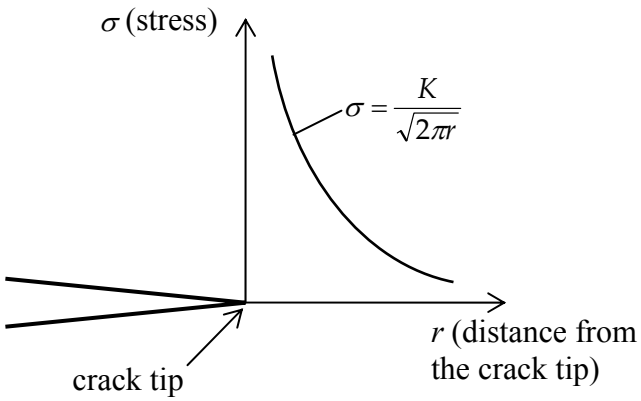

Figure 2.1 Variation of stress in front of a crack tip

The fracture toughness is a material property and a measure of the tensile strength of the material that takes into account the geometry and length of the initial cracks in a heterogeneous stress field at the crack tip. K_C is a material property that depends on loading rate, temperature, pressure, and chemical environment. The fracture toughness provides a measure of energy required to create a unit free surface. The crack propagation criterion states that longer cracks propagate first compared to short cracks if both are loaded with the same driving stress. If lengths are the same, then the one subjected to a higher driving stress will propagate first. A crack propagates only if $K \geq Kc$. Under special cases, however, e.g., when there is active corrosion at crack tips, fractures can propagate under critical stress conditions in which case subcritical crack growth occurs.

When a crack extends by a small amount, new surfaces are formed. Since atoms on the material surface contain more energy than those in the bulk, surface energy needs to be provided. In addition, when the crack propagates, energy is required to extend the inelastic region. To see where the required energy may come from, the structural component after the crack has propagated by a small amount can be

seen in Figures 2.2 & 2.3. With a slightly larger crack, the component becomes less stiff (i.e., it is easier to deform). If the specimen is fixed on its both ends, the stress will decrease all over the member and consequently energy is released (Figure 2.2). If the specimen is under fixed load, the displacement at the loading points will increase (Figure 2.3). Additional work is therefore done on the member. Part of the work is converted into additional strain energy that is stored in the member. The rest is available for extending the crack. In summary, for the two limiting cases described above, and all other cases in between, crack propagation will be accompanied by a release of energy from the system. If this energy is sufficient for the formation of new surfaces and the extension of the inelastic zone, fracture will occur.

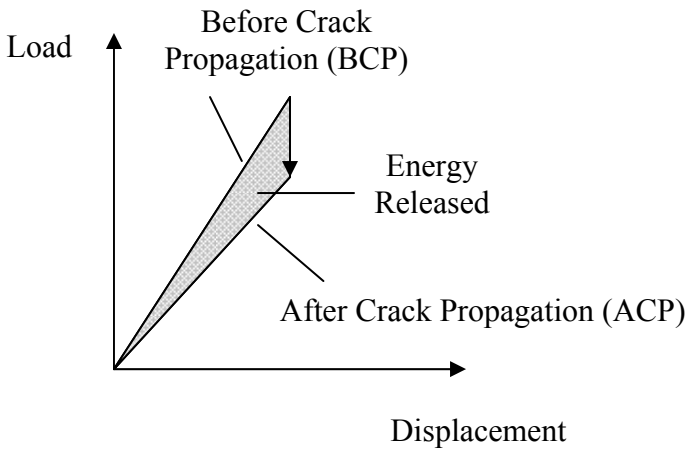

Figure 2.2 Change of energy as crack propagation occurs (specimen fixed on its both ends)

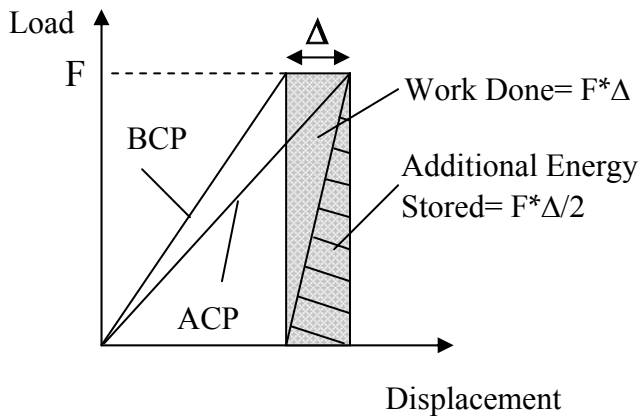

Figure 2.3 Change of energy as crack propagation occurs (specimen under fixed load)

2.2 Stress Intensity Factors

The stress intensity factors provide information about the stress field around the crack tip and the energy available to propagate the crack. They are used to define the magnitude of the singular stress and displacement fields (local stresses and displacements near the crack tip). The SIF depends on the loading, the crack size, the crack shape, and the geometric boundaries of the specimen. Failure will occur as the stress intensity factor reaches its critical value, which is known as fracture toughness.

The stress intensity factor completely characterizes the crack tip conditions for a linear elastic material. It relates the global applied stress and the local stress near the crack tip. The stress intensity approach is equivalent to the strain energy approach, and crack propagation occurs when critical stress intensity is achieved.

The stress intensity factor is defined for the three modes of crack tip displacement (I, II, or III), and incorporate both the effects of applied load and the geometry and length of the crack. Thus, for a homogeneous linear elastic material, the stress

intensity factor is the magnitude of the crack tip stress field for a given mode of propagation.

The remote stress, σ, is the tensile stress perpendicular to the crack plane for mode I, and is the shear stress parallel to the crack plane for modes II and III. The figure below shows the stress distribution around a crack tip.

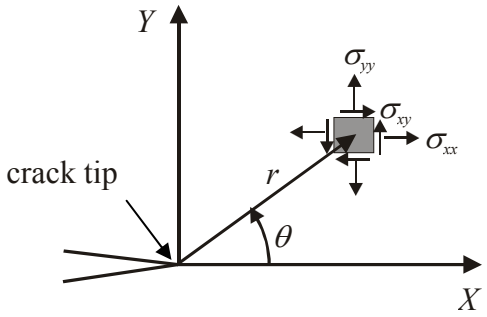

Figure 2.4 Distribution of stresses around the crack tip

2.2.1 Modes of Stress Intensity Factors (SIFs)

There are three types of modes of stress intensity factors to describe different crack surface displacements. A cracked body can be loaded in any of these modes, or a combination of two or three modes, which is known as mixed mode loading. The figure below shows these modes [25].

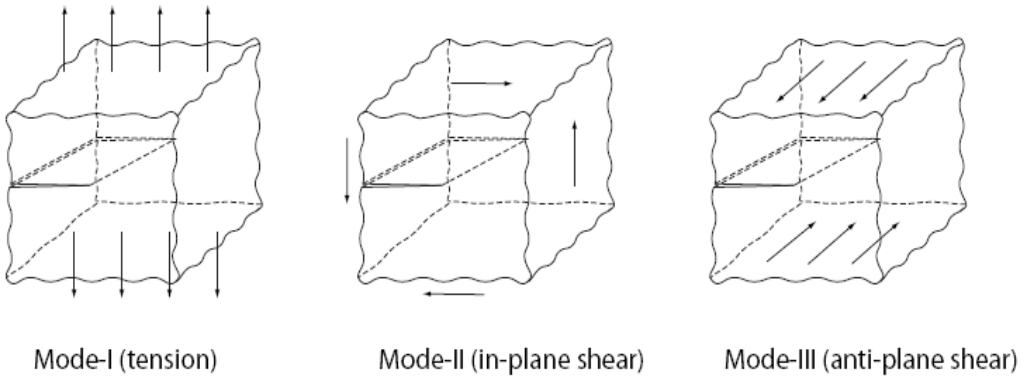

Figure 2.5 Modes of stress intensity factors (SIFs) [25]

2.2.1.1 Mode I Stress Intensity Factor

Mode I is opening or tensile mode where the crack surfaces move directly apart. This type of loading is normal to the crack plane, and tends to open the crack. The crack surfaces tend to separate symmetrically with respect to the crack plane. Mode I SIF is the most common load type encountered in engineering design.

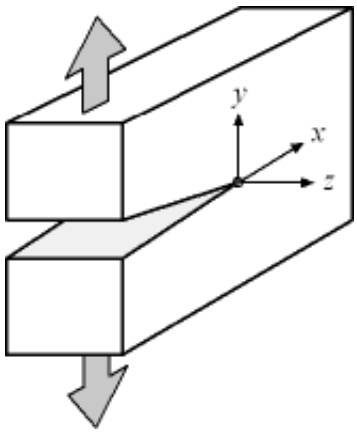

Figure 2.6 An illustration of mode I stress intensity factor [26]

The equations below are used for the calculation of mode I SIF [26].

$$\sigma_{XX} = \frac{K_I}{\sqrt{2\pi r}} \cos\left(\frac{\theta}{2}\right)\left[1 - \sin\left(\frac{\theta}{2}\right)\sin\left(\frac{3\theta}{2}\right)\right] \tag{2.5}$$

$$\sigma_{YY} = \frac{K_I}{\sqrt{2\pi r}} \cos\left(\frac{\theta}{2}\right)\left[1 + \sin\left(\frac{\theta}{2}\right)\sin\left(\frac{3\theta}{2}\right)\right] \tag{2.6}$$

$$\sigma_{ZZ} = \begin{cases} 0 & \text{(Plane Stress)} \\ \nu(\sigma_{XX} + \sigma_{YY}) & \text{(Plane Strain)} \end{cases} \tag{2.7}$$

$$\tau_{XY} = \frac{K_I}{\sqrt{2\pi r}} \cos\left(\frac{\theta}{2}\right)\sin\left(\frac{\theta}{2}\right)\cos\left(\frac{3\theta}{2}\right) \tag{2.8}$$

$$\tau_{YZ} = 0 \tag{2.9}$$

$$\tau_{ZX} = 0 \tag{2.10}$$

$$u_X = \frac{K_I}{2\mu}\sqrt{\frac{r}{2\pi}} \cos\left(\frac{\theta}{2}\right)\left[\kappa - 1 + 2\sin^2\left(\frac{\theta}{2}\right)\right] \tag{2.11}$$

$$u_Y = \frac{K_I}{2\mu}\sqrt{\frac{r}{2\pi}} \sin\left(\frac{\theta}{2}\right)\left[\kappa + 1 - 2\cos^2\left(\frac{\theta}{2}\right)\right] \tag{2.12}$$

$$u_Z = 0 \tag{2.13}$$

2.2.1.2 Mode II Stress Intensity Factor

Mode II SIF corresponds to in-plane shear loading and tends to slide one crack face with respect to the other (shearing mode). The stress is parallel to the crack growth direction. It is called as sliding or in-plane shear mode where the crack surfaces slide over one another in a direction perpendicular to the leading edge of the crack.

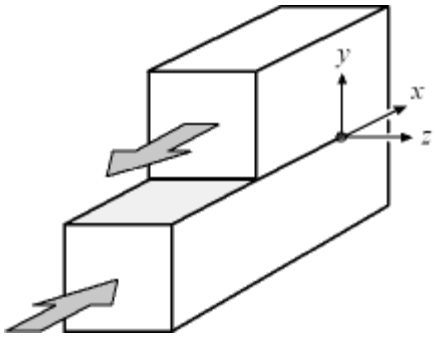

Figure 2.7 An illustration of mode II stress intensity factor [26]

The below equations are used for the calculation of mode II SIF [26].

$$\sigma_{XX} = -\frac{K_{II}}{\sqrt{2\pi r}}\sin\left(\frac{\theta}{2}\right)\left[2+\cos\left(\frac{\theta}{2}\right)\cos\left(\frac{3\theta}{2}\right)\right] \tag{2.14}$$

$$\sigma_{YY} = \frac{K_{II}}{\sqrt{2\pi r}}\sin\left(\frac{\theta}{2}\right)\cos\left(\frac{\theta}{2}\right)\cos\left(\frac{3\theta}{2}\right) \tag{2.15}$$

$$\sigma_{ZZ} = \begin{cases} 0 & \text{(Plane Stress)} \\ \nu(\sigma_{XX}+\sigma_{YY}) & \text{(Plane Strain)} \end{cases} \tag{2.16}$$

$$\tau_{XY} = \frac{K_{II}}{\sqrt{2\pi r}}\cos\left(\frac{\theta}{2}\right)\left[1-\sin\left(\frac{\theta}{2}\right)\sin\left(\frac{3\theta}{2}\right)\right] \tag{2.17}$$

$$\tau_{YZ} = 0 \tag{2.18}$$

$$\tau_{ZX} = 0 \tag{2.19}$$

$$u_X = \frac{K_{II}}{2\mu}\sqrt{\frac{r}{2\pi}}\sin\left(\frac{\theta}{2}\right)\left[\kappa+1+2\cos^2\left(\frac{\theta}{2}\right)\right] \tag{2.20}$$

$$u_Y = -\frac{K_{II}}{2\mu}\sqrt{\frac{r}{2\pi}}\cos\left(\frac{\theta}{2}\right)\left[\kappa-1-2\sin^2\left(\frac{\theta}{2}\right)\right] \tag{2.21}$$

$$u_Z = 0 \tag{2.22}$$

2.2.1.3 Mode III Stress Intensity Factor

Mode III SIF corresponds to out-of-plane shear, or tearing. It is the tearing and anti-plane shear mode where the crack surfaces move relative to one another and parallel to the leading edge of the crack.

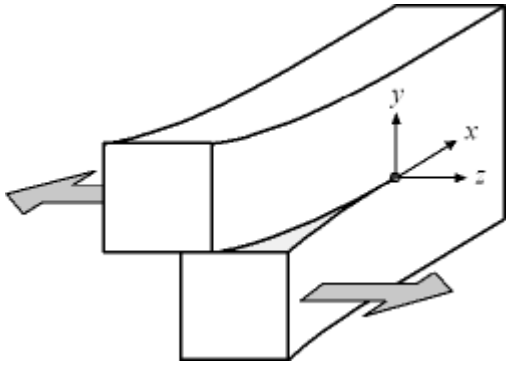

Figure 2.8 An illustration of mode III stress intensity factor [26]

To evaluate mode III SIF, the equations given below can be used [26].

$$\sigma_{XX} = 0 \tag{2.23}$$

$$\sigma_{YY} = 0 \tag{2.24}$$

$$\sigma_{ZZ} = 0 \tag{2.25}$$

$$\tau_{XY} = 0 \tag{2.26}$$

$$\tau_{YZ} = \frac{K_{III}}{\sqrt{2\pi r}} \cos\left(\frac{\theta}{2}\right) \tag{2.27}$$

$$\tau_{ZX} = -\frac{K_{III}}{\sqrt{2\pi r}} \sin\left(\frac{\theta}{2}\right) \tag{2.28}$$

$$u_X = 0 \tag{2.29}$$

$$u_Y = 0 \tag{2.30}$$

$$u_Z = \frac{K_{III}}{2\mu}\sqrt{\frac{r}{2\pi}}\sin\left(\frac{\theta}{2}\right) \tag{2.31}$$

2.3 Geometry of the Problem

The geometry of the semi-elliptical inclined surface crack in an FGM-bond coat-homogeneous substrate structure is shown at Figure 2.9 and 2.10. The thicknesses of the FGM coating, bond coat and the substrate are taken as t_1, t_2 and t_3, respectively. There is a semi-elliptic inclined surface crack which has a length of $2c$ and a depth of a. The semi-elliptic crack has an inclination angle α, on the surface of the FGM at x=0. The schematic of the crack front can be seen at Figure 2.11. This figure depicts a point P on the crack front that is located by the parametric angle, ϕ.

In this study the coating, bond coat and substrate relative dimensions are taken as

$$\frac{t_1}{t_2} = 2, \quad \frac{t_3}{t_2} = 8, \quad b = \frac{t_3}{2}, \quad h = \frac{t_3}{2}$$

In the numerical analysis conducted, two different crack depth/ FGM thickness (a/t_1) ratios are used. These are as follows

$$\frac{a}{t_1} = 0.2 \text{ and } \frac{a}{t_1} = 0.4$$

Additionally, the aspect ratio in this study is $\frac{a}{c} = \frac{1}{2}$

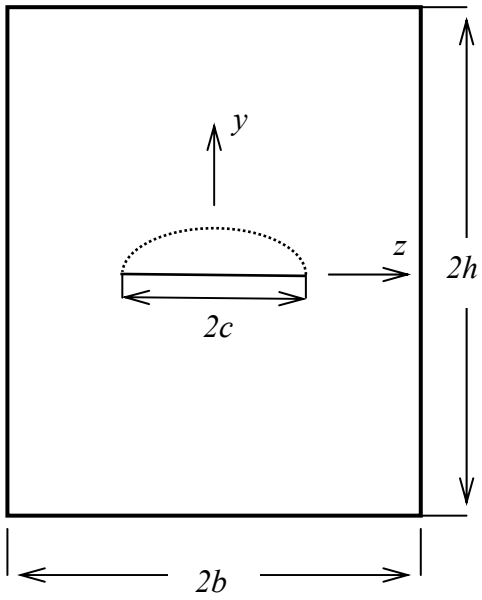

Figure 2.9 The geometry of the FGM coating, bond coat and substrate structure (front view)

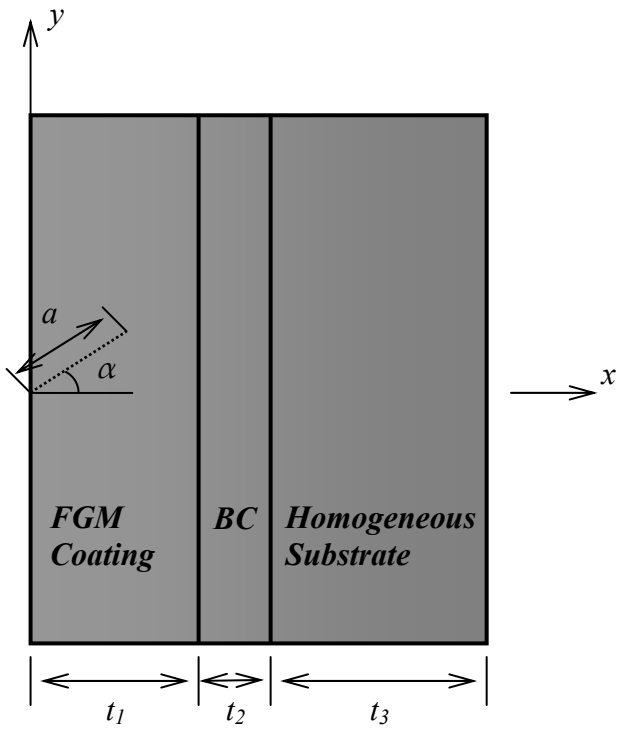

Figure 2.10 The geometry of the FGM coating, bond coat and substrate structure (side view)

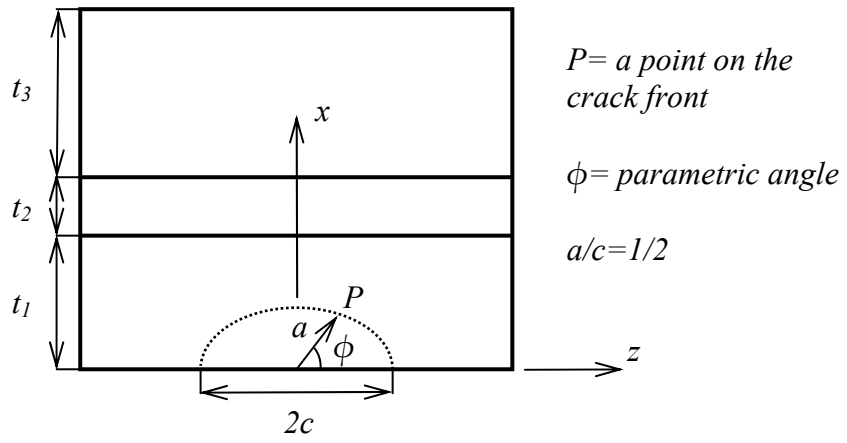

Figure 2.11 A point *P* located on the crack front by the parametric angle, ϕ

2.4 Material Property Variations and FGM Coating Types

In this study, the parametric analyses on FGMs are based upon zirconia-yttria (ZrO2-8wt%-Y_2O_3) FGM coating bonded to a substrate made of a nickel-based superalloy. There is a nickel-chromium–aluminum–zirconium (NiCrAlY) bond coat between the FGM coating and substrate. FGM coating is 100% zirconia-yttria (ZrO2-8wt%-Y_2O_3) at x=0 and 100% nickel-chromium–aluminum–zirconium (NiCrAlY) at x=t_1.

Assuming both the FGM coating and the substrate to be isotropic, a total of six material parameters are required to be known in order to carry out the transient thermal fracture analysis. These parameters are the modulus of elasticity (E), Poisson's ratio (υ), thermal expansion coefficient (α_t), thermal conductivity (k) and density multiplied by specific heat ($\rho.c_t$). ($\rho.c_t$) can be evaluated using the relationship $D = k / (\rho. c_t)$, where D is the thermal diffusivity. The subscripts c and bc in equations (2.32)-(2.36) refer to the coating (zirconia-yttria) and bond coat material properties, respectively. Moreover, the exponents p, q, r, s and n are positive constants that can be adjusted to obtain a certain type of variation profile in the FGM coating.

All these thermomechanical parameters in FGM are assumed to be continuously variable in the x direction. Thermomechanical properties of the material components used in the coating-bond coat-substrate structure of the numerical analysis conducted are the same as with those given in [27]. These material parameters are also presented in Table 2.1. Material property variations in the FGM coating are represented by power-law type functions as shown below

$$E(x) = E_c + (E_{bc} - E_c)\left(\frac{x}{t_1}\right)^p, \qquad \text{for } 0 < x < t_1 \tag{2.32}$$

$$\nu(x) = \nu_c + (\nu_{bc} - \nu_c)\left(\frac{x}{t_1}\right)^q, \qquad \text{for } 0 < x < t_1 \tag{2.33}$$

$$\alpha_t(x) = \alpha_{tc} + (\alpha_{tbc} - \alpha_{tc})\left(\frac{x}{t_1}\right)^r, \qquad \text{for } 0 < x < t_1 \tag{2.34}$$

$$k(x) = k_c + (k_{bc} - k_c)\left(\frac{x}{t_1}\right)^s, \qquad \text{for } 0 < x < t_1 \tag{2.35}$$

$$\rho.c_t(x) = (\rho.c_t)_c + \left[(\rho.c_t)_{bc} - (\rho.c_t)_c\right]\left(\frac{x}{t_1}\right)^n, \qquad \text{for } 0 < x < t_1 \tag{2.36}$$

Table 2.1 Thermomechanical properties of the material components used in the FGM coating-bond coat-substrate structure

Material	Modulus of elasticity (GPa)	Poisson's ratio	Coefficient of thermal expansion ($^oC^{-1}$)	Coefficient of thermal conductivity (W/mK)	Thermal diffusivity (m^2/s)
Substrate (Ni)	175.8	0.25	13.91×10^{-6}	7	2×10^{-6}
Bond Coat (NiCrAlY)	137.9	0.27	15.16×10^{-6}	25	8×10^{-6}
Zirconia-Yttria	27.6	0.25	10.01×10^{-6}	1	5×10^{-7}

The thermomechanical parameters of the bond coat and substrate are constant. These parameters are expressed in the APDL subroutine as

$$E(x)=\begin{cases} E_{\mathrm{bc}}, & t_1 < x < t_1+t_2 \\ E_{\mathrm{s}}, & t_1+t_2 < x < t_1+t_2+t_3 \end{cases} \tag{2.37}$$

$$\nu(x)=\begin{cases} \nu_{\mathrm{bc}}, & t_1 < x < t_1+t_2 \\ \nu_{\mathrm{s}}, & t_1+t_2 < x < t_1+t_2+t_3 \end{cases} \tag{2.38}$$

$$\alpha_t(x)=\begin{cases} \alpha_{t\,\mathrm{bc}}, & t_1 < x < t_1+t_2 \\ \alpha_{t\,\mathrm{s}}, & t_1+t_2 < x < t_1+t_2+t_3 \end{cases} \tag{2.39}$$

$$k(x)=\begin{cases} k_{\mathrm{bc}}, & t_1 < x < t_1+t_2 \\ k_{\mathrm{s}}, & t_1+t_2 < x < t_1+t_2+t_3 \end{cases} \tag{2.40}$$

$$\rho.c(x)=\begin{cases} (\rho.c)_{\mathrm{bc}}, & t_1 < x < t_1+t_2 \\ (\rho.c)_{\mathrm{s}}, & t_1+t_2 < x < t_1+t_2+t_3 \end{cases} \tag{2.41}$$

where the subscripts *bc* and *s* in equations (2.37)-(2.41) refer to the bond coat and substrate material properties, respectively. The above equations imply that the thermomechanical parameters are constant throughout the bond coat and substrate.

The exponents *p, q, r, s* and *n* in the equations (2.32)-(2.36) are positive constants that can be adjusted to obtain a certain type of power-law variation in the FGM coating. In this study, however, partly for simplicity and partly for lack of published data, same exponent *p* is used for each of the six material properties E, ν, α_t, k and $\rho.c_t$. In the numerical analysis conducted, four different types of material property variations are considered. These material property variations correspond to homogeneous ceramic (H), ceramic-rich (CR), linear variation (LN)

and metal-rich (MR) FGM coatings. The particular values of p used in this study are shown in Table 2.2.

Table 2.2 The values of the exponent p for the corresponding coating types

Coating type	Homogeneous ceramic (H)	Ceramic-rich (CR)	Linear variation (LN)	Metal-rich (MR)
p	∞	5	1	0.2

2.5 Model Validation and Types of Loading

In this study, the FGM coating, bond coat and homogeneous substrate structure is subjected to transient thermal loading. For this type of loading, the corresponding normalized mixed-mode stress intensity factors and energy release rates are calculated. In order to validate the model used in transient thermal analysis, two different analyses are carried out and the results are compared to that of the studies found in the literature.

2.5.1 The Validation of the Model

Prior to conducting the transient thermal analysis, the model is validated by doing two different analyses. The following sections give information about these validations and the formulas for the corresponding normalized mode I, mode II and mode III stress intensity factors.

2.5.1.1 First Analysis for Model Validation

In the first validation analysis, an inclined semi-elliptic surface crack (a/c=1) in a plate loaded by uniform tensile pressure loads at its ends, is examined. The Poisson's ratio of the plate is taken as 0.3. The half width and half length of the plate are taken as b/c=5 and h/c=5. The thickness of the plate t is assumed to have a ratio with the crack radius a as a/t=1/5. The semi-elliptic crack considered in this analysis is assumed to have an inclination angle α with respected to local x'

axis. This model has the same parameters with the model studied in the paper of Ayhan et al. [11].

For this type of analysis, the inclination angle α is taken as 0^o, 15^o, 30^o, 45^o, 60^o and 75^o. Then, the normalized mode I, mode II and mode III stress intensity factors are evaluated for the corresponding angles of inclination. The next figure depicts the model of the plate, which has an inclined semi-elliptic surface crack, used in this analysis.

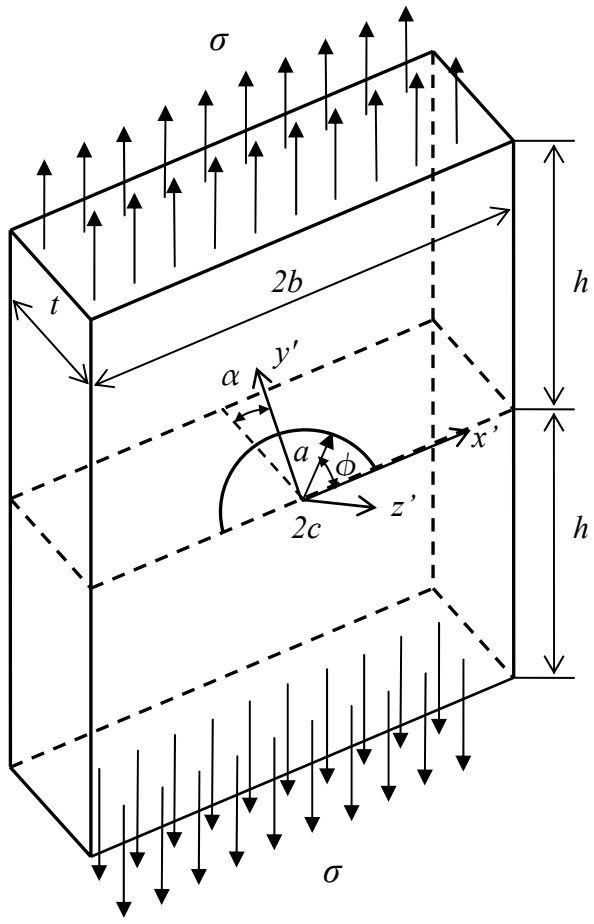

Figure 2.12 A semi-elliptic inclined surface crack in a plate under uniform tensile remote stresses

In this analysis, the mixed-mode stress intensity factors are normalized by

$$K_R = \sigma\sqrt{\frac{\pi.a}{Q}} \tag{2.42}$$

where

$$Q = 1 + 1.464(a/c)^{1.65} \tag{2.43}$$

In the above equations, σ is the applied uniform tensile remote stress, a is the crack depth and c is the crack length.

After the K_I, K_{II} and K_{III} are calculated with the help of commercial finite element code utilizing displacement correlation technique, the normalized mixed-mode stress intensity factors are evaluated as

$$K_{In} = \frac{K_I}{K_R} \tag{2.44}$$

$$K_{IIn} = \frac{K_{II}}{K_R} \tag{2.45}$$

$$K_{IIIn} = \frac{K_{III}}{K_R} \tag{2.46}$$

2.5.1.2 Second Analysis for Model Validation

Second validation analysis is conducted by using the parameters given in the paper of Isida et al. [9]. In this analysis, a semi-elliptical surface crack arbitrarily inclined to the free surface of a semi-infinite solid subjected to uniform tension is considered. The Poisson's ratio is taken as 0.3. The comparisons of the mixed-mode stress intensity factors are done for an aspect ratio of a/c=1. The semi-elliptic crack considered in this analysis is obliquely inclined to the solid surface with an inclination angle α with respect to the x-y plane. The model of the semi-elliptic surface crack in the solid is shown in Figure 2.13.

In this analysis, the inclination angle α is taken to be 15^o, 30^o, and 45^o. The dimensionless mode I, mode II and mode III stress intensity factors are calculated for the corresponding inclination angles.

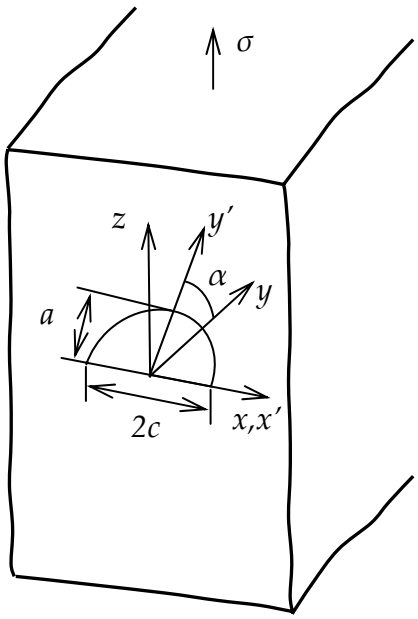

Figure 2.13 A semi-elliptic inclined surface crack in a semi-infinite solid under uniform tensile remote stresses

The dimensionless mixed mode stress intensity factors of this analysis are evaluated by using the following expressions

$$F_I(\phi) = \frac{K_I(\phi)}{\sqrt{\sigma(\pi.a)}} \tag{2.47}$$

$$F_{II}(\phi) = \frac{K_{II}(\phi)}{\sqrt{\sigma(\pi.a)}} \tag{2.48}$$

$$F_{III}(\phi) = \frac{K_{III}(\phi)}{\sqrt{\sigma(\pi.a)}} \tag{2.49}$$

where ϕ is the crack front angle, σ corresponds to the uniform tension load and a is the crack depth.

2.5.2 Transient Thermal Loading

In this loading type, a residual/thermal stress problem for the FGM coating, bond coat and homogeneous substrate structure is considered. It is assumed that the composite medium is initially stress-free at a high processing temperature of T_i = 1273 K. Afterwards, the coating, bond coat and substrate structure is left in an environment which is at a temperature of T_o = 300 K. It is further supposed that there exists free convection with a convection coefficient of h_c = 5 W/ (m^2.K) at all surfaces of the structure except the surface at x = 0. At this surface there is forced convection and the convection coefficient is h_c = 10000 W/ (m^2.K). The boundary conditions for this loading case are depicted in Figure 2.14. The thermomechanical parameters given at Table 2.1 are used in the analyses carried out.

Due to the forced convection applied to the FGM surface, temperature gradients are induced as the composite structure cools down from the high initial temperature. This results in the formation of self-equilibrating thermal stresses in the composite medium. The thermal and structural problems are solved using the three dimensional finite element technique and the coupling of the thermal and structural problems are assumed to be through the calculated temperature distribution only. In this loading case, firstly the transient temperature distribution in the composite structure is evaluated by considering the heat conduction in the nonhomogeneous medium. Then, this computed temperature distribution is used to solve the structural problem and to calculate transient thermal mixed-mode stress intensity factors and energy release rates around the crack front. In the analyses, it is assumed that the crack surfaces are completely insulated and the medium is free of any mechanical constraints. For the transient thermal analyses, 0^o, 15^o, 30^o, $45^o$and 60^o inclination angles of semi-elliptic surface crack are

considered. Four different material property variations, which are shown in Table 2.2, are used in conducting the analyses.

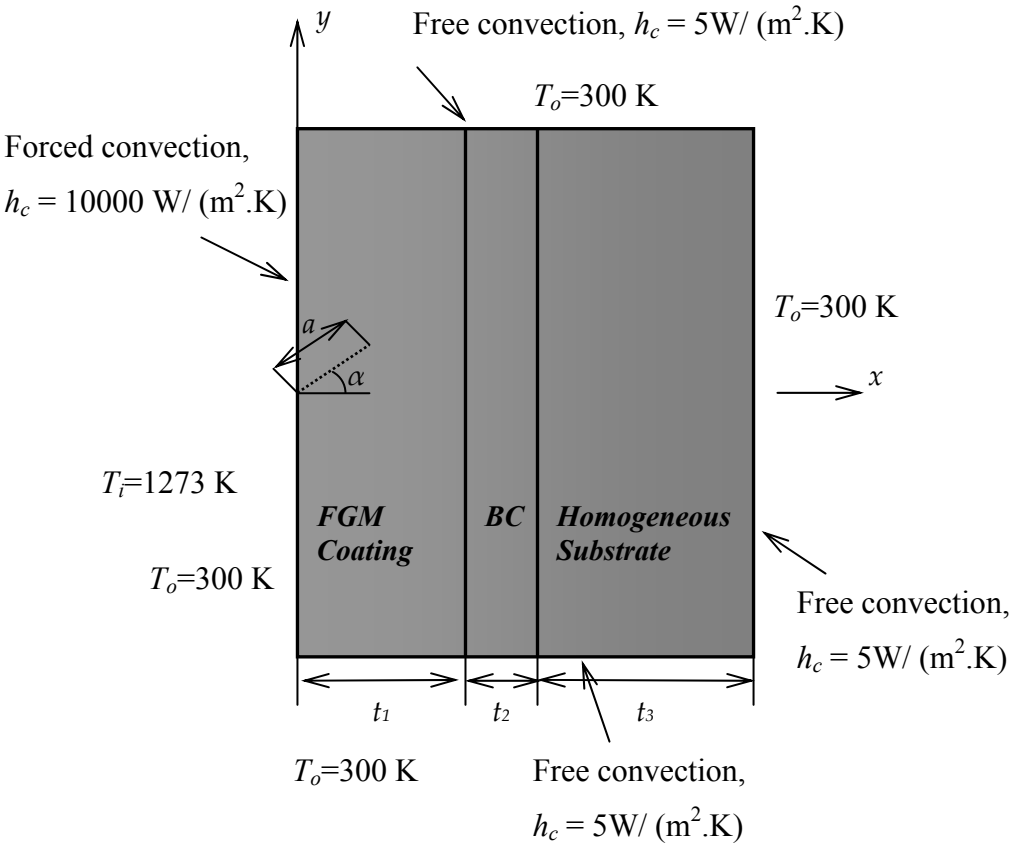

Figure 2.14 Thermal boundary conditions for the FGM coating, bond coat and substrate structure

In this analysis, the normalized mixed mode stress intensity factors are defined as

$$K_{In} = \frac{K_I}{S\sqrt{\frac{\pi.a}{Q}}} \tag{2.50}$$

$$K_{IIn} = \frac{K_{II}}{S\sqrt{\frac{\pi.a}{Q}}} \tag{2.51}$$

$$K_{IIIn} = \frac{K_{III}}{S\sqrt{\frac{\pi.a}{Q}}} \tag{2.52}$$

where a is the crack depth and S is the normalization stress which is defined by

$$S = \frac{\alpha_t E_c T_i}{1-\nu} \tag{2.53}$$

In the above expression, α_t, E_c and ν are the thermal expansion coefficient, modulus of elasticity and Poisson's ratio of the FGM coating, respectively. T_i is the initial temperature of the composite medium which is 1273 K.

The variable Q in the equations (2.50) – (2.52) is a function of the semi-ellipse aspect ratio (a / c) and is expressed by [28] as

$$Q = \begin{cases} 1 + 1.464(\mathrm{a/c})^{1.65} & \text{for} \quad (\mathrm{a/c}) \le 1, \\ 1 + 1.464(\mathrm{c/a})^{1.65} & \text{for} \quad (\mathrm{a/c}) > 1. \end{cases} \tag{2.54}$$

In addition, the normalized energy release rate calculated in this loading type is found from the formula

$$G_n = \frac{GE_c(1-\nu^2)}{S^2\left(\frac{\pi.a}{Q}\right)} \tag{2.55}$$

In this problem the normalized mixed mode stress intensity factors and energy release rates are computed with respect to normalized time τ which is defined as

$$\tau = \frac{D.t}{t_1^{\,2}} \tag{2.56}$$

where t is time, t_1 is the thickness and D is the thermal diffusivity coefficient of the FGM coating. D is expressed as

$$D = \frac{k}{\rho.c} \tag{2.57}$$

The parameters k, ρ and c are the thermal conductivity, density and specific heat of the FGM coating, respectively.

CHAPTER 3

FINITE ELEMENT MODELING AND ANALYSIS OF FUNCTIONALLY GRADED MATERIALS

3.1 The Finite Element Models

The finite element models of the problems studied in this thesis are generated by the use of general purpose finite element analysis code ANSYS [29]. During the model creation and while performing the analyses, ANSYS Parametric Design Language (APDL) subroutines are highly used. Since the geometry used both in mechanical (model validation) and transient thermal analyses has one symmetry plane, it is sufficient to model one-half of the geometry in order to carry out the analyses and calculate mixed mode stress intensity factors.

The commercial finite element programs are able to create the models and meshes and elements related to those models by using two different methods. In the first method, the solid model of the geometry is created and then the meshes, elements and nodes are generated. On the other hand, in the second method, the solid model is created directly from the nodes. In this study, the first method is utilized in order to generate the finite element models used in the analyses.

3.1.1 Finite Element Modeling and Analysis of Solid under Uniform Tension

As it is explained in section 2.5.1, the models used for the validation purposes are analyzed under uniform tension. The model with finite dimensions in part 2.5.1.1

is composed of 220558 elements and 393271 nodes, whereas the semi-infinite solid in part 2.5.1.2 has totally 402965 elements and 668392 nodes for 45^o inclination angle of the semi-elliptic crack. Figure 3.1 depicts the general view of the finite element mesh for 45^o inclination angle and a/c=1, a/t=0.2, a/h=0.2 and a/b=0.2. In Figure 3.2, a close-up view of the crack is shown.

The elements used for the mesh generation in the uniform tension analyses are MESH200, SOLID92 and SOLID95 elements.

MESH200 is known as "meshing facet". In fact, it is a "mesh-only" element which contributes nothing to the solution. This element is mostly used for line-meshing in 2-D or 3-D, area-meshing or volume-meshing in 3-D space with triangles, quadrilaterals, tetrahedral, or bricks with or without midside nodes and temporary storage of elements when the physics of the analysis has not yet been specified. MESH200 elements can be used in conjunction with any other ANSYS element types.

SOLID92 is a 3-D 10-node tetrahedral structural solid element. It has a quadratic displacement behavior and is well suited to model irregular meshes. This element is defined by ten nodes having three degrees of freedom, which are translations in the nodal x, y, and z directions, at each node. Moreover, SOLID92 has plasticity, creep, swelling, stress stiffening, large deflection, and large strain capabilities. An illustration of SOLID92 element is shown in Figure 3.3 [30].

SOLID95 is a 3-D 20-node structural solid element which is a higher order version of the 3-D 8-node solid element SOLID45. It can tolerate irregular shapes without as much loss of accuracy. SOLID95 elements have compatible displacement shapes and are well suited to model curved boundaries. This element is described by 20 nodes having three degrees of freedom, which are translations in the nodal x, y, and z directions, at each node. This element may have any spatial orientation. Furthermore, the element SOLID95 has plasticity, creep, stress

stiffening, large deflection, and large strain capabilities. In Figure 3.4, an illustrative picture of SOLID95 element is depicted [30].

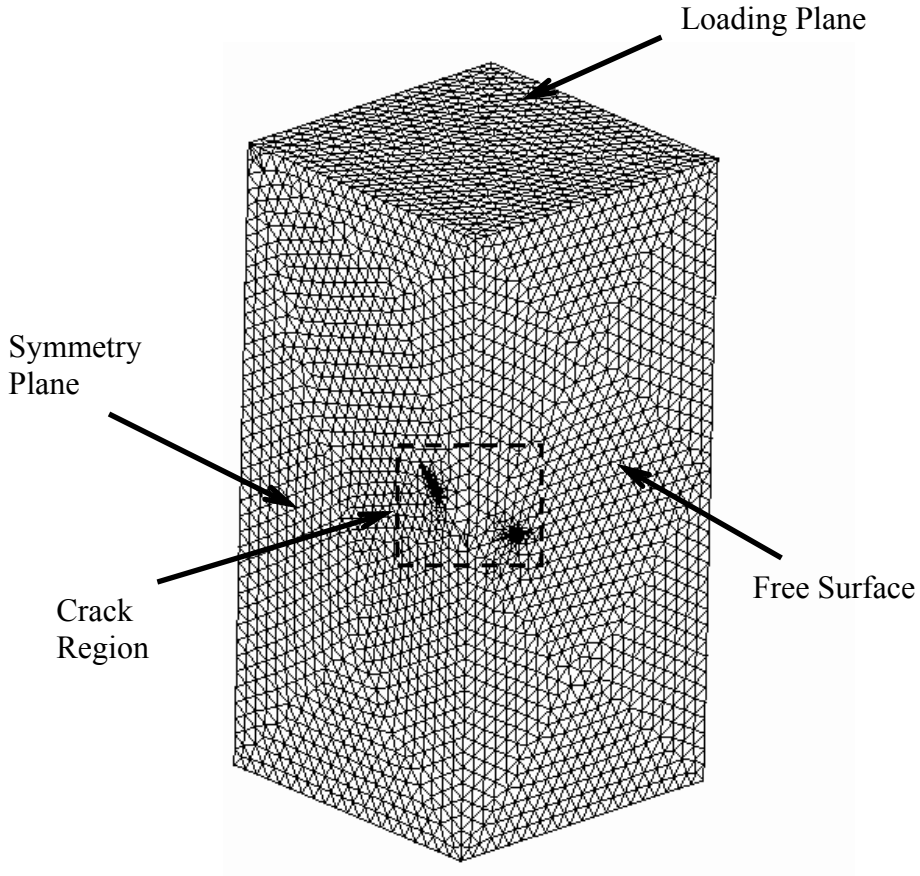

Figure 3.1 Global view of the plate containing semi-elliptic crack for 45^{o} inclination angle

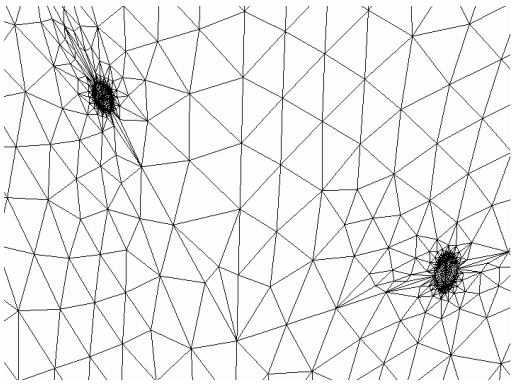

Figure 3.2 A close-up view of the crack for 45^{o} inclination angle

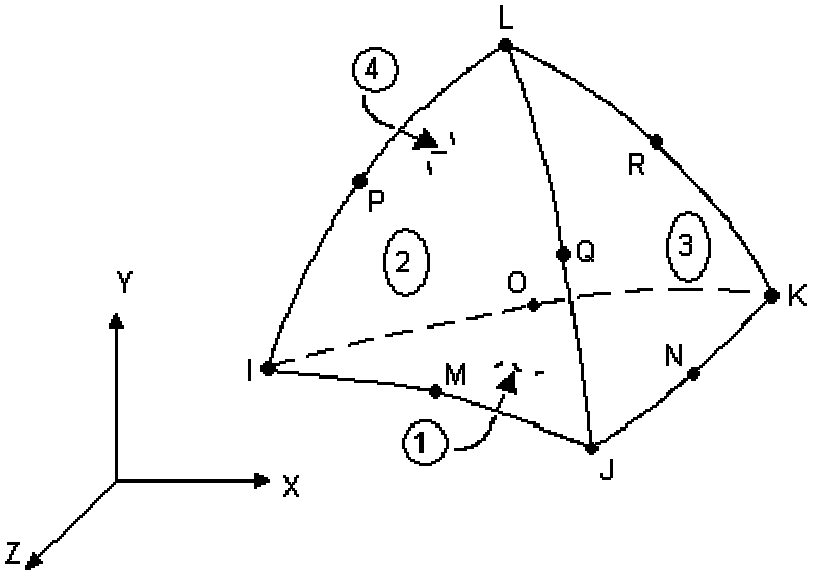

Figure 3.3 The SOLID92 element [30]

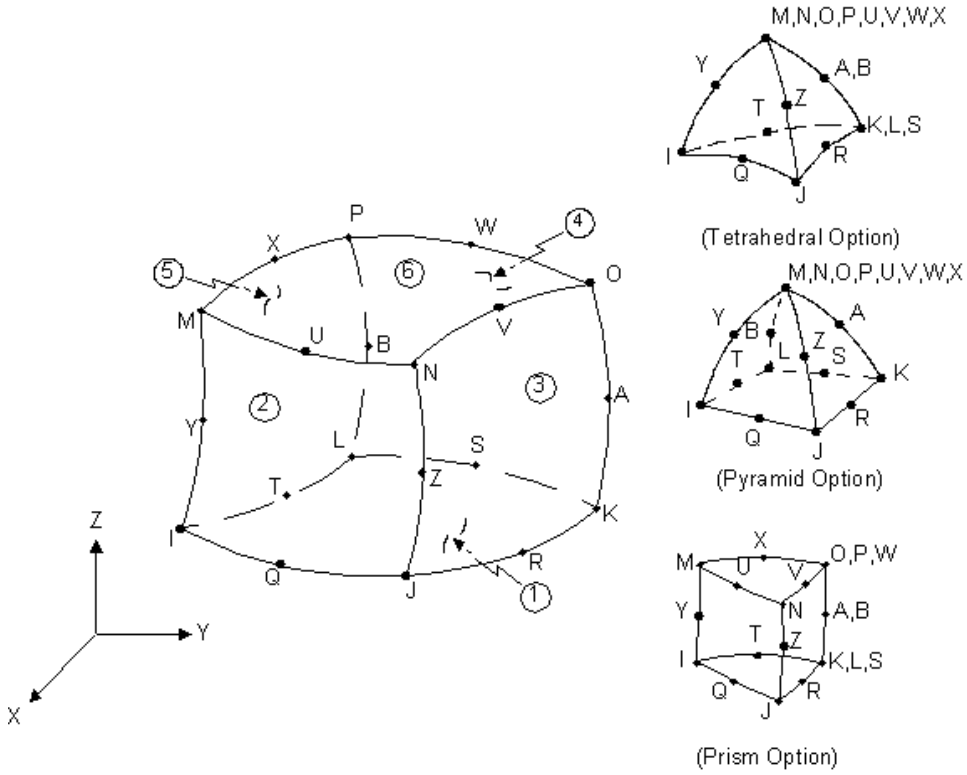

Figure 3.4 The SOLID95 element [30]

For the finite element analysis of the fracture problem, in order to simulate the square-root strain singularity around the crack front, collapsed 20-node isoparametric three dimensional brick elements are utilized. These elements are shown in Figures 3.5 and 3.6 [20]. The formulation of the collapsed elements is given in [31]. The main feature of the collapsed 20-node isoparametric three dimensional brick elements is that the mid-point nodes of these elements are moved to the quarter points in order to simulate the square-root singularity around the crack front.

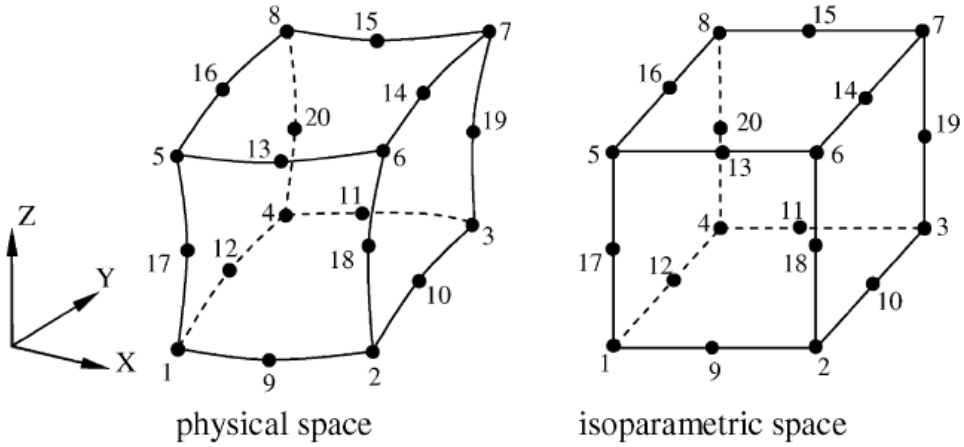

Figure 3.5 Node numbering of a 20-node isoparametric brick element [20]

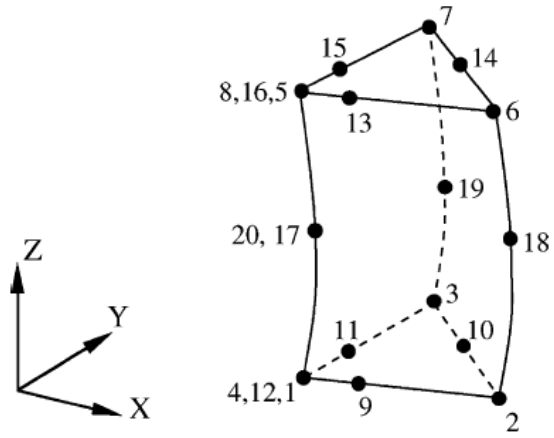

Figure 3.6 Collapsed 20-node isoparametric brick element [20]

Figure 3.7 depicts the elements around the crack front of a semi-elliptic surface crack. In Figure 3.8, the meshes with singular elements at $\pi/2$ crack front angle are shown.

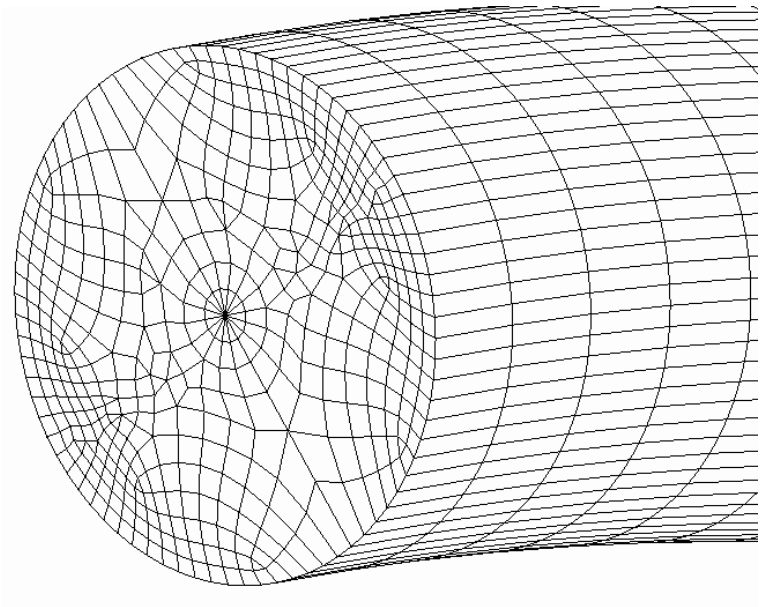

Figure 3.7 The elements around the crack-front of a semi-elliptic surface crack

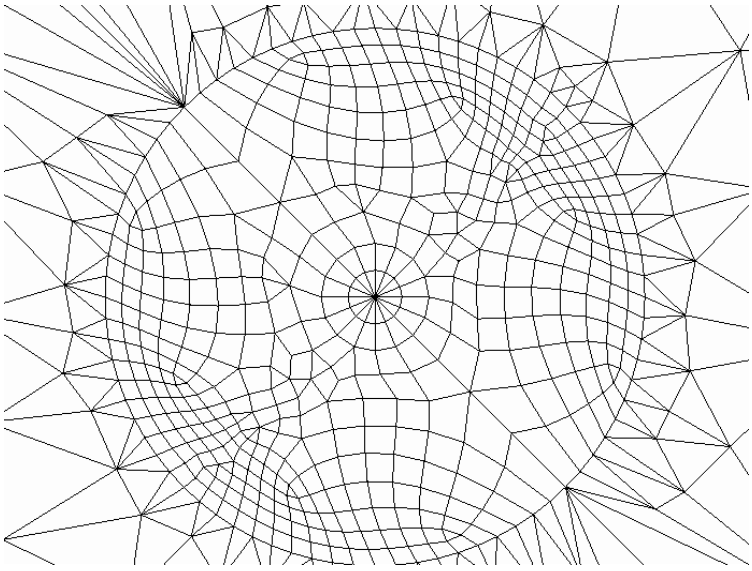

Figure 3.8 Meshes with singular elements at $\pi/2$ crack front angle

The radius of the singular elements is taken as a /1000. Moreover, sixteen singular elements are used around the crack front. A close-up view of the singular elements around the crack front can be seen in Figure 3.9.

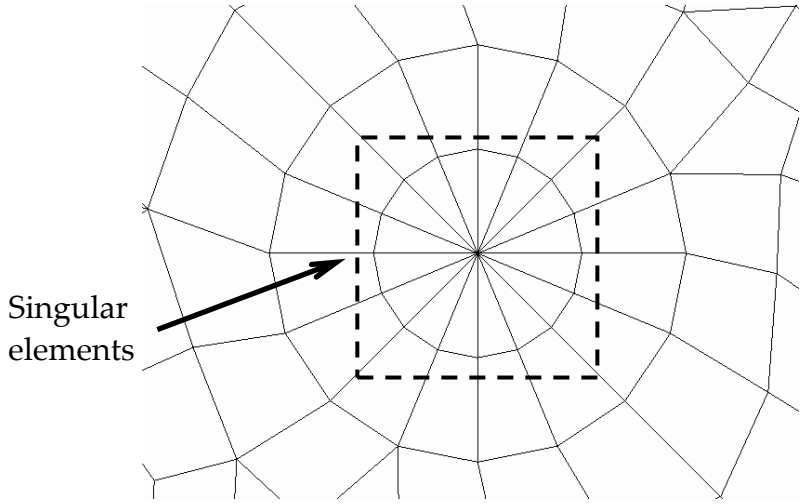

Figure 3.9 Singular elements around the crack front

As stated earlier, ANSYS APDL subroutines are highly used during the model generation and in conducting the finite element analyses. The procedure below summarizes the steps used for modeling and analysis of the semi-elliptic surface crack in a solid under uniform remote tensile loads.

- Choose structural for the analysis type,
- Select MESH200, SOLID92 and SOLID95 elements,
- Ask user to input the parameters (crack depth a, crack length c, thickness of the solid t, half-length of the solid h, half-width of the solid b and the inclination angle α),
- Create a local coordinate system for the crack front generation,
- Generate keypoints on the crack front,

♦ Create a circular area of specified radius at the first keypoint of the crack front,

♦ Form lines on the crack front by using the generated keypoints,

♦ Drag the circular area through the formed lines along the crack front and generate volumes around the crack front,

♦ Generate keypoints which are to be used for the solid boundaries,

♦ Create lines from the generated keypoints,

♦ Form the areas of the solid by using the created lines,

♦ Constitute the volume of the solid by utilizing the formed areas,

♦ Overlap the volumes around the crack front and the volume of the solid,

♦ Delete the unneeded volumes after the overlap operation,

♦ Delete the unwanted lines before the merging operation around the crack front,

♦ Merge the keypoints around the crack front that are not used for crack simulation,

♦ State the last keypoint of the crack front about which an area mesh will be skewed by specifying the radius and number of the singular elements around it,

♦ Specify line divisions around the mesh area and drag line of the crack front,

♦ Mesh the area at the last keypoint of the crack front,

♦ Fill the unmeshed volumes around the crack front with elements by sweeping the generated area through the volume,

♦ Generate nodes and elements within the solid by specifying the element size,

♦ Choose the symmetry planes,

♦ Select the plane on which the uniform tensile loads are to be applied,

♦ Solve the problem,

♦ Select and define the crack front nodes that are to be used for the calculation of mixed mode stress intensity factors,

♦ Compute the mixed mode stress intensity factors at the crack front nodes by utilizing the displacement correlation technique.

3.1.2 Finite Element Modeling and Analysis of the FGM Coating-Bond Coat-Substrate Structure under Transient Thermal Load

The model used for the transient thermal analysis of the FGM coating-bond coat-substrate structure is shown in Figure 3.10. This figure depicts the general view of finite element mesh of the composite medium for 30^o inclination angle of semi-elliptic crack and a/c=1/2, a/t_1=0.4, t_1/t_2=2, t_3/t_2=8, b/t_3=1/2 and h/t_3=1/2. There exist 132,758 elements and 330,972 nodes in this model for a/t_1=0.2 and 30^o inclination angle.

Prior to creating this model, a model with fewer meshes around the crack region was generated. This model, which has 64,664 elements and 167,395 nodes for a/t_1=0.2 and 30^o inclination angle, can be seen in Figure 3.11.

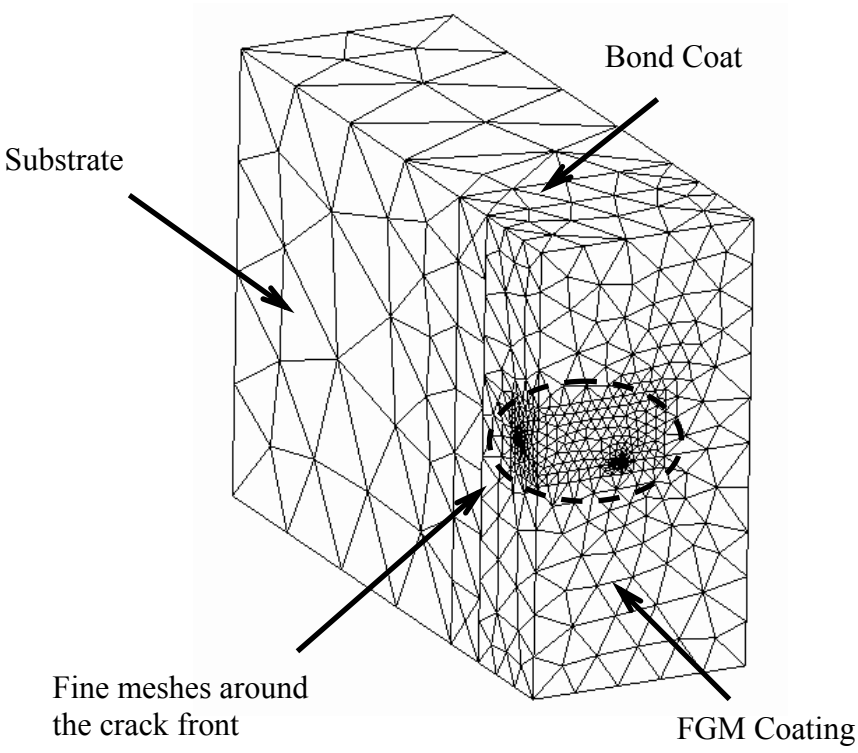

Figure 3.10 Finite element mesh of the FGM coating-bond coat-substrate structure

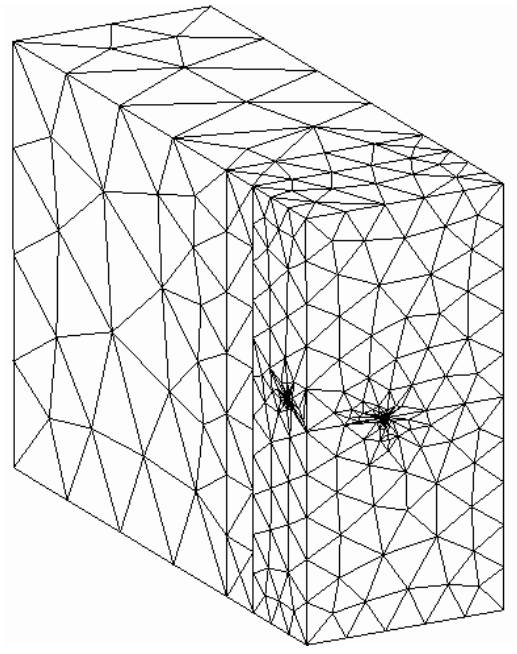

Figure 3.11 Initial finite element mesh of the FGM coating-bond coat-substrate structure

After the transient thermal analyses were carried out and the results of mixed mode stress intensity factors were obtained, the graphs related to these analyses were sketched and analyzed. It was observed from the generated graphs that the variations of the results were not good. At some crack front angles, unexpected behaviors were seen due to the oscillation of the graph at those points. Due to this unwanted behavior, it was thought that a finer mesh might give better results. However, owing to the hard physics of the transient thermal problem and inclination of the crack, it was realized that a finer mesh with this model was impossible to generate since the program was giving memory allocation errors due to lack of memory even in powerful workstations. Then, the idea of creating new volumes around the "crack tunnel", that is placing the inclined crack region in a separate volume to obtain fine meshes around the crack front, came to mind. It was thought that this new method might be the solution for this problem because of the ability to obtain more elements around the crack region, locally. Afterwards, as it can be seen in Figure 3.12, new volumes around the crack region were generated and the finite element analysis code was able to perform the analyses and cope up with the memory allocations. Figure 3.13 depicts an enlarged view of the fine meshes around the crack front with the help of these created new volumes. As a consequence of the local fine meshes around the crack front, the expected variations of the results could have been obtained.

In the transient thermal analyses, the elements MESH200 and SOLID90 are utilized. The characteristics of MESH200 can be found in section 3.1.1.

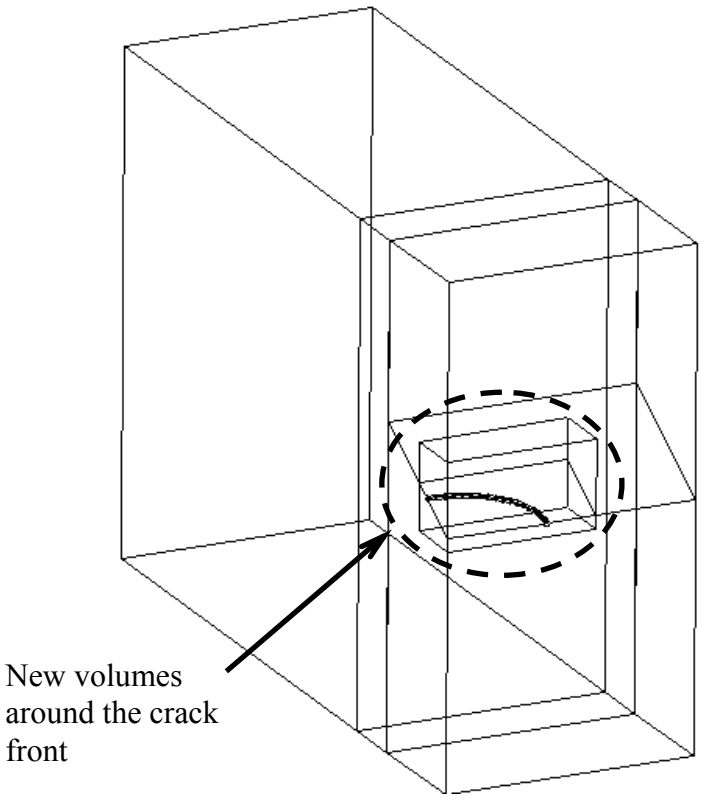

Figure 3.12 New volumes around the “crack tunnel”

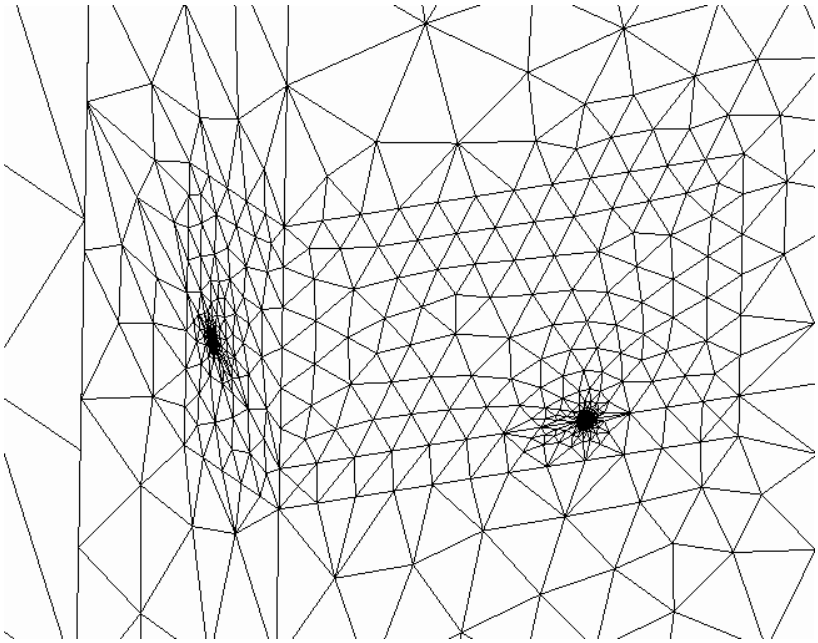

Figure 3.13 An enlarged view of the fine meshes around the crack front

SOLID90 is a three dimensional 20-node thermal solid element. It is a higher order version of the 3-D eight node thermal element, SOLID70. This element has 20 nodes with a single degree of freedom of temperature at its each node. It has compatible temperature shapes and is well suited to model curved boundaries. Furthermore, it is applicable to a 3-D, steady-state or transient thermal analysis. A demonstrative picture of the SOLID90 element is given in Figure 3.14 [30].

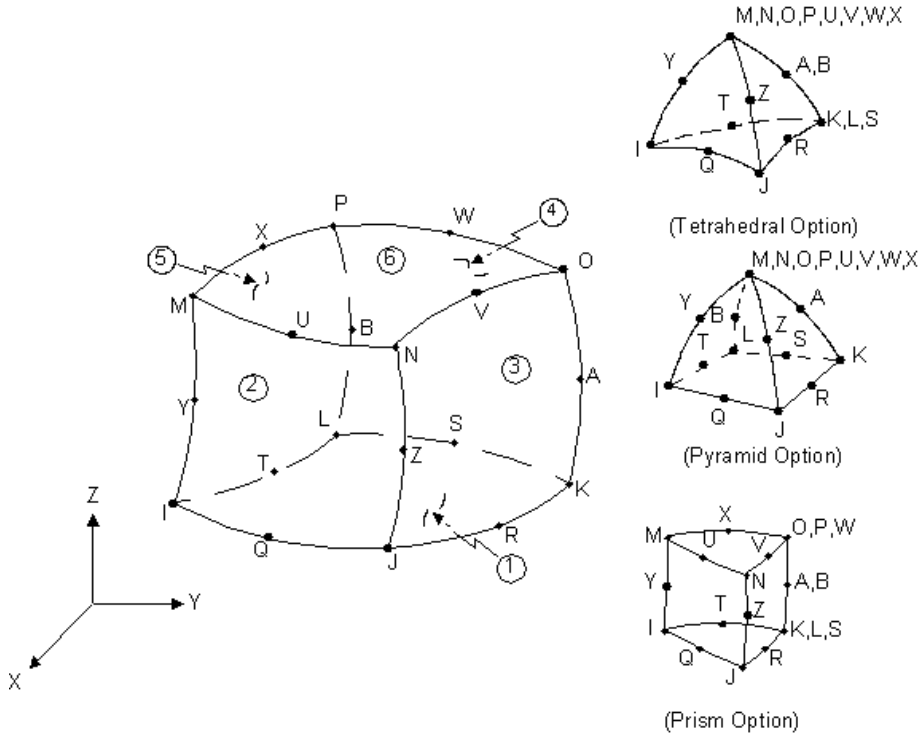

Figure 3.14 The SOLID90 element [30]

The modeling of the semi-elliptic crack in the FGM coating-bond coat-substrate structure is the same with the one explained in part 3.1.1. The thermomechanical properties of the composite structure are assigned according to variation function by using the centroid of each finite element. This procedure is developed by utilizing ANSYS APDL codes. During the analyses, a unique material property is assigned to each element with the help of this method.

In the analysis of the transient thermal loading problem, combined thermal-structural analysis is studied. In the thermal analysis, first transient heat conduction in the FGM coating-bond coat-substrate structure is conducted and consequently temperature distribution within the composite structure is computed. Afterwards, this temperature distribution is utilized as an input for the structural problem. While performing the analyses, it is assumed that the crack surfaces are completely insulated and the medium is free of any mechanical constraints. Furthermore, coupling of the thermal and structural problems are assumed to be through the calculated temperature distribution only since the inertia effects are not taken into account. Moreover, the temperature of the environment and free and forced convection coefficients given in section 2.5.2 are applied as surface loads at the relevant surfaces.

During the solution, minimum and maximum time step sizes are entered. In order to overcome oscillations in the distribution of temperature, minimum time step size is taken to be very small and maximum time step size is chosen as not to be very large.

The steps below explain the method used for modeling and analysis of the semi-elliptic surface crack in an FGM coating-bond coat-substrate structure under coupled transient thermal-structural analysis.

- Choose thermal for the analysis type,
- Select MESH200 and SOLID90 elements,
- Ask user to input the parameters (crack depth a, crack length c, thickness of the FGM coating t_1, thickness of the bond coat t_2, thickness of the substrate t_3, half-length of the solid h, half-width of the solid b, material property variation p and the inclination angle α),
- Create a local coordinate system for the crack front generation,
- Generate keypoints on the crack front,

♦ Create a circular area of specified radius at the first keypoint of the crack front,

♦ Form lines on the crack front by using the generated keypoints,

♦ Drag the circular area through the formed lines along the crack front and generate volumes around the crack front,

♦ Generate keypoints which are to be used for the solid boundaries,

♦ Create lines from the generated keypoints,

♦ Form the areas of the solid by using the created lines,

♦ Constitute the volumes of the solid by utilizing the formed areas,

♦ Generate keypoints which are to be used for local volume around the crack region,

♦ Create lines from the generated keypoints,

♦ Form the areas of the local volume by using the created lines,

♦ Constitute the local volumes around the crack front by utilizing the formed areas,

♦ Overlap the volumes around the crack front and the volume of the solid,

♦ Delete the unneeded volumes after the overlap operation,

♦ Delete the unwanted lines before the merging operation around the crack front,

♦ Merge the keypoints around the crack front that are not used for crack simulation,

♦ State the last keypoint of the crack front about which an area mesh will be skewed with specifying the radius and number of the singular elements around it,

♦ Specify line divisions around the mesh area and drag line of the crack front,

♦ Mesh the area at the last keypoint of the crack front,

♦ Fill the unmeshed volumes around the crack front with elements by sweeping the generated area through the volume,

♦ Generate keypoints which are to be used for the boundaries of bond coat and substrate,

♦ Form the areas of the bond coat and substrate by using the generated keypoints,

♦ Constitute the volumes of the bond coat and substrate by utilizing the formed areas,

♦ Merge FGM coating and bond coat,

♦ Glue the volumes of bond coat and substrate,

♦ Generate nodes and elements within the local volume of FGM coating around the crack front by specifying the element size,

♦ Perform the same operation for the remaining part of the coating,

♦ Carry out nodes and elements generation within the volumes of bond coat and substrate by specifying the element size,

♦ Specify the thermomechanical properties at the centroid of each element,

♦ Choose transient for the analysis type,

♦ Enter the initial temperature,

♦ Enter the temperature of the environment and apply free and forced convection coefficients on related surfaces of the composite structure,

♦ Specify end time and min. and max. time step sizes with activating the automatic time-stepping option,

♦ Solve the problem and calculate the temperatures at each node,

♦ Specify time steps,

♦ Choose static for the analysis type,

♦ Enter the reference temperature,

- Choose the symmetry planes,
- Select and define the crack front nodes that are to be used for the calculation of mixed mode stress intensity factors,
- Read the results from the thermal results file for a given time and apply them as loads,
- Solve the problem,
- Compute the mixed mode stress intensity factors at the crack front nodes by utilizing the displacement correlation technique,
- Also calculate the energy release rate,
- Repeat the last four steps for each required time until the end time is reached.

As stated in the preceding steps, in order to compute the mixed mode stress intensity factors at the crack front nodes, the displacement correlation technique is utilized. Details of this solution method can be found in Chapter 4. In conducting the numerical analyses, an APDL subroutine using this method is generated. In this subroutine, the computed displacements of the nodes at the edge of collapsed 20 – node brick elements are used as inputs for displacement correlation method.

CHAPTER 4

STRESS INTENSITY FACTORS AND ENERGY RELEASE RATE CALCULATIONS

4.1 The Displacement Correlation Technique (DCT)

After the displacement values around the crack front of the FGM coating-bond coat-substrate structure are obtained with the help of the commercial analysis code by applying finite element method, the displacement correlation technique (DCT) can be utilized in order to calculate mode I, mode II and mode III stress intensity factors.

In Figure 4.1, a three dimensional crack front, which is assumed to be embedded in an FGM coating, is shown. In this figure, the parameter s is the arc length of the crack front. The local coordinate system located at point P is composed of the tangential (t), normal (n) and binormal (b) directions and (r, θ) are the polar coordinates in the normal plane (n, b). In the papers of Eischen et al. [32] and Noda et al. [33], it was shown that the asymptotic fields for a crack in an FGM with continuous and piecewise differentiable mechanical properties are same as those of a crack embedded in a homogeneous material. In addition, the asymptotic displacement expressions for the homogeneous materials can be used for FGMs on condition that the material properties are calculated at the crack-front location. Therefore, in the implementation of DCT for FGMs, the expressions in the subsequent sections can be utilized with appropriate modifications in order to calculate mixed mode stress intensity factors around the crack front.

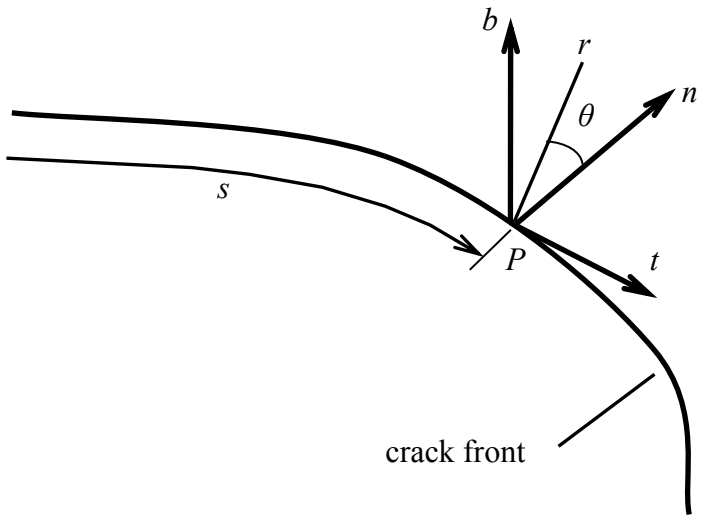

Figure 4.1 Crack front and the local coordinate system at a point P

4.2 Mode I (K_I) SIF Calculations

The displacement component, which is required to calculate K_I, at point P on the crack front can be expressed as

$$u_b(r,\theta)=\left(\frac{1+\nu}{E}\right)\sqrt{\frac{2r}{\pi}}\left\{K_I(s)\sin\left(\frac{\theta}{2}\right)\left[2(1-\nu)-\cos^2\left(\frac{\theta}{2}\right)\right]\right.$$

$$\left.-K_{II}(s)\cos\left(\frac{\theta}{2}\right)\left[(1-2\nu)-\sin^2\left(\frac{\theta}{2}\right)\right]\right\} \qquad (4.1)$$

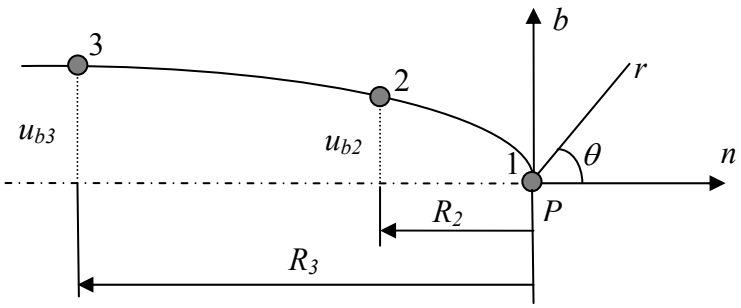

Figure 4.2 Deformed shape of the crack surface (symmetric)

In Figure 4.2, the deformed shape of the crack surface is shown. Point *P* is on the crack front and it is parallel to the normal plane (*n, b*). In this figure, a section at point *P* is taken in order to calculate K_I. Here, nodes 1, 2 and 3 are at the edge of a collapsed 20-node quarter point brick element. From equation (4.1), the displacement field on the crack surface (for $\theta = \pi$) can be written as

$$u_b(r,\pi) = \left(\frac{1+\nu}{E}\right)\sqrt{\frac{2r}{\pi}}\, K_I 2(1-\nu) \tag{4.2}$$

The above equation can be used to obtain

$$u_b(r,\pi) = \frac{4(1-\nu^2)}{E}\left(\sqrt{\frac{r}{2\pi}}\right)K_I \tag{4.3}$$

The mode I stress intensity factor can then be evaluated from equation (4.3) as shown in the below expression

$$K_I = \frac{\sqrt{2\pi}\times E}{4(1-\nu^2)}\left[\lim_{r\to 0}\left\{\frac{u_b(r,\pi)}{\sqrt{r}}\right\}\right] \tag{4.4}$$

Supposing $\frac{u_b(r,\pi)}{\sqrt{r}}$ is to be linear, one can obtain

$$\frac{u_b(r,\pi)}{\sqrt{r}} = \mathrm{X} + \mathrm{Y}r \tag{4.5}$$

As it can be seen from Figure 4.2, there are two boundary conditions. These are

(i) $u_b = u_{b2}$ when $r = R_2$ and
(ii) $u_b = u_{b3}$ when $r = R_3$

Therefore,

$$\text{for } r = R_2 \longrightarrow \quad \frac{u_b(R_2,\pi)}{\sqrt{R_2}} = \frac{u_{b2}}{\sqrt{R_2}} = \mathrm{X} + \mathrm{Y}R_2 \tag{4.6}$$

and

$$\text{for } r = R_3 \longrightarrow \frac{u_b(R_3,\pi)}{\sqrt{R_3}} = \frac{u_{b3}}{\sqrt{R_3}} = \mathrm{X} + \mathrm{Y}R_3 \tag{4.7}$$

In the above equations, the two unknowns, namely X and Y are to be found. Using equations (4.6) and (4.7) one can find X as

$$\mathrm{X} = \frac{R_3^{3/2}u_{b2} - R_2^{3/2}u_{b3}}{\sqrt{R_2}\sqrt{R_3}\left(R_3 - R_2\right)} \tag{4.8}$$

At the crack tip (i.e. $r \to 0$), $\lim_{r\to 0}\left\{\frac{u_b(r,\pi)}{\sqrt{r}}\right\}$ equals to X [equation (4.5)]. Thus, equation (4.4) becomes

$$K_I = \frac{\sqrt{2\pi}\times E}{4\left(1-\nu^2\right)}.\mathrm{X} \tag{4.9}$$

Therefore,

$$K_I = \frac{\sqrt{2\pi}\times E}{4\left(1-\nu^2\right)}.\left[\frac{R_3^{3/2}u_{b2} - R_2^{3/2}u_{b3}}{\sqrt{R_2}\sqrt{R_3}\left(R_3 - R_2\right)}\right] \tag{4.10}$$

The above equations are valid only if the crack region is symmetric. Since the problem considered in this study is related to the inclined cracks (unsymmetrical), a complete crack model is needed to calculate the stress intensity factors. The figure below shows the full model which is to be used for mode I stress intensity factor calculation of an inclined crack.

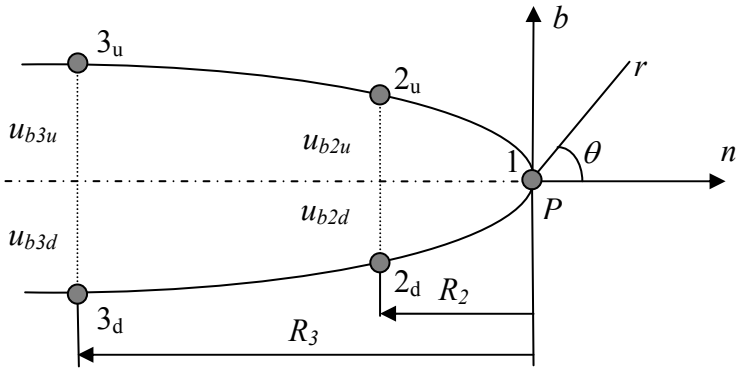

Figure 4.3 Deformed shape of the crack surface (non-symmetric)

As shown in equation (4.2), $u_b(r,\pi)$ is calculated by using equation (4.1). For the non-symmetric crack model, $u_b(r,-\pi)$ is also required. Thus, substituting $\theta = -\pi$ into equation (4.1) yields

$$u_b(r,-\pi) = -\left(\frac{1+\nu}{E}\right)\sqrt{\frac{2r}{\pi}}\ K_I 2(1-\nu) \tag{4.11}$$

From (4.11) the below expression can be obtained

$$u_b(r,-\pi) = -\frac{4(1-\nu^2)}{E}\left(\sqrt{\frac{r}{2\pi}}\right)K_I \tag{4.12}$$

Subtracting equation (4.12) from (4.3) yields

$$u_b(r,\pi) - u_b(r,-\pi) = \frac{8(1-\nu^2)}{E}\sqrt{\frac{r}{2\pi}}K_I \tag{4.13}$$

From equation (4.13), K_I can be obtained as

$$K_I = \frac{\sqrt{2\pi}\times E}{8(1-\nu^2)} \times \left[\lim_{r\to 0}\left\{\frac{u_b(r,\pi)-u_b(r,-\pi)}{\sqrt{r}}\right\}\right] \tag{4.14}$$

Assuming $\frac{u_b(r,\pi)-u_b(r,-\pi)}{\sqrt{r}}$ is to be linear, one can get

$$\frac{u_b(r,\pi)-u_b(r,-\pi)}{\sqrt{r}} = \mathrm{X} + \mathrm{Y}r \tag{4.15}$$

As it can be seen from Figure 4.3, there exist two boundary conditions. These are

(i) when $r = R_2$, $u_b(R_2,\pi)=u_{b2u}$ and $u_b(R_2,-\pi)= u_{b2d}$

(ii) when $r = R_3$, $u_b(R_3,\pi)=u_{b3u}$ and $u_b(R_3,-\pi)= u_{b3d}$

where "u=up" stands for the upper nodal displacements and "d=down" stands for the lower nodal displacements. Applying the two boundary conditions results in

$$\text{for } r = R_2 \longrightarrow \frac{u_b(R_2,\pi)-u_b(R_2,-\pi)}{\sqrt{R_2}} = \frac{u_{b2u}-u_{b2d}}{\sqrt{R_2}} = \mathrm{X} + \mathrm{Y}R_2 \tag{4.16}$$

and

$$\text{for } r = R_3 \longrightarrow \frac{u_b(R_3,\pi)-u_b(R_3,-\pi)}{\sqrt{R_3}} = \frac{u_{b3u}-u_{b3d}}{\sqrt{R_3}} = \mathrm{X} + \mathrm{Y}R_3 \tag{4.17}$$

From equations (4.16) and (4.17), X can be obtained as

$$\mathrm{X} = \frac{R_3^{3/2}(u_{b2u}-u_{b2d})-R_2^{3/2}(u_{b3u}-u_{b3d})}{\sqrt{R_2}\sqrt{R_3}(R_3-R_2)} \tag{4.18}$$

At the crack tip (i.e. $r \to 0$), $\lim_{r\to 0}\left\{\frac{u_b(r,\pi)-u_b(r,-\pi)}{\sqrt{r}}\right\}$=X. Hence, equation (4.14) becomes

$$K_I = \frac{\sqrt{2\pi}\times E}{8\left(1-\nu^2\right)}.\mathrm{X} \tag{4.19}$$

Therefore,

$$K_I = \frac{\sqrt{2\pi} \times E}{8(1-\nu^2)} \cdot \left[\frac{R_3^{3/2}(u_{b2u} - u_{b2d}) - R_2^{3/2}(u_{b3u} - u_{b3d})}{\sqrt{R_2}\sqrt{R_3}(R_3 - R_2)} \right] \tag{4.20}$$

4.3 Mode II (K_{II}) SIF Calculations

The displacement component at point P on crack front which is required to calculate K_{II} can be expressed for a full (non-symmetric) crack model as

$$u_b(r,\theta) = \left(\frac{1+\nu}{E}\right)\sqrt{\frac{2r}{\pi}}\left\{K_I(s)\cos\left(\frac{\theta}{2}\right)\left[(1-2\nu) + \sin^2\left(\frac{\theta}{2}\right)\right]\right.$$

$$\left. + K_{II}(s)\sin\left(\frac{\theta}{2}\right)\left[2(1-\nu) + \cos^2\left(\frac{\theta}{2}\right)\right]\right\} \tag{4.21}$$

Therefore,

$$u_n(r,\pi) = \left(\frac{1+\nu}{E}\right)\sqrt{\frac{2r}{\pi}}K_{II}\,2(1-\nu) = \frac{4(1-\nu^2)}{E}\sqrt{\frac{r}{2\pi}}K_{II} \tag{4.22}$$

and

$$u_n(r,-\pi) = -\left(\frac{1+\nu}{E}\right)\sqrt{\frac{2r}{\pi}}K_{II}\,2(1-\nu) = -\frac{4(1-\nu^2)}{E}\sqrt{\frac{r}{2\pi}}K_{II} \tag{4.23}$$

From equations (4.22) and (4.23), the expression below can be obtained

$$u_n(r,\pi) - u_n(r,-\pi) = \frac{8(1-\nu^2)}{E}\sqrt{\frac{r}{2\pi}}K_{II} \tag{4.24}$$

From equation (4.24), K_{II} can be obtained as

$$K_{II} = \frac{\sqrt{2\pi} \times E}{8(1-\nu^2)} \times \left[\lim_{r\to 0}\left\{\frac{u_n(r,\pi) - u_n(r,-\pi)}{\sqrt{r}}\right\}\right] \tag{4.25}$$

Assuming $\frac{u_n(r,\pi)-u_n(r,-\pi)}{\sqrt{r}}$ is to be linear, one can get

$$\frac{u_n(r,\pi)-u_n(r,-\pi)}{\sqrt{r}} = \mathrm{X} + \mathrm{Y}r \tag{4.26}$$

The two boundary conditions in this case are

(i) when $r = R_2$, $u_n(R_2,\pi) = u_{n2u}$ and $u_n(R_2,-\pi) = u_{n2d}$

and

(ii) when $r = R_3$, $u_n(R_3,\pi) = u_{n3u}$ and $u_n(R_3,-\pi) = u_{n3d}$

Therefore,

$$\text{for } r = R_2 \longrightarrow \frac{u_n(R_2,\pi)-u_n(R_2,-\pi)}{\sqrt{R_2}} = \frac{u_{n2u}-u_{n2d}}{\sqrt{R_2}} = \mathrm{X} + \mathrm{Y}R_2 \tag{4.27}$$

and

$$\text{for } r = R_3 \longrightarrow \frac{u_n(R_3,\pi)-u_n(R_3,-\pi)}{\sqrt{R_3}} = \frac{u_{n3u}-u_{n3d}}{\sqrt{R_3}} = \mathrm{X} + \mathrm{Y}R_3 \tag{4.28}$$

From equations (4.27) and (4.28), X can be evaluated as

$$\mathrm{X} = \frac{R_3^{3/2}(u_{n2u}-u_{n2d}) - R_2^{3/2}(u_{n3u}-u_{n3d})}{\sqrt{R_2}\sqrt{R_3}\left(R_3-R_2\right)} \tag{4.29}$$

At the crack tip, (i.e. $r \to 0$) $\lim_{r\to 0}\left\{\frac{u_n(r,\pi)-u_n(r,-\pi)}{\sqrt{r}}\right\}$=X. Hence, equation (4.25) becomes

$$K_{II} = \frac{\sqrt{2\pi}\times E}{8\left(1-\nu^2\right)}.\mathrm{X} \tag{4.30}$$

Therefore, substituting the value of X [equation (4.29)] into equation (4.30) yields

$$K_{II}=\frac{\sqrt{2\pi}\times E}{8\left(1-\nu^{2}\right)}\cdot\left[\frac{R_3^{\,3/2}(u_{n2u}-u_{n2d})-R_2^{\,3/2}(u_{n3u}-u_{n3d})}{\sqrt{R_2}\sqrt{R_3}\left(R_3-R_2\right)}\right] \tag{4.31}$$

4.4 Mode III (K_{III}) SIF Calculations

K_{III} can be calculated by the tangential displacement component at point P on the crack front. The tangential displacement component at this point is

$$u_t(r,\theta)=2\left(\frac{1+\nu}{E}\right)\sqrt{\frac{2r}{\pi}}K_{III}(s)\sin\left(\frac{\theta}{2}\right) \tag{4.32}$$

From equation (4.32) $u_t(r,\pi)$ and $u_t(r,-\pi)$ can be evaluated as

$$u_t(r,\pi)=2\left(\frac{1+\nu}{E}\right)\sqrt{\frac{2r}{\pi}}K_{III}=\frac{4(1+\nu)}{E}\sqrt{\frac{r}{2\pi}}K_{III} \tag{4.33}$$

and

$$u_t(r,-\pi)=-2\left(\frac{1+\nu}{E}\right)\sqrt{\frac{2r}{\pi}}K_{III}=-\frac{4(1+\nu)}{E}\sqrt{\frac{r}{2\pi}}K_{III} \tag{4.34}$$

From equations (4.33) and (4.34), the below expression can be obtained.

$$u_t(r,\pi)-u_t(r,-\pi)=\frac{8(1+\nu)}{E}\sqrt{\frac{r}{2\pi}}K_{III} \tag{4.35}$$

From equation (4.35), K_{III} can be obtained as

$$K_{III}=\frac{\sqrt{2\pi}\times E}{8\left(1+\nu\right)}\times\left[\lim_{r\to 0}\left\{\frac{u_t(r,\pi)-u_t(r,-\pi)}{\sqrt{r}}\right\}\right] \tag{4.36}$$

Assuming $\dfrac{u_t(r,\pi)-u_t(r,-\pi)}{\sqrt{r}}$ is to be linear, one can get

$$\frac{u_t(r,\pi)-u_t(r,-\pi)}{\sqrt{r}} = \mathrm{X} + \mathrm{Y}r \tag{4.37}$$

The two boundary conditions in this case are

(i) when $r = R_2$, $u_t(R_2,\pi) = u_{t2u}$ and $u_t(R_2,-\pi) = u_{t2d}$

and

(ii) when $r = R_3$, $u_t(R_3,\pi) = u_{t3u}$ and $u_t(R_3,-\pi) = u_{t3d}$

Thus,

$$\text{for } r = R_2 \longrightarrow \frac{u_t(R_2,\pi)-u_t(R_2,-\pi)}{\sqrt{R_2}} = \frac{u_{t2u}-u_{t2d}}{\sqrt{R_2}} = \mathrm{X} + \mathrm{Y}R_2 \tag{4.38}$$

and

$$\text{for } r = R_3 \longrightarrow \frac{u_t(R_3,\pi)-u_t(R_3,-\pi)}{\sqrt{R_3}} = \frac{u_{t3u}-u_{t3d}}{\sqrt{R_3}} = \mathrm{X} + \mathrm{Y}R_3 \tag{4.39}$$

From equations (4.38) and (4.39), X can be obtained as

$$\mathrm{X} = \frac{R_3^{3/2}(u_{t2u}-u_{t2d}) - R_2^{3/2}(u_{t3u}-u_{t3d})}{\sqrt{R_2}\sqrt{R_3}\left(R_3-R_2\right)} \tag{4.40}$$

At the tip of the crack i.e. as $r \to 0$, $\lim_{r\to 0}\left\{\frac{u_t(r,\pi)-u_t(r,-\pi)}{\sqrt{r}}\right\}$=X. Hence, equation (4.36) becomes

$$K_{III} = \frac{\sqrt{2\pi}\times E}{8\left(1+\nu\right)}.\mathrm{X} \tag{4.41}$$

By substituting equation (4.40) into (4.41), K_{III} can be expressed as

$$K_{III} = \frac{\sqrt{2\pi} \times E}{8(1+\nu)} \cdot \left[\frac{R_3^{3/2}(u_{t2u} - u_{t2d}) - R_2^{3/2}(u_{t3u} - u_{t3d})}{\sqrt{R_2}\sqrt{R_3}(R_3 - R_2)} \right] \tag{4.42}$$

4.5 Energy Release Rate (*G*) Calculations

Once mode I, mode II and mode III stress intensity factors are calculated, energy release rate can also be evaluated. The following expressions show the relationship between stress intensity factors and energy release rate.

for mode I crack:

$$G_I = \frac{\kappa + 1}{8\mu} K_I^{\,2} \tag{4.43}$$

for mode II crack:

$$G_{II} = \frac{\kappa + 1}{8\mu} K_{II}^{\,2} \tag{4.44}$$

and for mode III crack:

$$G_{III} = \frac{K_{III}^{\,2}}{2\mu} \tag{4.45}$$

where for the plane strain condition

$$\mu = \frac{E}{2(1+\nu)} \tag{4.46}$$

and

$$\kappa = 3 - 4\nu \tag{4.47}$$

Since the problem analyzed in this study is also a plane strain problem, the values of μ and κ can be substituted into equations (4.43), (4.44) and (4.45) yielding

$$G_I = \frac{(1-\nu^2)}{E} K_I^{\,2} \tag{4.48}$$

$$G_{II} = \frac{(1-\nu^2)}{E} K_{II}^{\,2} \tag{4.49}$$

$$G_{III} = \frac{(1+\nu)}{E} K_{III}^{\,2} \tag{4.50}$$

Therefore, the total strain energy release rate under mixed mode loading is

$$G_T = G_I + G_{II} + G_{III} = \frac{(1-\nu^2)}{E}\left\{ K_I^{\,2} + K_{II}^{\,2} + \frac{K_{III}^{\,2}}{1-\nu} \right\} \tag{4.51}$$

CHAPTER 5

NUMERICAL RESULTS AND DISCUSSION

5.1 Introduction

In this chapter, sample results obtained by the numerical analyses conducted are presented and discussed. First, the calculated finite element model results are compared to that of Ayhan et al. [11] and Isida et al. [9]. In the first comparison, a plate with finite dimensions and in the second comparison a semi-infinite solid is modeled and finite element analyses are carried out for various inclination of semi-elliptic surface crack. After the accuracy of the finite element model is checked out, the same model is used for the analyses of semi-elliptic inclined surface crack embedded in the FGM coating of composite structure. The finite element analyses of FGM coating-bond coat-substrate structure are carried out and the numerical results are calculated for various inclinations of three dimensional semi-elliptic surface crack, coating types, crack front angles and relative dimension of the crack with respect to FGM coating thickness.

5.2 Comparisons to Results of Ayhan et al. [11]

In the first comparison, the validation of the model is done by modeling and analyzing the plate, which contains a semi-elliptic inclined surface crack, with finite dimensions subjected to uniform tension as illustrated in Figure 2.12.

For this type of analysis, the inclination angle α is taken as 0^o, 15^o, 30^o, 45^o, 60^o and 75^o. Then, the normalized mode I, mode II and mode III stress intensity factors are evaluated for the corresponding angles of inclination. The calculated mixed mode normalized stress intensity factors are tabulated in Table 5.1-Table 5.6.

Table 5.1 Calculated normalized mixed mode stress intensity factors K_{In} ,K_{IIn} ,K_{IIIn} for a homogeneous plate subjected to uniform tension, $\alpha=0^o$.

Calculated results for $\alpha=0^o$			
Crack front angle, ϕ	K_{In}	K_{IIn}	K_{IIIn}
0,0	1,1710	-0,0013	-0,0005
6,4	1,2014	-0,0011	-0,0002
12,9	1,1625	-0,0008	-0,0002
19,3	1,1379	-0,0008	-0,0002
25,7	1,1202	-0,0008	-0,0002
32,2	1,1070	-0,0007	-0,0002
38,6	1,0970	-0,0005	-0,0002
45,0	1,0892	-0,0005	-0,0002
51,4	1,0833	-0,0004	-0,0003
57,9	1,0787	-0,0003	-0,0002
64,3	1,0751	-0,0003	-0,0002
70,7	1,0724	-0,0003	-0,0001
77,2	1,0706	-0,0002	-0,0001
83,6	1,0565	-0,0002	0,0000
90,0	1,0551	-0,0005	0,0000

Table 5.2 Calculated normalized mixed mode stress intensity factors K_{In} ,K_{IIn} ,K_{IIIn} for a homogeneous plate subjected to uniform tension, α=15^o.

Calculated results for α=15^o			
Crack front angle, ϕ	K_{In}	K_{IIn}	K_{IIIn}
6,4	1,1320	-0,0489	-0,2006
12,9	1,1039	-0,0010	-0,1841
19,3	1,0827	0,0364	-0,1741
25,7	1,0663	0,0698	-0,1644
32,2	1,0534	0,1003	-0,1535
38,6	1,0434	0,1279	-0,1410
45,0	1,0354	0,1528	-0,1268
51,4	1,0291	0,1746	-0,1109
57,9	1,0243	0,1933	-0,0936
64,3	1,0207	0,2086	-0,0749
70,7	1,0179	0,2205	-0,0552
77,2	1,0160	0,2287	-0,0347
83,6	1,0024	0,2315	-0,0138
90,0	1,0015	0,2325	0,0000

Table 5.3 Calculated normalized mixed mode stress intensity factors K_{In} ,K_{IIn} ,K_{IIIn} for a homogeneous plate subjected to uniform tension, α=30^o.

Calculated results for α=30^o			
Crack front angle, ϕ	K_{In}	K_{IIn}	K_{IIIn}
6,4	0,9343	-0,0877	-0,3577
12,9	0,9353	0,0013	-0,3309
19,3	0,9251	0,0657	-0,3124
25,7	0,9134	0,1244	-0,2941
32,2	0,9029	0,1778	-0,2738
38,6	0,8936	0,2261	-0,2509
45,0	0,8859	0,2693	-0,2251

51,4	0,8795	0,3073	-0,1966
57,9	0,8743	0,3399	-0,1656
64,3	0,8703	0,3666	-0,1324
70,7	0,8673	0,3870	-0,0975
77,2	0,8653	0,4011	-0,0612
83,6	0,8533	0,4057	-0,0244
90,0	0,8521	0,4065	0,0000

Table 5.4 Calculated normalized mixed mode stress intensity factors K_{In} ,K_{IIn} ,K_{IIIn} for a homogeneous plate subjected to uniform tension, α=45^o.

Calculated results for α=45^o			
Crack front angle, ϕ	K_{In}	K_{IIn}	K_{IIIn}
6,4	0,6424	-0,0999	-0,4336
12,9	0,6806	0,0071	-0,4060
19,3	0,6893	0,0890	-0,3826
25,7	0,6884	0,1595	-0,3583
32,2	0,6840	0,2223	-0,3314
38,6	0,6786	0,2787	-0,3016
45,0	0,6732	0,3288	-0,2688
51,4	0,6682	0,3724	-0,2331
57,9	0,6639	0,4094	-0,1947
64,3	0,6603	0,4394	-0,1540
70,7	0,6575	0,4623	-0,1115
77,2	0,6555	0,4775	-0,0678
83,6	0,6463	0,4817	-0,0234
90,0	0,6454	0,4821	0,0000

Table 5.5 Calculated normalized mixed mode stress intensity factors K_{In} ,K_{IIn} ,K_{IIIn} for a homogeneous plate subjected to uniform tension, α=60^o.

Calculated results for α=60^o			
Crack front angle, ϕ	K_{In}	K_{IIn}	K_{IIIn}
6,4	0,3184	-0,0677	-0,4008
12,9	0,3848	0,0362	-0,3809
19,3	0,4140	0,1135	-0,3593
25,7	0,4279	0,1774	-0,3343
32,2	0,4349	0,2335	-0,3064
38,6	0,4376	0,2820	-0,2754
45,0	0,4390	0,3246	-0,2420
51,4	0,4381	0,3609	-0,2062
57,9	0,4369	0,3913	-0,1686
64,3	0,4358	0,4146	-0,1290
70,7	0,4347	0,4321	-0,0885
77,2	0,4345	0,4425	-0,0474
83,6	0,4270	0,4439	-0,0057
90,0	0,4328	0,4499	0,0000

Table 5.6 Calculated normalized mixed mode stress intensity factors K_{In} ,K_{IIn} ,K_{IIIn} for a homogeneous plate subjected to uniform tension, α=75^o.

Calculated results for α=75^o			
Crack front angle, ϕ (deg.)	K_{In}	K_{IIn}	K_{IIIn}
6,4	0,0630	-0,0492	-0,2580
12,9	0,1217	0,0255	-0,2533
19,3	0,1543	0,0808	-0,2406
25,7	0,1797	0,1268	-0,2264
32,2	0,1962	0,1653	-0,2077
38,6	0,2099	0,1976	-0,1874
45,0	0,2190	0,2260	-0,1646

51,4	0,2254	0,2498	-0,1401
57,9	0,2308	0,2699	-0,1146
64,3	0,2337	0,2849	-0,0879
70,7	0,2366	0,2961	-0,0599
77,2	0,2379	0,3013	-0,0318
83,6	0,2353	0,3008	-0,0042
90,0	0,2382	0,3045	0,0000

In Figures 5.1-5.6, the variations of normalized mixed mode stress intensity factors versus crack front angles are plotted for 0^o, 15^o, 30^o, 45^o, 60^o and 75^o inclination angles. As it can be seen from these figures, the results of this study are plotted for $\phi \geq 6.4^o$ except for 0^o inclination angle. The reason is that for the inclination angles except 0^o, due to the inclination of the crack, it is not possible to calculate mixed mode stress intensity factors correctly at the point intersecting free surface. During the implementation of displacement correlation technique, the program calculates mixed mode SIFs by defining a new coordinate system perpendicular to the crack front. Since the free surface is perpendicular to the crack front for only 0^o inclination angle, the results, which are tabulated in Table 5.2-5.6 for 15^o, 30^o, 45^o, 60^o and 75^o inclination angles, do not include 0^o crack front angle.

It can be observed from Figures 5.1-5.6 that, for inclination angles $\alpha \leq 45^o$, K_{In} attains the largest values compared to K_{IIn} and K_{IIIn} for all crack front angles. In addition, K_{In} reaches its maximum value near free surface region at $\phi \cong 6^o$ and decreases along the crack front towards the symmetry plane for $\alpha \leq 45^o$. As can be seen in Figures 5.1-5.6, K_{In} is maximum along the whole crack front when the crack is not inclined, i.e., $\alpha = 0^o$ and continuously decreases with increasing inclination angle.

From Figure 5.1, it can be seen that K_{IIn} and K_{IIIn} are zero along the whole crack front for $\alpha = 0^o$ as this case represents pure mode I conditions. With increasing

inclination angle, K_{IIn} also increases until $\alpha = 45^o$ where it reaches its maximum value in magnitude. Then, for $\alpha = 60^o$ and $\alpha = 75^o$, K_{IIn} decreases as the inclination angle increases. Since the plate analyzed in this study is under pure tension, the fact that K_{IIn} has its maximum value at $\alpha = 45^o$ among the cases considered, agrees well with the orientation of maximum shear stress.

Another interesting conclusion derived from Figures 5.2-5.6, where the inclination angle is non-zero, is that the normalized mode II stress intensity factors change their signs near $\phi = 15^o$ where they get a value of zero.

Similar behavior is also seen for normalized mode III stress intensity factor. With increasing inclination angle, K_{IIIn} also increases until $\alpha = 45^o$ where it reaches its maximum value in magnitude. Then, for $\alpha = 60^o$ and $\alpha = 75^o$, K_{IIIn} is lower on the whole crack front compared to the $\alpha = 45^o$ case. An interesting behavior of the mode III stress intensity factor is seen at the symmetry point (i.e., when $\phi = 90^o$) where K_{IIIn} becomes zero.

If Figures 5.1-5.6 are analyzed, it can be said that the obtained results are in good agreement with that of Ayhan et al. [11] especially for $\alpha \leq 45^o$. For large inclination angle (i.e., $\alpha > 45^o$), however, there are quite differences between the behavior of the plots. The reason of the quite deviations of the figures is due to the fact that three dimensional mixed mode analysis of cracks is more difficult than mode I cracks because of triple number of unknown functions and boundary conditions, [10] (Noda et al.). It is further stated in the same paper that, it is hard to obtain accurate stress intensity factors for large inclination angle since the effect of free surface on the stress intensity factors is complicated and becomes larger.

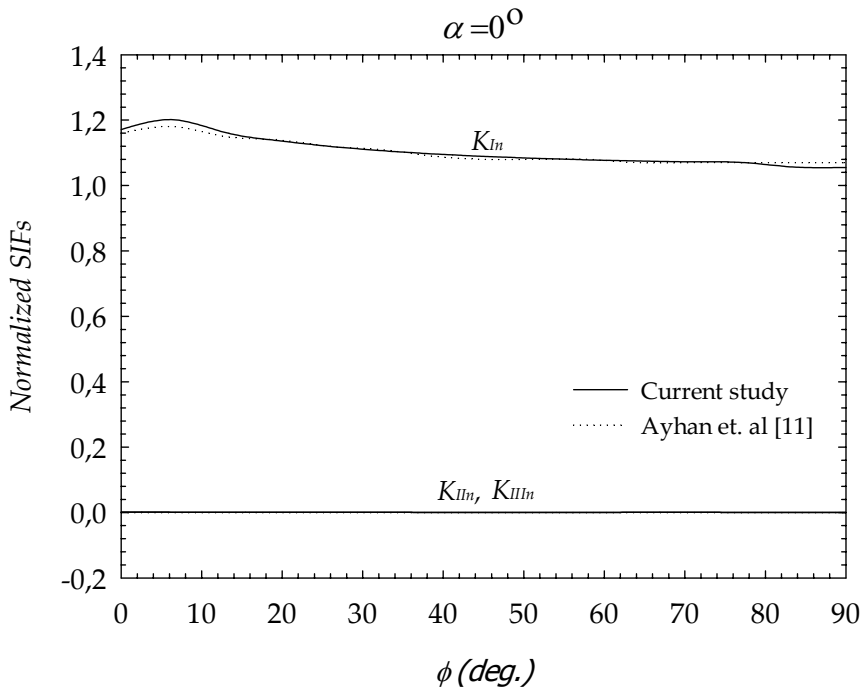

Figure 5.1 Comparisons of normalized mixed mode stress intensity factors for 0^o inclination angle

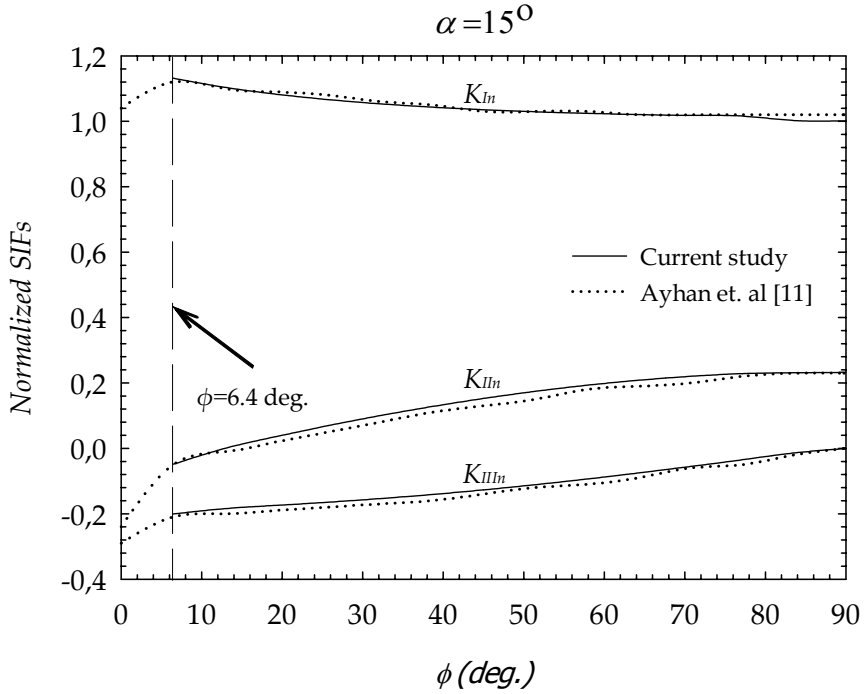

Figure 5.2 Comparisons of normalized mixed mode stress intensity factors for 15^o inclination angle

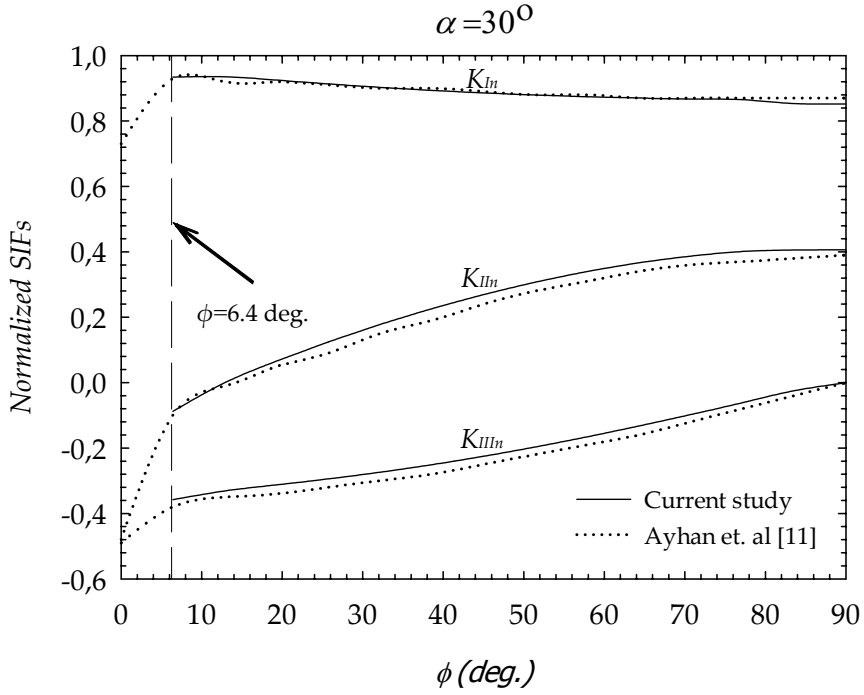

Figure 5.3 Comparisons of normalized mixed mode stress intensity factors for 30° inclination angle

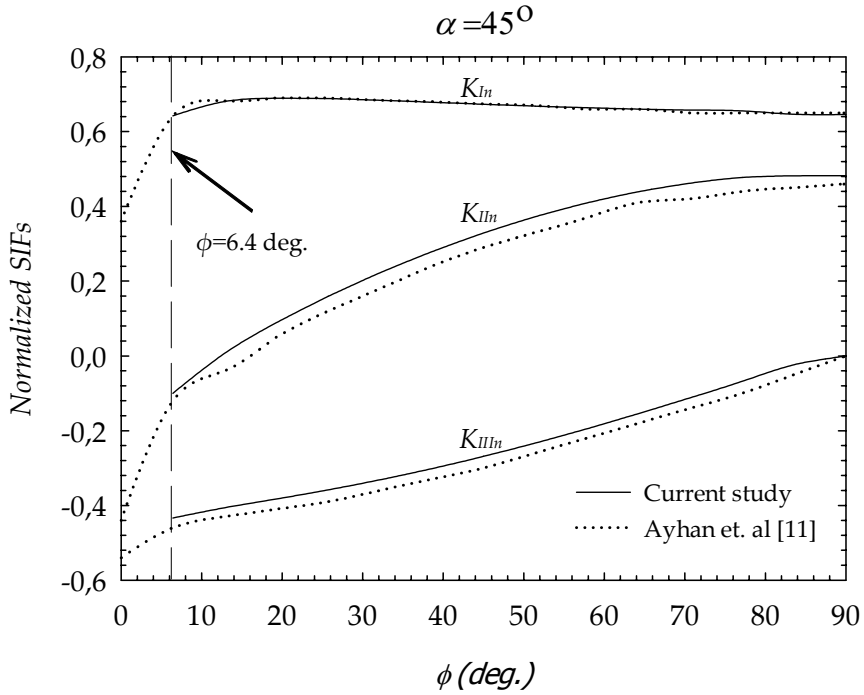

Figure 5.4 Comparisons of normalized mixed mode stress intensity factors for 45° inclination angle

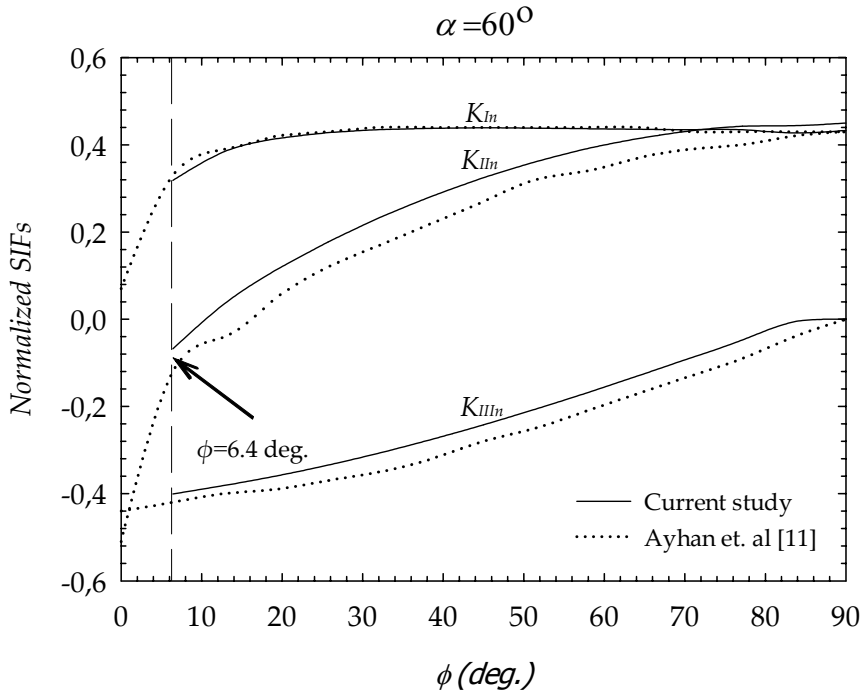

Figure 5.5 Comparisons of normalized mixed mode stress intensity factors for 60° inclination angle

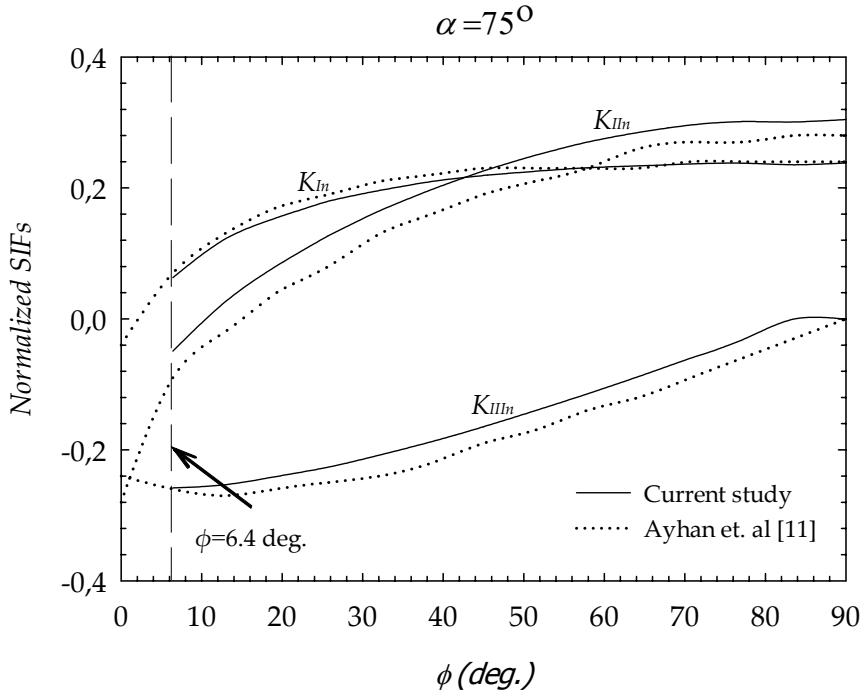

Figure 5.6 Comparisons of normalized mixed mode stress intensity factors for 75° inclination angle

5.3 Comparisons to Results of Isida et al. [9]

In the second comparison, the validation of the model is done by modeling and analyzing a semi-infinite solid, which contains a semi-elliptic inclined surface crack, under uniform tension as shown in Figure 2.13. For all the computations, the Poisson's ratio is taken as 0.3. The comparisons of the mixed-mode stress intensity factors are done for an aspect ratio of a/c=1. The semi-elliptic crack considered in this analysis is also obliquely inclined to the solid surface with an inclination angle α.

In this analysis, the inclination angle α is taken to be 15^o, 30^o, and 45^o. The dimensionless mode I, mode II and mode III stress intensity factors are calculated for the corresponding inclination angles. The calculated dimensionless mixed mode stress intensity factors are tabulated in Table 5.7-Table 5.9.

In Figures 5.7-5.9, the variations of the dimensionless mixed mode stress intensity factors are plotted with respect to crack front angle and compared to the results of Isida et al. [9]. In these figures, the results are plotted for $\phi > 5^o$ crack front angle due to the same reason stated in section 5.1.1.

If these figures are analyzed, it is again observed that dimensionless mode I stress intensity factor is larger than mode II and mode III for all inclination angles presented in the figures. It is seen that the dimensionless mode I stress intensity factor is maximum near the free surface ($\phi \cong 0^o$) and then starts to decrease as $\phi \to 90^o$ (symmetry surface) for 15^o and 30^o inclination angles. In the case of 45^o inclination angle, F_I gets its maximum value at $\phi \cong 15^o$ and again starts decreasing as the crack front angle goes to the symmetry surface. For all these three inclination angles, it is further observed that the value of F_I decreases as the inclination angle increases.

The value of dimensionless mode II stress intensity factor, however, is minimum near the free surface and reaches maximum near the symmetry surface for all three inclination angles. From these figures, it can be seen that as the inclination angle increases, the value of F_{II} also increases.

Like the behavior of dimensionless mode I stress intensity factor, the dimensionless mode III stress intensity factor is also maximum near the free surface and starts to decrease as $\phi \to 90^o$ for all three types of inclination angles. As in the case of dimensionless mode II stress intensity factor, the value of F_{III} also increases when the inclination angle increases.

The plots in Figures 5.7-5.9 are also in good agreement and they state that the model is validated and can be used for the analysis of FGM coating-bond coat-substrate structure.

Table 5.7 Calculated dimensionless mixed mode stress intensity factors F_I ,F_{II} and F_{III} for a semi-infinite solid subjected to uniform tension, α=15^o.

Calculated results for α=15^o			
Crack front angle, ϕ (deg.)	F_I	F_{II}	F_{III}
5	0,7025	-0,0362	0,1289
10	0,6905	-0,0089	0,1182
15	0,6791	0,0106	0,1121
20	0,6693	0,0284	0,1074
25	0,6610	0,0448	0,1026
30	0,6536	0,0583	0,0975
35	0,6478	0,0717	0,0924
40	0,6433	0,0846	0,0859
45	0,6403	0,0967	0,0790
50	0,6380	0,1071	0,0710
55	0,6350	0,1165	0,0628

60	0,6332	0,1250	0,0541
65	0,6314	0,1308	0,0450
70	0,6293	0,1353	0,0360
75	0,6290	0,1392	0,0264
80	0,6289	0,1415	0,0167
85	0,6217	0,1393	0,0070
90	0,6222	0,1400	0,0000

Table 5.8 Calculated dimensionless mixed mode stress intensity factors F_I ,F_{II} and F_{III} for a semi-infinite solid subjected to uniform tension, α=30^o.

Calculated results for α=30^o			
Crack front angle, ϕ (deg.)	F_I	F_{II}	F_{III}
5	0,5772	-0,0704	0,2287
10	0,5824	-0,0206	0,2126
15	0,5793	0,0164	0,2023
20	0,5742	0,0475	0,1935
25	0,5684	0,0757	0,1846
30	0,5624	0,1018	0,1754
35	0,5583	0,1266	0,1648
40	0,5545	0,1486	0,1530
45	0,5511	0,1692	0,1403
50	0,5477	0,1879	0,1265
55	0,5442	0,2037	0,1118
60	0,5418	0,2160	0,0959
65	0,5406	0,2286	0,0803
70	0,5391	0,2404	0,0632
75	0,5385	0,2483	0,0454
80	0,5382	0,2531	0,0277
85	0,5325	0,2541	0,0102
90	0,5363	0,2565	0,0000

Table 5.9 Calculated dimensionless mixed mode stress intensity factors F_I ,F_{II} and F_{III} for a semi-infinite solid subjected to uniform tension, α=45^o.

Calculated results for α=45^o			
Crack front angle, ϕ (deg.)	F_I	F_{II}	F_{III}
5	0,5772	-0,0704	0,2287
10	0,5824	-0,0206	0,2126
15	0,5793	0,0164	0,2023
20	0,5742	0,0475	0,1935
25	0,5684	0,0757	0,1846
30	0,5624	0,1018	0,1754
35	0,5583	0,1266	0,1648
40	0,5545	0,1486	0,1530
45	0,5511	0,1692	0,1403
50	0,5477	0,1879	0,1265
55	0,5442	0,2037	0,1118
60	0,5418	0,2160	0,0959
65	0,5406	0,2286	0,0803
70	0,5391	0,2404	0,0632
75	0,5385	0,2483	0,0454
80	0,5382	0,2531	0,0277
85	0,5325	0,2541	0,0102
90	0,5363	0,2565	0,0000

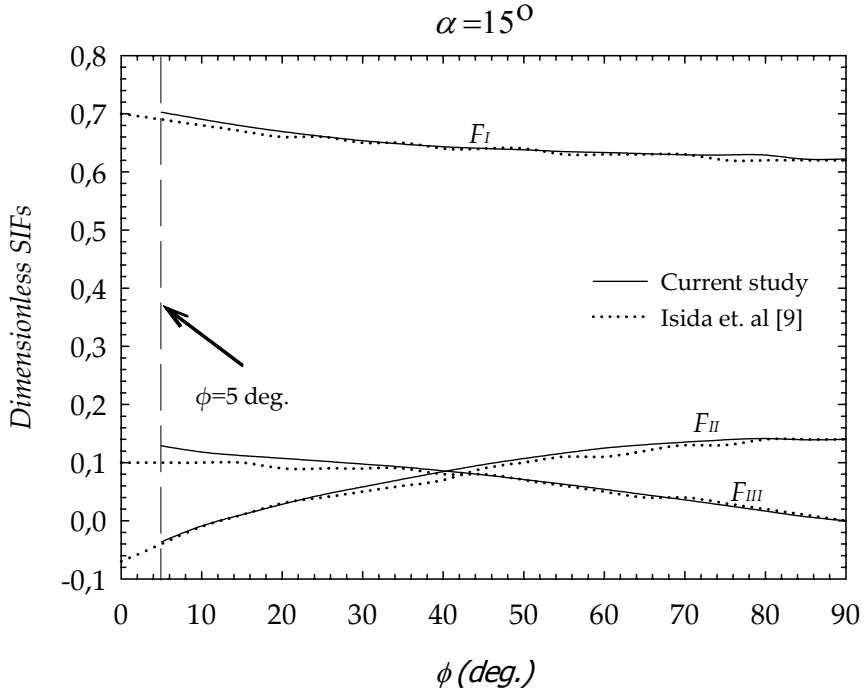

Figure 5.7 Comparisons of dimensionless mixed mode stress intensity factors for 15° inclination angle

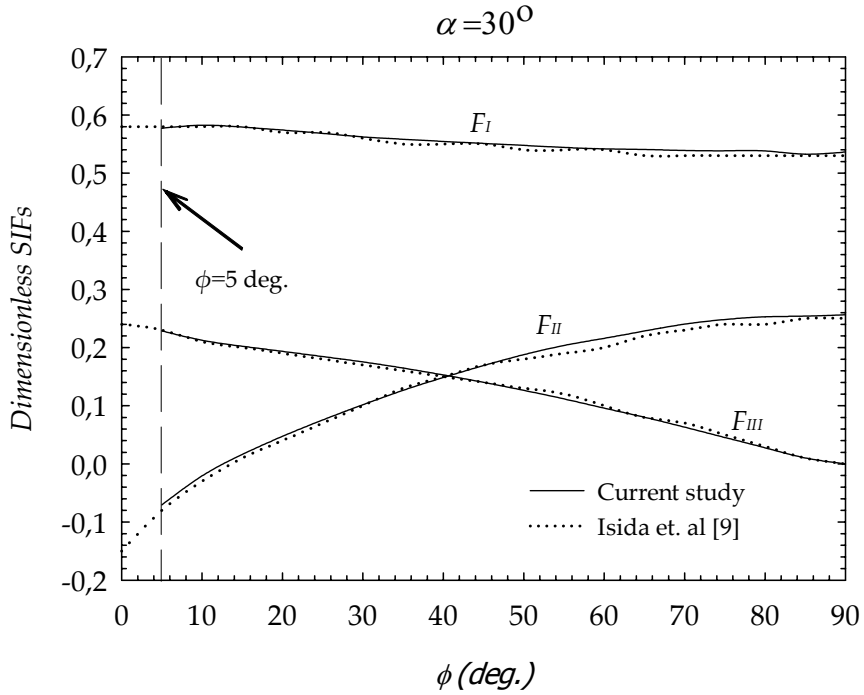

Figure 5.8 Comparisons of dimensionless mixed mode stress intensity factors for 30° inclination angle

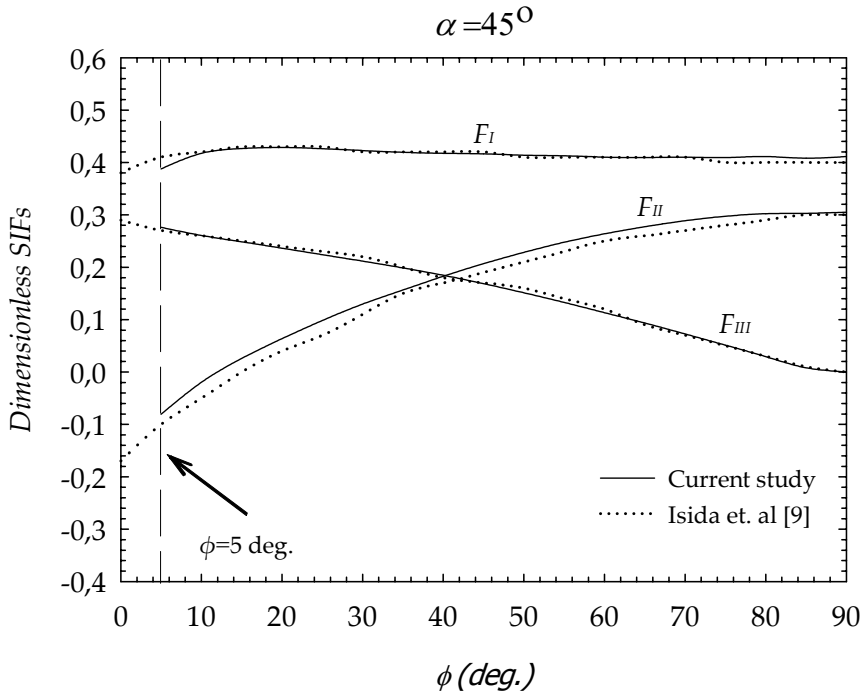

Figure 5.9 Comparisons of dimensionless mixed mode stress intensity factors for 45^o inclination angle

5.4 Transient Thermal Loading

After the model to be used for the analyses of FGM coating, bond coat and substrate structure is validated, the transient thermal analyses of the composite medium is carried out. As it is explained in Chapter 2, for the analyses it is assumed that the composite medium is initially stress-free at a high processing temperature of T_i = 1273 K. Then, the coating, bond coat and substrate structure is left in an environment which has a temperature of T_o = 300 K. The boundary conditions for this loading case are depicted in Figure 2.14. The thermomechanical parameters used in the transient thermal analyses are given at Table 2.1. For the transient thermal analyses, 0^o, 15^o, 30^o, $45^o$and 60^o inclination angles of semi-elliptic surface crack are considered. Four different material property variations shown in Table 2.2 are used in the conducted analyses.

During the analyses, it is observed that the inclined semi-elliptic surface crack remains fully open only for a short time interval as the FGM coating, bond coat and substrate structure starts cooling. It is seen that the normalized stress intensity factors and energy release rates go through a maximum in a short time period and then starts to decrease. Furthermore, as expected the temperature around the crack front starts decreasing as the hot composite structure left in the environment which has a temperature of T_o = 300 K.

5.4.1 SIFs, G and Temperature Distributions around the Crack Front for $\alpha=0^o$

Figures 5.10-5.15 depicts normalized mode I stress intensity factors, energy release rates and temperature distributions around the crack front for $\alpha = 0^o$ and a/t_1=0.2 and a/t_1=0.4. For a/t_1=0.2, the maximum values of normalized mode I stress intensity factors and energy release rates around the crack front are obtained at τ=0.003, 0.006, 0.008 and 0.008 for MR, LN, CR and H coatings, respectively. On the other hand, for a/t_1=0.4 these maximums are seen at τ=0.008, 0.008, 0.02 and 0.016 for MR, LN, CR and H coatings, respectively. After these peak values are reached, the stress intensity factors and energy release rates start to decrease. The maximum values obtained around the crack front are shown in Figures 5.10-5.13. If these figures are analyzed, for a/t_1=0.2 maximum normalized mode I stress intensity factor is calculated for MR coating and its value is 0.355. For a/t_1=0.4, this value is obtained by CR coating and it is 0.187. In addition, maximum normalized energy release rate is calculated for CR coating and has the value of 0.078 for a/t_1=0.2. This maximum is again calculated for CR coating for a/t_1=0.4 and it has a value of 0.035. It can be seen from Figure 5.11 that K_{In} becomes zero at $2\phi/\pi = 0.75$, 0.75, 0.62 and 0.53 for MR, LN, CR and H coatings, respectively for a/t_1=0.4. It can be observed from Figure 5.12 that G_n is almost zero for all coating types as $2\phi/\pi \to 1.0$. From Figure 5.13, it is seen that G_n almost becomes zero at $2\phi/\pi \cong 0.5$ for all coating types and remains at this value from this point to $2\phi/\pi = 1.0$.

Since for 0 degree the crack is not "inclined", normalized mode II and mode III stress intensity factors are zero for this case. Figures 5.14-5.15 shows the normalized temperature distributions around the crack front at the time the maximum values of normalized mode I stress intensity factors and energy release rates are obtained. If these figures are analyzed, it can be seen that for all coating types the normalized temperature increases as the crack front angle increases. This is not surprising since the temperature of the points inside the coating is higher than that of the points close to the free surface. From these figures it can be observed that for MR coating the temperature difference between the first point, which is close to free surface, and the deepest point is less than that of the other coating types. Moreover, it is seen that for CR and H coatings, the distribution of temperature around the crack front coincides for a/t_1=0.2 and exhibits the same pattern for a/t_1=0.4.

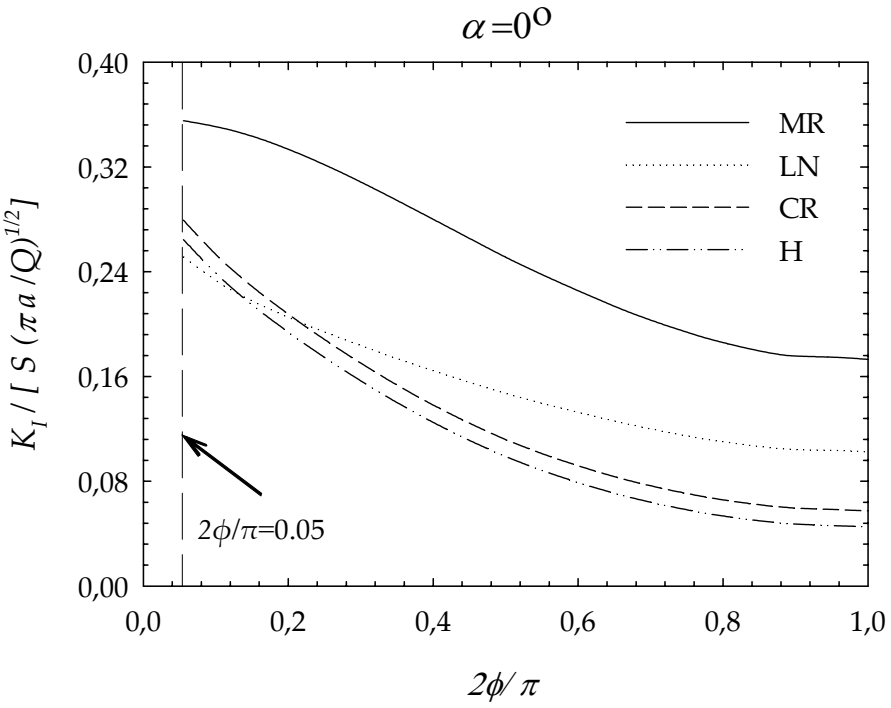

Figure 5.10 Distribution of normalized mode I stress intensity factors around crack front for 0^o inclination angle and a/t_1=0.2

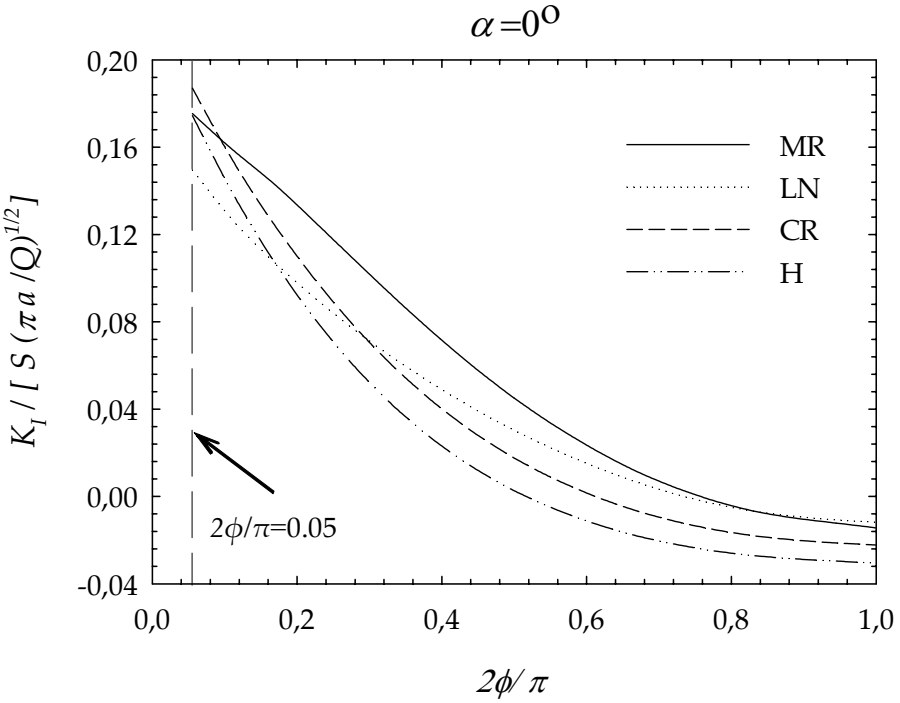

Figure 5.11 Distribution of normalized mode I stress intensity factors around crack front for 0^o inclination angle and a/t_1=0.4

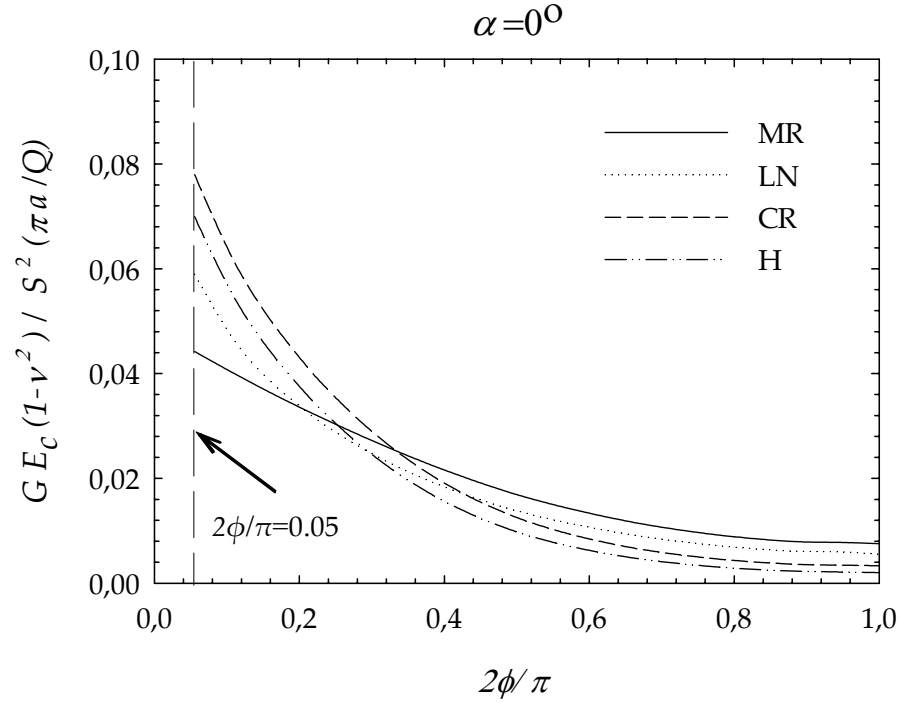

Figure 5.12 Distribution of normalized energy release rates around crack front for 0^o inclination angle and a/t_1=0.2

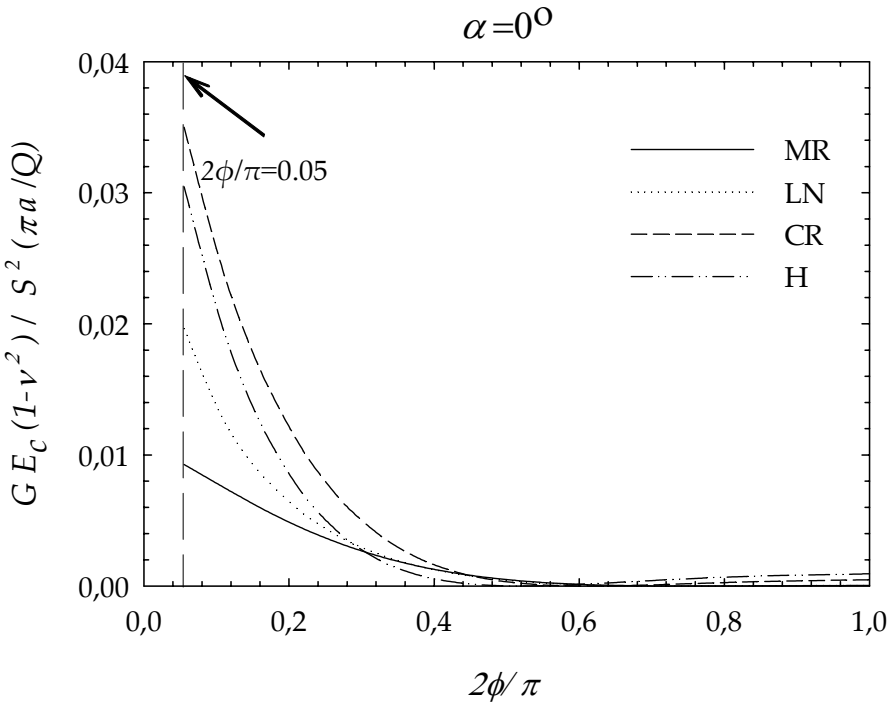

Figure 5.13 Distribution of normalized energy release rates around crack front for 0^o inclination angle and a/t_1=0.4

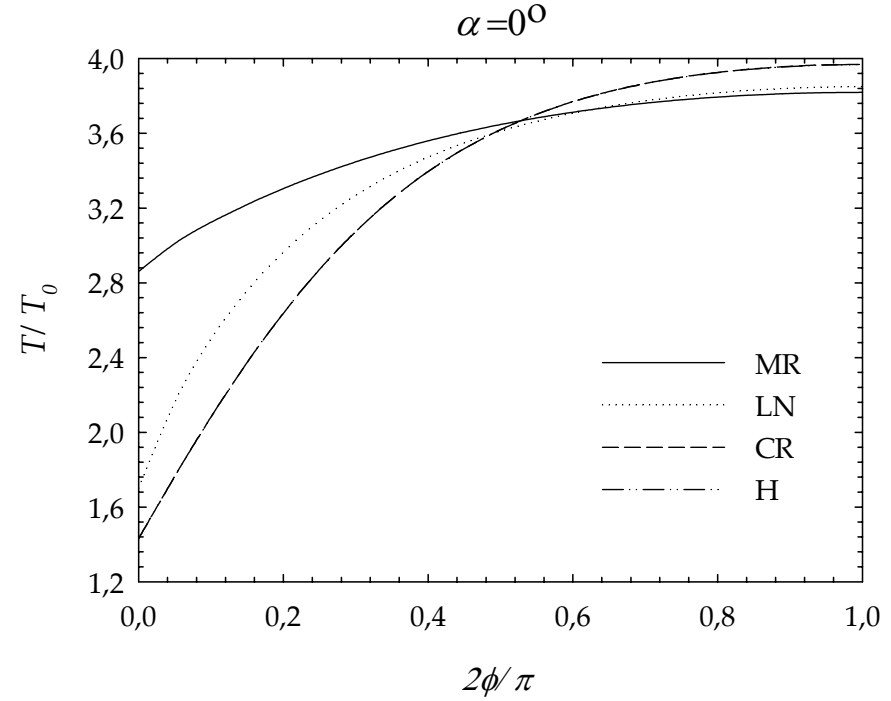

Figure 5.14 Distribution of temperature around crack front for 0^o inclination angle and a/t_1=0.2

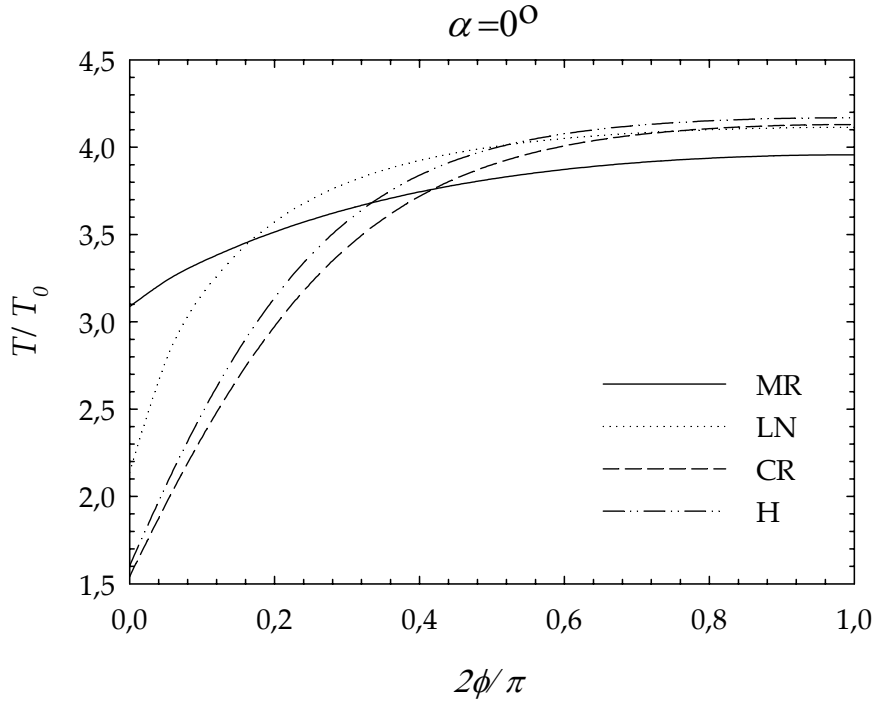

Figure 5.15 Distribution of temperature around crack front for 0° inclination angle and a/t_1=0.4

5.4.2 SIFs, G and Temperature Distributions around the Crack Front for α=15°

For $\alpha = 15^{o}$ and for a/t_1=0.2, the maximum values of normalized mixed mode stress intensity factors and energy release rates are obtained at τ=0.003, 0.005, 0.009 and 0.008 for MR, LN, CR and H coatings, respectively. For a/t_1=0.4, these maximums are seen at τ=0.008, 0.008, 0.02 and 0.016 for MR, LN, CR and H coatings, respectively. After these peak values are reached, again K_{In}, K_{IIn}, K_{IIIn} and G_n start decreasing. These maximum values obtained around the crack front are shown in Figures 5.16-5.23. As it can be seen from Figure 5.16, for a/t_1=0.2, maximum K_{In} is calculated for MR coating and its value is 0.329. For a/t_1=0.4, maximum K_{In} is obtained by CR coating and its value is 0.180 (Figure 5.17). If Figure 5.17 is analyzed, it can be seen that K_{In} becomes zero at $2\phi/\pi \cong 0.85$, 0.85, 0.70 and 0.55 for MR, LN, CR and H coatings, respectively.

For a/t_1=0.2, as it is seen from Figure 5.18, the maximum value of K_{IIn} is obtained near free surface, and then it starts decreasing and becomes zero at $2\phi/\pi \cong 0.12$. After this point, it again starts increasing up to $2\phi/\pi \cong 0.28$ for CR and H coating and $2\phi/\pi \cong 0.33$ for LN coating and $2\phi/\pi \cong 0.50$ for MR coating. At these points K_{IIn} again starts to decrease until $2\phi/\pi \to 1.0$. While it decreases, it again encounters the value of zero at $2\phi/\pi \cong 0.75$, 0.68 and 0.58 for LN, CR and H coatings, respectively. From Figure 5.19 for a/t_1=0.4, K_{IIn} first decrease and becomes zero for LN, CR and H coatings. Then it increases up to one point and then starts decreasing and again becomes zero. The first point at which K_{IIn} becomes zero is $2\phi/\pi \cong 0.18$, 0.14 and 0.15 for LN, CR and H coatings, respectively. The second point is $2\phi/\pi \cong 0.28$, 0.28 and 0.23 for LN, CR and H coatings, respectively. The maximum K_{IIn} for a/t_1=0.2 is calculated for MR coating and it is -0.032. For a/t_1=0.4, it is attained again by MR coating and it is -0.023.

The K_{IIIn} distribution around crack front for this inclination angle is shown at Figures 5.20 and 5.21. The maximum values are seen at the points nearer the free surface. K_{IIIn} is then decreasing and becoming zero at $2\phi/\pi \cong 1.0$. The maximum value is obtained for MR coating and it has a value of -0.075 for a/t_1=0.2. For a/t_1=0.4, it is again attained by MR coating and it is -0.044.

Additionally, the maximum values of G_n, which are depicted at Figures 5.22 and 5.23, are calculated again for CR coating and they are 0.073 and 0.034 for a/t_1=0.2 and a/t_1=0.4, respectively.

Figure 5.24 and 5.25 show the normalized temperature distribution around the crack front at the time the maximum values of normalized mixed mode SIFs and energy release rates are obtained. If these figures are analyzed, as in the case of 0 degree inclination angle, it can be seen that for all coating types the normalized temperature increases as the crack front angle increases.

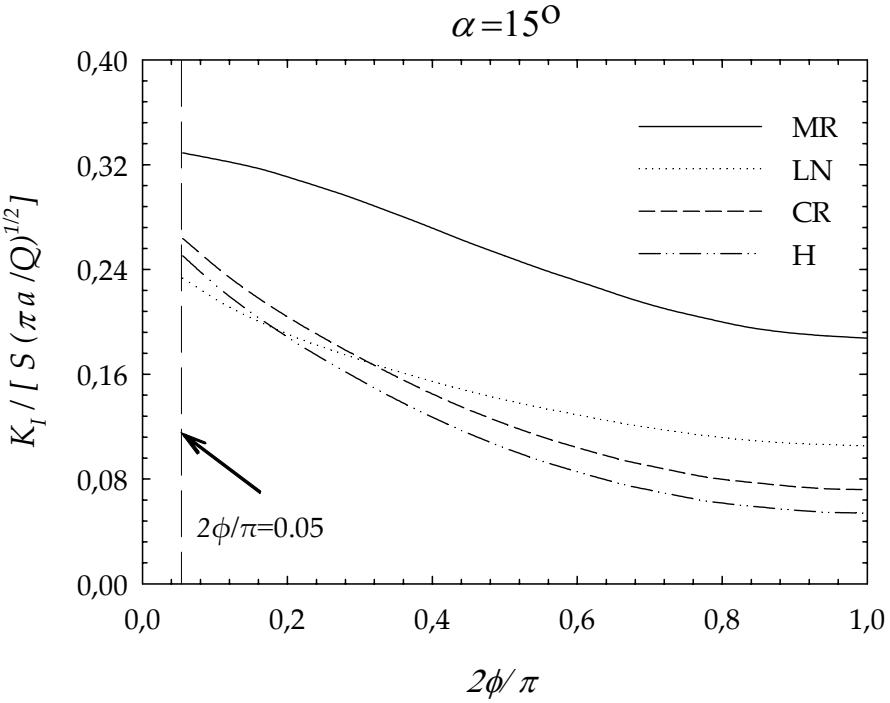

Figure 5.16 Distribution of normalized mode I stress intensity factors around crack front for 15° inclination angle and a/t_1=0.2

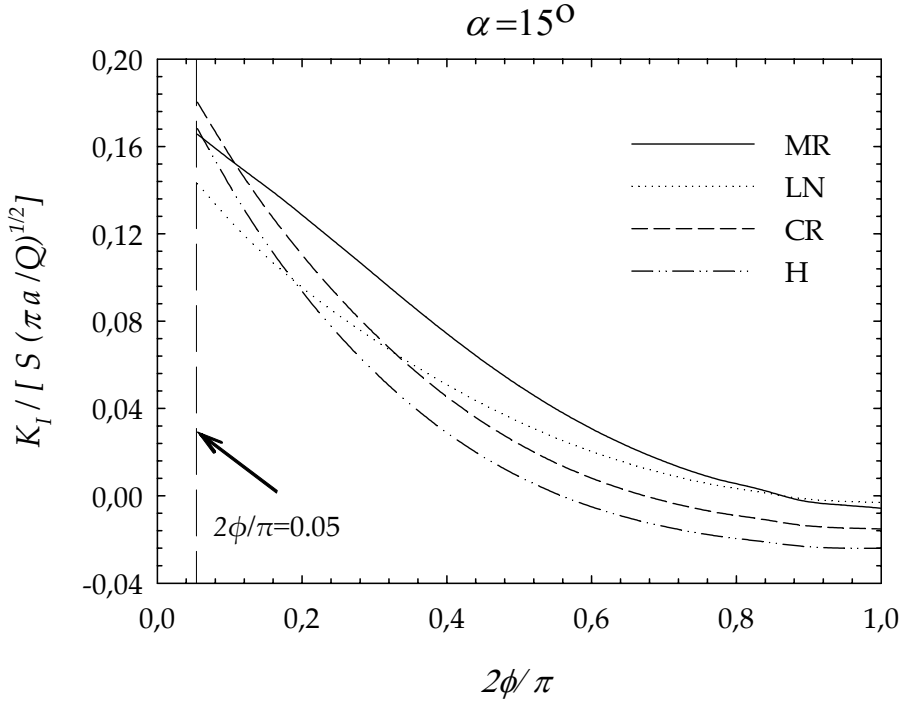

Figure 5.17 Distribution of normalized mode I stress intensity factors around crack front for 15° inclination angle and a/t_1=0.4

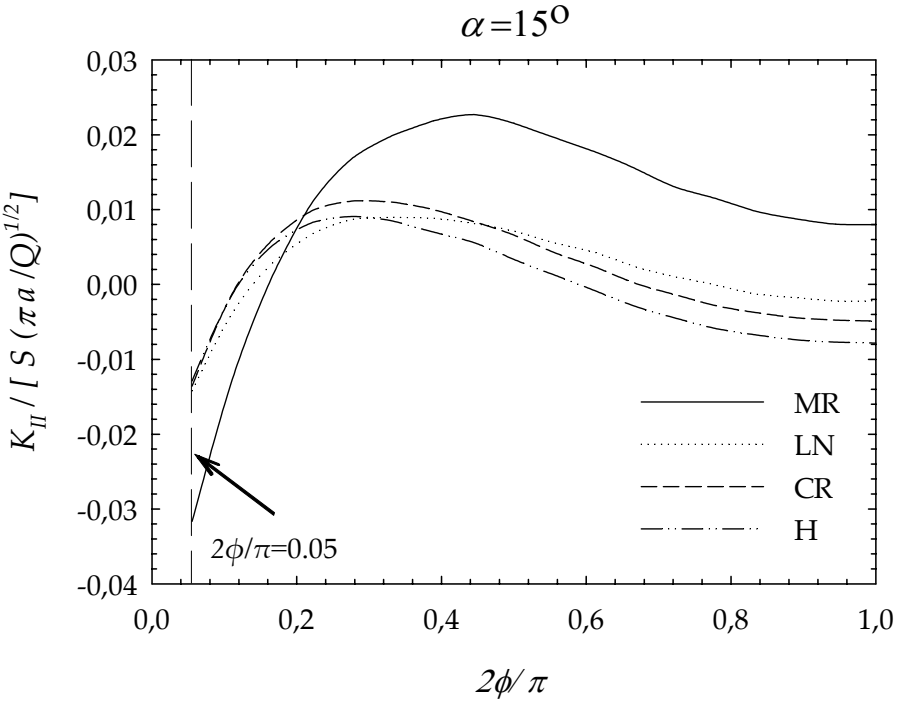

Figure 5.18 Distribution of normalized mode II stress intensity factors around crack front for 15° inclination angle and a/t_1=0.2

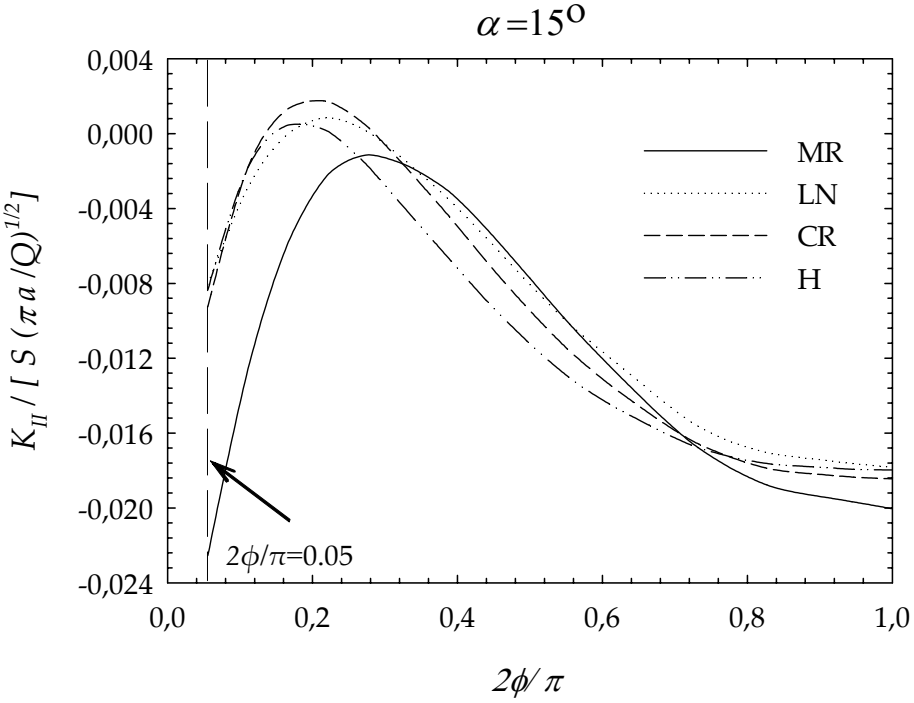

Figure 5.19 Distribution of normalized mode II stress intensity factors around crack front for 15° inclination angle and a/t_1=0.4

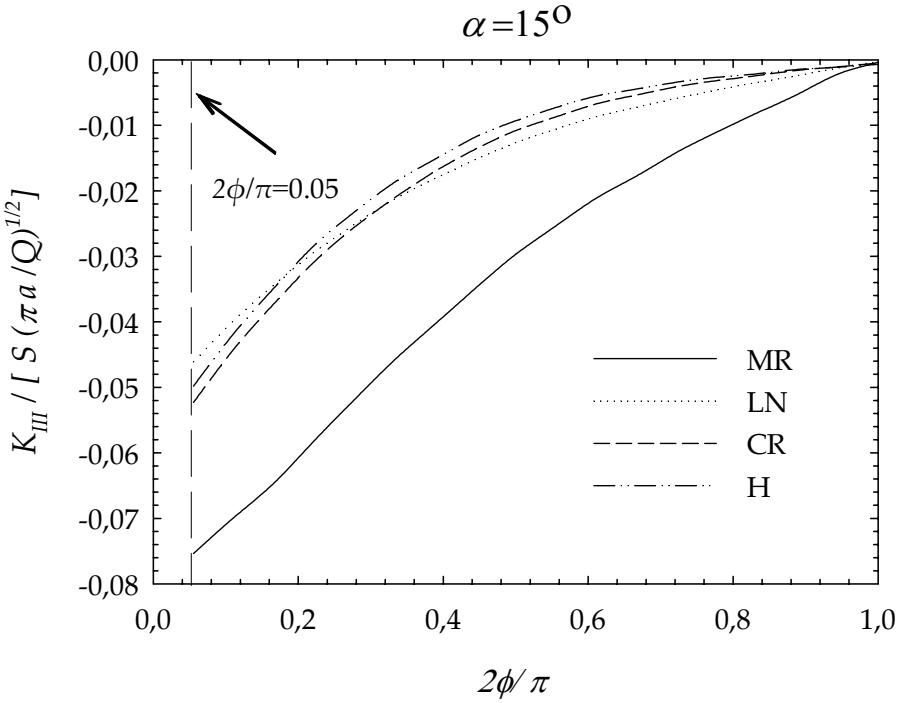

Figure 5.20 Distribution of normalized mode III stress intensity factors around crack front for 15° inclination angle and a/t_1=0.2

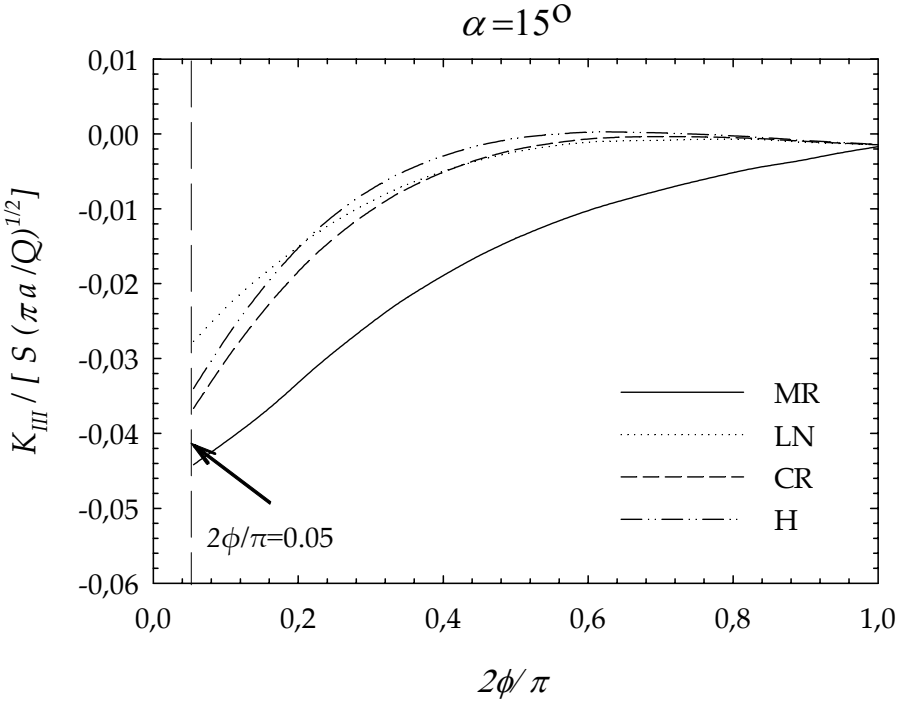

Figure 5.21 Distribution of normalized mode III stress intensity factors around crack front for 15° inclination angle and a/t_1=0.4

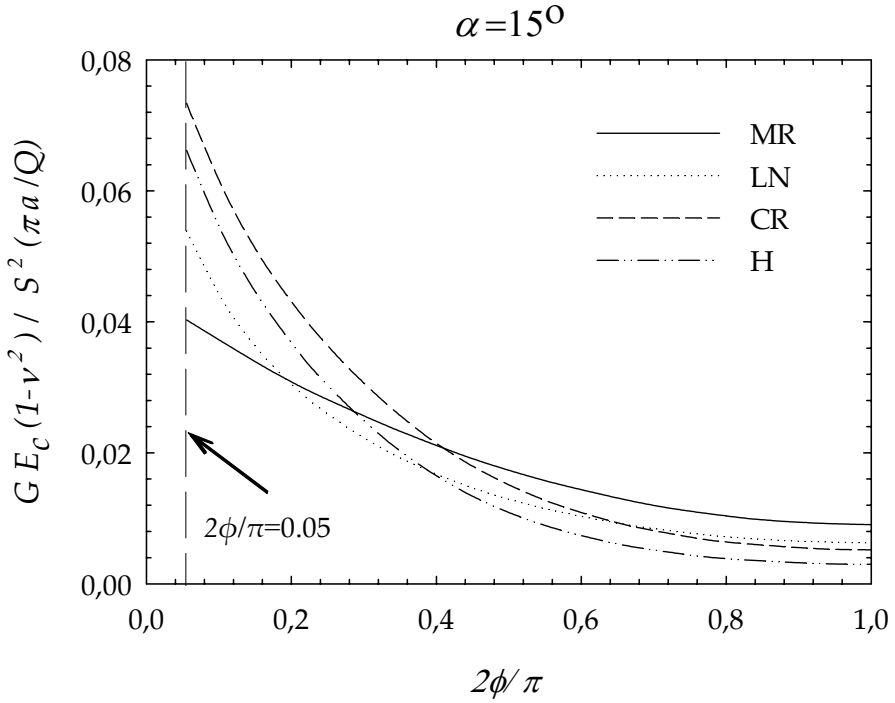

Figure 5.22 Distribution of normalized energy release rates around the crack front for 15° inclination angle and a/t_1=0.2

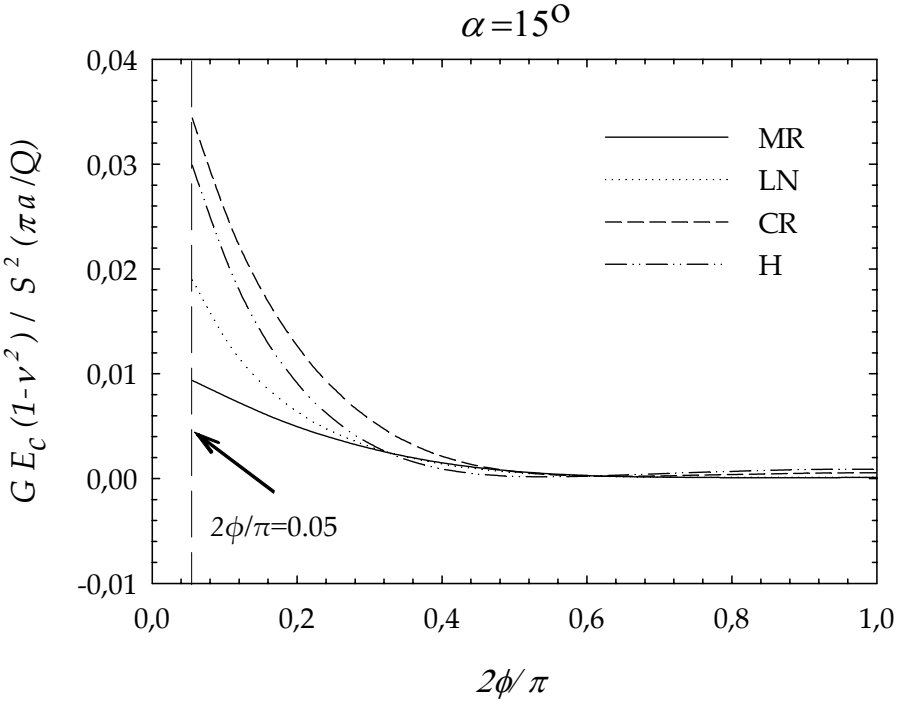

Figure 5.23 Distribution of normalized energy release rates around crack front for 15° inclination angle and a/t_1=0.4

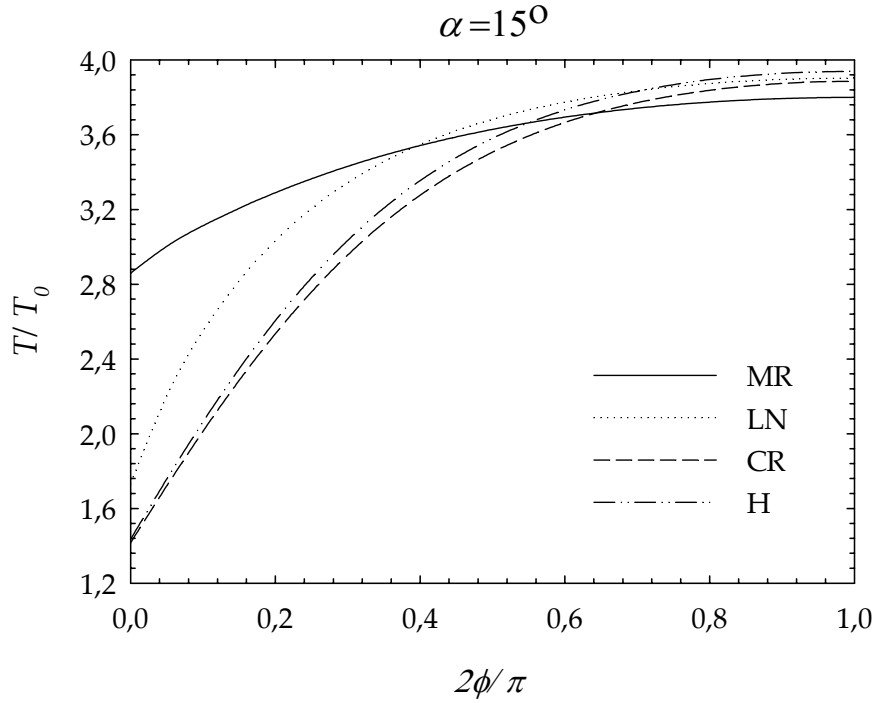

Figure 5.24 Distribution of temperature around crack front for 15° inclination angle and a/t_1=0.2

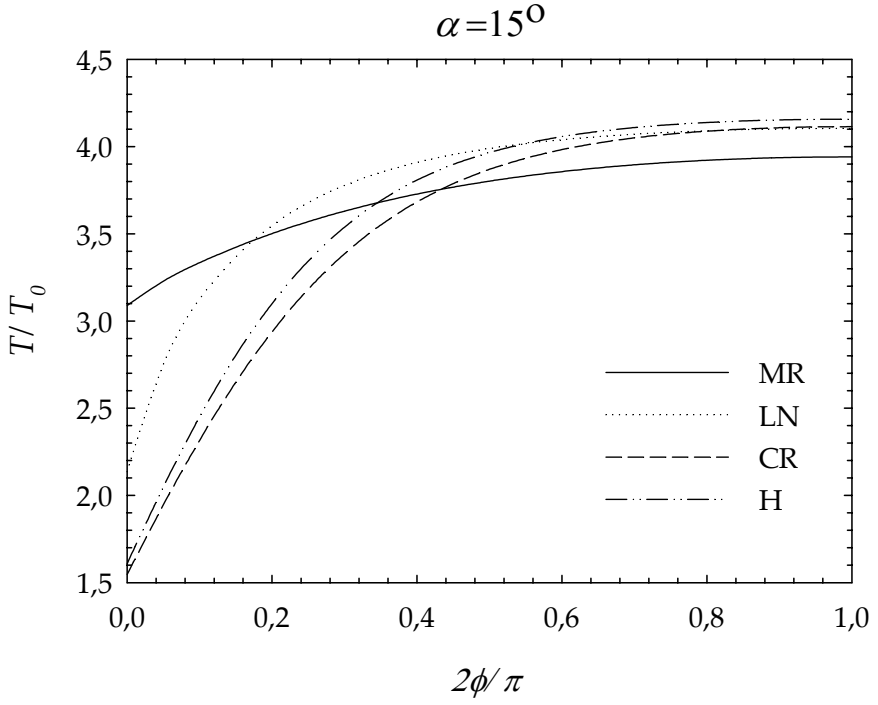

Figure 5.25 Distribution of temperature around crack front for 15° inclination angle and a/t_1=0.4

5.4.3 SIFs, G and Temperature Distributions around the Crack Front for α=30^o

In the case of $\alpha = 30^o$ and for a/t_1=0.2, the maximum values of normalized mixed mode SIFs and energy release rates are obtained at τ=0.003, 0.005, 0.008 and 0.008 for MR, LN, CR and H coatings, respectively. For a/t_1=0.4, these maximums are seen at τ=0.008, 0.008, 0.016 and 0.016 for MR, LN, CR and H coatings, respectively. Figures 5.26-5.33 depicts these maximum values obtained around the crack front. The maximum values of K_{In}, which are 0.287 and 0.159, are calculated for MR coating for a/t_1=0.2 and for CR coating for a/t_1=0.4, respectively.

For a/t_1=0.2, the maximum value of K_{IIn} is seen at the point near the free surface for MR coating and it has the value of -0.057. This maximum is obtained again for MR coating at the point near the free surface and it is -0.046 for a/t_1=0.4.

The maximum values of K_{IIIn} are obtained at the points near the free surface for a/t_1=0.2 and a/t_1=0.4. It is observed that K_{IIIn} then decreases and becomes zero as $2\phi/\pi \to 1.0$. These values are attained by MR coating and they are -0.136 and -0.082 for a/t_1=0.2 and a/t_1=0.4, respectively.

For a/t_1=0.2, the maximum value of G_n is 0.065 and it is obtained for CR coating. As seen in Figure 5.32, G_n is then decreasing as $2\phi/\pi \to 1.0$. The maximum value of G_n calculated for a/t_1=0.4 is 0.032 and is attained by again CR coating. If Figure 5.33 is analyzed, it is observed that G_n becomes almost zero at $2\phi/\pi \cong 0.5$ and stays at this value as $2\phi/\pi \to 1.0$.

Figures 5.34 and 5.35 show the distribution of temperature around the crack front at the time maximum values of normalized SIFs and energy release rates are reached. As seen from these figures, the behavior of the temperature distribution is same with the previous inclination angles.

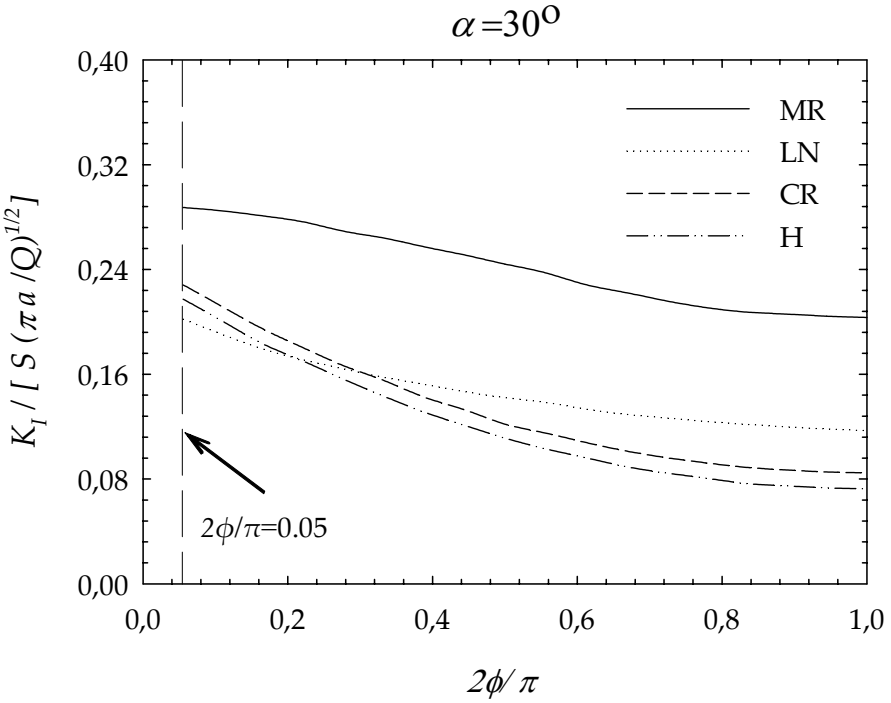

Figure 5.26 Distribution of normalized mode I stress intensity factors around crack front for 30° inclination angle and a/t_1=0.2

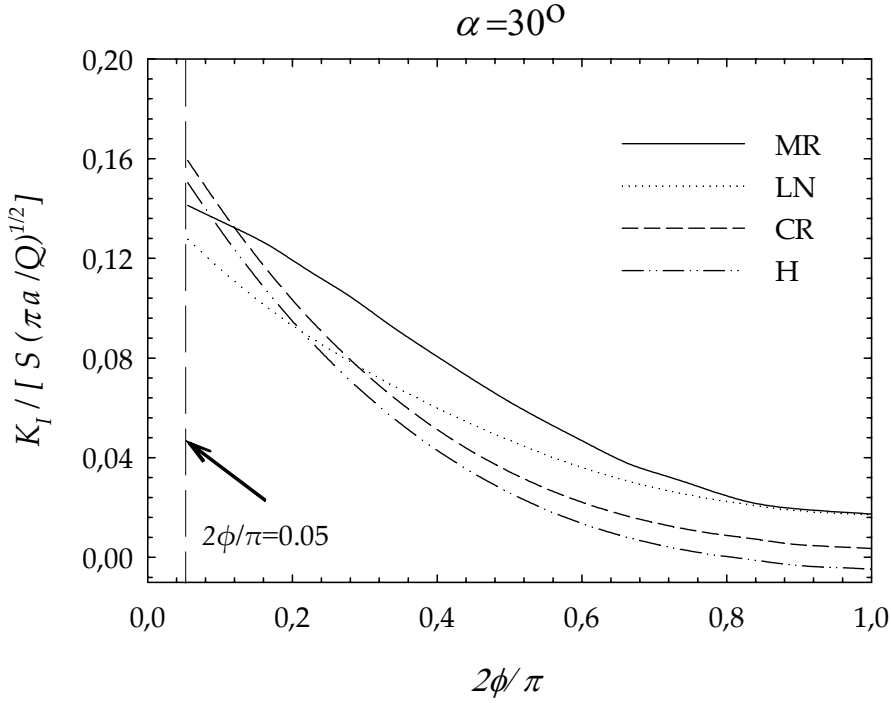

Figure 5.27 Distribution of normalized mode I stress intensity factors around crack front for 30° inclination angle and a/t_1=0.4

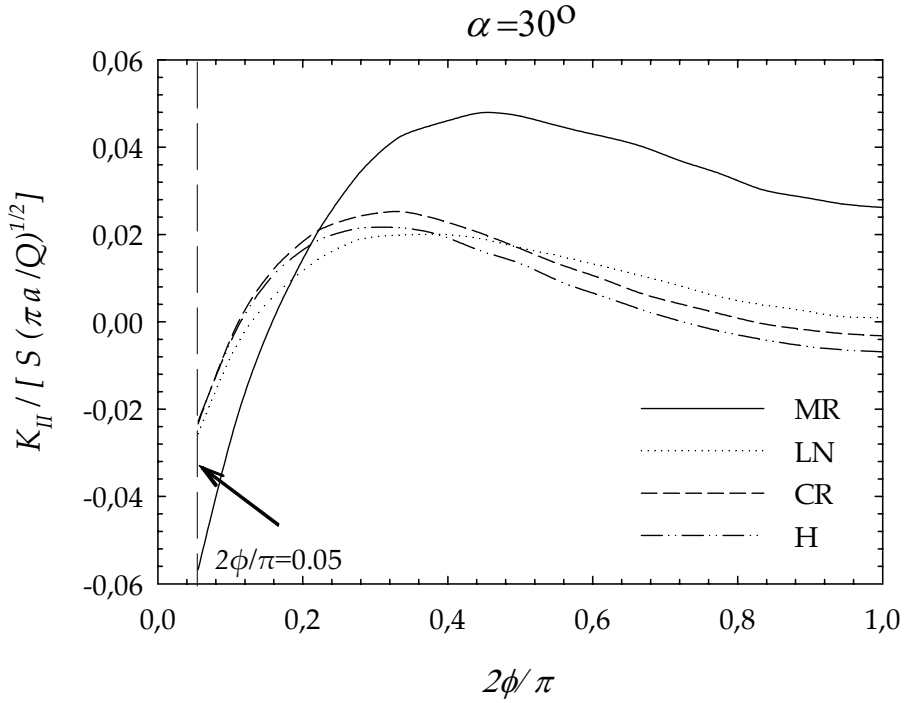

Figure 5.28 Distribution of normalized mode II stress intensity factors around crack front for 30° inclination angle and a/t_1=0.2

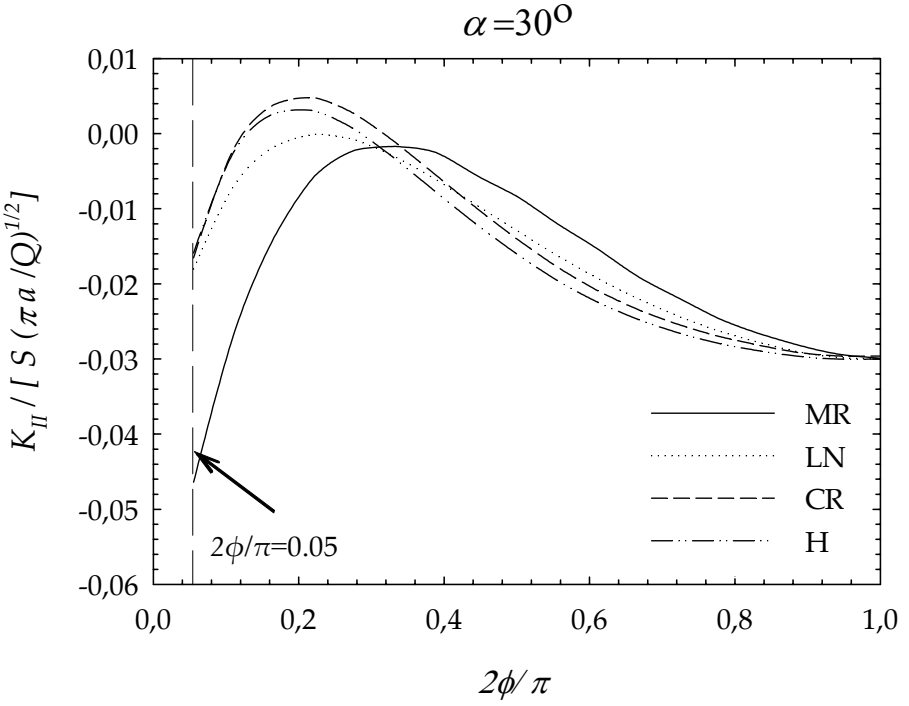

Figure 5.29 Distribution of normalized mode II stress intensity factors around crack front for 30° inclination angle and a/t_1=0.4

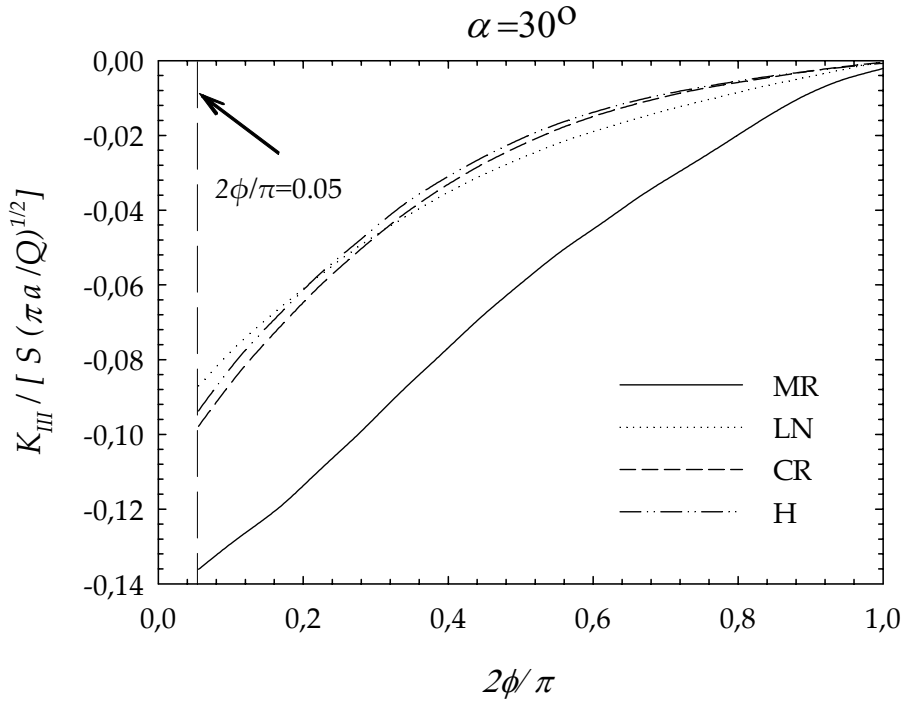

Figure 5.30 Distribution of normalized mode III stress intensity factors around crack front for 30° inclination angle and a/t_1=0.2

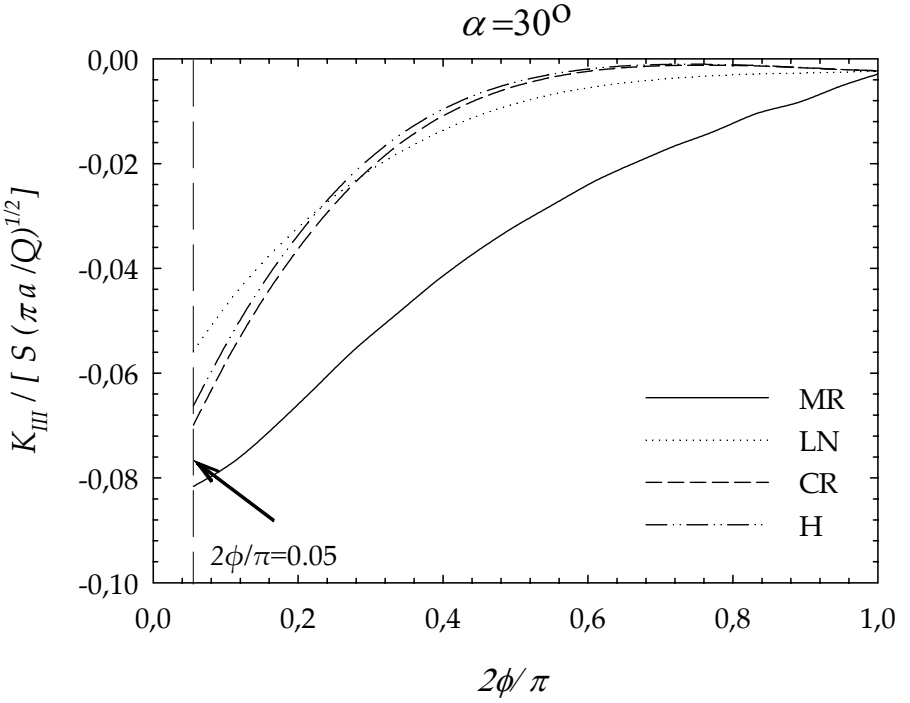

Figure 5.31 Distribution of normalized mode III stress intensity factors around crack front for 30° inclination angle and a/t_1=0.4

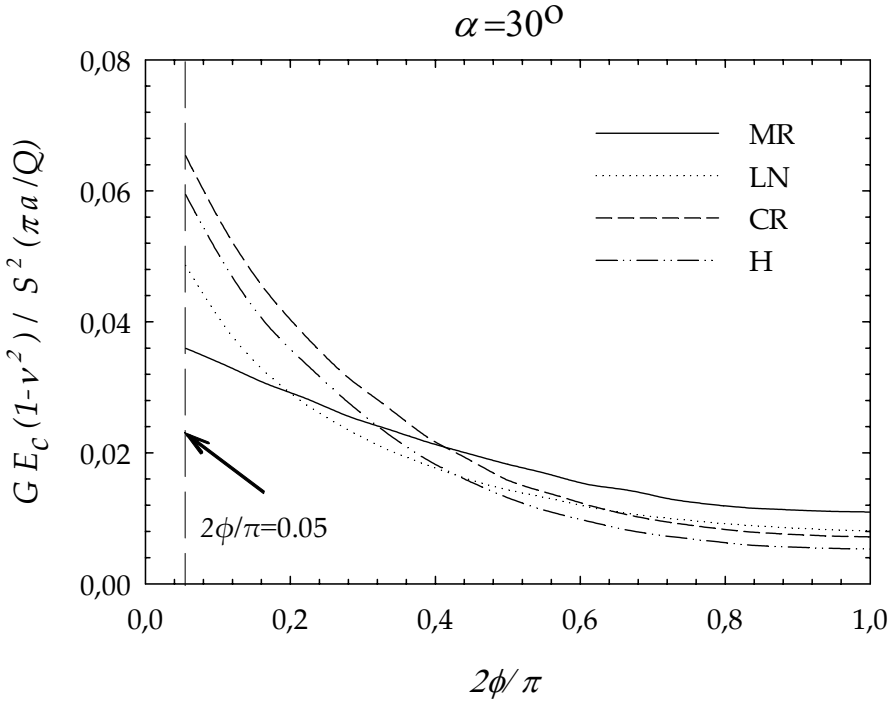

Figure 5.32 Distribution of normalized energy release rates around crack front for 30° inclination angle and a/t_1=0.2

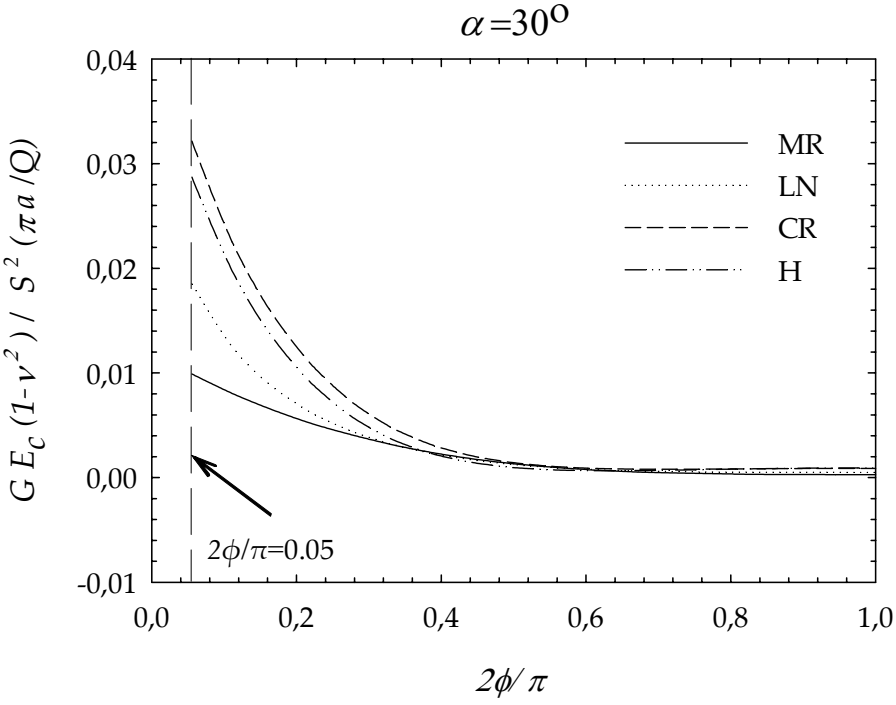

Figure 5.33 Distribution of normalized energy release rates around crack front for 30° inclination angle and a/t_1=0.4

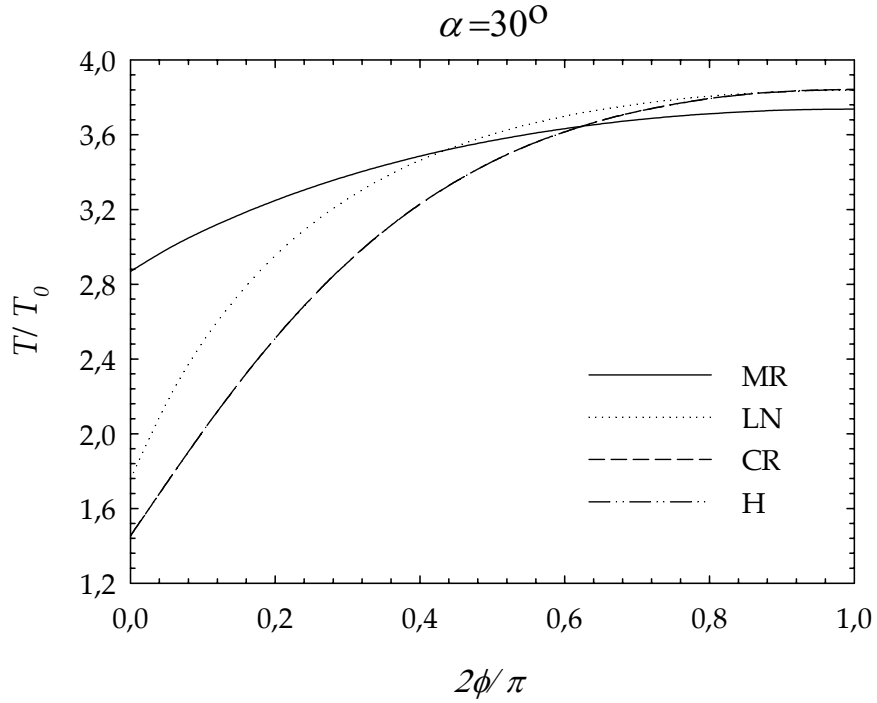

Figure 5.34 Distribution of temperature around crack front for 30° inclination angle and a/t_1=0.2

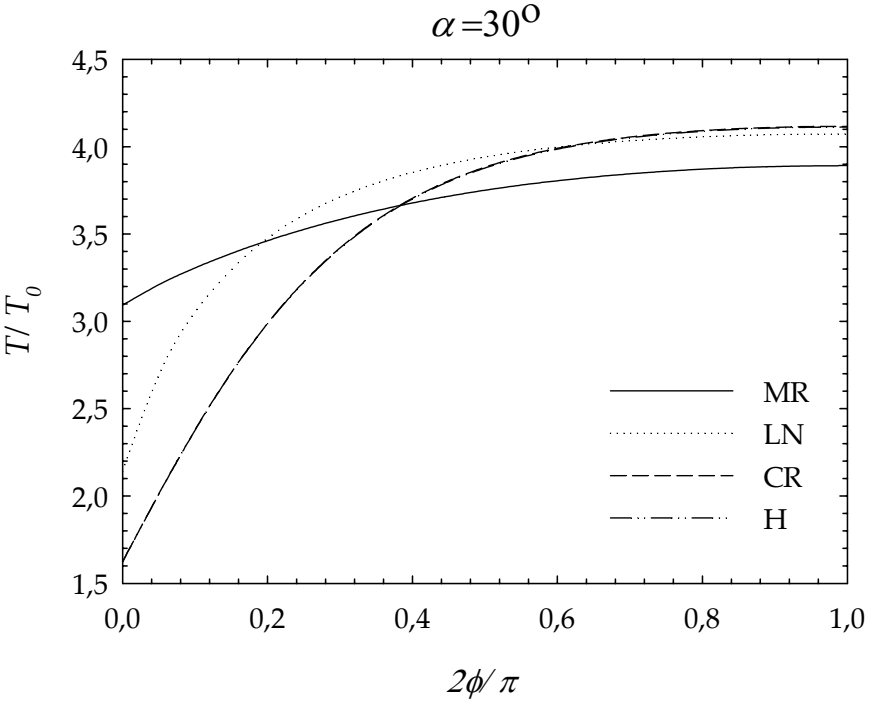

Figure 5.35 Distribution of temperature around crack front for 30° inclination angle and a/t_1=0.4

5.4.4 SIFs, G and Temperature Distributions around the Crack Front for α=45^o

For $\alpha = 45^o$ and for a/t_1=0.2, the maximum values of normalized mixed mode SIFs and energy release rates are obtained at τ=0.003, 0.005, 0.008 and 0.008 for MR, LN, CR and H coatings, respectively. For a/t_1=0.4, these maximums are observed at τ=0.004, 0.008, 0.016 and 0.016 for MR, LN, CR and H coatings, respectively. Figures 5.36-5.43 shows these maximum values obtained around the crack front. The maximum value of K_{In} is calculated for MR coating and its value is 0.263 for a/t_1=0.2. For a/t_1=0.4, the maximum value of K_{In} is calculated for CR coating and it has the value of 0.122.

For a/t_1=0.2, the maximum value of K_{IIn} is seen at the point near the free surface for MR coating and it has the value of -0.081. This maximum is obtained again for MR coating at the point near the free surface and it is -0.052 for a/t_1=0.4.

The maximum values of K_{IIIn} are obtained at the points near the free surface for a/t_1=0.2 and a/t_1=0.4. It is observed that K_{IIIn} then decreases and becomes zero as $2\phi/\pi \rightarrow 1.0$. These values are attained by MR coating and they are -0.171 and -0.100 for a/t_1=0.2 and a/t_1=0.4, respectively.

For a/t_1=0.2, the maximum value of G_n is 0.051 and it is obtained for CR coating. As seen in Figure 5.42, G_n is then decreasing as $2\phi/\pi \rightarrow 1.0$. The maximum value of G_n calculated for a/t_1=0.4 is 0.028 and is attained by again CR coating. If Figure 5.43 is analyzed, it is observed that G_n again tends to zero as $2\phi/\pi \rightarrow 1.0$.

Figures 5.44 and 5.45 show the distribution of temperature around the crack front at the time maximum values of normalized SIFs and energy release rates are reached. As seen from these figures, the behavior of the temperature distribution is same with the other inclination angles studied previously.

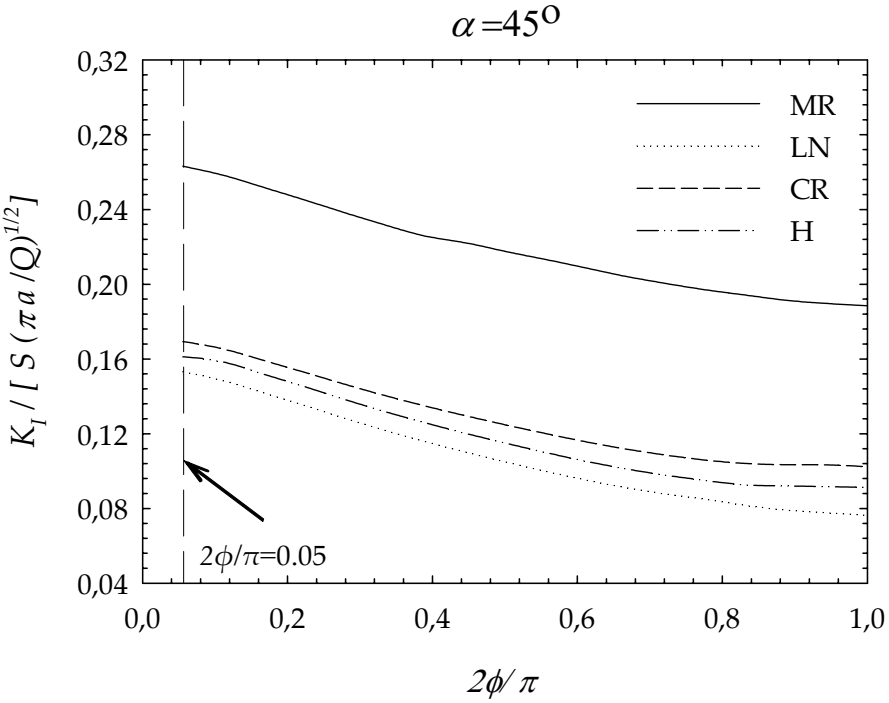

Figure 5.36 Distribution of normalized mode I stress intensity factors around crack front for 45° inclination angle and a/t_1=0.2

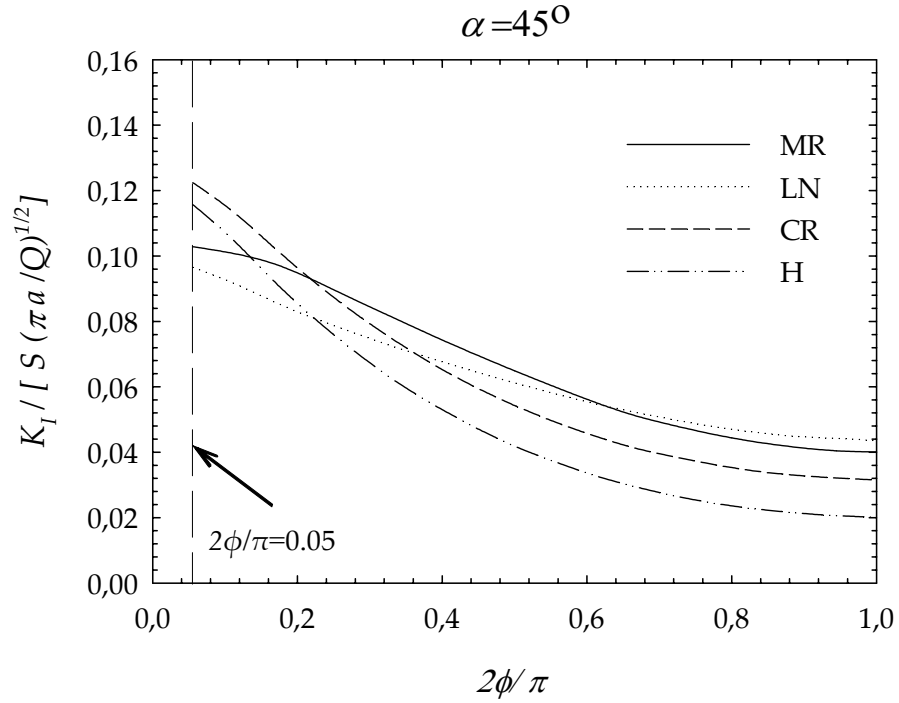

Figure 5.37 Distribution of normalized mode I stress intensity factors around crack front for 45° inclination angle and a/t_1=0.4

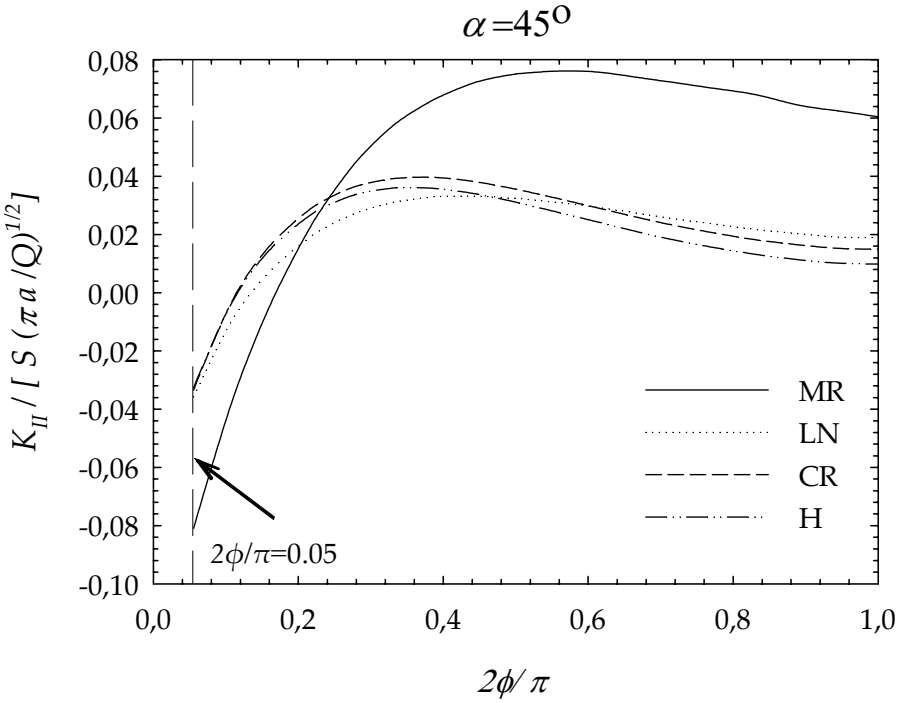

Figure 5.38 Distribution of normalized mode II stress intensity factors around crack front for 45° inclination angle and a/t_1=0.2

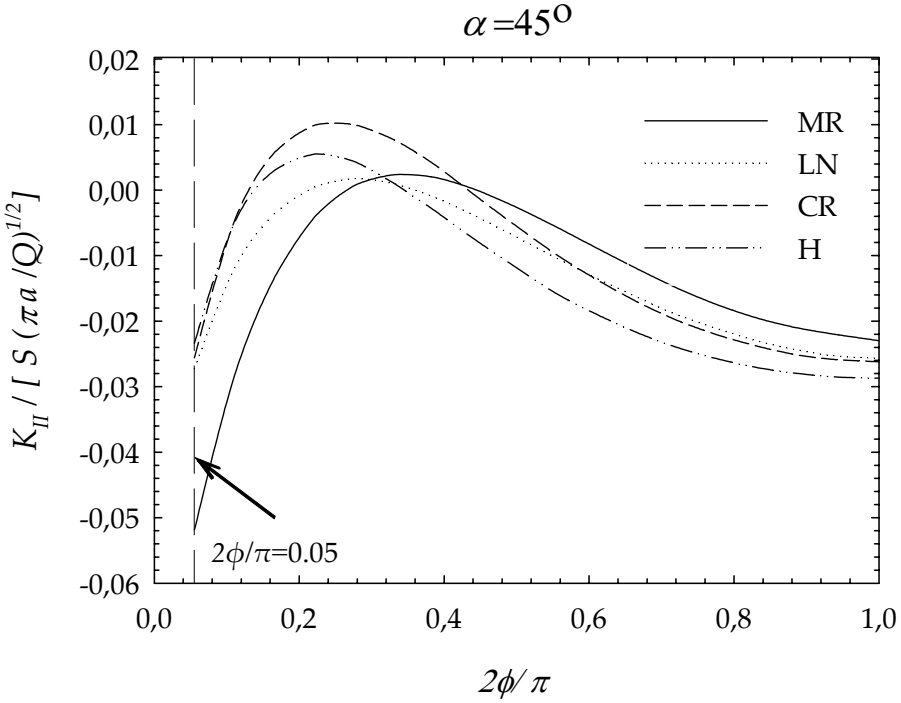

Figure 5.39 Distribution of normalized mode II stress intensity factors around crack front for 45° inclination angle and a/t_1=0.4

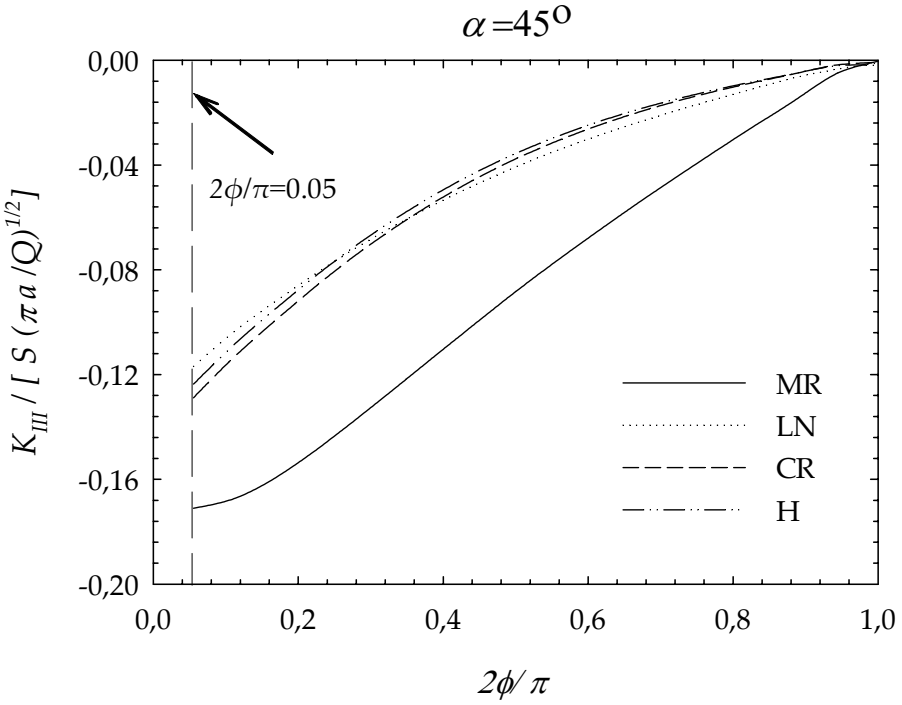

Figure 5.40 Distribution of normalized mode III stress intensity factors around crack front for 45° inclination angle and a/t_1=0.2

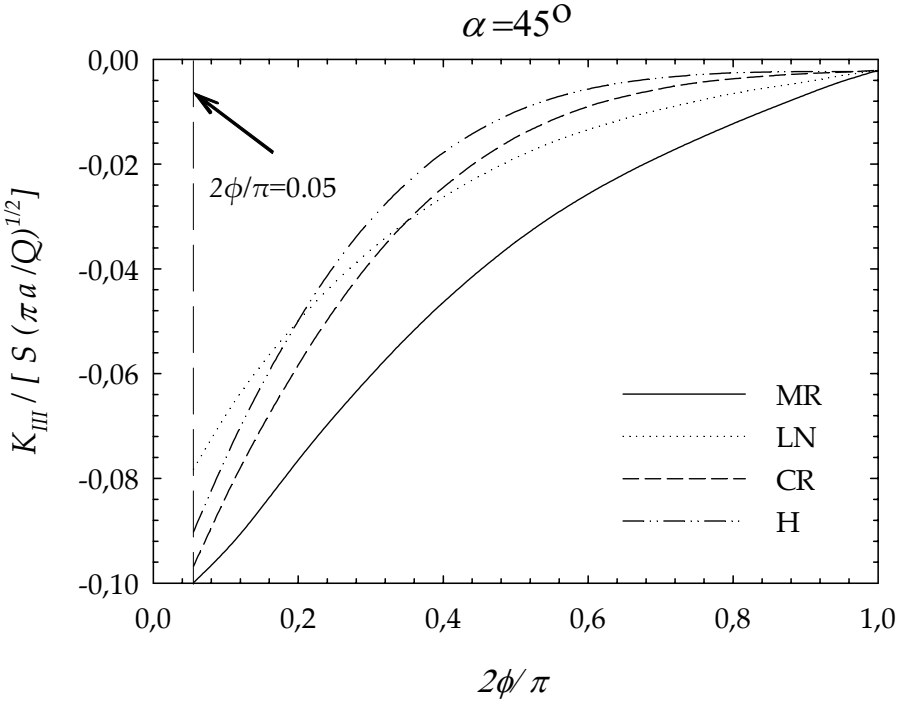

Figure 5.41 Distribution of normalized mode III stress intensity factors around crack front for 45° inclination angle and a/t_1=0.4

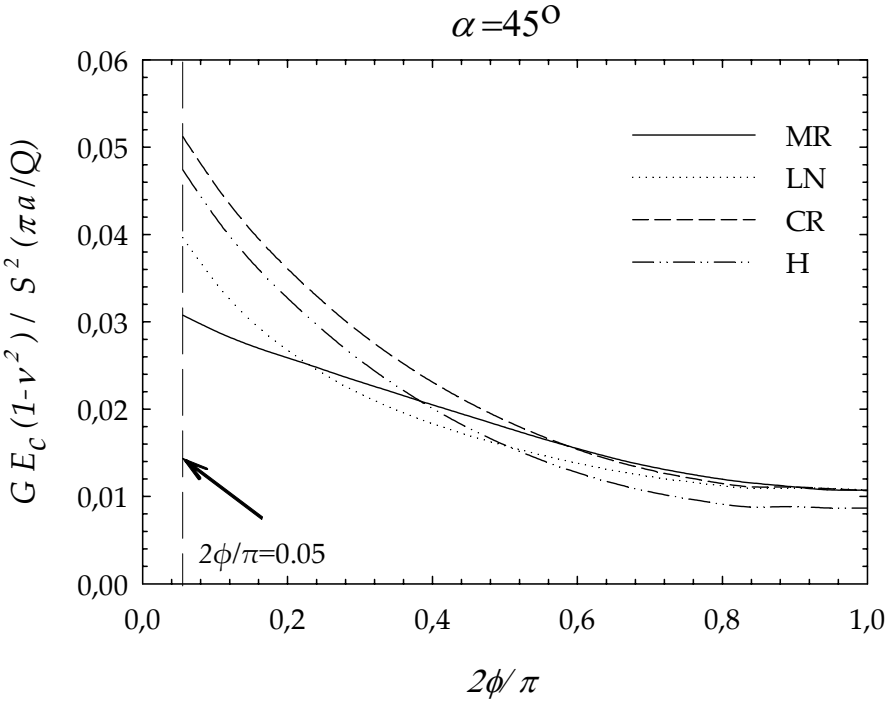

Figure 5.42 Distribution of normalized energy release rates around crack front for 45° inclination angle and a/t_1=0.2

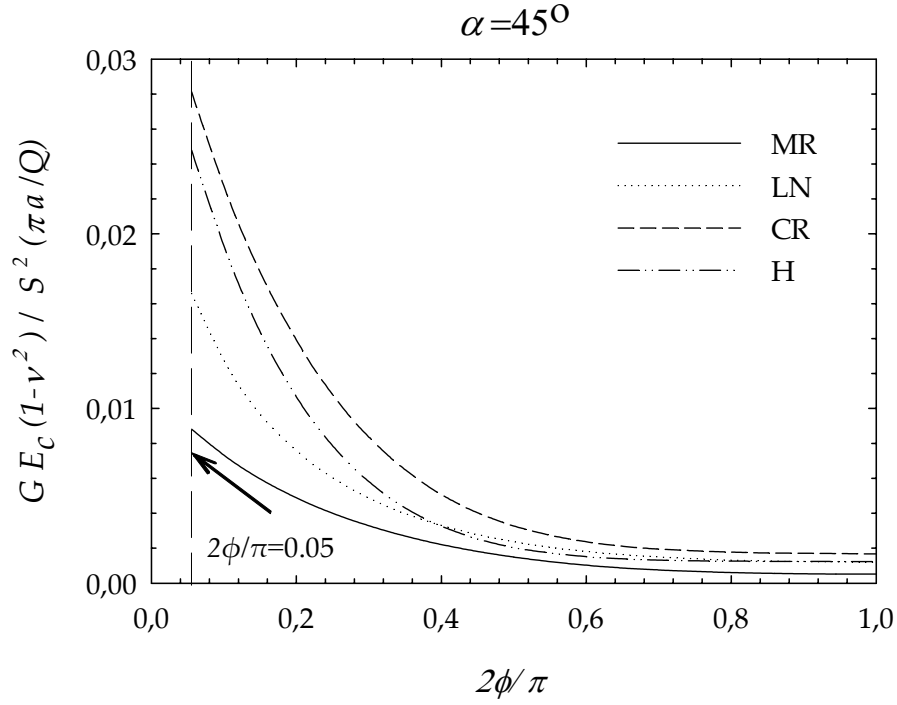

Figure 5.43 Distribution of normalized energy release rates around crack front for 45° inclination angle and a/t_1=0.4

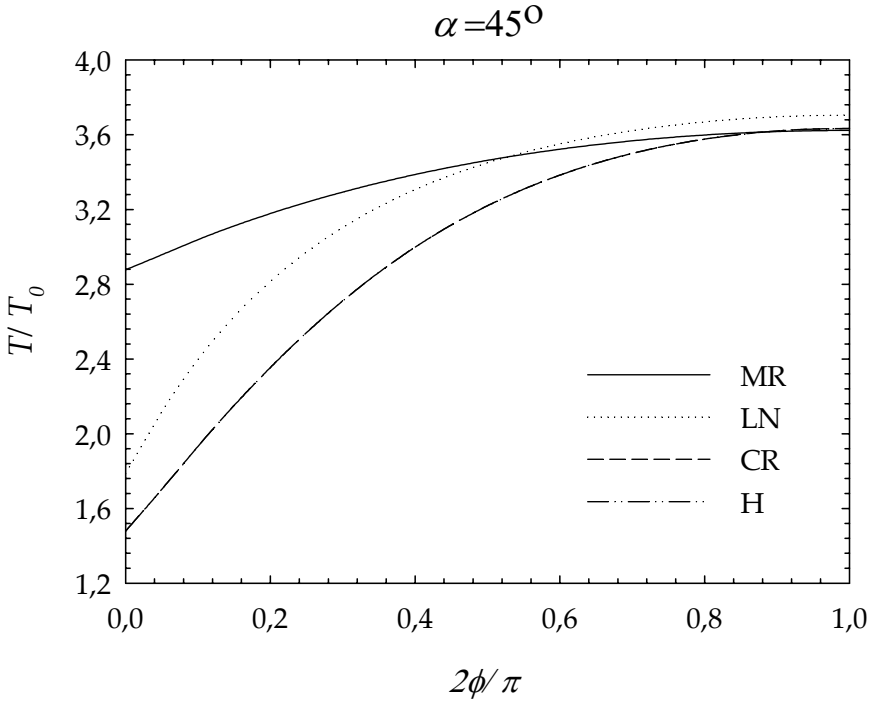

Figure 5.44 Distribution of temperature around crack front for 45° inclination angle and a/t_1=0.2

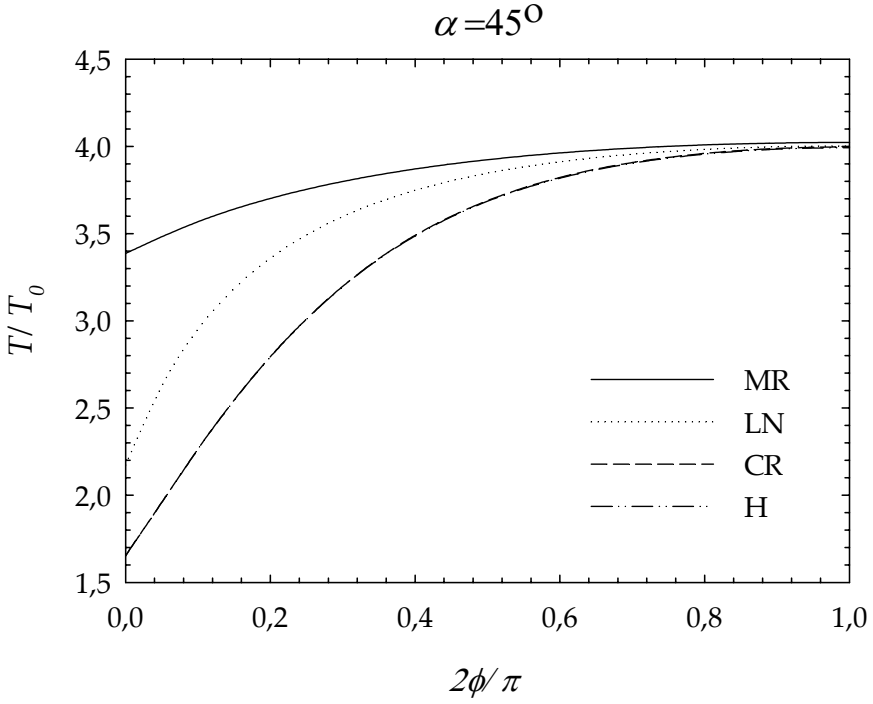

Figure 5.45 Distribution of temperature around crack front for 45° inclination angle and a/t_1=0.4

5.4.5 SIFs, G and Temperature Distributions around the Crack Front for α=60^o

For $\alpha = 60^o$ and for a/t_1=0.2, the maximum values of normalized mixed mode SIFs and energy release rates are obtained at τ=0.002, 0.004, 0.006 and 0.006 for MR, LN, CR and H coatings, respectively. For a/t_1=0.4, these maximums are seen at τ=0.004, 0.008, 0.012 and 0.012 for MR, LN, CR and H coatings, respectively. Figures 5.46-5.53 shows these maximum values obtained around the crack front. The maximum value of K_{In} is calculated for MR coating at the deepest point of crack front and it is 0.163 for a/t_1=0.2. For a/t_1=0.4, it has the value of 0.073 and it is obtained for CR coating at the point closest to free surface.

The maximum values of K_{IIn} are seen at the point closest to free surface for MR coatings and they are -0.071 and -0.055, for a/t_1=0.2 and a/t_1=0.4, respectively.

The maximum values of K_{IIIn} are obtained at the points near the free surface for a/t_1=0.2 and a/t_1=0.4. It is observed that K_{IIIn} then decreases and becomes zero as $2\phi/\pi \rightarrow 1.0$. These values are attained by MR coating and they are -0.179 and -0.115 for a/t_1=0.2 and a/t_1=0.4, respectively.

For a/t_1=0.2, the maximum value of G_n is 0.032 and it is obtained for CR coating. In addition, the maximum value of G_n is 0.020 and it is obtained for CR coating for a/t_1=0.4. Then the values of G_n decreases as $2\phi/\pi \rightarrow 1.0$.

Figures 5.54 and 5.55 show the distribution of temperature around the crack front at the time maximum values of normalized SIFs and energy release rates are reached. As seen from these figures, the behavior of the temperature distribution is same with the other inclination angles. It should be noted that the distribution of temperature coincides for CR and H coatings.

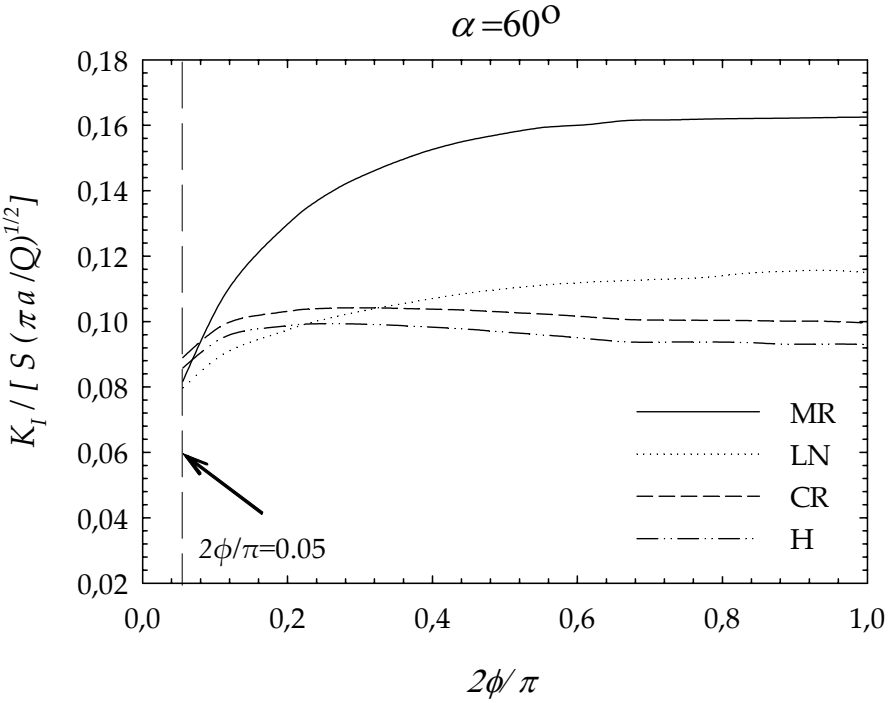

Figure 5.46 Distribution of normalized mode I stress intensity factors around crack front for 60° inclination angle and a/t_1=0.2

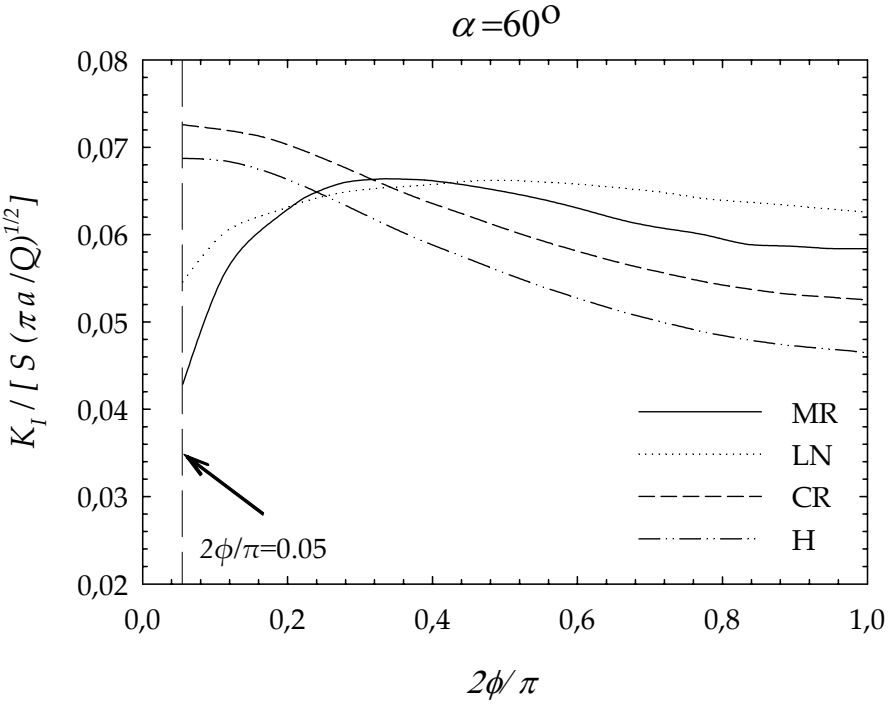

Figure 5.47 Distribution of normalized mode I stress intensity factors around crack front for 60° inclination angle and a/t_1=0.4

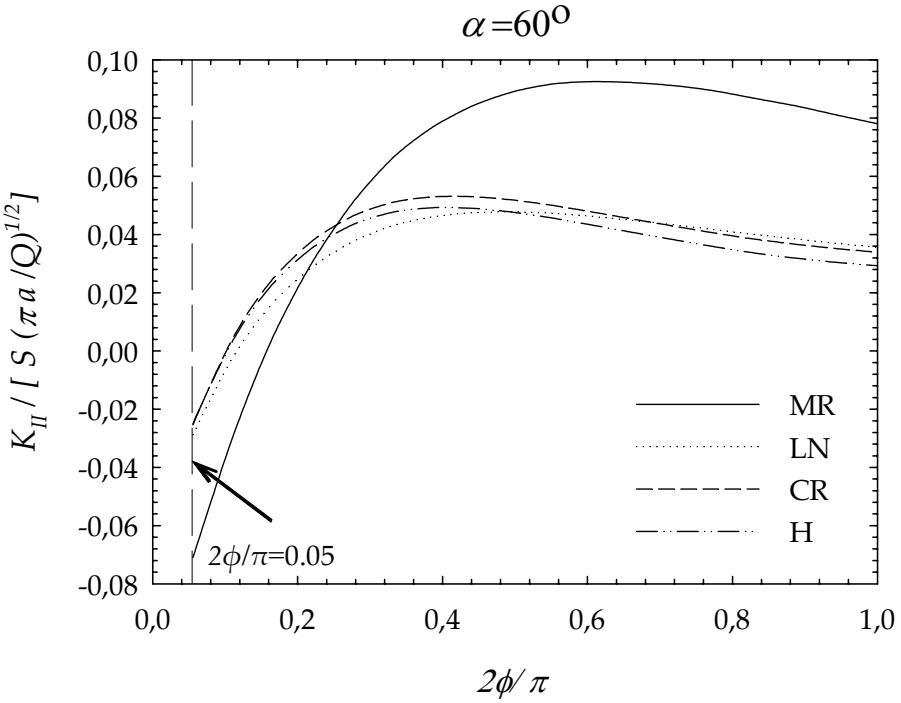

Figure 5.48 Distribution of normalized mode II stress intensity factors around crack front for 60° inclination angle and a/t_1=0.2

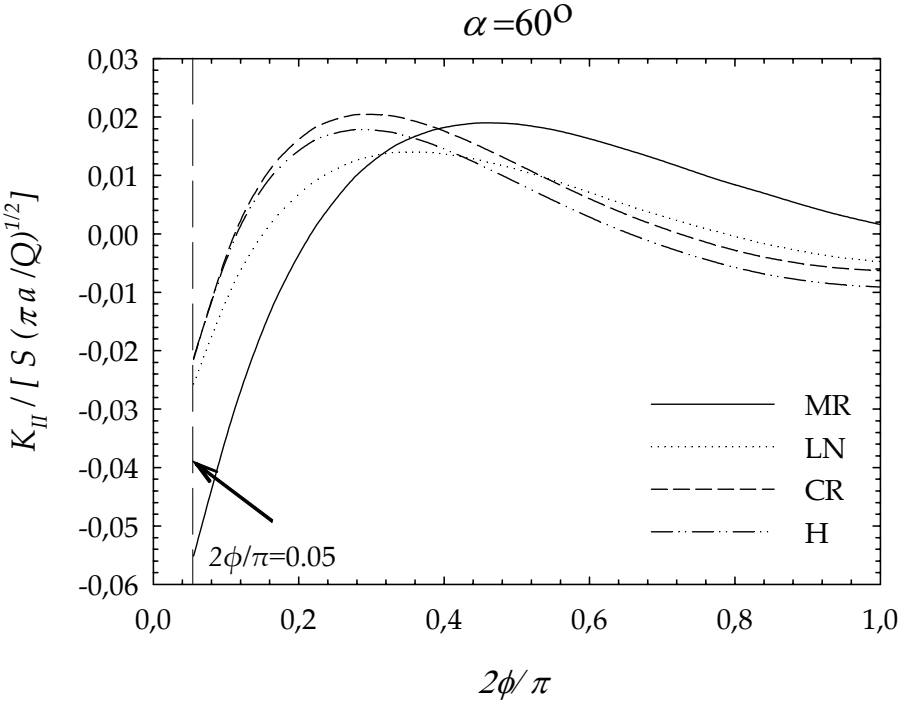

Figure 5.49 Distribution of normalized mode II stress intensity factors around crack front for 60° inclination angle and a/t_1=0.4

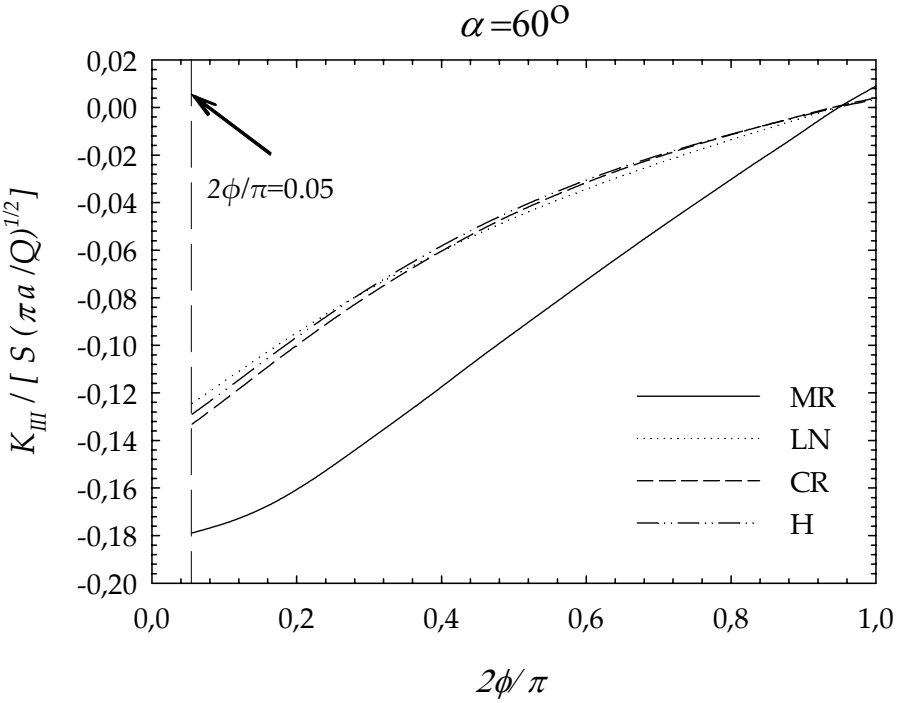

Figure 5.50 Distribution of normalized mode III stress intensity factors around crack front for 60° inclination angle and a/t_1=0.2

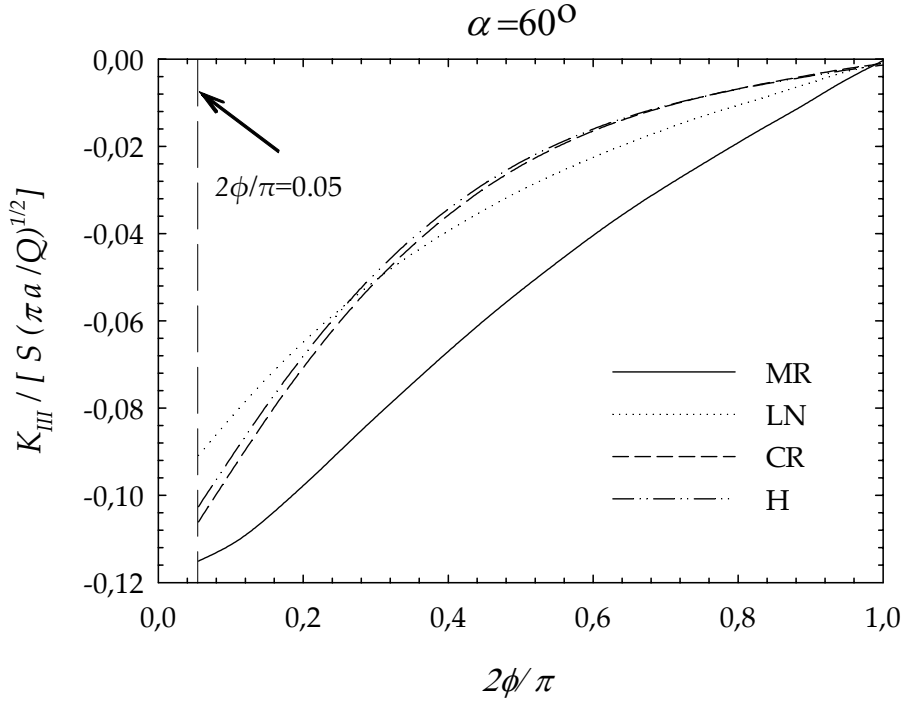

Figure 5.51 Distribution of normalized mode III stress intensity factors around crack front for 60° inclination angle and a/t_1=0.4

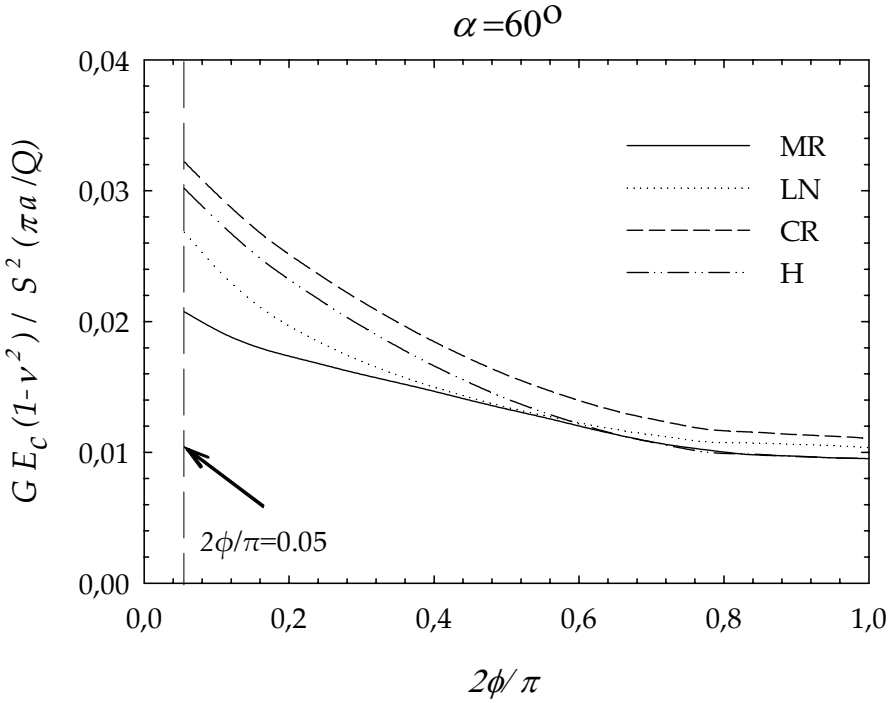

Figure 5.52 Distribution of normalized energy release rates around crack front for 60° inclination angle and a/t_1=0.2

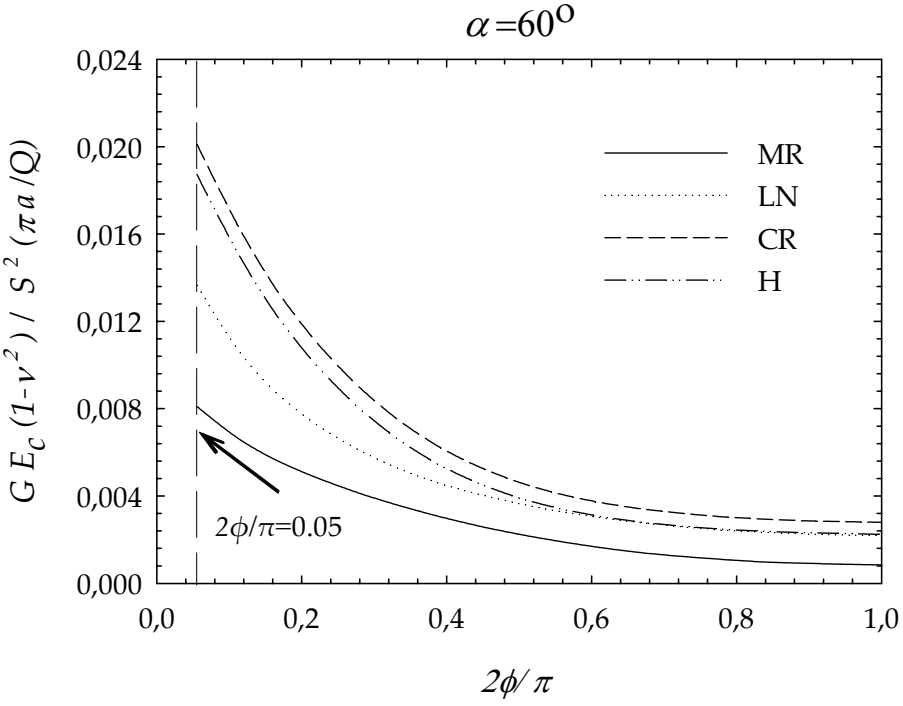

Figure 5.53 Distribution of normalized energy release rates around crack front for 60° inclination angle and a/t_1=0.4

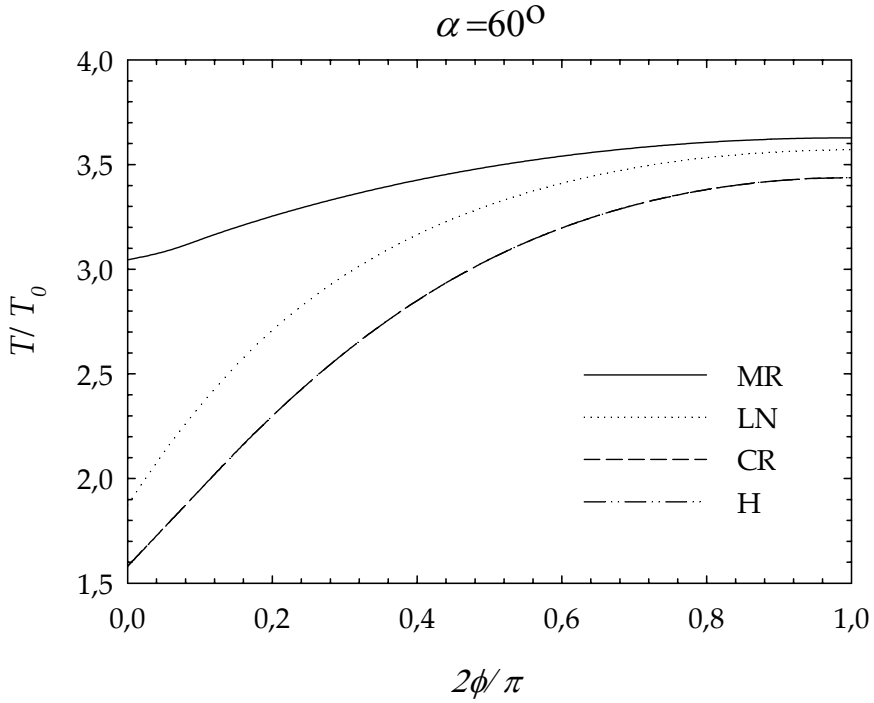

Figure 5.54 Distribution of temperature around crack front for 60° inclination angle and a/t_1=0.2

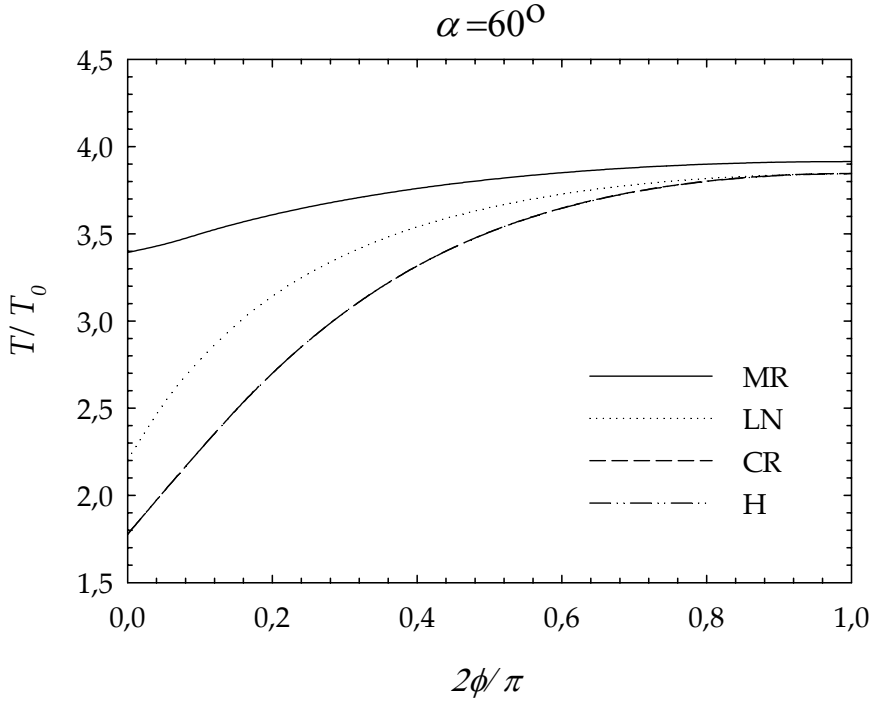

Figure 5.55 Distribution of temperature around crack front for 60° inclination angle and a/t_1=0.4

5.4.6 Peak Values of Normalized SIFs and G Obtained at Various Inclination Angles for 30^o Crack Front Angle

As seen in Figure 5.56, for $\phi = 30^o$ and for a/t_1=0.2, the maximum peak value of K_{In} is calculated for MR coating at $\alpha = 0^o$ and it is 0.299. Then as the inclination angle increases, the value of peaks decreases. For a/t_1=0.4, the highest peak value of K_{In} is again calculated for MR coating at $\alpha = 30^o$ and it is 0.094. It can be seen from Figure 5.57 that for a/t_1=0.4, the peak values of K_{In} increase up to $\alpha = 30^o$ as the inclination angle increases. After this point, the peaks start decreasing.

The maximum peak value of K_{IIn} is obtained by MR coating for a/t_1=0.2 and it is 0.071 at $\alpha = 60^o$. As seen in Figure 5.58, as inclination angle increases, peaks of K_{IIn} increase, too. For a/t_1=0.4, the highest peak value of K_{IIn} is calculated for MR coating at $\alpha = 60^o$ and it is -0.085. For this case, as it can be observed from Figure 5.59, as inclination angle increases, peaks of K_{IIn} also increase for MR and LN coatings. For CR and H coatings, the peak values of K_{IIn} slightly increase as the inclination angle increases up to $\alpha = 45^o$. At about $\alpha = 50^o$, peaks of K_{IIn} become zero and then start to increase as inclination angle increases.

It can be seen from Figure 5.60 that for a/t_1=0.2, the peak values of K_{IIIn} increase as the inclination angle increases. The maximum peak is obtained at $\alpha = 60^o$ by MR coating and it is -0.138. For a/t_1=0.4, the highest peak value of K_{IIIn} is calculated for MR coating at $\alpha = 60^o$ and it is -0.099. As it can be seen from Figure 5.61, for this case the peak values of K_{IIIn} also increase as the inclination angle increases.

If Figure 5.62 is analyzed, it can be seen that for a/t_1=0.2, as the inclination angle increases, the peak values of G_n decrease. For this case, the maximum peak of G_n is attained by CR coating and it has a value of 0.034 at $\alpha = 0^o$. From Figure 5.63, it can be seen that for MR coating, the peak values of G_n increase as the inclination angle increases for a/t_1=0.4 up to $\alpha = 30^o$. At $\alpha = 30^o$ G_n reaches its

maximum value attained by MR coating which is 0.014. For LN coating, as α increases, peaks of G_n decreases up to $\alpha = 45^o$. After this point, peaks of G_n start increasing as α increases. It can be observed from this figure that for CR and H coatings, as α increases, the peaks of G_n also increase.

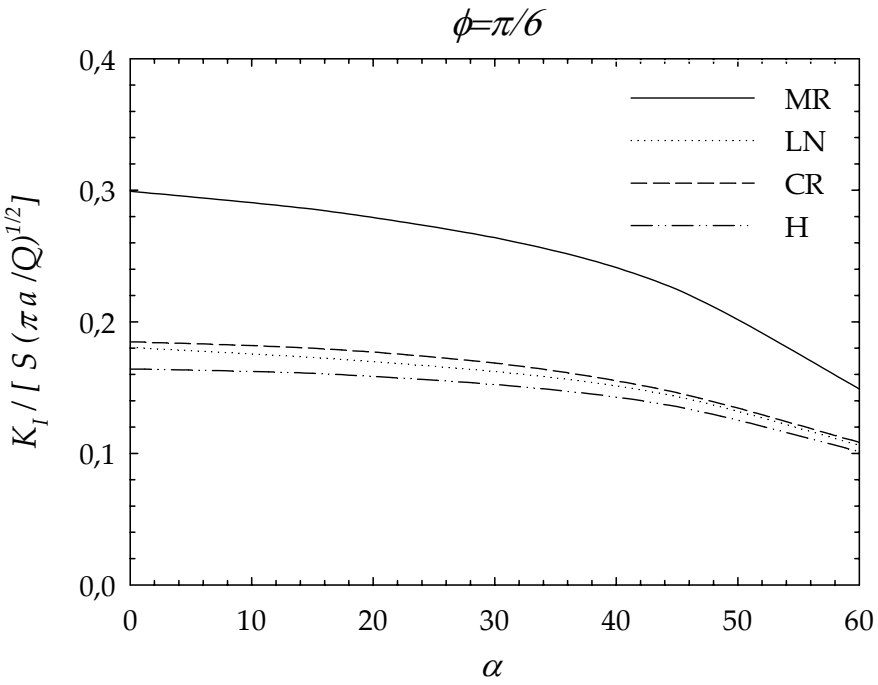

Figure 5.56 Peak values of normalized mode I stress intensity factors obtained at various inclination angles for 30° crack front angle and a/t_1=0.2

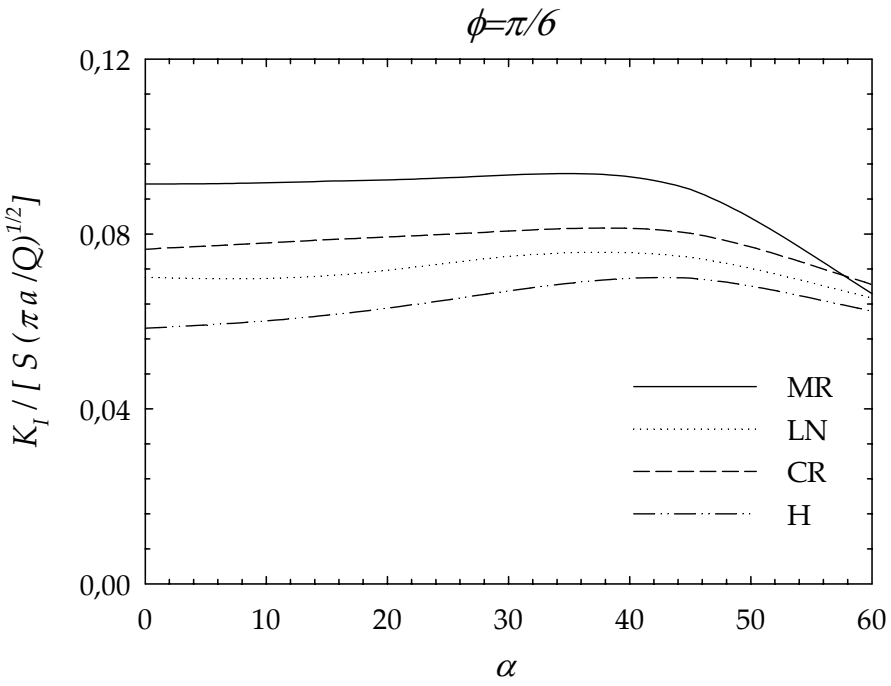

Figure 5.57 Peak values of normalized mode I stress intensity factors obtained at various inclination angles for 30^o crack front angle and a/t_1=0.4

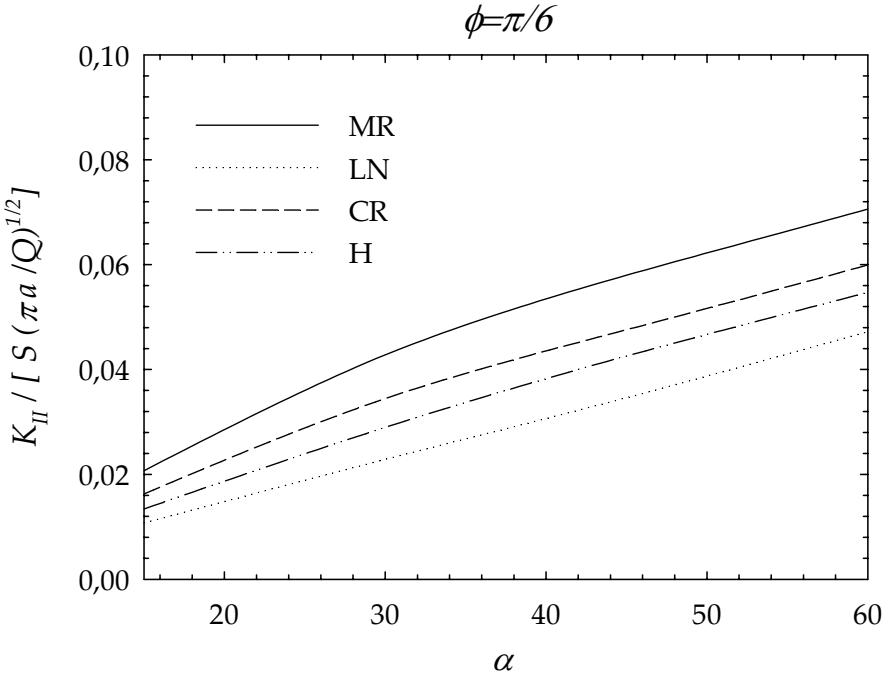

Figure 5.58 Peak values of normalized mode II stress intensity factors obtained at various inclination angles for 30^o crack front angle and a/t_1=0.2

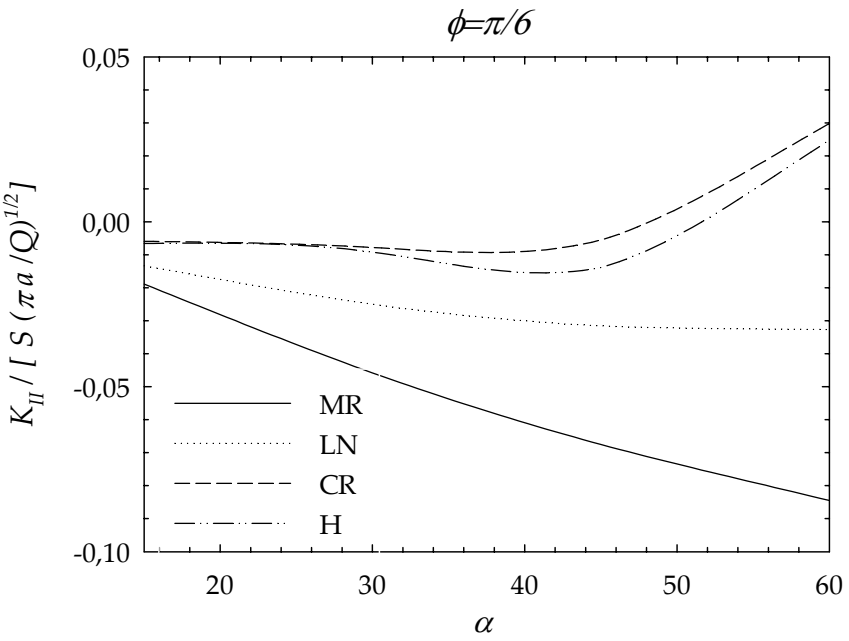

Figure 5.59 Peak values of normalized mode II stress intensity factors obtained at various inclination angles for 30^o crack front angle and a/t_1=0.4

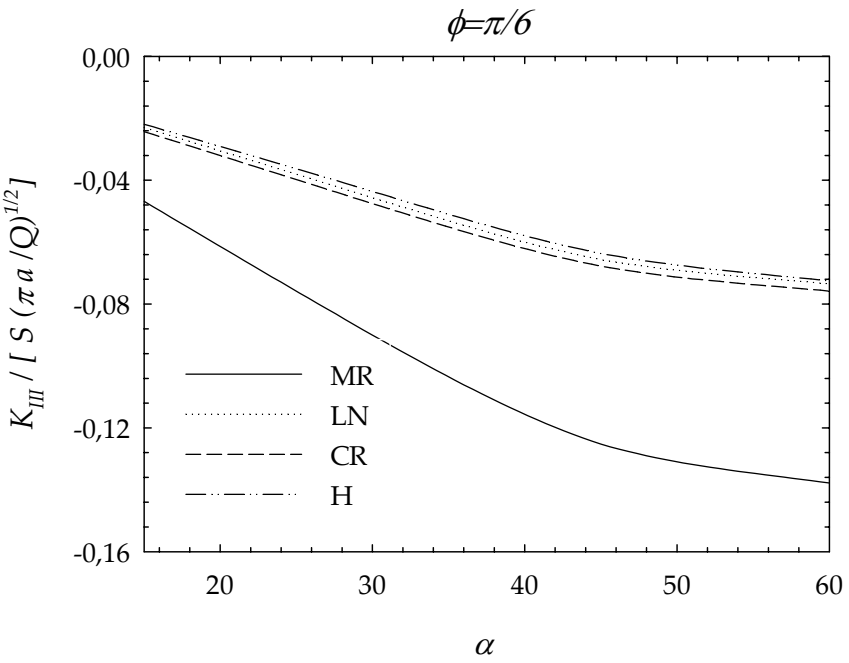

Figure 5.60 Peak values of normalized mode III stress intensity factors obtained at various inclination angles for 30^o crack front angle and a/t_1=0.2

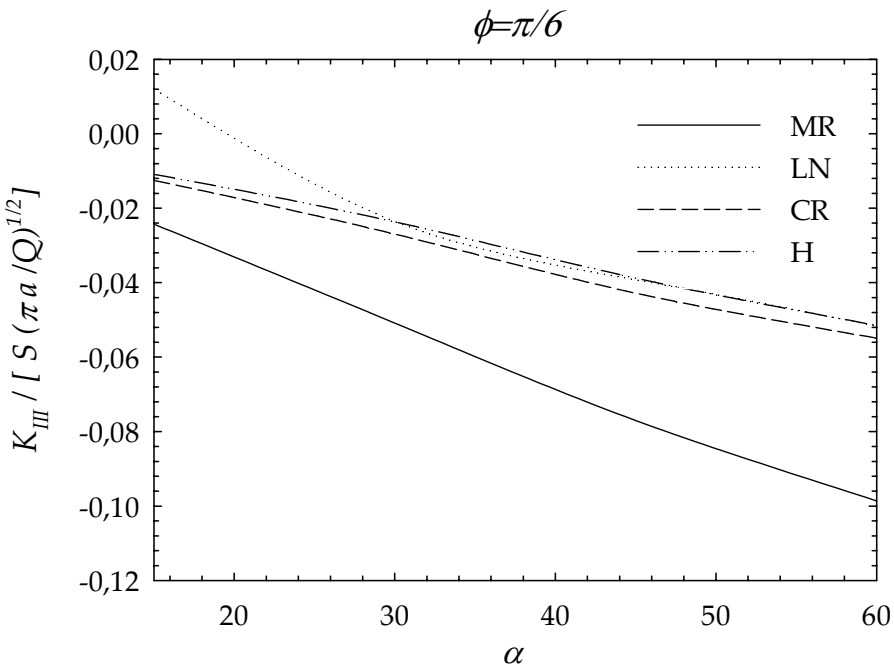

Figure 5.61 Peak values of normalized mode III stress intensity factors obtained at various inclination angles for 30^o crack front angle and a/t_1=0.4

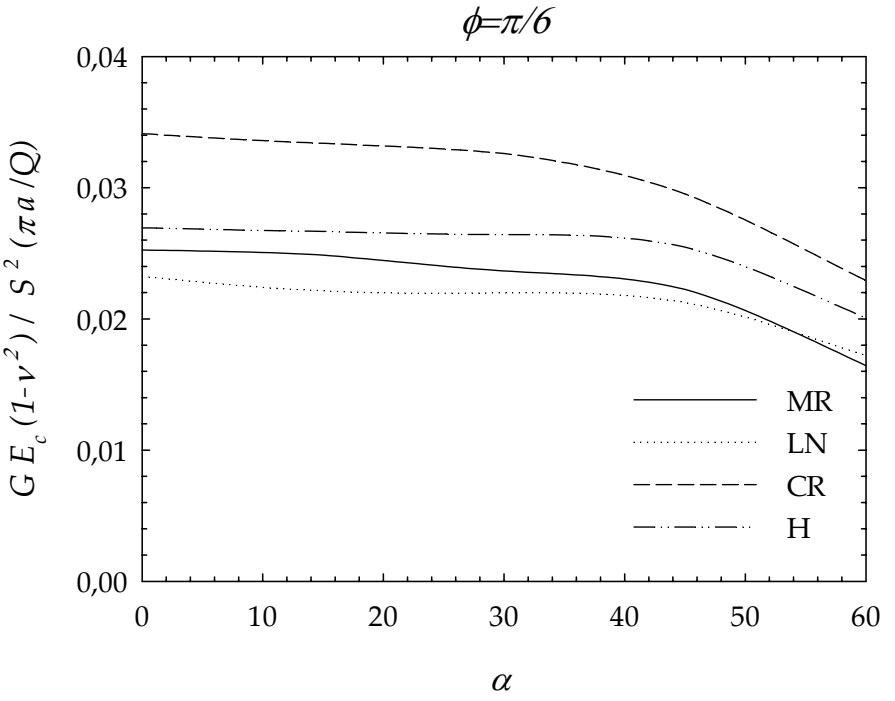

Figure 5.62 Peak values of normalized energy release rates obtained at various inclination angles for 30^o crack front angle and a/t_1=0.2

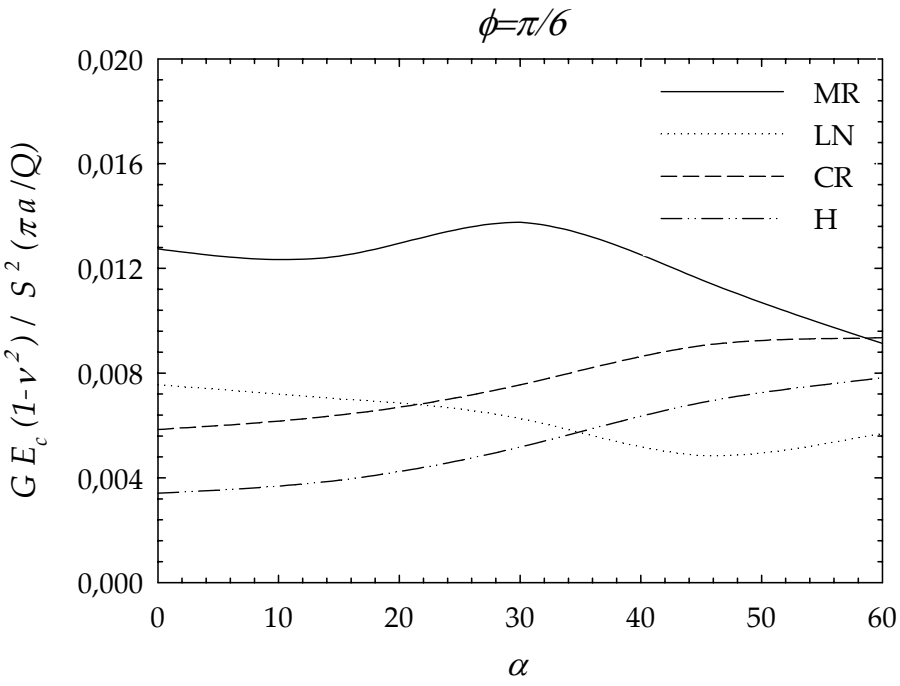

Figure 5.63 Peak values of normalized energy release rates obtained at various inclination angles for 30° crack front angle and a/t_1=0.4

5.4.7 Peak Values of Normalized SIFs and G Obtained at Various Inclination Angles for 45° Crack Front Angle

As seen in Figure 5.64, for $\phi = 45^o$ and for a/t_1=0.2, the maximum peak value of K_{In} is calculated for MR coating at $\alpha = 0^o$ and it is 0.256. Then as the inclination angle increases, the value of peaks decreases. For a/t_1=0.4, the highest peak value of K_{In} is again calculated for CR coating at $\alpha = 45^o$ and it is 0.075. It can be seen from Figure 5.65 that for a/t_1=0.4, the peak values of K_{In} increase as the inclination angle increases up to $\alpha = 45^o$. Then, they start to decrease.

The maximum peak value of K_{IIn} is obtained by MR coating for a/t_1=0.2 and it is -0.109 at $\alpha = 60^o$. As seen in Figure 5.66 as inclination angle increases, peaks of K_{IIn} increase, for MR, CR and H coatings. For LN coating, they first increase, then decrease and then increase again. For a/t_1=0.4, the highest peak value of K_{IIn} is calculated again for MR coating at $\alpha = 60^o$ and it is -0.089. For this case, as it can

be observed from Figure 5.67, as inclination angle increases, peaks of K_{IIn} also increase as for MR and LN coatings. For CR and H coatings, up to $\alpha = 45^o$, as α increases, peaks of K_{IIn} also increase. After this point the peaks of K_{IIn} start decreasing and at $\alpha \approx 50^o$, they reach the value of zero. Then, they again start to increase.

It can be seen from Figure 5.68 that for a/t_1=0.2, the peak values of K_{IIIn} increase as the inclination angle increases. The maximum peak is obtained at $\alpha = 60^o$ by MR coating and it is -0.010. For a/t_1=0.4, the highest peak value of K_{IIIn} is again calculated for MR coating at $\alpha = 60^o$ and it is -0.074. As it can be seen from Figure 5.69, for this case the peak values of K_{IIIn} also increase as the inclination angle increases.

If Figure 5.70 is analyzed, it can be seen that for a/t_1=0.2, as the inclination angle increases, the peak values of G_n also increase up to $\alpha = 45^o$, then it starts decreasing for LN, CR and H coatings. For this case, the maximum peak of G_n is attained by CR coating and it has a value of 0.023 at $\alpha = 45^o$. From Figure 5.71, it can be seen that the peak values of G_n increase as the inclination angle increases for a/t_1=0.4. At $\alpha = 60^o$ G_n reaches its maximum value, which is 0.009, attained by MR coating at $\alpha = 30^o$ then it starts decreasing. For LN coating, as α increases, the peaks of G_n decrease. On the other hand, for CR and H coatings as α increases, the peaks of *Gn* also increase.

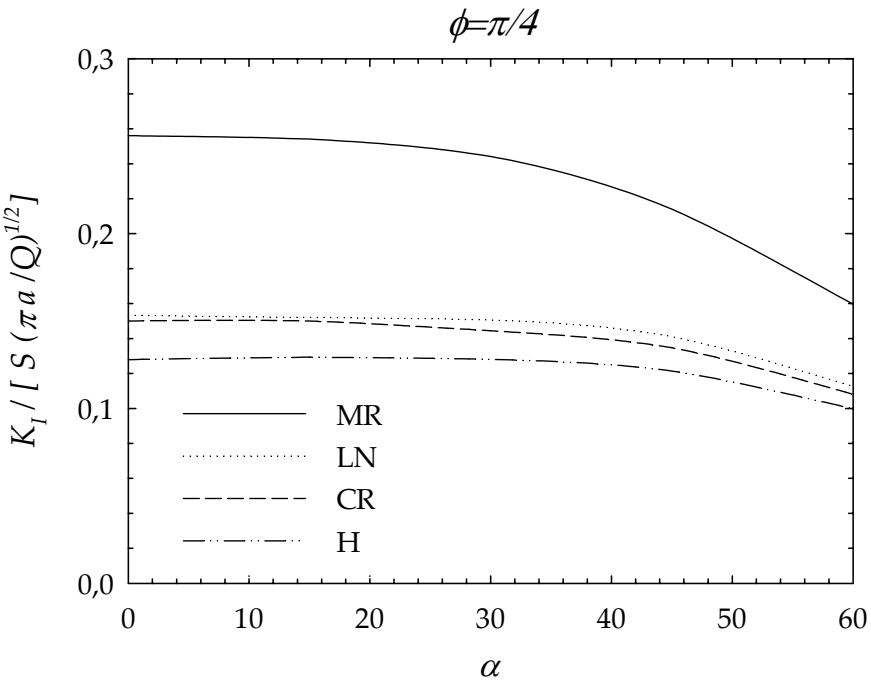

Figure 5.64 Peak values of normalized mode I stress intensity factors obtained at various inclination angles for 45^o crack front angle and a/t_1=0.2

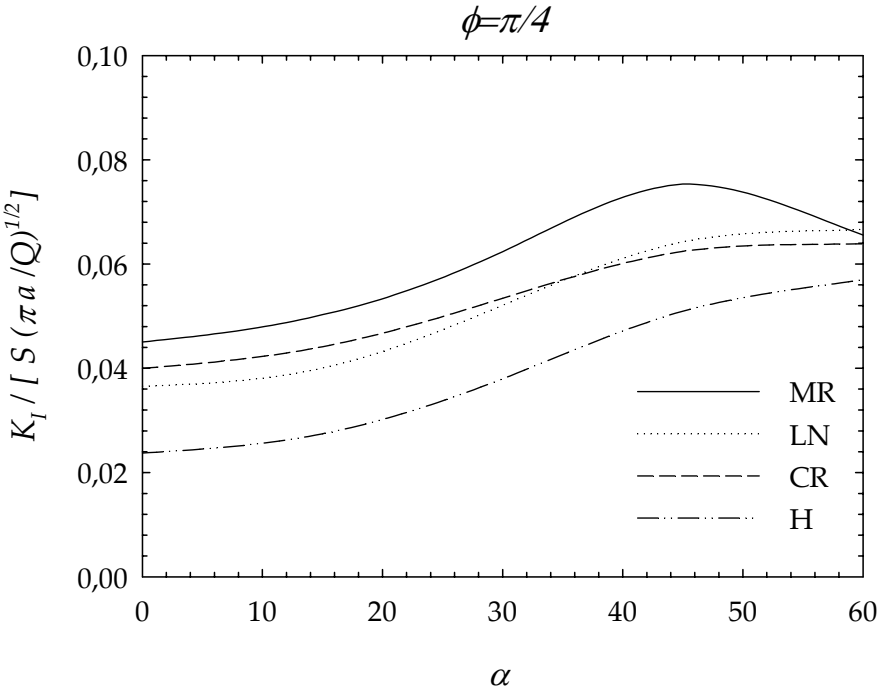

Figure 5.65 Peak values of normalized mode I stress intensity factors obtained at various inclination angles for 45^o crack front angle and a/t_1=0.4

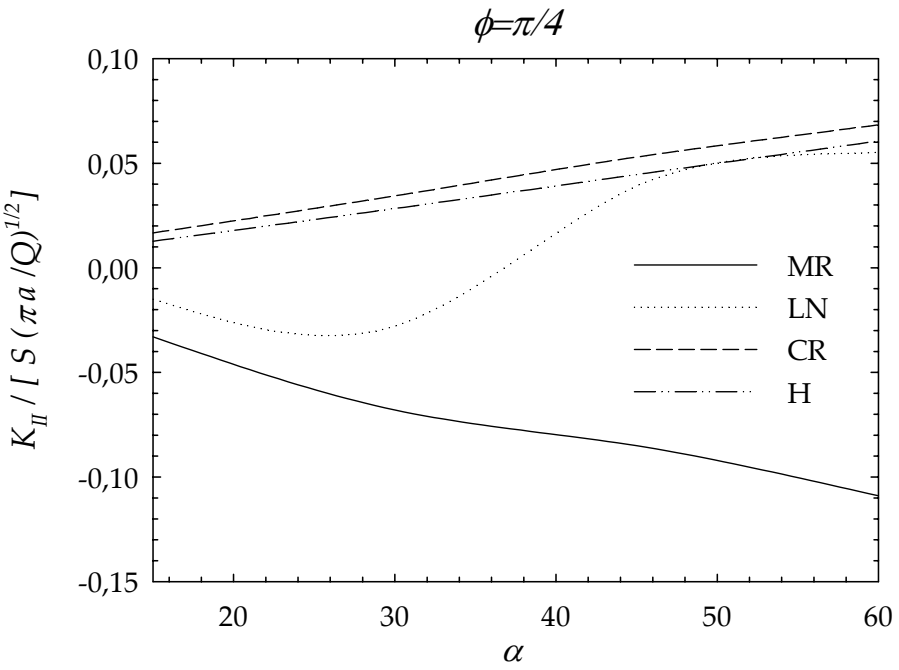

Figure 5.66 Peak values of normalized mode II stress intensity factors obtained at various inclination angles for 45^o crack front angle and a/t_1=0.2

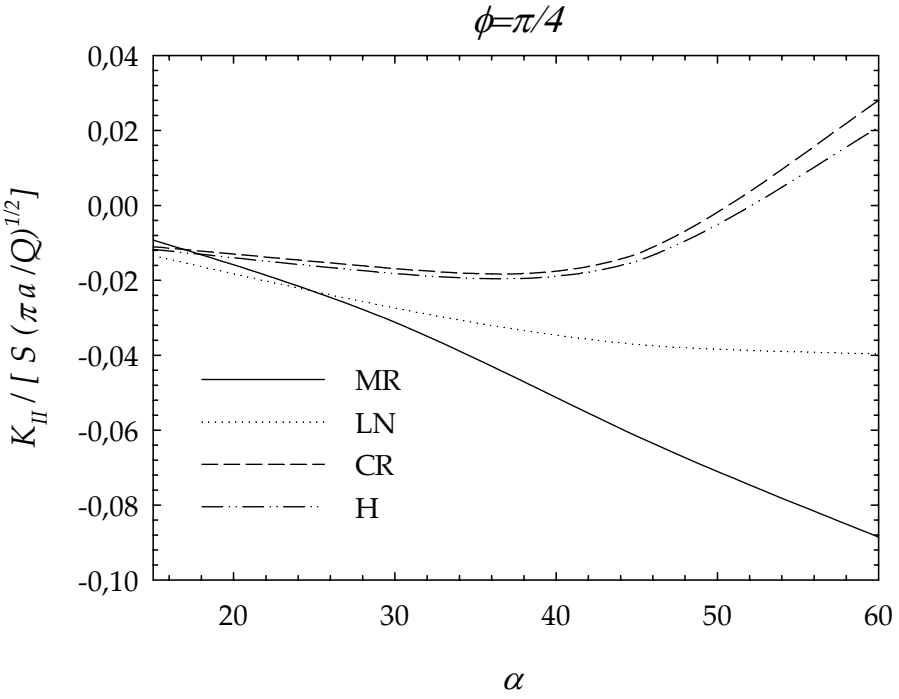

Figure 5.67 Peak values of normalized mode II stress intensity factors obtained at various inclination angles for 45^o crack front angle and a/t_1=0.4

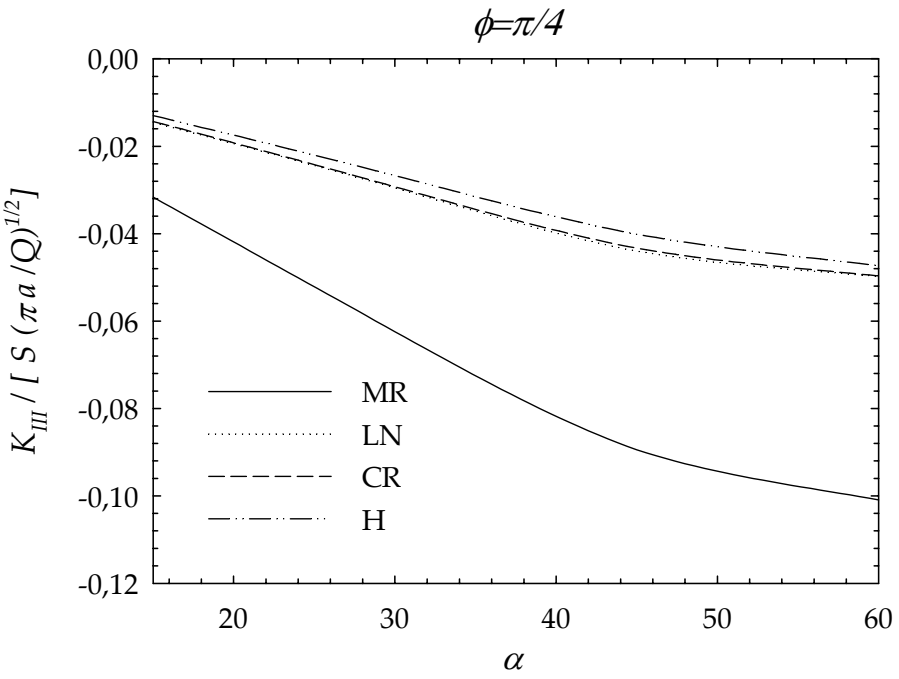

Figure 5.68 Peak values of normalized mode III stress intensity factors obtained at various inclination angles for 45^o crack front angle and a/t_1=0.2

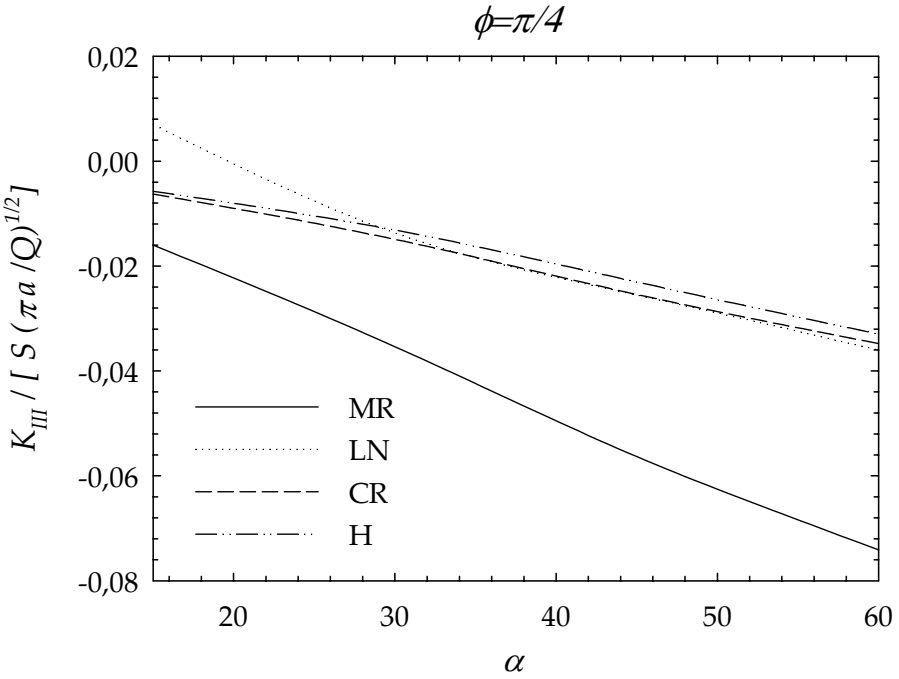

Figure 5.69 Peak values of normalized mode III stress intensity factors obtained at various inclination angles for 45^o crack front angle and a/t_1=0.4

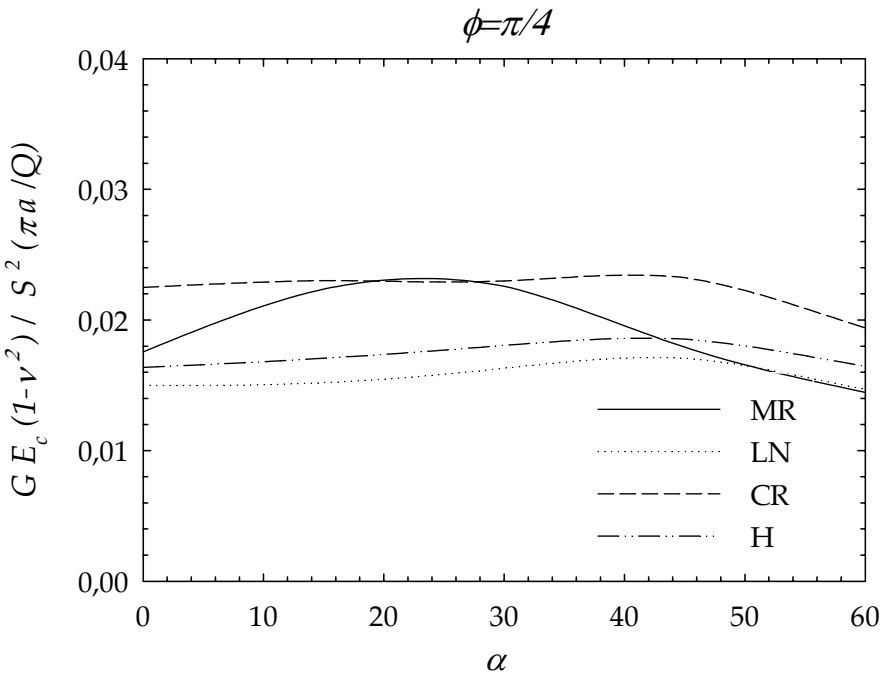

Figure 5.70 Peak values of normalized energy release rates obtained at various inclination angles for 45° crack front angle and a/t_l=0.2

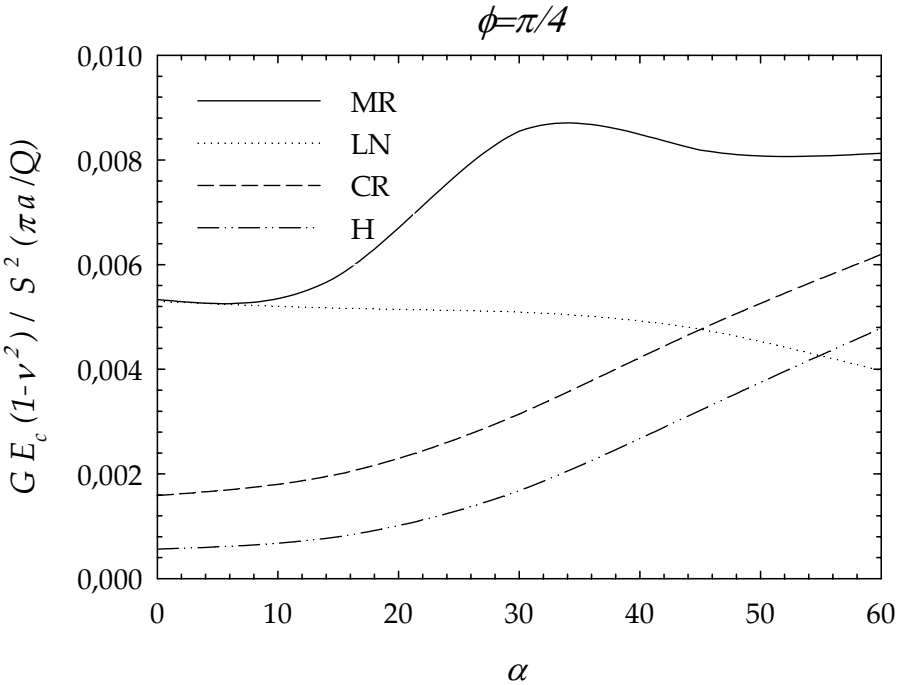

Figure 5.71 Peak values of normalized energy release rates obtained at various inclination angles for 45° crack front angle and a/t_l=0.4

5.4.8 Peak Values of Normalized SIFs and G Obtained at Various Inclination Angles for 60^o Crack Front Angle

As seen in Figure 5.72, for $\phi = 60^o$ and for a/t_1=0.2, the maximum peak value of K_{In} is calculated for MR coating at $\alpha = 30^o$ and it is 0.227. Then after this point, as the inclination angle increases, the value of peaks decreases. For a/t_1=0.4, the highest peak value of K_{In} is calculated for LN coating at $\alpha = 60^o$ and it is 0.066. It can be seen from Figure 5.73 that for a/t_1=0.4, the peak values of K_{In} increase as the inclination angle increases.

The maximum peak value of K_{IIn} is obtained by MR coating for a/t_1=0.2 and it is 0.103 at $\alpha = 60^o$. As seen in Figure 5.74 as inclination angle increases, peaks of K_{IIn} increase, too. For a/t_1=0.4, the highest peak value of K_{IIn} is calculated again for MR coating at $\alpha = 60^o$ and it is -0.081. For this case, as it can be observed from Figure 5.75, as inclination angle increases, peaks of K_{IIn} also increase for MR and LN coatings. For CR and H coatings, peak values of K_{IIn} increase up to $\alpha = 45^o$. After this point, they start decreasing as inclination angle increases.

It can be seen from Figure 5.76 that for a/t_1=0.2, the peak values of K_{IIIn} increase as the inclination angle increases. The maximum peak is obtained at $\alpha = 60^o$ by MR coating and it is -0.063. For a/t_1=0.4, the highest peak value of K_{IIIn} is again calculated for MR coating at $\alpha = 60^o$ and it is -0.050. As it can be seen from Figure 5.77, for this case the peak values of K_{IIIn} also increase as the inclination angle increases.

If Figure 5.78 is analyzed, it can be seen that for a/t_1=0.2, as the inclination angle increases, the peak values of G_n also increase up to $\alpha = 45^o$, then they start decreasing. For this case, the maximum peak of G_n is attained by MR coating and it has a value of 0.02 at $\alpha = 45^o$. From Figure 5.79 for a/t_1=0.4, it can be seen that the peak values of G_n increase for MR, CR and H coatings as the inclination angle increases. At $\alpha = 60^o$ G_n reaches its maximum value attained by MR coating

which is 0.007. For LN coating, as α increases, G_n also increases up to $\alpha = 45^o$; then it starts decreasing.

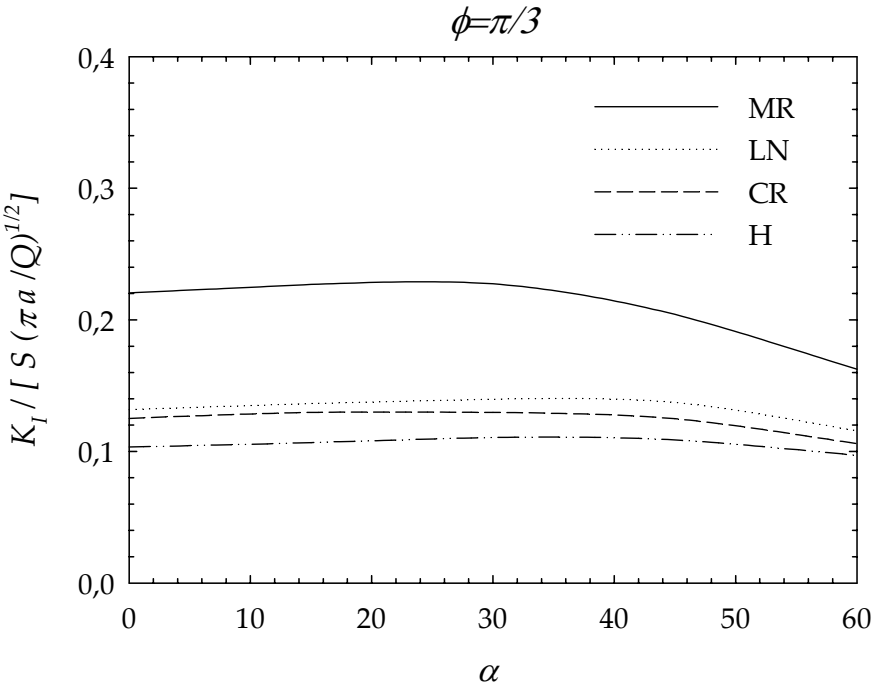

Figure 5.72 Peak values of normalized mode I stress intensity factors obtained at various inclination angles for 60^o crack front angle and a/t_1=0.2

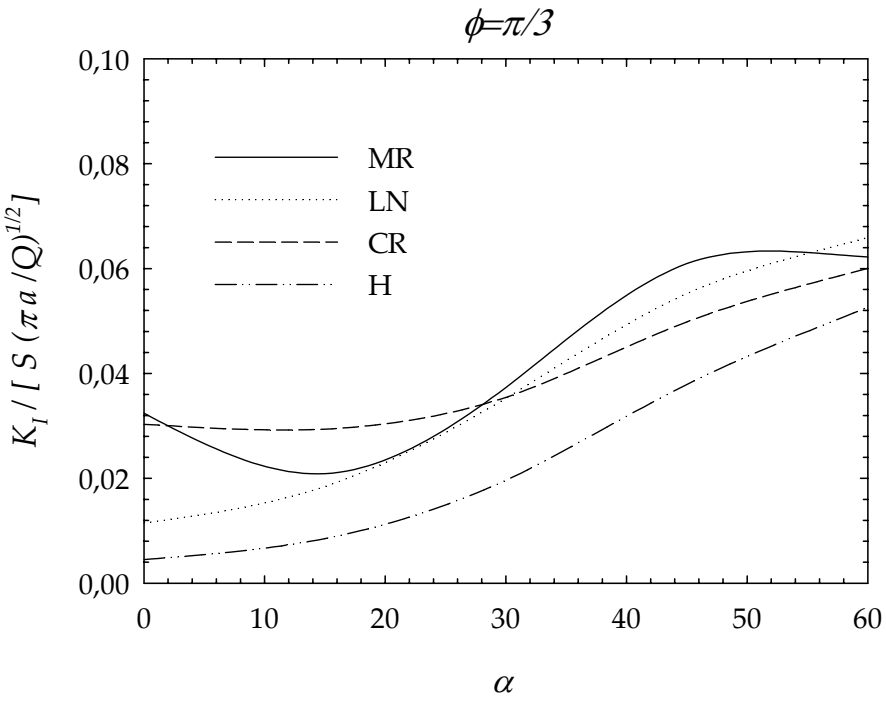

Figure 5.73 Peak values of normalized mode I stress intensity factors obtained at various inclination angles for 60^o crack front angle and a/t_1=0.4

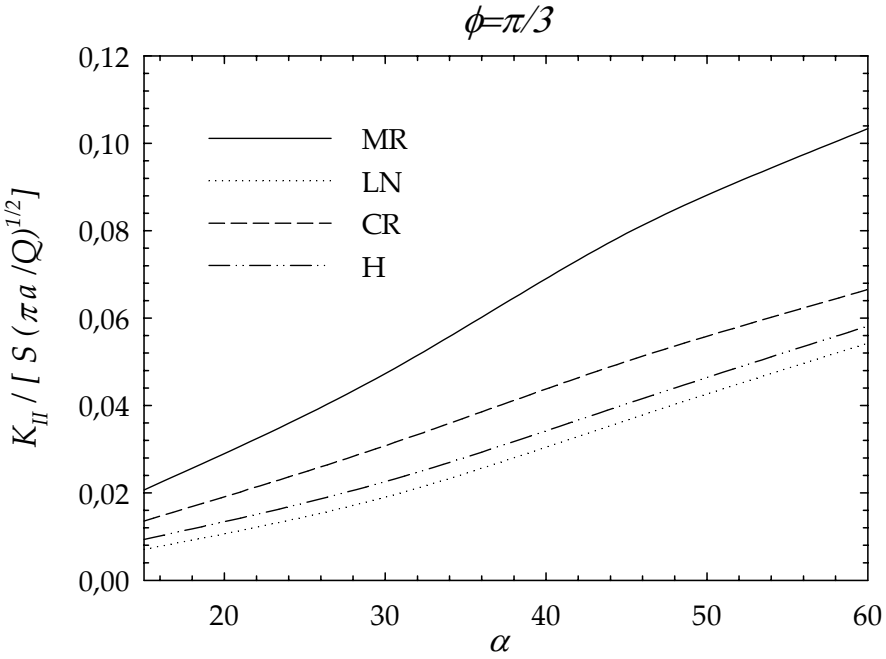

Figure 5.74 Peak values of normalized mode II stress intensity factors obtained at various inclination angles for 60^o crack front angle and a/t_1=0.2

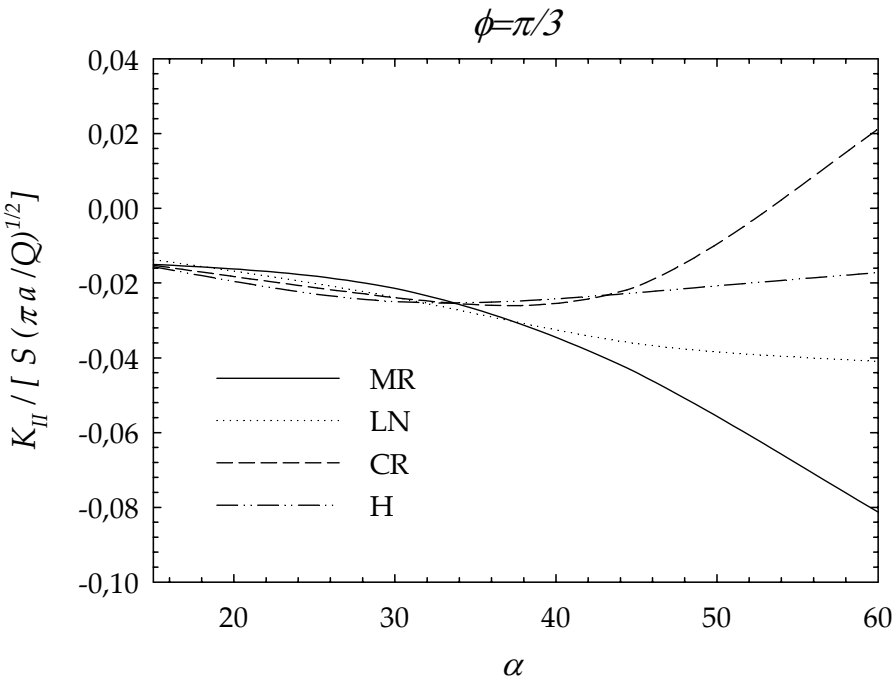

Figure 5.75 Peak values of normalized mode II stress intensity factors obtained at various inclination angles for 60^o crack front angle and a/t_1=0.4

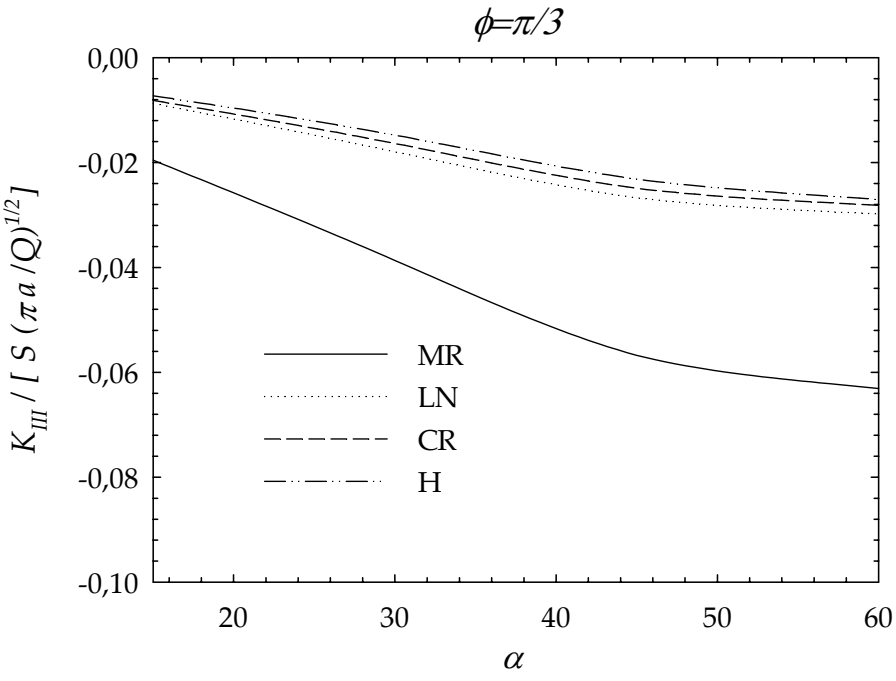

Figure 5.76 Peak values of normalized mode III stress intensity factors obtained at various inclination angles for 60^o crack front angle and a/t_1=0.2

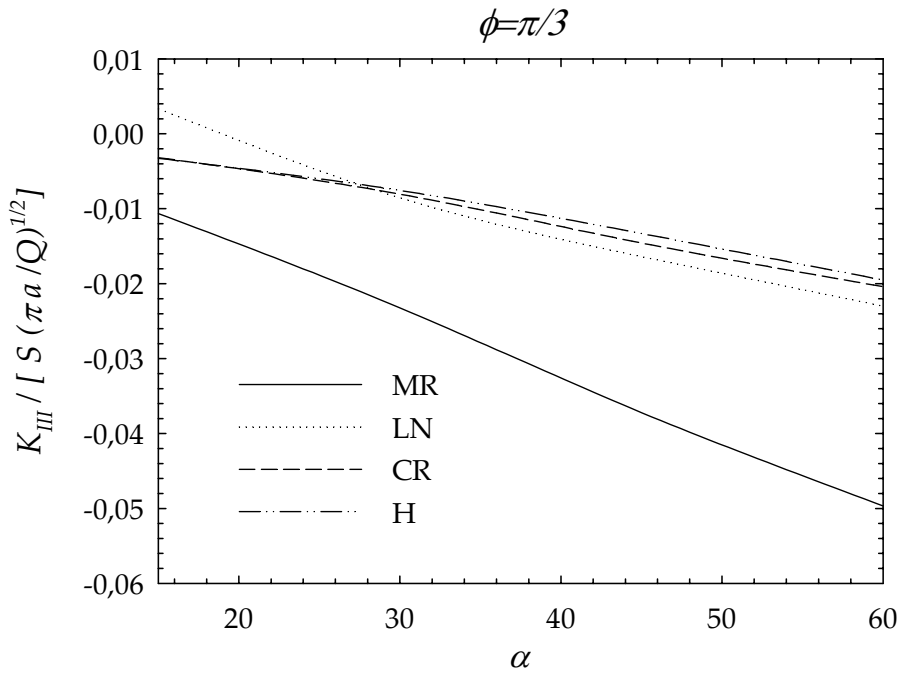

Figure 5.77 Peak values of normalized mode III stress intensity factors obtained at various inclination angles for 60^o crack front angle and a/t_1=0.4

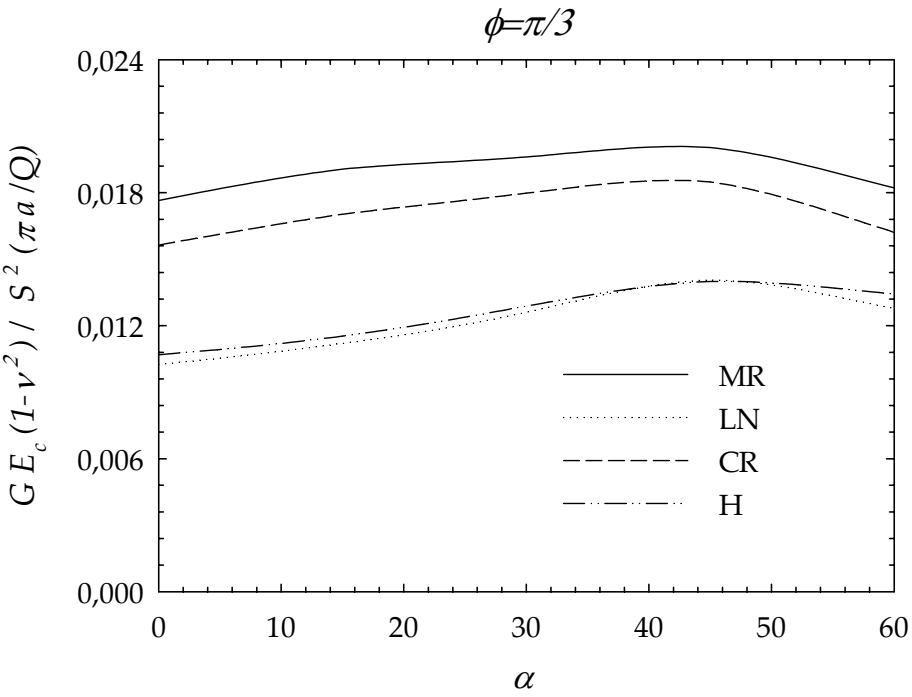

Figure 5.78 Peak values of normalized energy release rates obtained at various inclination angles for 60^o crack front angle and a/t_1=0.2

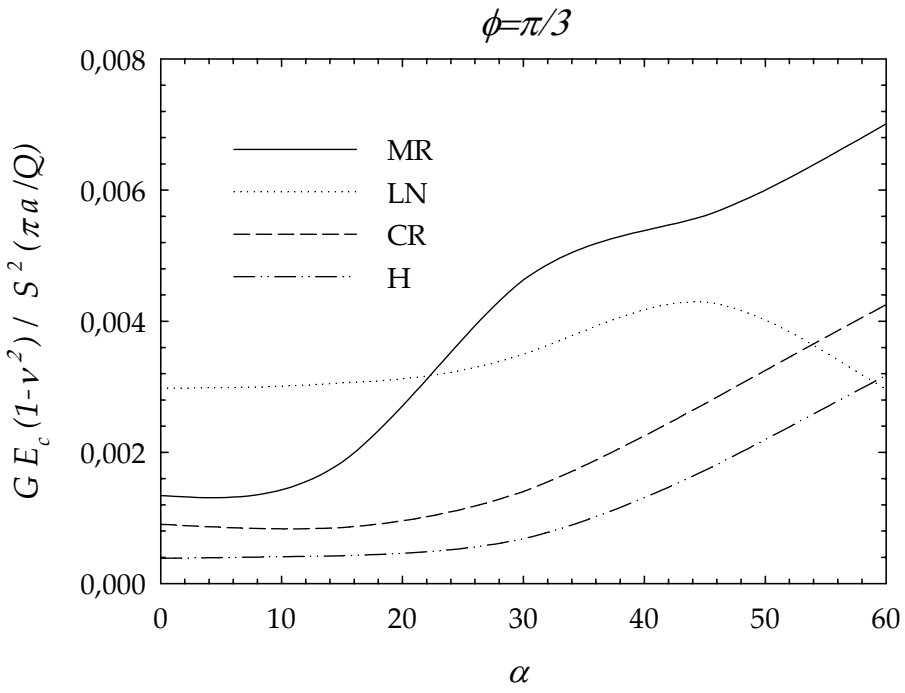

Figure 5.79 Peak values of normalized energy release rates obtained at various inclination angles for 60° crack front angle and a/t_1=0.4

5.4.9 Peak Values of Normalized SIFs and G Obtained at Various Inclination Angles for 90° Crack Front Angle

As seen in Figure 5.80, for $\phi = 90^o$ and for a/t_1=0.2, the maximum peak value of K_{In} is calculated for MR coating at $\alpha = 45^o$ and it is 0.209. Then after this point, as the inclination angle increases, the value of peaks decreases. For a/t_1=0.4, the highest peak value of K_{In} is calculated for LN coating at $\alpha = 60^o$ and it is 0.063. It can be seen from Figure 5.81 that for a/t_1=0.4, the peak values of K_{In} increase as the inclination angle increases for LN and CR coatings. For MR and H coatings, however, up to $\alpha = 15^o$, as α increases the peaks of K_{In} decrease and after this point they start to increase.

The maximum peak value of K_{IIn} is obtained by MR coating for a/t_1=0.2 and it is -0.110 at $\alpha = 60^o$. As seen in Figure 5.82 for MR, CR and H coatings, as inclination angle increases, peaks of K_{IIn} increase, too. In the case of LN coating,

up to $\alpha = 45^o$ K_{IIn} increases, after this point it starts decreasing and becomes zero and then again starts to increase as α increases. For a/t_1=0.4, the highest peak value of K_{IIn} is calculated for MR coating at $\alpha = 60^o$ and it is -0.068. For this case, as it can be observed from Figure 5.83, as inclination angle increases, for MR coating peaks of K_{IIn} first decrease, then increase, then decrease and then again increase. For LN coating, as α increases, peaks of K_{IIn} also increase. In the case of CR coating, as α increases, peaks of K_{IIn} also increase first, then decrease and become zero and then again start increasing. For H coating, the peaks increase up to $\alpha = 45^o$, after this point they start decreasing.

It can be seen from Figure 5.84 that for a/t_1=0.2, the maximum peak of K_{IIIn} is obtained at $\alpha = 60^o$ by MR coating and it is -0.014. It is observed that for MR and LN coatings, as the inclination angle increases the peak values of K_{IIIn} first increase, then decrease and then increase again. In the cases of CR and H coatings, the peak values of K_{IIIn} first increase, then decrease and become zero and then increase again. For a/t_1=0.4, the highest peak value of K_{IIIn} is calculated again for MR coating at $\alpha = 60^o$ and it is -0.008. As it can be seen from Figure 5.85 for this case, the peak values of K_{IIIn} first increase, then decrease and then increase again for MR and LN coatings as the inclination angle increases. On the other hand, for CR and H coatings, the peaks first increase, then start decreasing.

If Figure 5.86 is analyzed, it can be seen that for a/t_1=0.2, as the inclination angle increases, the peak values of G_n also increase up to $\alpha = 30^o$. At this point, the maximum peak of G_n is attained by MR coating and it has a value of 0.018. Then the peak values of G_n start to decrease for MR coating. For LN, CR and H coatings, the peaks increase up to $\alpha = 45^o$ and then they start decreasing. From Figure 5.87, it can be seen that for MR, CR and H coatings, the peak values of G_n increase as the inclination angle increases for a/t_1=0.4. At $\alpha = 60^o$ G_n reaches its maximum value attained by MR coating which is 0.007. In the case of LN coating, the peaks of G_n increase up to $\alpha = 45^o$ and then they start decreasing.

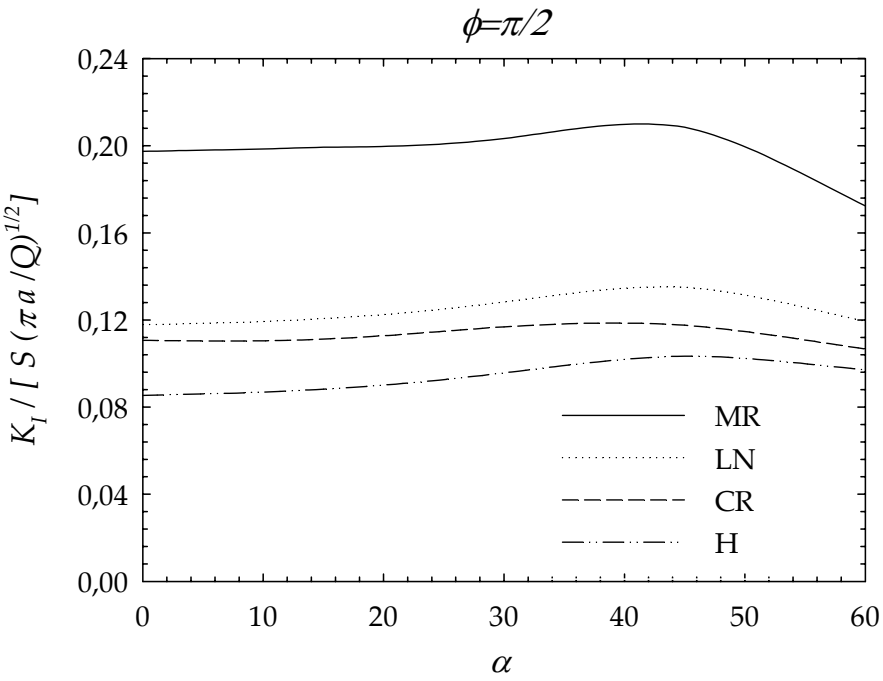

Figure 5.80 Peak values of normalized mode I stress intensity factors obtained at various inclination angles for 90° crack front angle and a/t_1=0.2

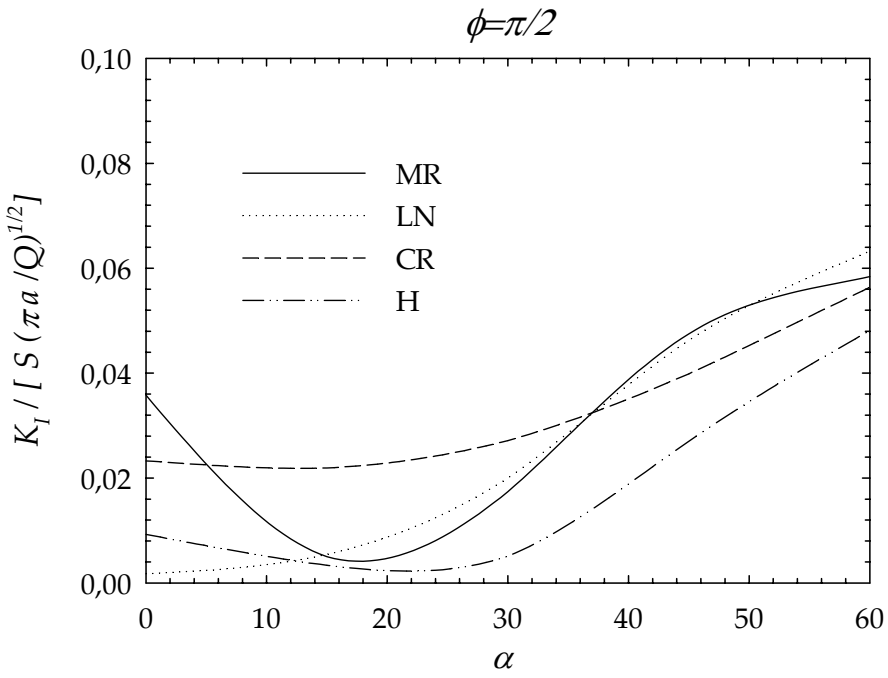

Figure 5.81 Peak values of normalized mode I stress intensity factors obtained at various inclination angles for 90° crack front angle and a/t_1=0.4

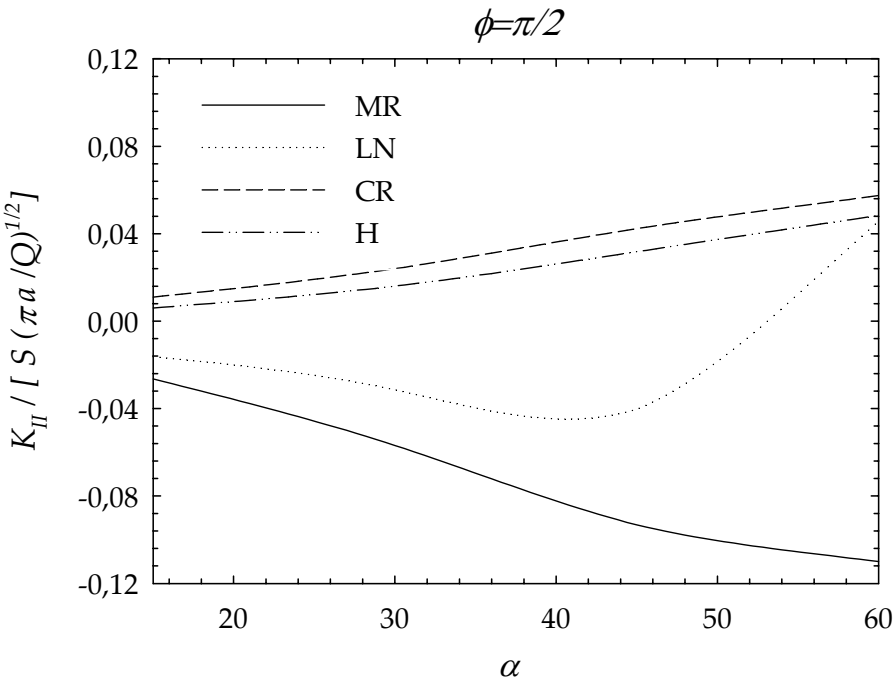

Figure 5.82 Peak values of normalized mode II stress intensity factors obtained at various inclination angles for 90° crack front angle and a/t_1=0.2

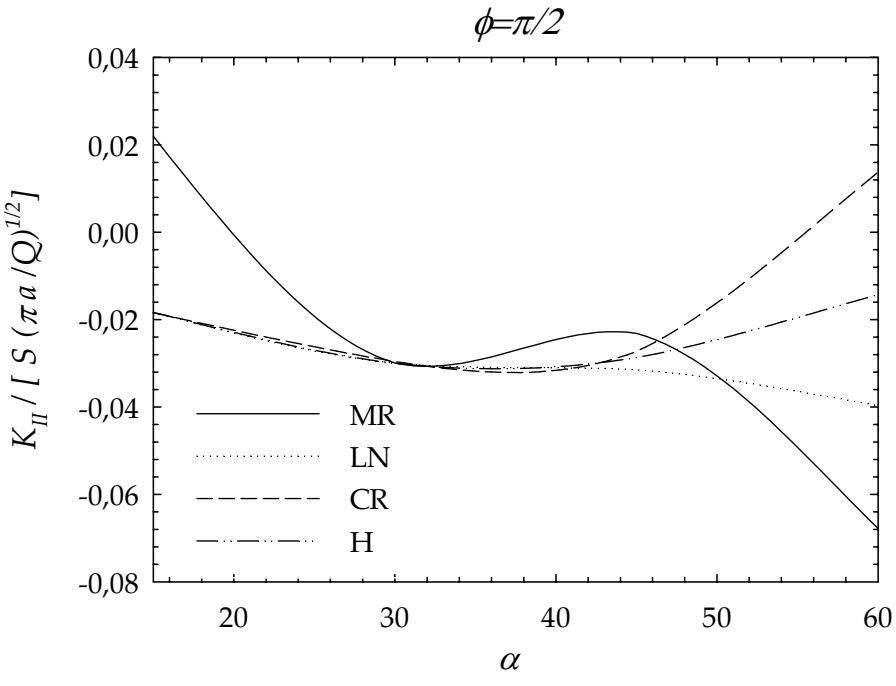

Figure 5.83 Peak values of normalized mode II stress intensity factors obtained at various inclination angles for 90° crack front angle and a/t_1=0.4

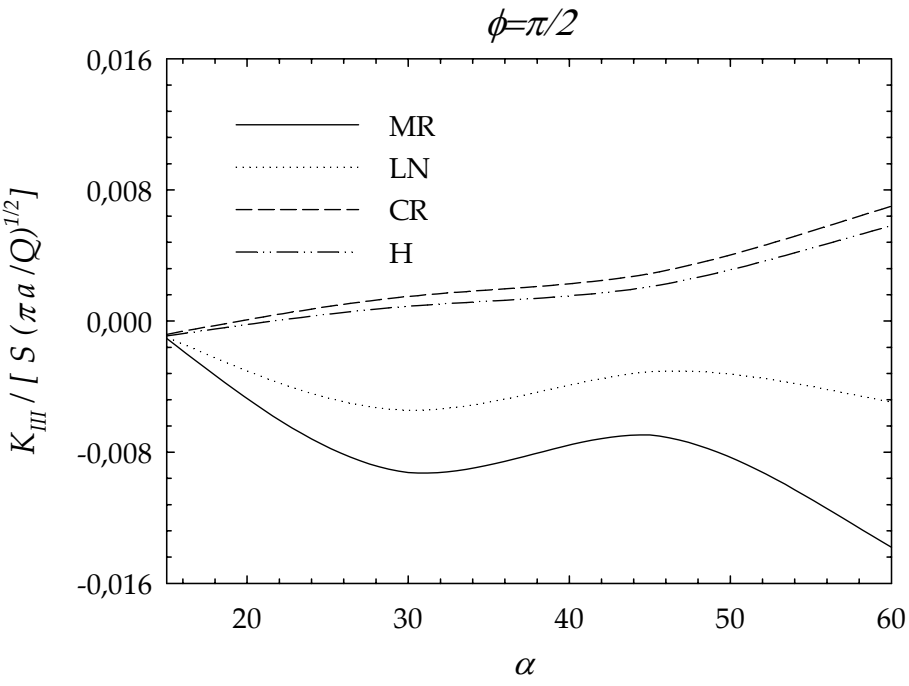

Figure 5.84 Peak values of normalized mode III stress intensity factors obtained at various inclination angles for 90^o crack front angle and a/t_1=0.2

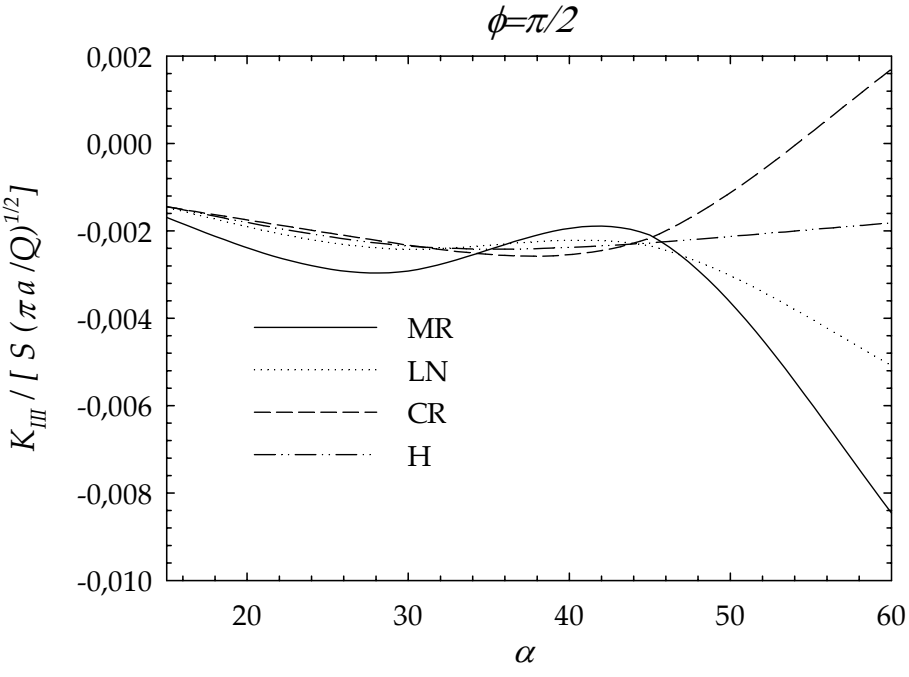

Figure 5.85 Peak values of normalized mode III stress intensity factors obtained at various inclination angles for 90^o crack front angle and a/t_1=0.4

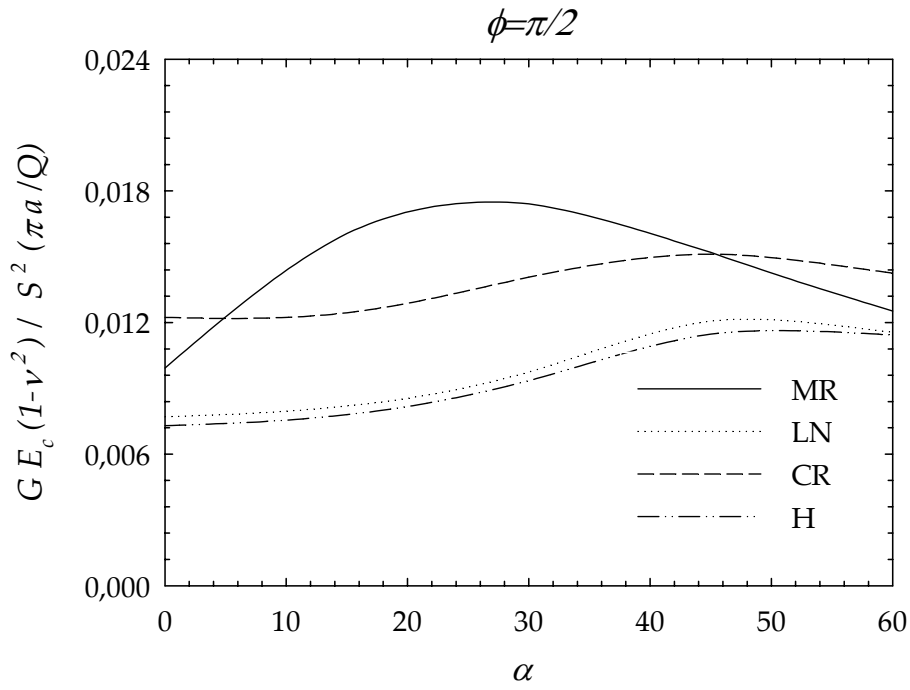

Figure 5.86 Peak values of normalized energy release rates obtained at various inclination angles for 90° crack front angle and a/t_l=0.2

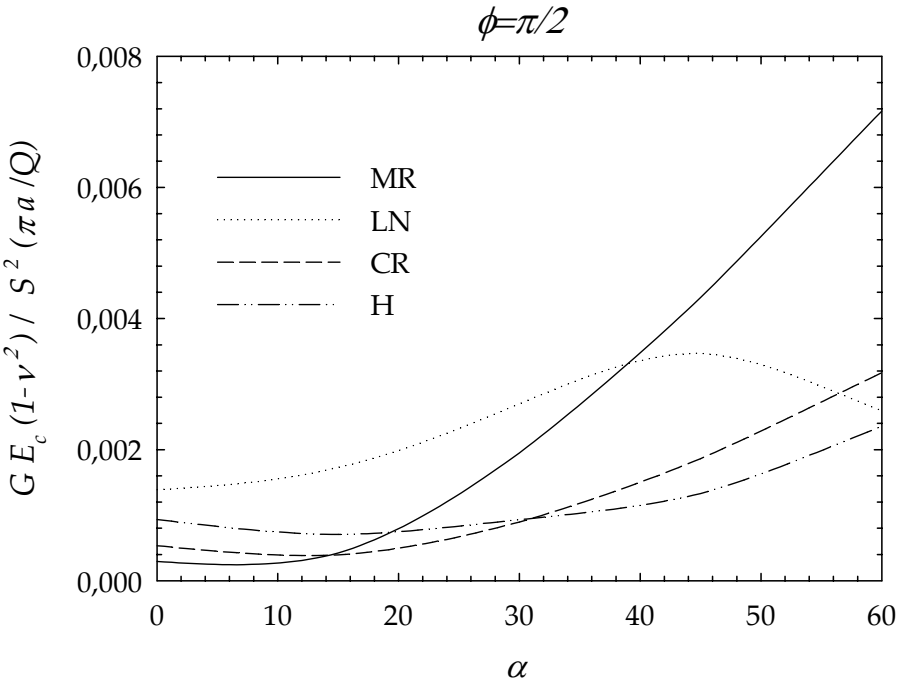

Figure 5.87 Peak values of normalized energy release rates obtained at various inclination angles for 90° crack front angle and a/t_l=0.4

5.4.10 Normalized SIFs and G Distributions with respect to Normalized Time for ϕ=45^o and α=0^o

Figure 5.88 shows normalized mode I stress intensity factor, K_{In} with respect to normalized time, τ for a/t_1=0.2. From this figure it can be seen that the maximum values of K_{In}, which are 0.266, 0.153, 0.150 and 0.128, are obtained at $\tau \cong 0.005$, 0.008, 0.028 and 0.02 for MR, LN, CR and H coatings, respectively. In Figure 5.89, K_{In} distributions with respect to τ is given for a/t_1=0.4. In this case, the maximum values of K_{In}, which are 0.045, 0.037, 0.040 and 0.024, are obtained at $\tau \cong 0.008$, 0.016, 0.072 and 0.072 for MR, LN, CR and H coatings, respectively.

The normalized energy release rate, G_n distributions with respect to normalized time, τ for a/t_1=0.2 is presented in Figure 5.90. It can be observed from this figure that the maximum values of G_n, which are 0.018, 0.015, 0.023 and 0.016, are obtained at $\tau \cong 0.005$, 0.008, 0.028 and 0.02 for MR, LN, CR and H coatings, respectively. In the case of a/t_1=0.4, as it can be seen in Figure 5.91, the maximum values of G_n, which are 0.0053, 0.0053, 0.0016 and 0.0006, are obtained at $\tau \cong 0.264$, 0.424, 0.068 and 0.072 for MR, LN, CR and H coatings, respectively. In Figure 5.92, the normalized temperature with respect to normalized time is shown.

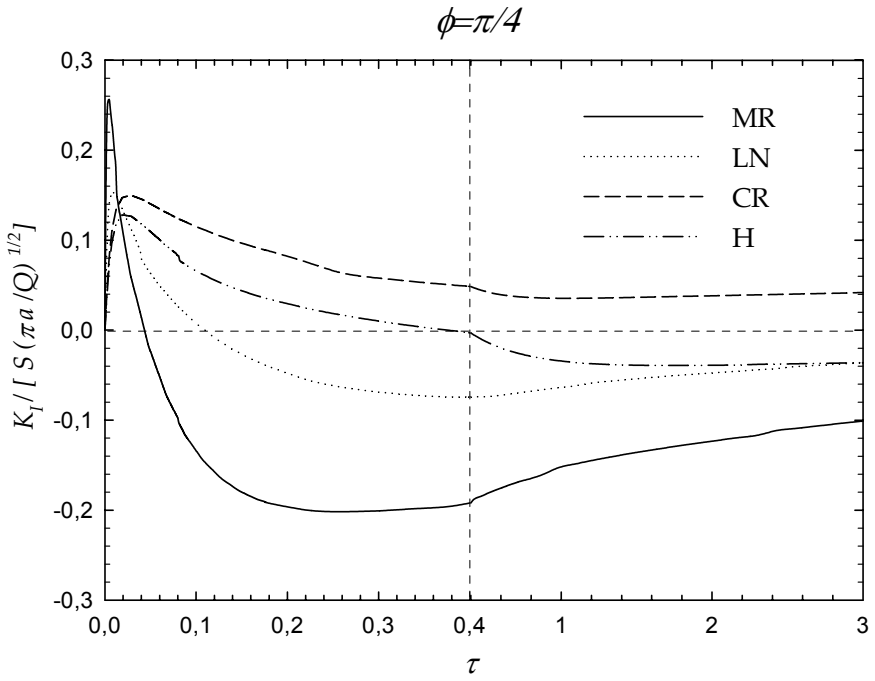

Figure 5.88 Normalized mode I stress intensity factors at 45^o crack front angle with respect to normalized time, a/t_1=0.2 and α=0^o

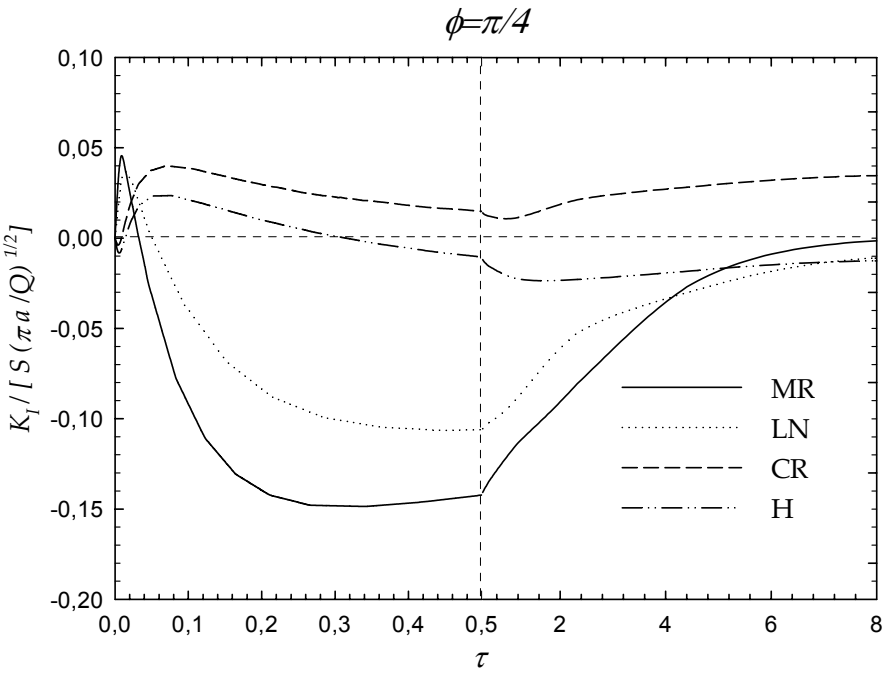

Figure 5.89 Normalized mode I stress intensity factors at 45^o crack front angle with respect to normalized time, a/t_1=0.4 and α=0^o

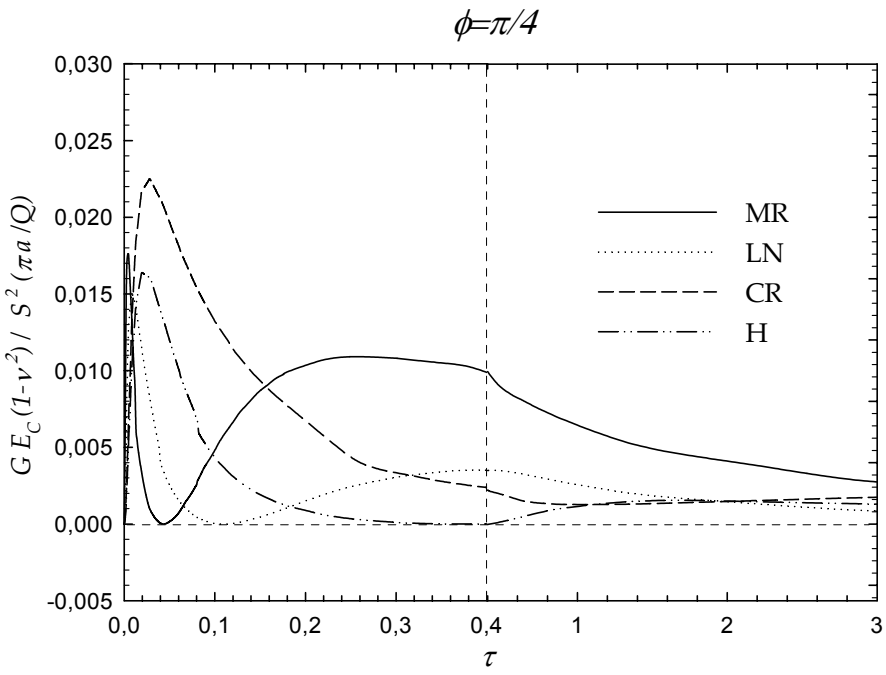

Figure 5.90 Normalized energy release rate at 45° crack front angle with respect to normalized time, a/t_1=0.2 and α=0°

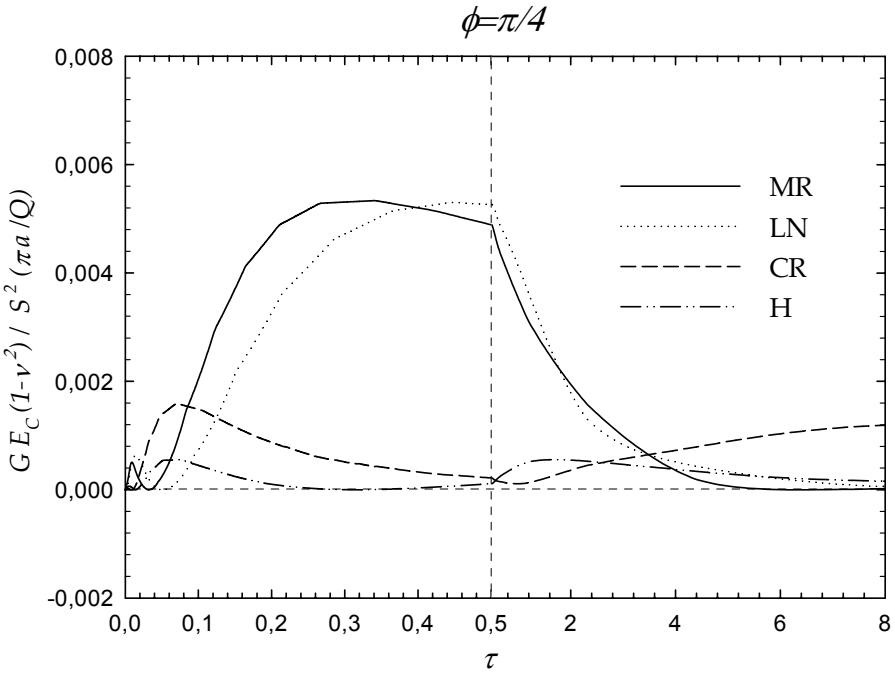

Figure 5.91 Normalized energy release rate at 45° crack front angle with respect to normalized time, a/t_1=0.4 and α=0°

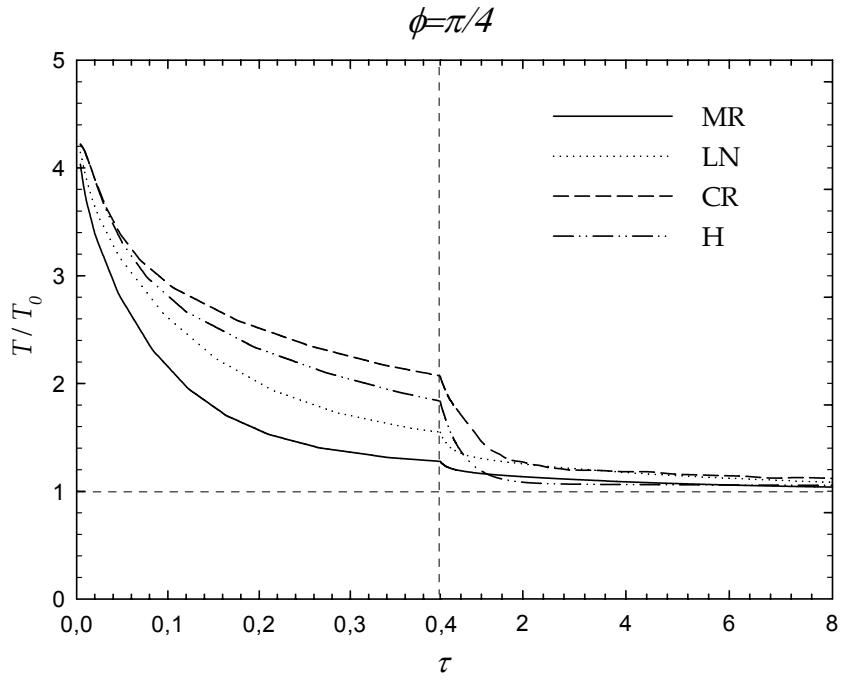

Figure 5.92 Normalized temperature at 45° crack front angle with respect to normalized time, a/t_1=0.4 and α=0°

5.4.11 Normalized SIFs and G Distributions with respect to Normalized Time for ϕ=45° and α=15°

Figure 5.93 shows normalized mode I stress intensity factor, K_{In} with respect to normalized time, τ for a/t_1=0.2. From this figure it can be seen that the maximum values of K_{In}, which are 0.254, 0.152, 0.150 and 0.129, are obtained at $\tau \cong 0.004$, 0.008, 0.028 and 0.020 for MR, LN, CR and H coatings, respectively. In Figure 5.94, K_{In} distributions with respect to τ are given for a/t_1=0.4. In this case, the maximum values of K_{In}, which are 0.050, 0.040, 0.044 and 0.027, are obtained at $\tau \cong 0.008$, 0.016, 0.068 and 0.052 for MR, LN, CR and H coatings, respectively.

Figure 5.95 depicts normalized mode II stress intensity factor, K_{IIn} with respect to normalized time, τ for a/t_1=0.2. From this figure it can be observed that the

maximum values of K_{IIn}, which are -0.033, -0.015, 0.017 and 0.013, are obtained at $\tau \cong 0.261$, 0.381, 0.042 and 0.029 for MR, LN, CR and H coatings, respectively. In Figure 5.96, K_{IIn} distributions with respect to τ are given for a/t_1=0.4. In this case, the maximum values of K_{IIn}, which are -0.009, -0.013, -0.011 and -0.012, are obtained at $\tau \cong 0.004$, 0.384, 0.012 and 0.012 for MR, LN, CR and H coatings, respectively.

In Figure 5.97, normalized mode III stress intensity factor, K_{IIIn} with respect to normalized time, τ for a/t_1=0.2 is given. From this figure it can be seen that the maximum values of K_{IIIn}, which are -0.032, -0.015, -0.014 and -0.013, are obtained at $\tau \cong 0.005$, 0.010, 0.024 and 0.020 for MR, LN, CR and H coatings, respectively. In Figure 5.98, K_{IIIn} distributions with respect to τ are given for a/t_1=0.4. In this case, the maximum values of K_{IIIn}, which are -0.016, 0.007, -0.006 and -0.006, are obtained at $\tau \cong 0.012$, 0.444, 0.068 and 0.076 for MR, LN, CR and H coatings, respectively.

The normalized energy release rate, G_n distributions with respect to normalized time, τ for a/t_1=0.2 are presented in Figure 5.99. It can be observed from this figure that the maximum values of G_n, which are 0.022, 0.015, 0.023 and 0.017, are obtained at $\tau \cong 0.261$, 0.008, 0.027 and 0.020 for MR, LN, CR and H coatings, respectively. In the case of a/t_1=0.4, as it can be seen in Figure 5.100, the maximum values of G_n, which are 0.0058, 0.0052, 0.0020 and 0.0008, are obtained at $\tau \cong 0.264$, 0.444, 0.064 and 0.048 for MR, LN, CR and H coatings, respectively. In Figure 5.101, the normalized temperature with respect to normalized time is shown.

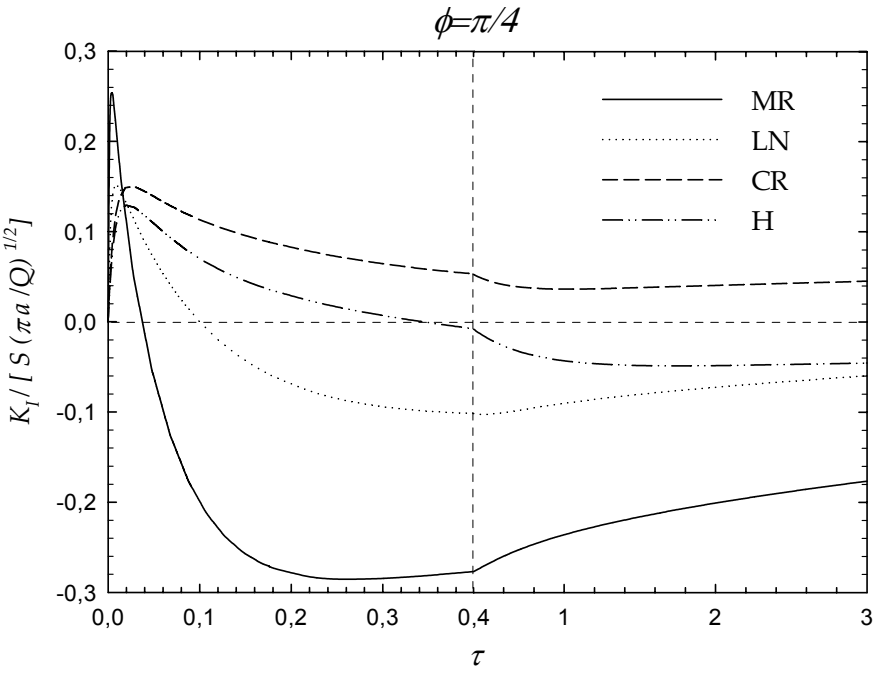

Figure 5.93 Normalized mode I stress intensity factors at 45^o crack front angle with respect to normalized time, a/t_1=0.2 and α=15^o

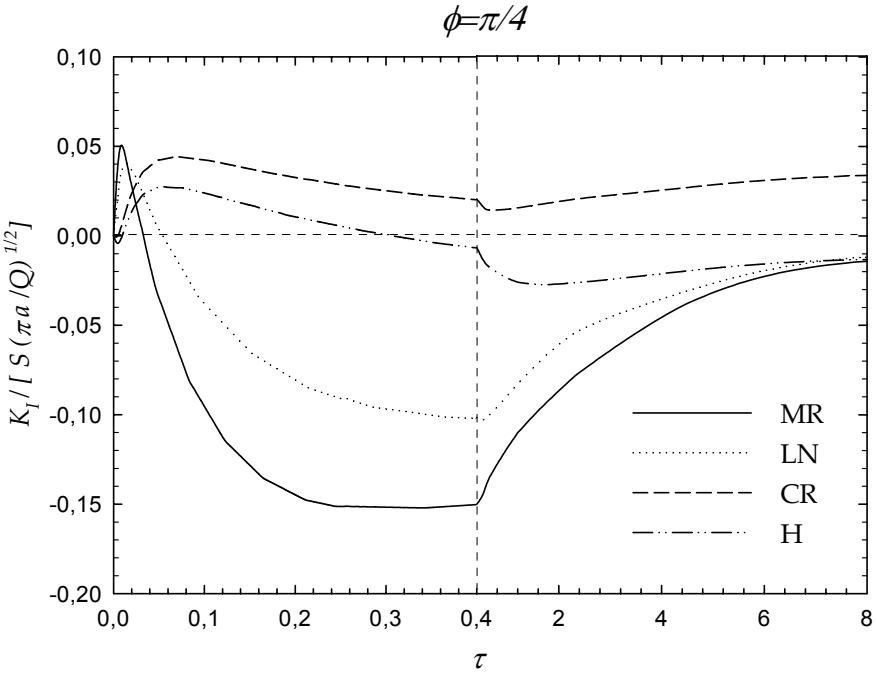

Figure 5.94 Normalized mode I stress intensity factors at 45^o crack front angle with respect to normalized time, a/t_1=0.4 and α=15^o

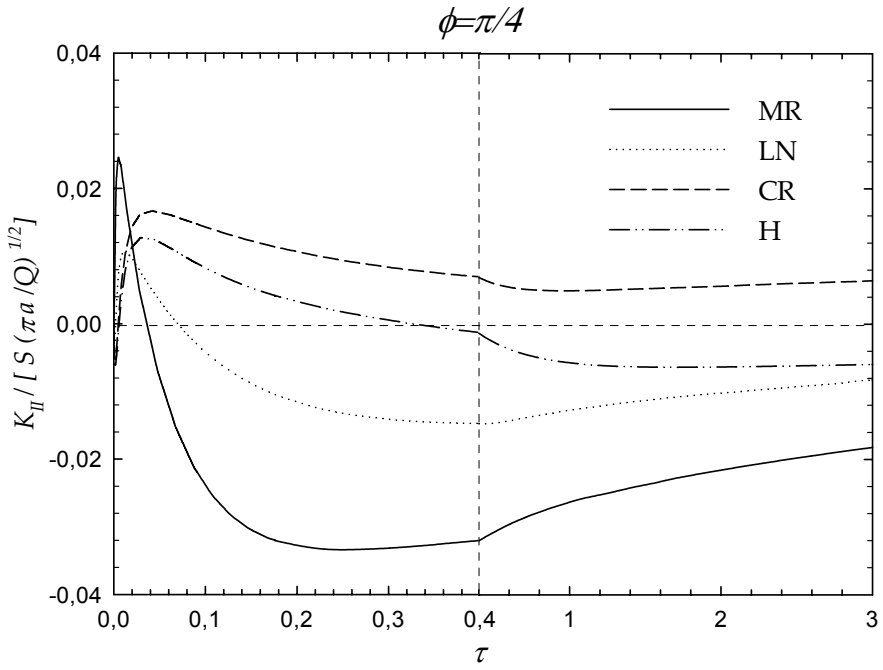

Figure 5.95 Normalized mode II stress intensity factors at 45° crack front angle with respect to normalized time, a/t_1=0.2 and α=15°

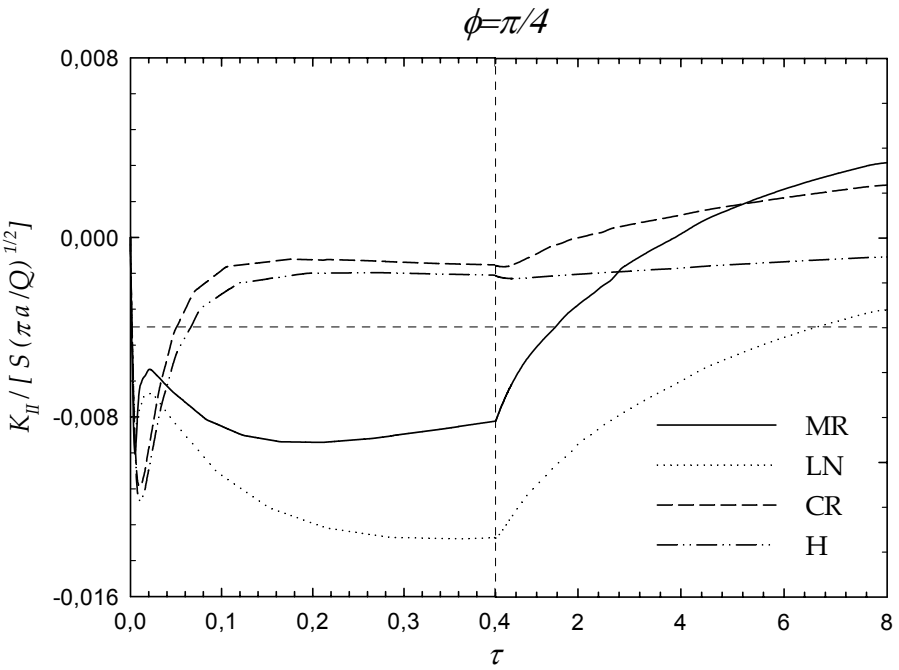

Figure 5.96 Normalized mode II stress intensity factors at 45° crack front angle with respect to normalized time, a/t_1=0.4 and α=15°

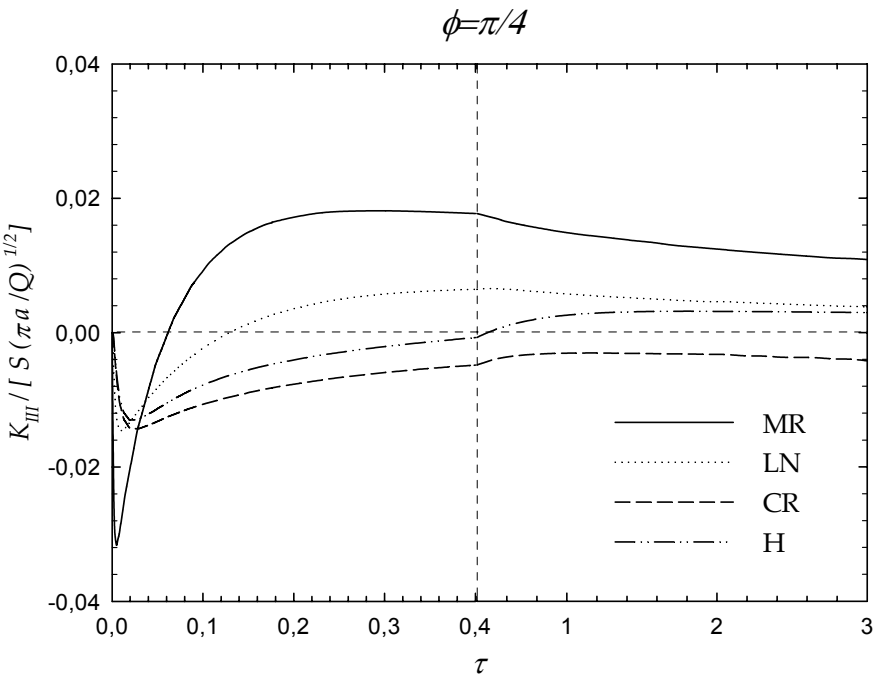

Figure 5.97 Normalized mode III stress intensity factors at 45° crack front angle with respect to normalized time, a/t_1=0.2 and α=15°

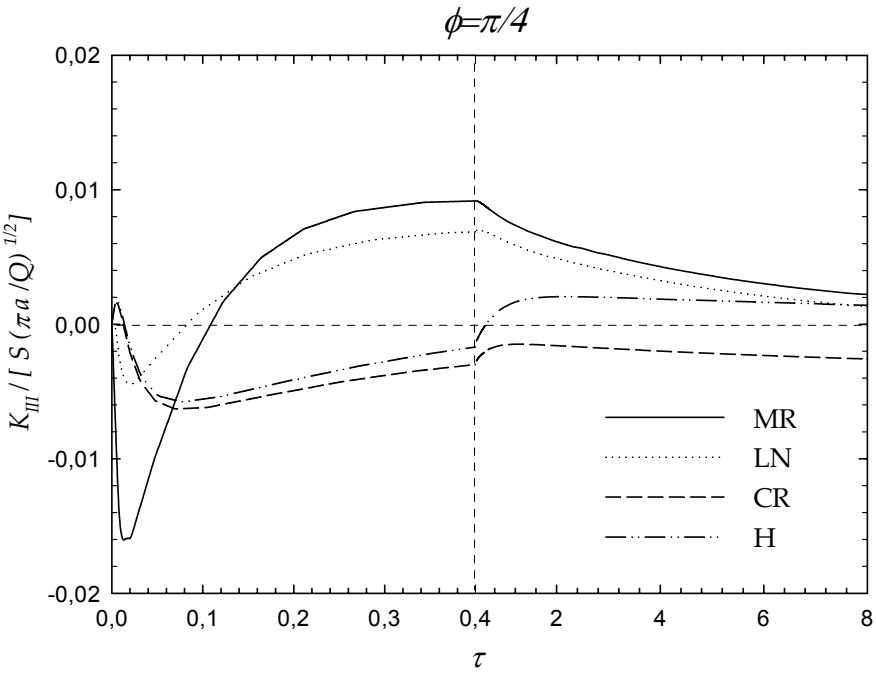

Figure 5.98 Normalized mode III stress intensity factors at 45° crack front angle with respect to normalized time, a/t_1=0.4 and α=15°

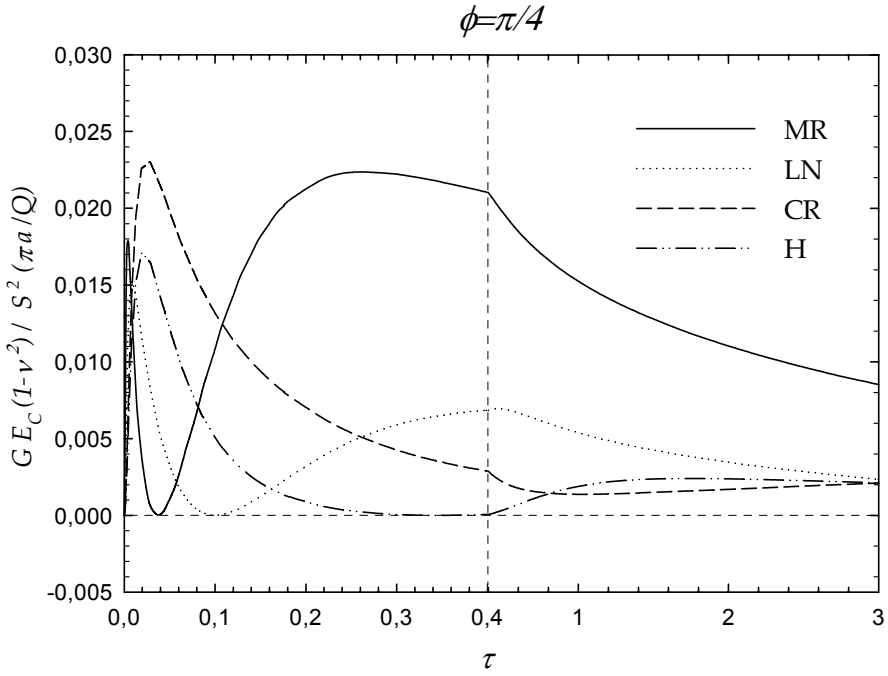

Figure 5.99 Normalized energy release rate at 45° crack front angle with respect to normalized time, a/t_1=0.2 and α=15°

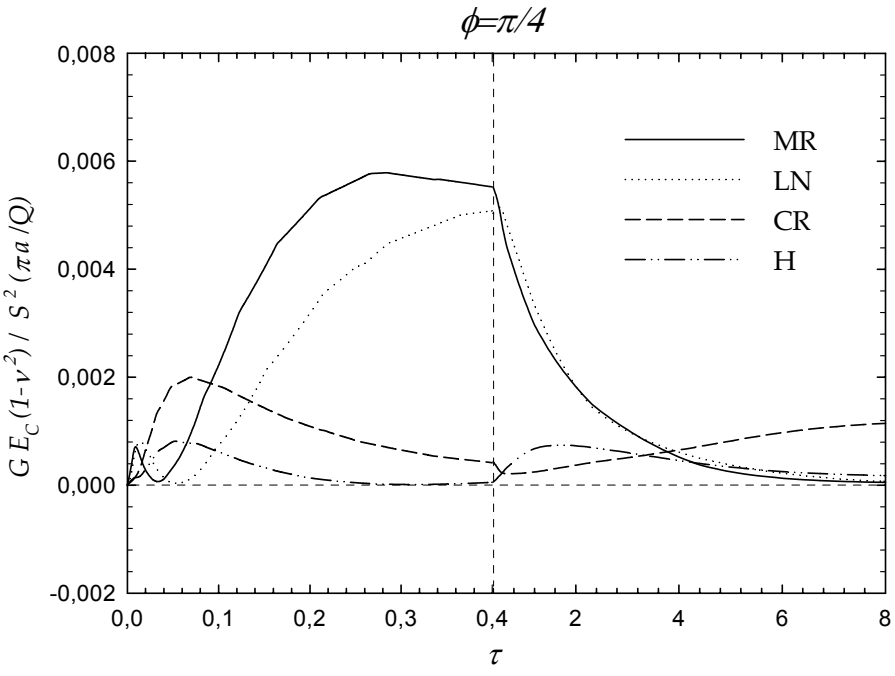

Figure 5.100 Normalized energy release rate at 45° crack front angle with respect to normalized time, a/t_1=0.4 and α=15°

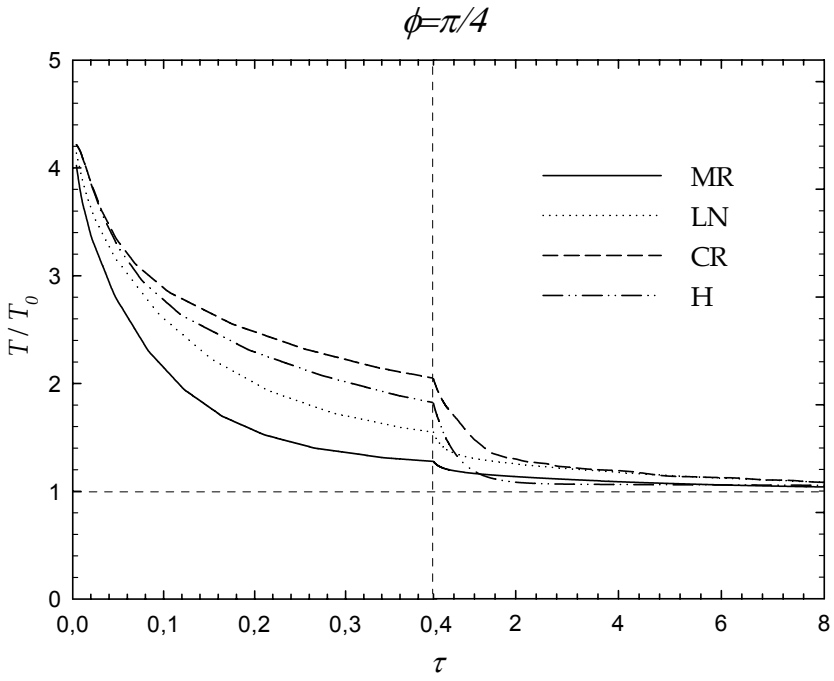

Figure 5.101 Normalized temperature at 45° crack front angle with respect to normalized time, a/t_1=0.4 and α=15°

5.4.12 Normalized SIFs and G Distributions with respect to Normalized Time for ϕ=45° and α=30°

Figure 5.102 shows normalized mode I stress intensity factor, K_{In} with respect to normalized time, τ for a/t_1=0.2. From this figure it can be seen that the maximum values of K_{In}, which are 0.244, 0.151, 0.144 and 0.128, are obtained at $\tau \cong 0.004$, 0.008, 0.021 and 0.019 for MR, LN, CR and H coatings, respectively. In Figure 5.103, K_{In} distributions with respect to τ are given for a/t_1=0.4. In this case, the maximum values of K_{In}, which are 0.062, 0.052, 0.053 and 0.038, are obtained at $\tau \cong 0.008$, 0.012, 0.048 and 0.048 for MR, LN, CR and H coatings, respectively.

Figure 5.104 depicts normalized mode II stress intensity factor, K_{IIn} with respect to normalized time, τ for a/t_1=0.2. From this figure it can be observed that the maximum values of K_{IIn}, which are -0.068, -0.028, 0.034 and 0.028, are obtained

at $\tau \cong 0.261$, 0.421, 0.029 and 0.029 for MR, LN, CR and H coatings, respectively. In Figure 5.105, K_{IIn} distributions with respect to τ are given for a/t_1=0.4. In this case, the maximum values of K_{IIn}, which are -0.031, -0.027, -0.017 and -0.018, are obtained at $\tau \cong 0.256$, 0.340, 0.008 and 0.008 for MR, LN, CR and H coatings, respectively.

In Figure 5.106, normalized mode III stress intensity factor, K_{IIIn} with respect to normalized time, τ for $a/t_1=0.2$ is given. From this figure it can be seen that the maximum values of K_{IIIn}, which are -0.062, -0.030, -0.029 and -0.027, are obtained at $\tau \cong 0.005$, 0.009, 0.019 and 0.019 for MR, LN, CR and H coatings, respectively. In Figure 5.107, K_{IIIn} distributions with respect to τ are given for a/t_1=0.4. In this case, the maximum values of K_{IIIn}, which are -0.035, -0.014, -0.015 and -0.013, are obtained at $\tau \cong 0.012$, 0.024, 0.068 and 0.076 for MR, LN, CR and H coatings, respectively.

The normalized energy release rate, G_n distributions with respect to normalized time, τ for a/t_1=0.2 are presented in Figure 5.108. It can be observed from this figure that the maximum values of G_n, which are 0.023, 0.016, 0.023 and 0.018, are obtained at $\tau \cong 0.261$, 0.008, 0.019 and 0.019 for MR, LN, CR and H coatings, respectively. In the case of a/t_1=0.4, as it can be seen in Figure 5.109, the maximum values of G_n, which are 0.0085, 0.0051, 0.0031 and 0.0017, are obtained at $\tau \cong 0.300$, 0.444, 0.048 and 0.044 for MR, LN, CR and H coatings, respectively. In Figure 5.110, the normalized temperature with respect to normalized time is shown.

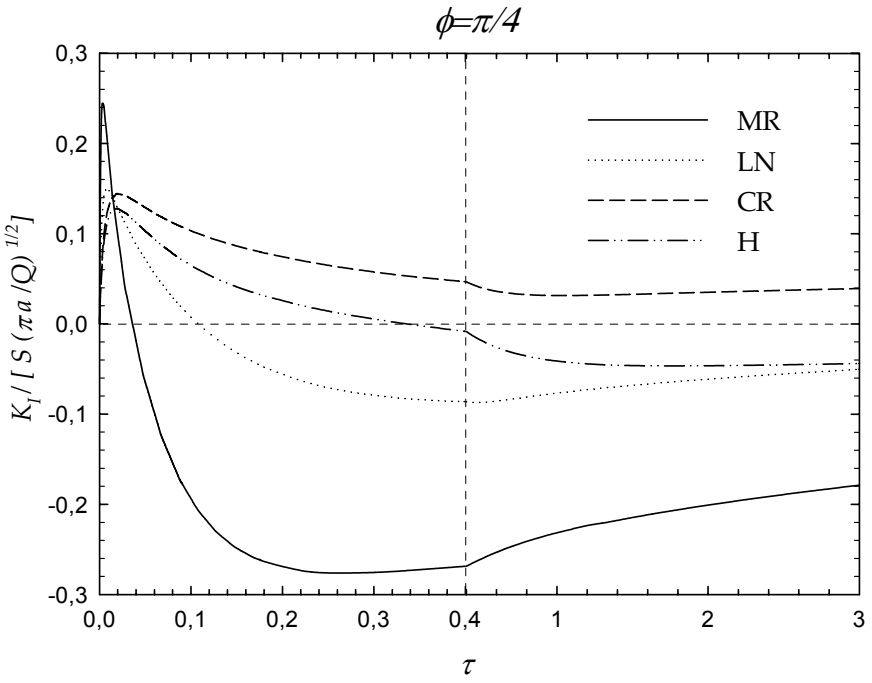

Figure 5.102 Normalized mode I stress intensity factors at 45^o crack front angle with respect to normalized time, a/t_1=0.2 and α=30^o

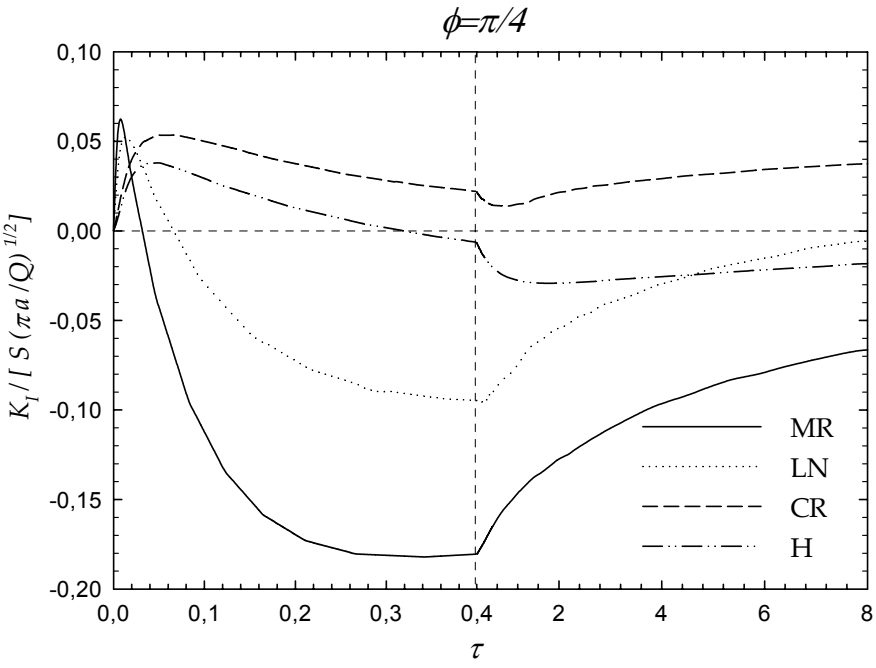

Figure 5.103 Normalized mode I stress intensity factors at 45^o crack front angle with respect to normalized time, a/t_1=0.4 and α=30^o

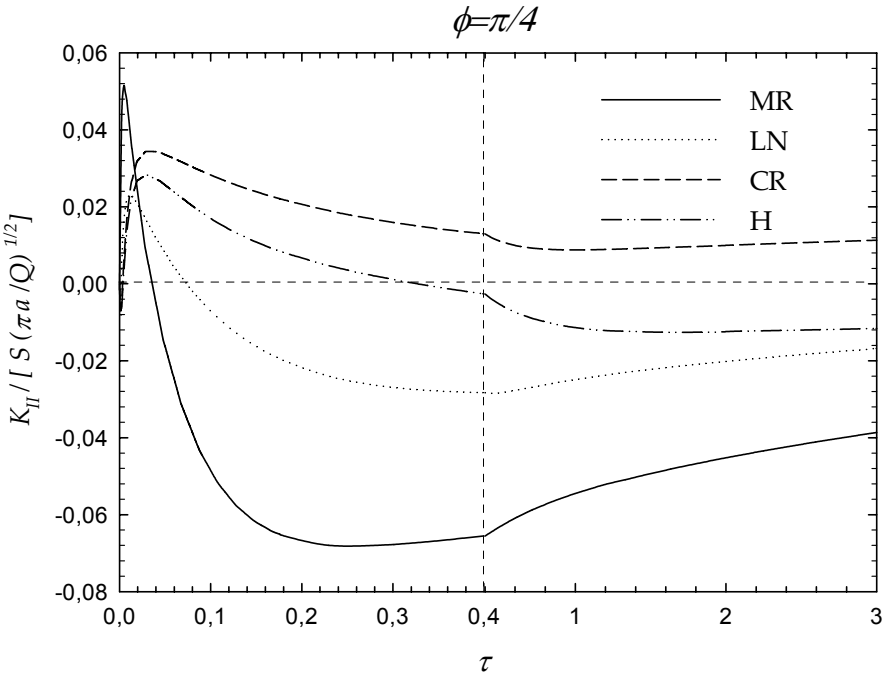

Figure 5.104 Normalized mode II stress intensity factors at 45^{o} crack front angle with respect to normalized time, a/t_1=0.2 and α=30^{o}

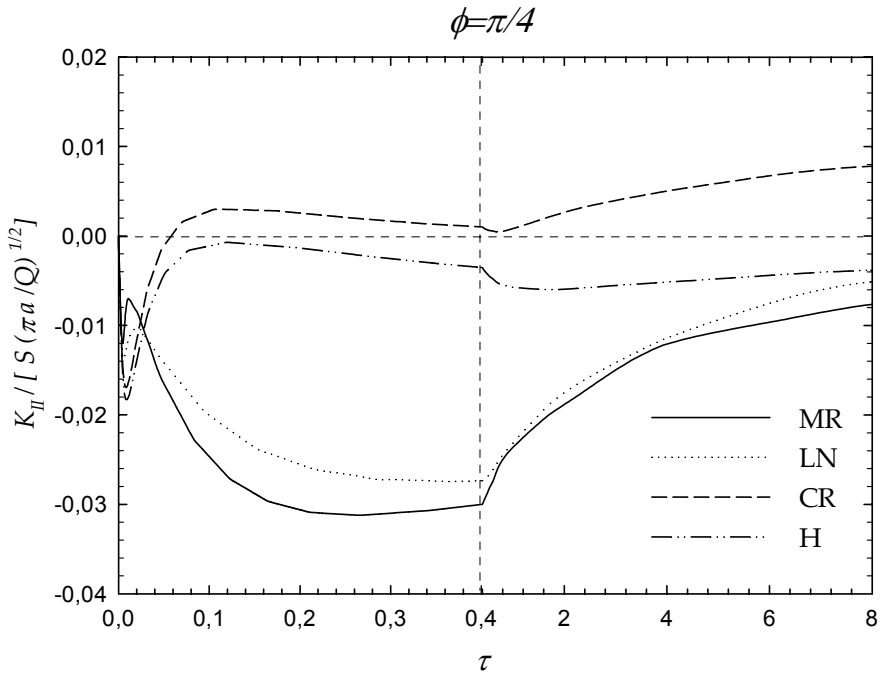

Figure 5.105 Normalized mode II stress intensity factors at 45^{o} crack front angle with respect to normalized time, a/t_1=0.4 and α=30^{o}

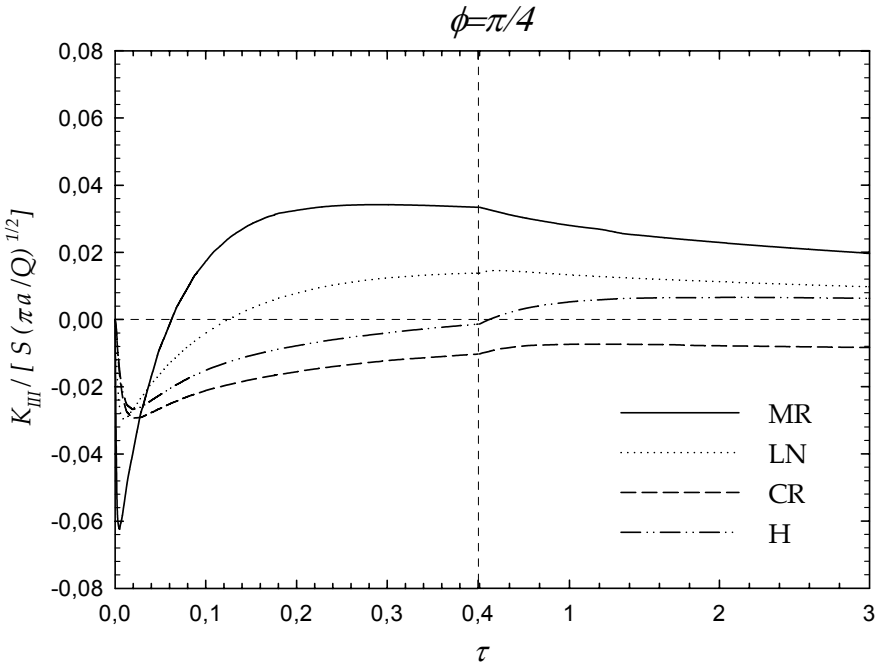

Figure 5.106 Normalized mode III stress intensity factors at 45° crack front angle with respect to normalized time, a/t_1=0.2 and α=30°

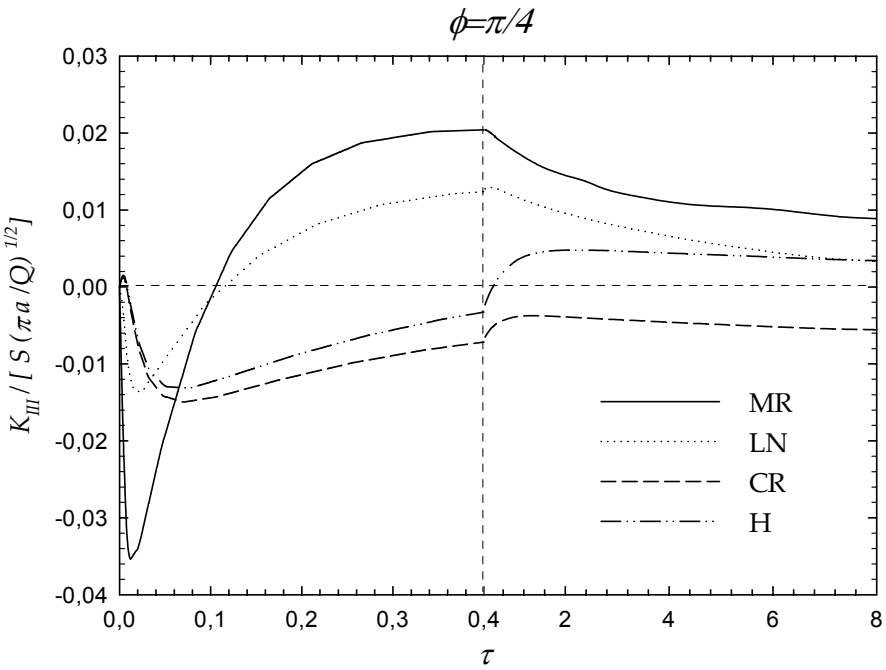

Figure 5.107 Normalized mode III stress intensity factors at 45° crack front angle with respect to normalized time, a/t_1=0.4 and α=30°

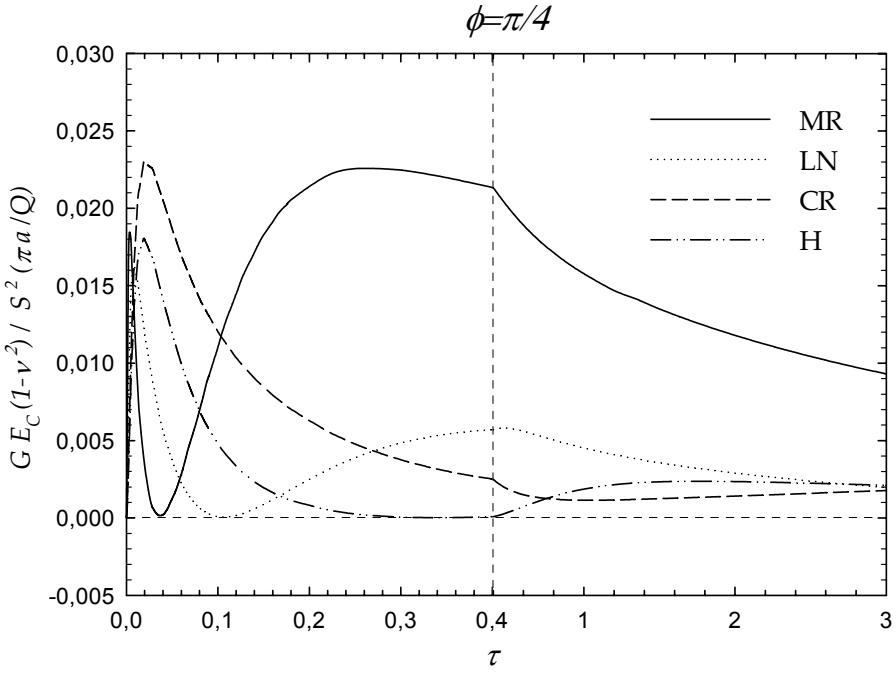

Figure 5.108 Normalized energy release rate at 45° crack front angle with respect to normalized time, a/t_1=0.2 and α=30°

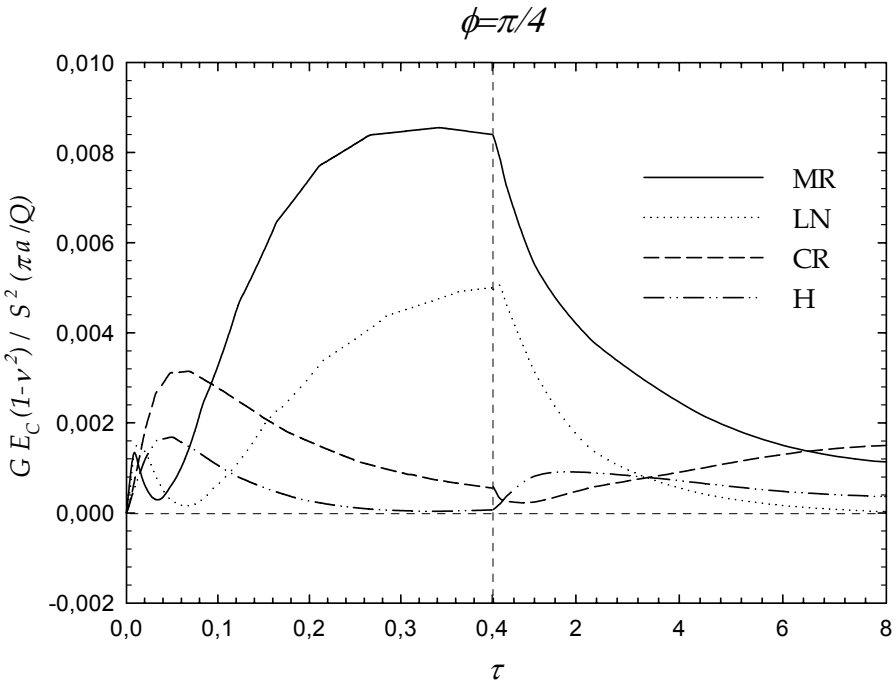

Figure 5.109 Normalized energy release rate at 45° crack front angle with respect to normalized time, a/t_1=0.4 and α=30°

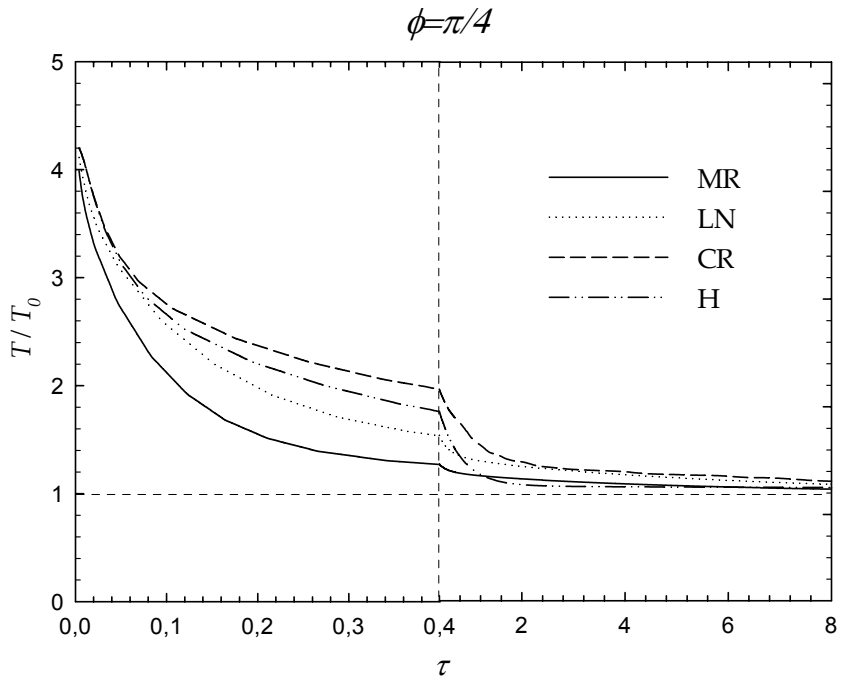

Figure 5.110 Normalized temperature at 45° crack front angle with respect to normalized time, a/t_1=0.4 and α=30°

5.4.13 Normalized SIFs and G Distributions with respect to Normalized Time for ϕ=45° and α=45°

Figure 5.111 shows normalized mode I stress intensity factor, K_{In} with respect to normalized time, τ for a/t_1=0.2. From this figure it can be seen that the maximum values of K_{In}, which are 0.197, 0.141, 0.135 and 0.121, are obtained at $\tau \cong 0.006$, 0.008, 0.019 and 0.013 for MR, LN, CR and H coatings, respectively. In Figure 5.112, K_{In} distributions with respect to τ are given for a/t_1=0.4. In this case, the maximum values of K_{In}, which are 0.075, 0.064, 0.062 and 0.051, are obtained at $\tau \cong 0.008$, 0.012, 0.032 and 0.032 for MR, LN, CR and H coatings, respectively.

Figure 5.113 depicts normalized mode II stress intensity factor, K_{IIn} with respect to normalized time, τ for a/t_1=0.2. From this figure it can be observed that the maximum values of K_{IIn}, which are -0.085, 0.039, 0.053 and 0.045, are obtained

at $\tau \cong 0.261$, 0.012, 0.033 and 0.020 for MR, LN, CR and H coatings, respectively. In Figure 5.114, K_{IIn} distributions with respect to τ are given for a/t_1=0.4. In this case, the maximum values of K_{IIn}, which are -0.062, -0.037, -0.013 and -0.015, are obtained at $\tau \cong 0.268$, 0.384, 0.008 and 0.008 for MR, LN, CR and H coatings, respectively.

In Figure 5.115, normalized mode III stress intensity factor, K_{IIIn} with respect to normalized time, τ for a/t_1=0.2 is given. From this figure it can be seen that the maximum values of K_{IIIn}, which are -0.089, -0.044 -0.043 and -0.042, are obtained at $\tau \cong 0.004$, 0.008, 0.019 and 0.019 for MR, LN, CR and H coatings, respectively. In Figure 5.116, K_{IIIn} distributions with respect to τ are given for a/t_1=0.4. In this case, the maximum values of K_{IIIn}, which are -0.056, -0.026, -0.025 and -0.023, are obtained at $\tau \cong 0.012$, 0.020, 0.048 and 0.052 for MR, LN, CR and H coatings, respectively.

The normalized energy release rate, G_n distributions with respect to normalized time, τ for a/t_1=0.2 are presented in Figure 5.117. It can be observed from this figure that the maximum values of G_n, which are 0.018, 0.017, 0.023 and 0.019, are obtained at $\tau \cong 0.003$, 0.008, 0.019 and 0.013 for MR, LN, CR and H coatings, respectively. In the case of a/t_1=0.4, as it can be seen in Figure 5.118, the maximum values of G_n, which are 0.0082, 0.0048, 0.0048 and 0.0032, are obtained at $\tau \cong 0.340$, 0.504, 0.048 and 0.032 for MR, LN, CR and H coatings, respectively. In Figure 5.119, the normalized temperature with respect to normalized time is shown.

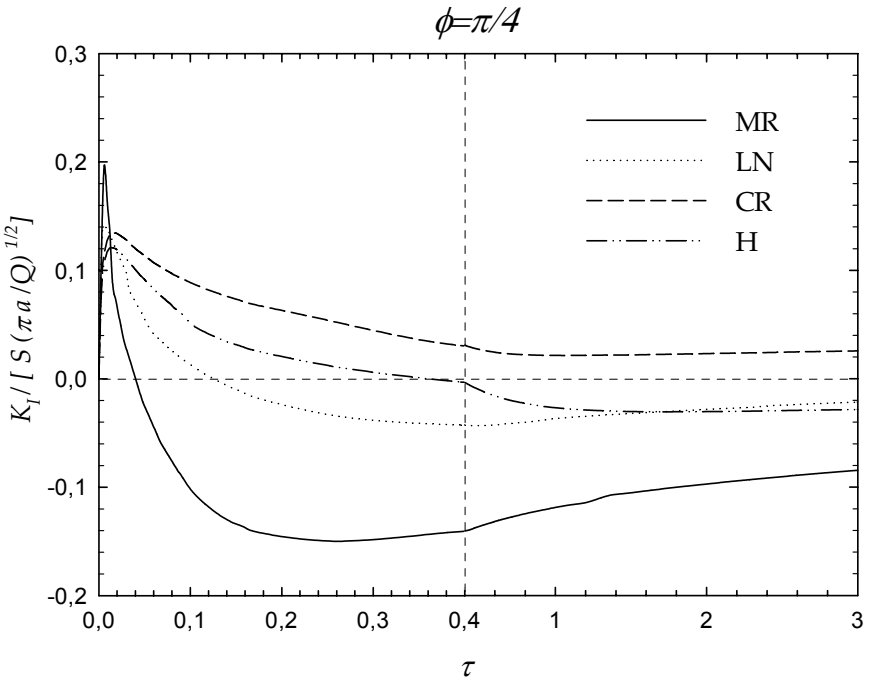

Figure 5.111 Normalized mode I stress intensity factors at 45° crack front angle with respect to normalized time, a/t_1=0.2 and α=45°

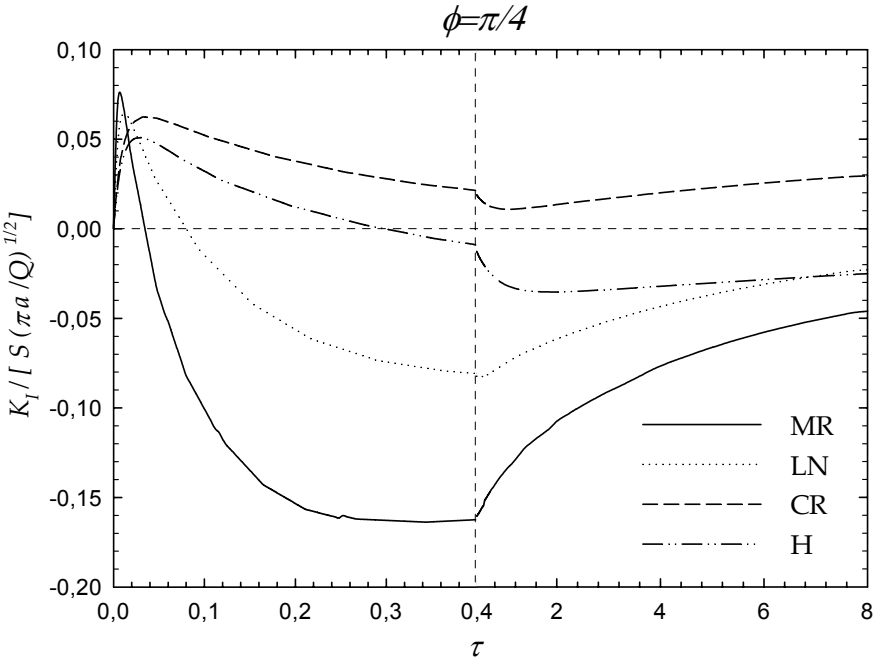

Figure 5.112 Normalized mode I stress intensity factors at 45° crack front angle with respect to normalized time, a/t_1=0.4 and α=45°

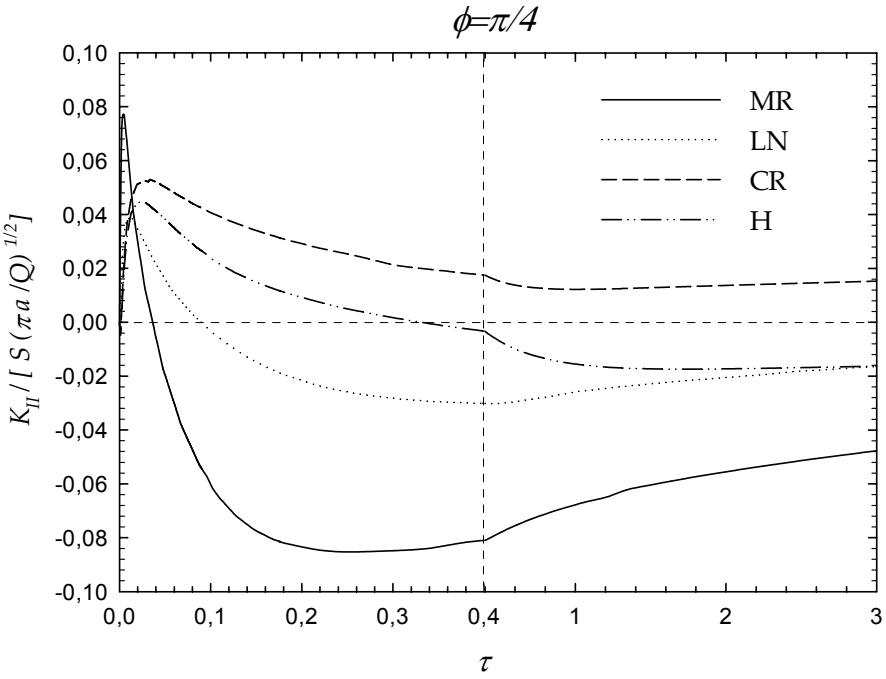

Figure 5.113 Normalized mode II stress intensity factors at 45° crack front angle with respect to normalized time, a/t_1=0.2 and α=45°

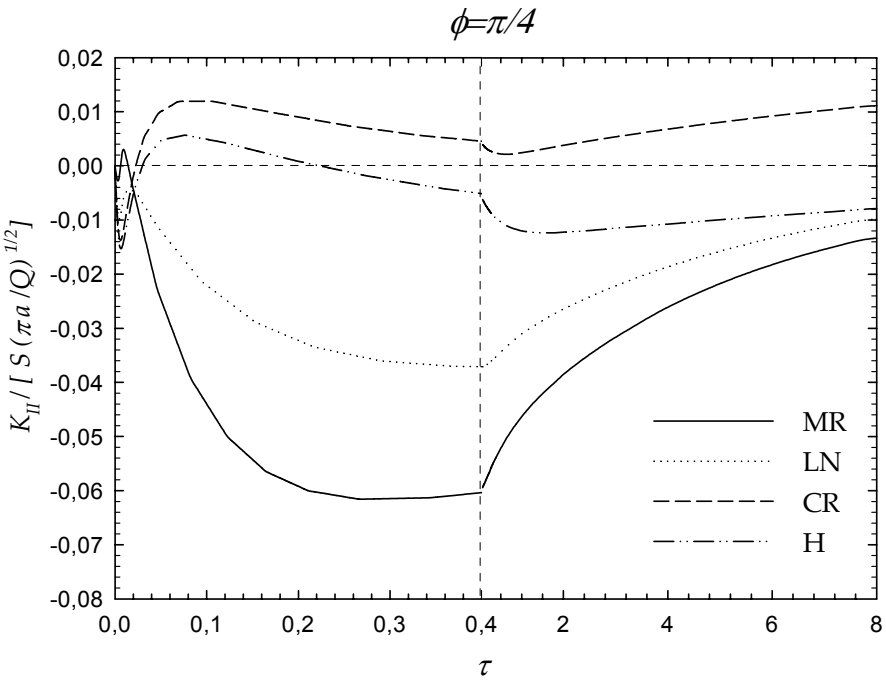

Figure 5.114 Normalized mode II stress intensity factors at 45° crack front angle with respect to normalized time, a/t_1=0.4 and α=45°

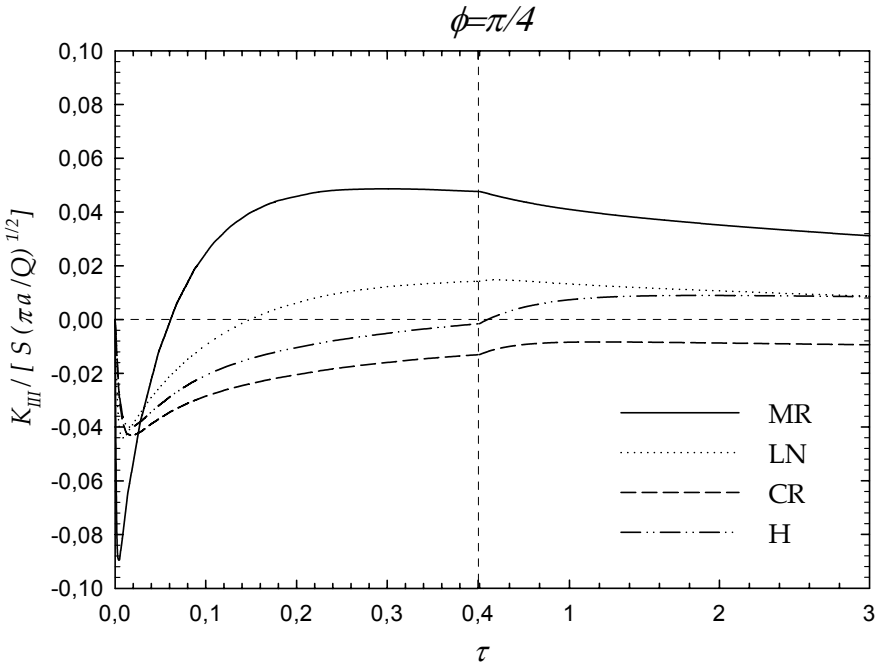

Figure 5.115 Normalized mode III stress intensity factors at 45° crack front angle with respect to normalized time, a/t_1=0.2 and α=45°

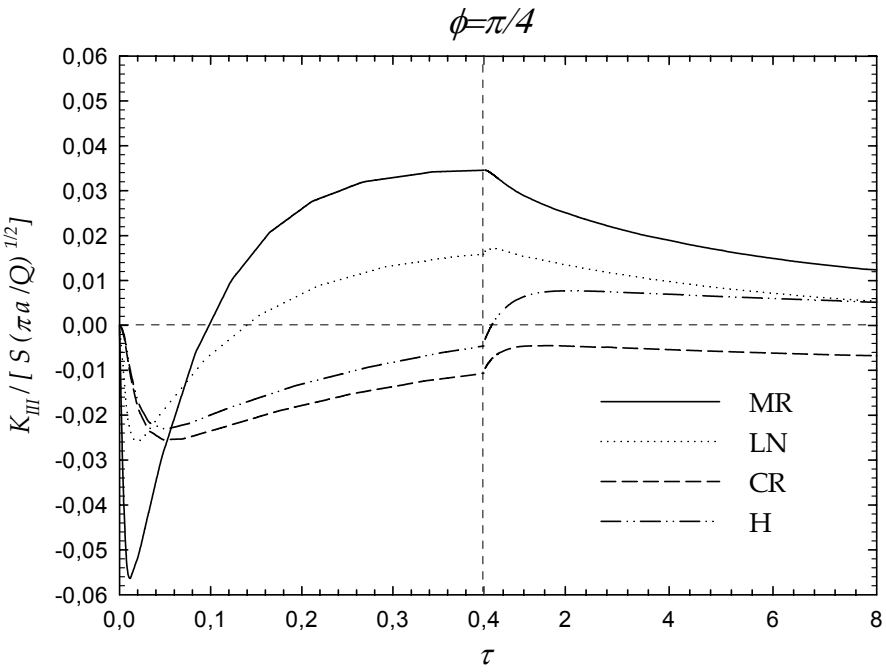

Figure 5.116 Normalized mode III stress intensity factors at 45° crack front angle with respect to normalized time, a/t_1=0.4 and α=45°

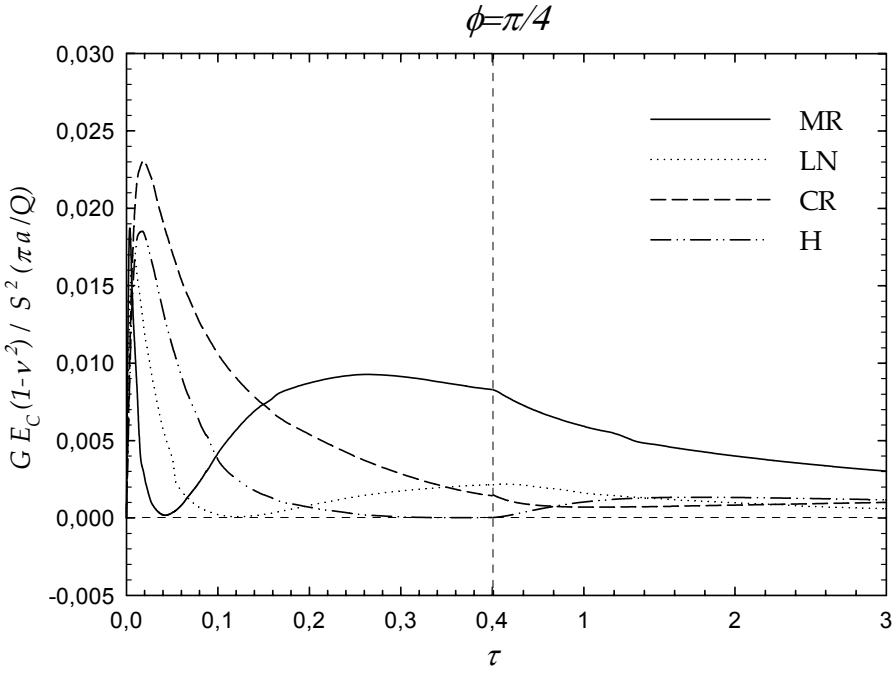

Figure 5.117 Normalized energy release rate at 45° crack front angle with respect to normalized time, a/t_1=0.2 and α=45°

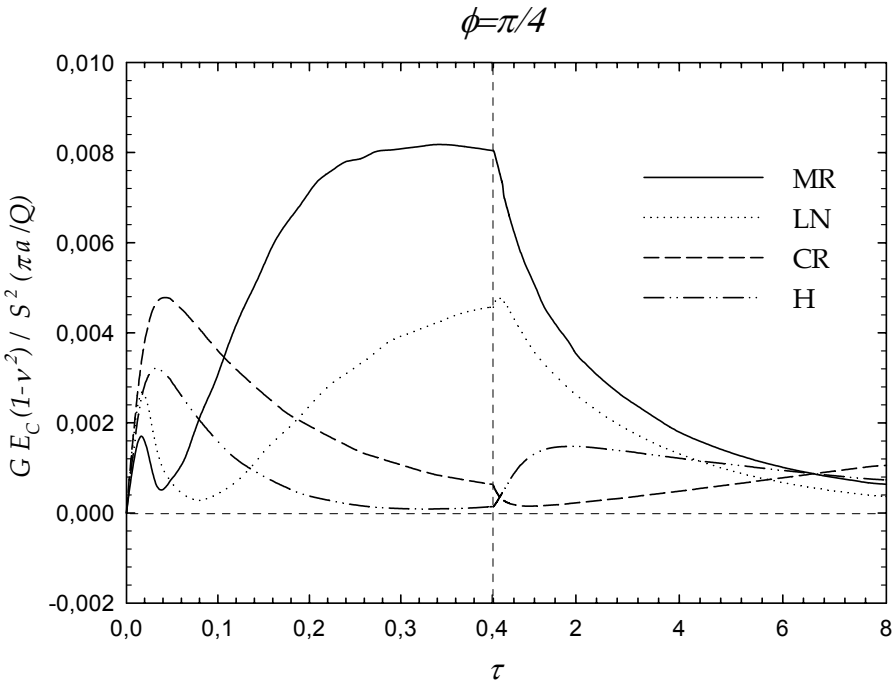

Figure 5.118 Normalized energy release rate at 45° crack front angle with respect to normalized time, a/t_1=0.4 and α=45°

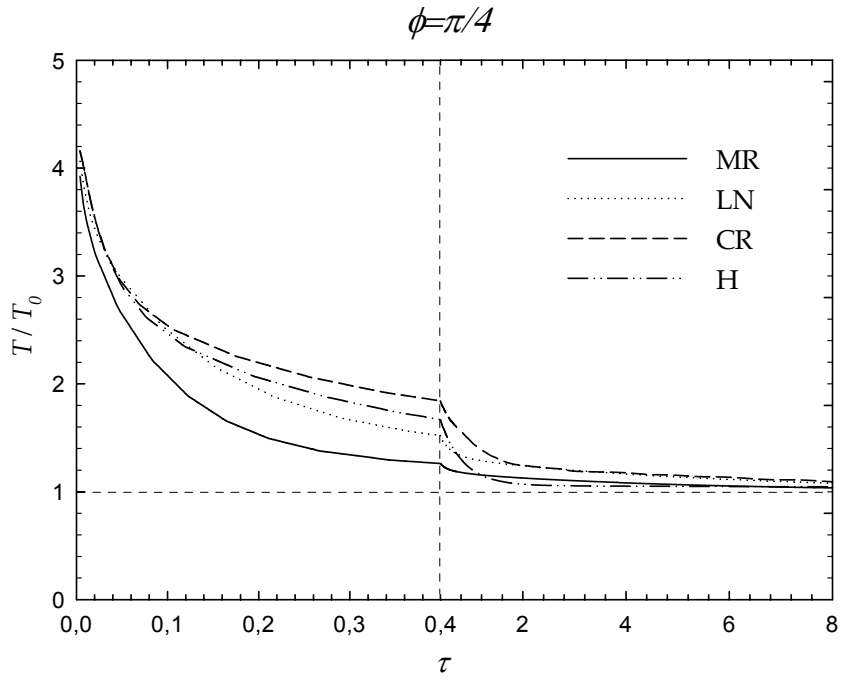

Figure 5.119 Normalized temperature at 45° crack front angle with respect to normalized time, a/t_1=0.4 and α=45°

5.4.14 Normalized SIFs and G Distributions with respect to Normalized Time for ϕ=45° and α=60°

Figure 5.120 shows normalized mode I stress intensity factor, K_{In} with respect to normalized time, τ for a/t_1=0.2. From this figure it can be seen that the maximum values of K_{In}, which are 0.160, 0.113, 0.108 and 0.100, are obtained at $\tau \cong 0.003$, 0.006, 0.012 and 0.010 for MR, LN, CR and H coatings, respectively. In Figure 5.121, K_{In} distributions with respect to τ are given for a/t_1=0.4. In this case, the maximum values of K_{In}, which are 0.066, 0.067, 0.064 and 0.057, are obtained at $\tau \cong 0.008$, 0.012, 0.020 and 0.016 for MR, LN, CR and H coatings, respectively.

Figure 5.122 depicts normalized mode II stress intensity factor, K_{IIn} with respect to normalized time, τ for a/t_1=0.2. From this figure it can be observed that the maximum values of K_{IIn}, which are -0.109, 0.055, 0.068 and 0.061, are obtained

at $\tau \cong 0.261$, 0.008, 0.019 and 0.019 for MR, LN, CR and H coatings, respectively. In Figure 5.123, K_{IIn} distributions with respect to τ are given for a/t_1=0.4. In this case, the maximum values of K_{IIn}, which are -0.089, -0.040, 0.028 and 0.021, are obtained at $\tau \cong 0.332$, 0.444, 0.048 and 0.048 for MR, LN, CR and H coatings, respectively.

In Figure 5.124, normalized mode III stress intensity factor, K_{IIIn} with respect to normalized time, τ for a/t_1=0.2 is given. From this figure it can be seen that the maximum values of K_{IIIn}, which are -0.10, -0.05 -0.047 and -0.048, are obtained at $\tau \cong 0.003$, 0.008, 0.013 and 0.013 for MR, LN, CR and H coatings, respectively. In Figure 5.125, K_{IIIn} distributions with respect to τ are given for a/t_1=0.4. In this case, the maximum values of K_{IIIn}, which are -0.074, -0.036, -0.035 and -0.033, are obtained at $\tau \cong 0.012$, 0.016, 0.032 and 0.032 for MR, LN, CR and H coatings, respectively.

The normalized energy release rate, G_n distributions with respect to normalized time, τ for a/t_1=0.2 are presented in Figure 5.126. It can be observed from this figure that the maximum values of G_n, which are 0.015, 0.006, 0.013 and 0.013, are obtained at $\tau \cong 0.003$, 0.006, 0.013 and 0.013 for MR, LN, CR and H coatings, respectively. In the case of a/t_1=0.4, as it can be seen in Figure 5.127, the maximum values of G_n, which are 0.0081, 0.0040, 0.0062 and 0.0048, are obtained at $\tau \cong 0.324$, 0.012, 0.032 and 0.024 for MR, LN, CR and H coatings, respectively. In Figure 5.128, the normalized temperature with respect to normalized time is shown.

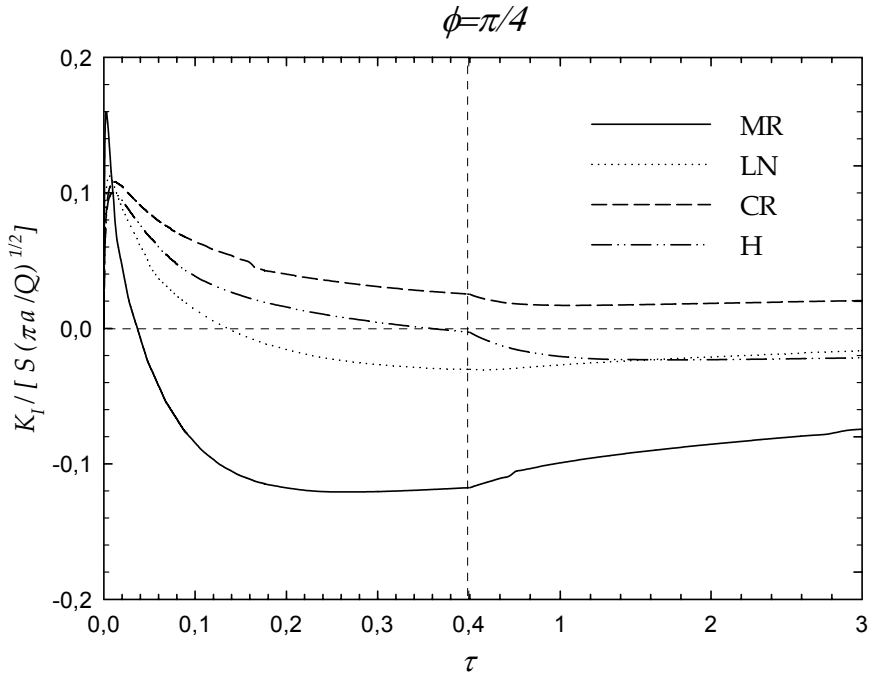

Figure 5.120 Normalized mode I stress intensity factors at 45^o crack front angle with respect to normalized time, a/t_1=0.2 and α=60^o

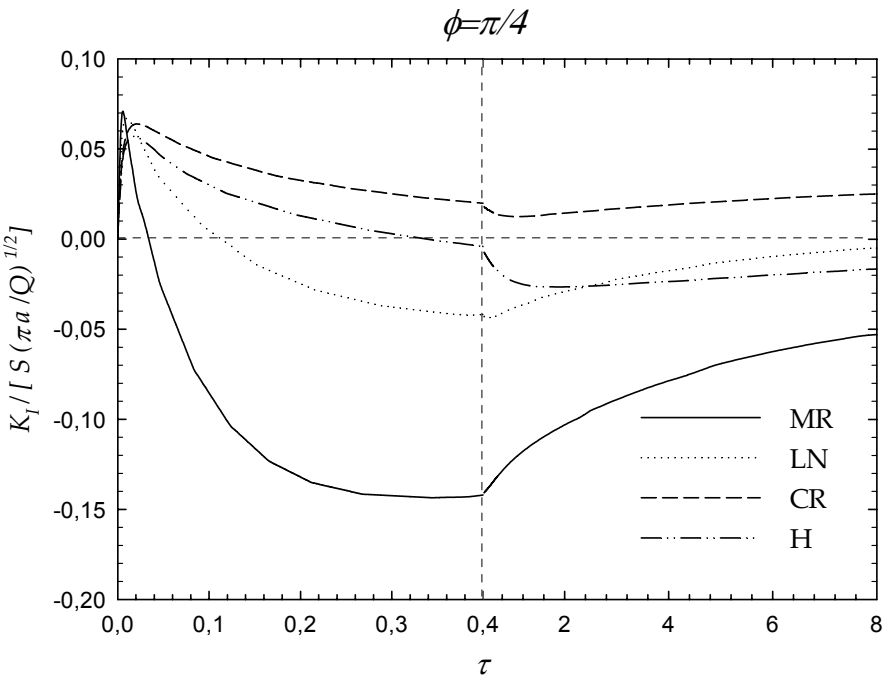

Figure 5.121 Normalized mode I stress intensity factors at 45^o crack front angle with respect to normalized time, a/t_1=0.4 and α=60^o

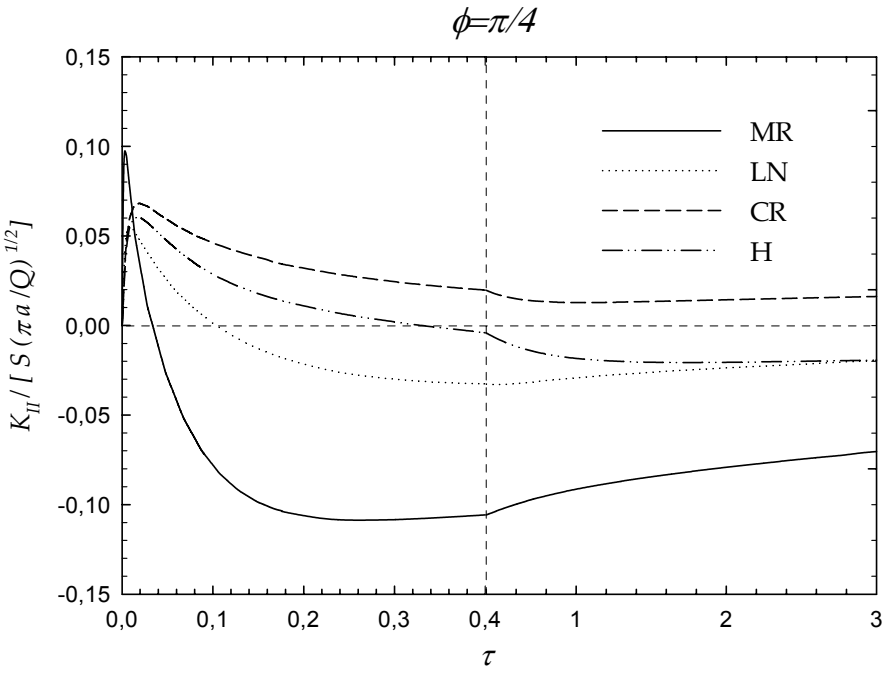

Figure 5.122 Normalized mode II stress intensity factors at 45° crack front angle with respect to normalized time, a/t_1=0.2 and α=60°

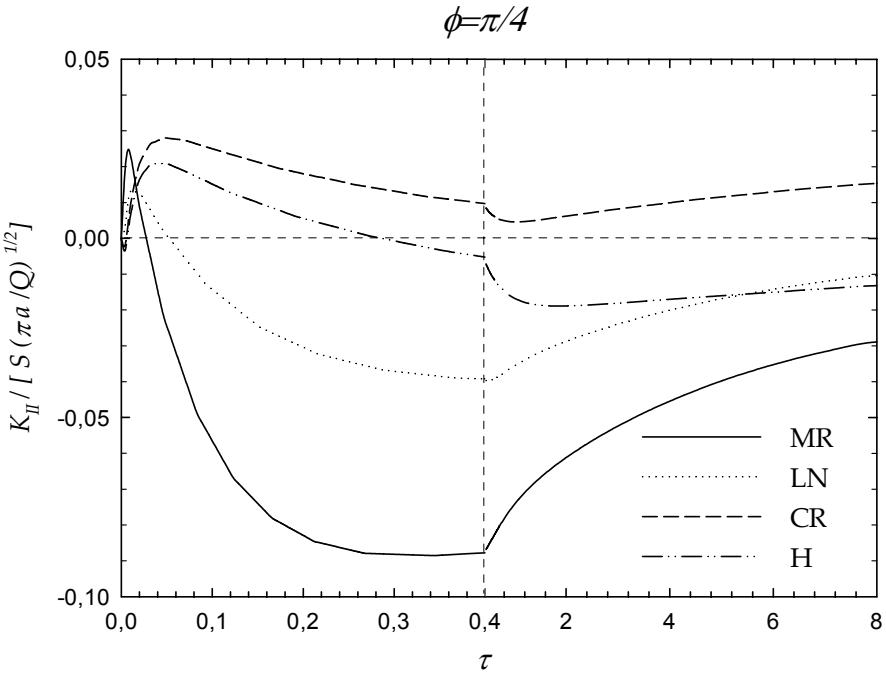

Figure 5.123 Normalized mode II stress intensity factors at 45° crack front angle with respect to normalized time, a/t_1=0.4 and α=60°

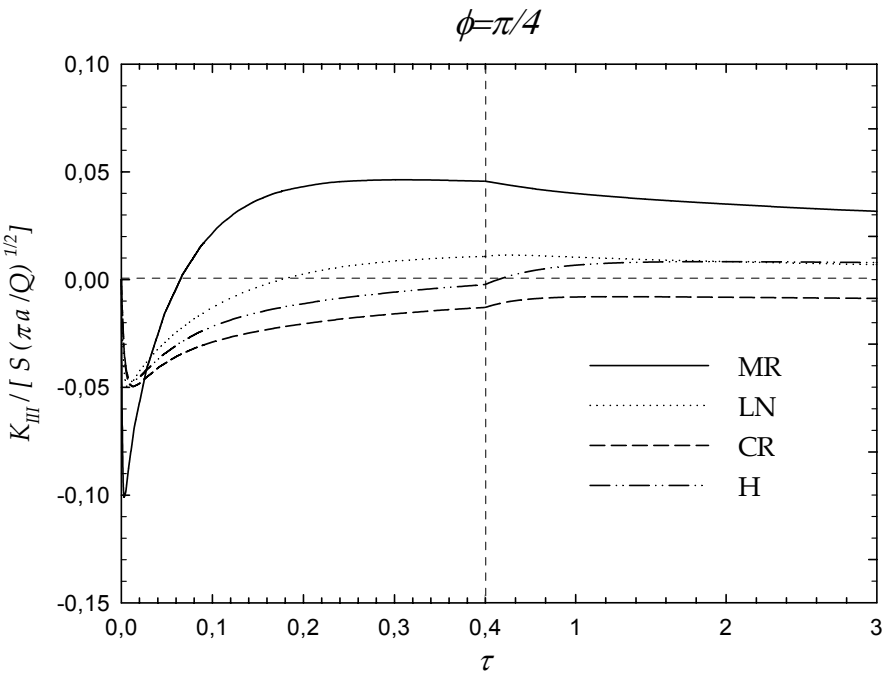

Figure 5.124 Normalized mode III stress intensity factors at 45° crack front angle with respect to normalized time, a/t_1=0.2 and α=60°

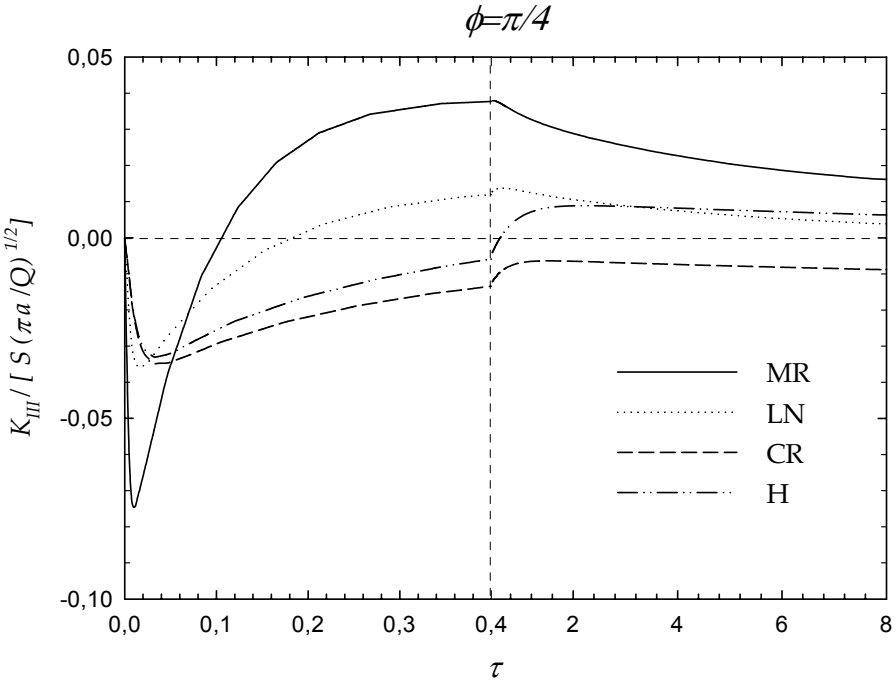

Figure 5.125 Normalized mode III stress intensity factors at 45° crack front angle with respect to normalized time, a/t_1=0.4 and α=60°

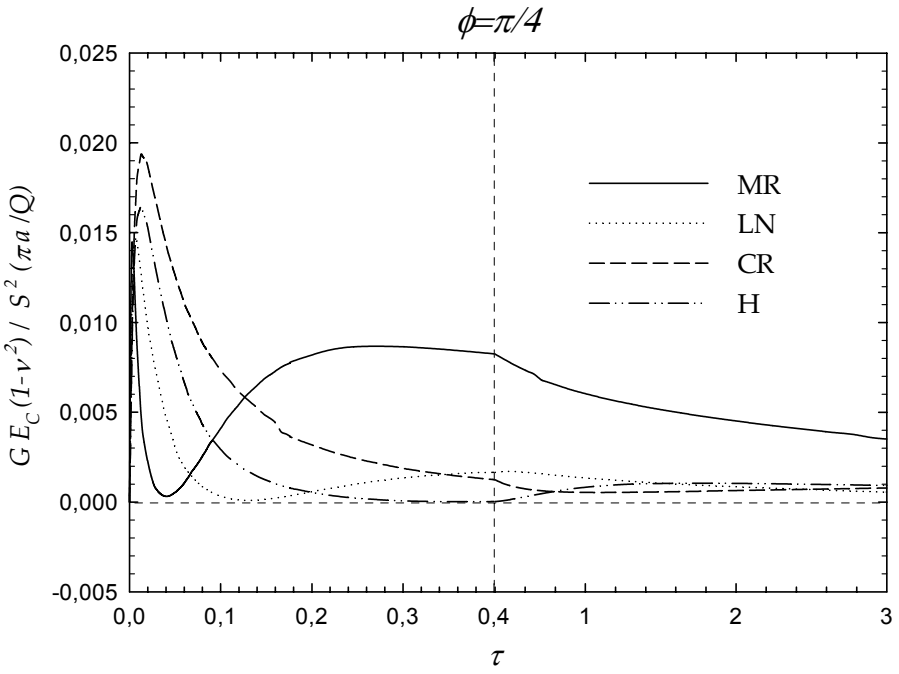

Figure 5.126 Normalized energy release rate at 45° crack front angle with respect to normalized time, a/t_1=0.2 and α=60°

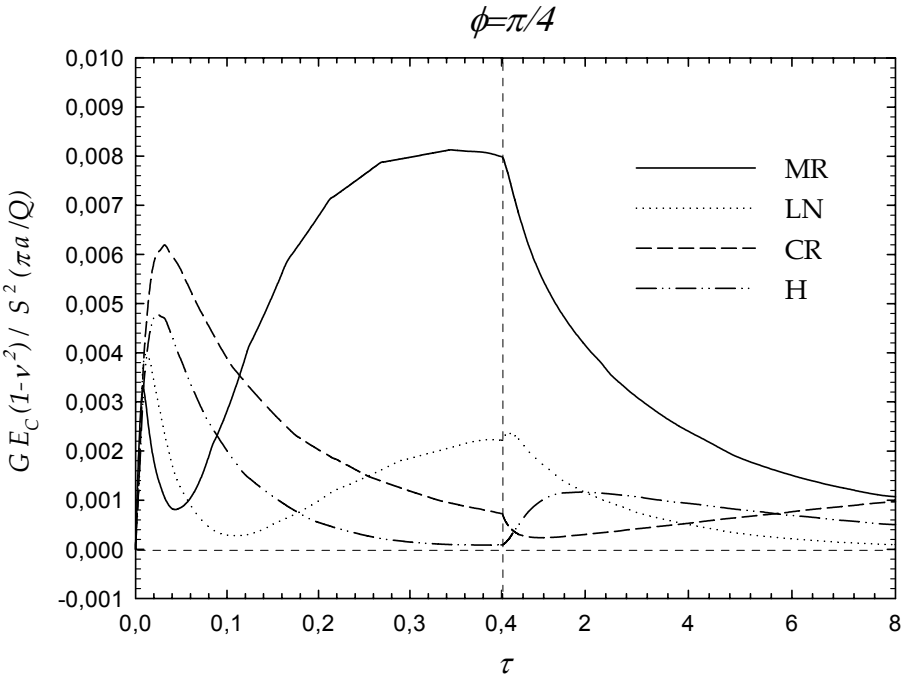

Figure 5.127 Normalized energy release rate at 45° crack front angle with respect to normalized time, a/t_1=0.4 and α=60°

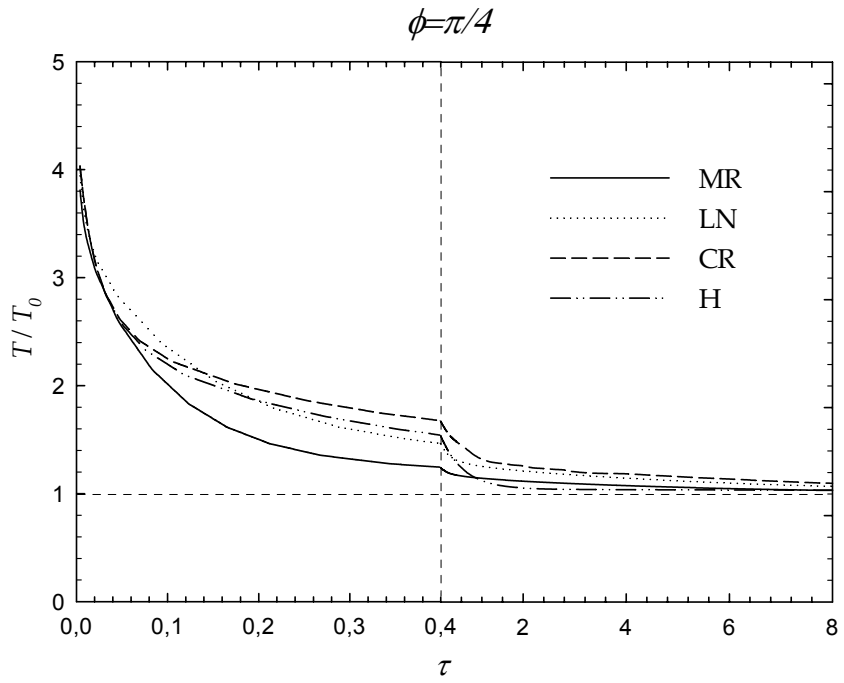

Figure 5.128 Normalized temperature at 45° crack front angle with respect to normalized time, a/t_1=0.4 and α=60°

5.4.15 Normalized SIFs and G Distributions with respect to Normalized Time for ϕ=90° and α=0°

Figure 5.129 shows normalized mode I stress intensity factor, K_{In} with respect to normalized time, τ for a/t_1=0.2. From this figure it can be seen that the maximum values of K_{In}, which are 0.197, 0.118, 0.111 and 0.085, are obtained at $\tau \cong 0.005$, 0.009, 0.042 and 0.029 for MR, LN, CR and H coatings, respectively. In Figure 5.130, K_{In} distributions with respect to τ is given for a/t_1=0.4. In this case, the maximum values of K_{In}, which are 0.036, 0.002, 0.023 and 0.009, are obtained at $\tau \cong 7{,}764$, 7,764, 7,764 and 7,764 for MR, LN, CR and H coatings, respectively.

The normalized energy release rate, G_n distributions with respect to normalized time, τ for a/t_1=0.2 is presented in Figure 5.131. It can be observed from this figure that the maximum values of G_n, which are 0.010, 0.008, 0.012 and 0.007,

are obtained at $\tau \cong 0.005$, 0.008, 0.040 and 0.030 for MR, LN, CR and H coatings, respectively. In the case of a/t_1=0.4, as it can be seen in Figure 5.132, the maximum values of G_n, which are 0.0003, 0.0014, 0.0005 and 0.0009, are obtained at $\tau \cong 7.764$, 0.360, 0.020 and 0.020 for MR, LN, CR and H coatings, respectively. In Figure 5.133, the normalized temperature with respect to normalized time is shown.

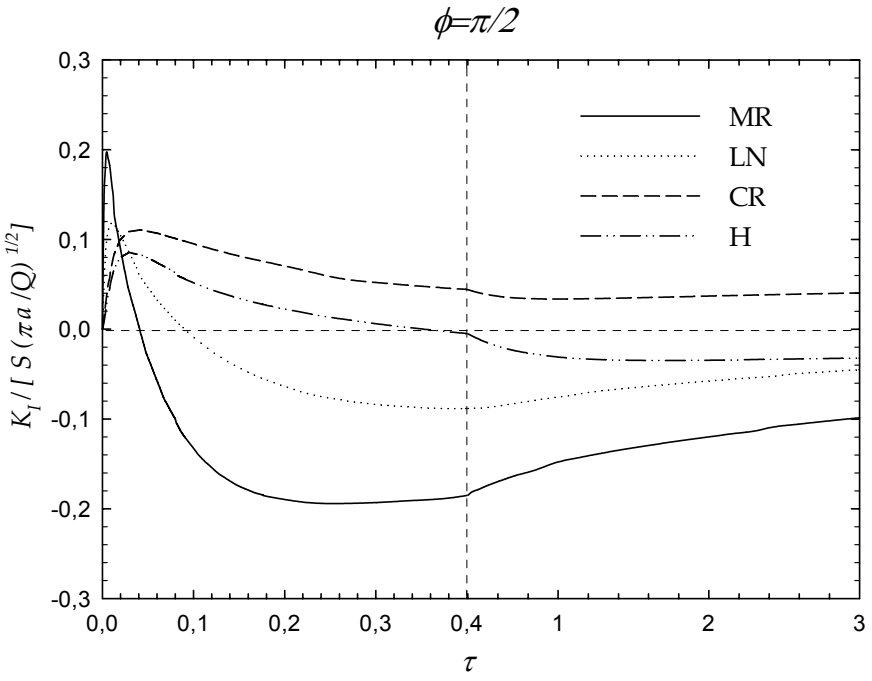

Figure 5.129 Normalized mode I stress intensity factors at 90° crack front angle with respect to normalized time, a/t_1=0.2 and α=0°

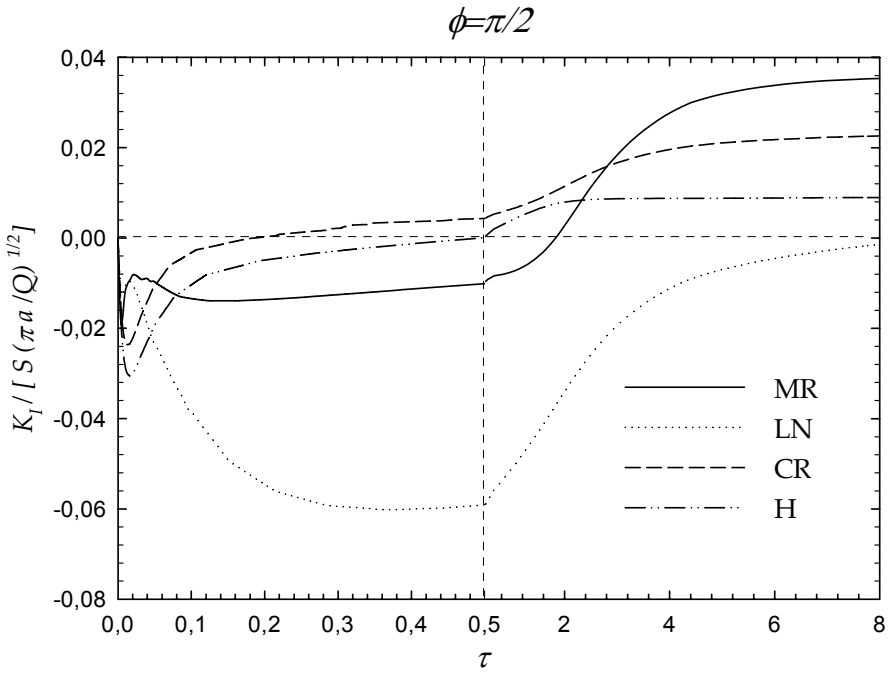

Figure 5.130 Normalized mode I stress intensity factors at 90° crack front angle with respect to normalized time, a/t_1=0.4 and α=0°

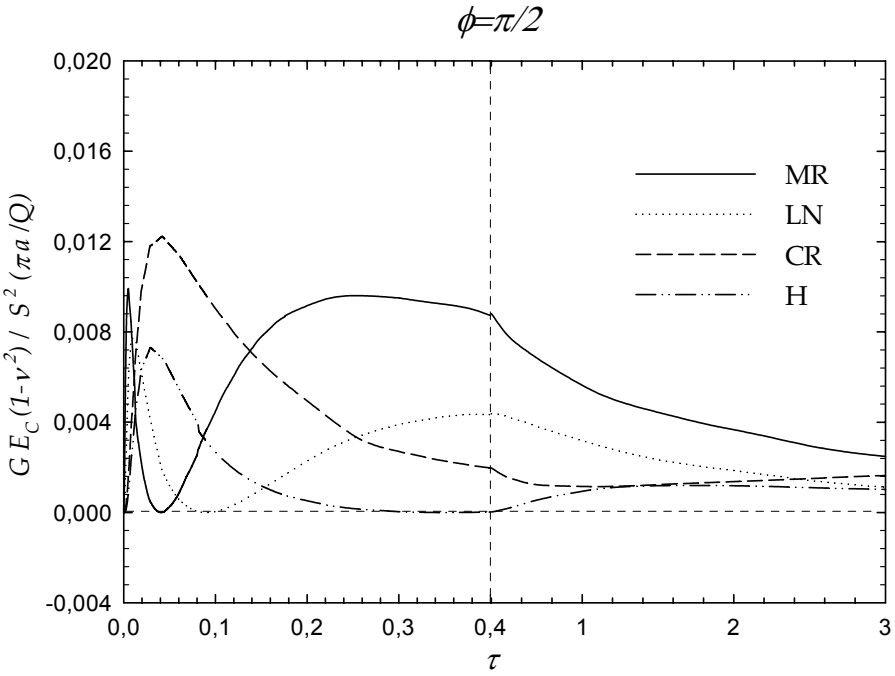

Figure 5.131 Normalized energy release rate at 90° crack front angle with respect to normalized time, a/t_1=0.2 and α=0°

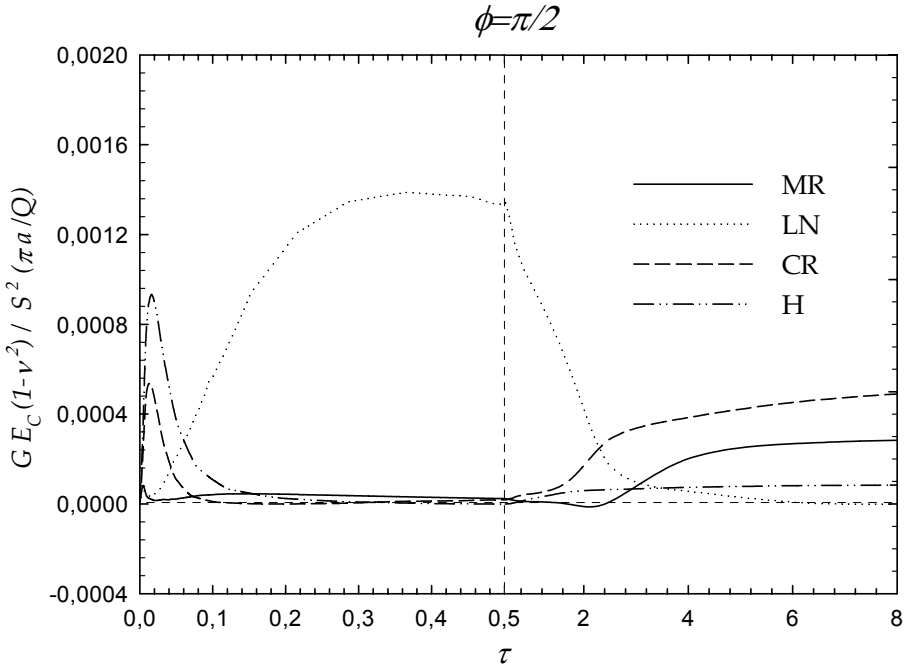

Figure 5.132 Normalized energy release rate at 90° crack front angle with respect to normalized time, a/t_1=0.4 and α=0°

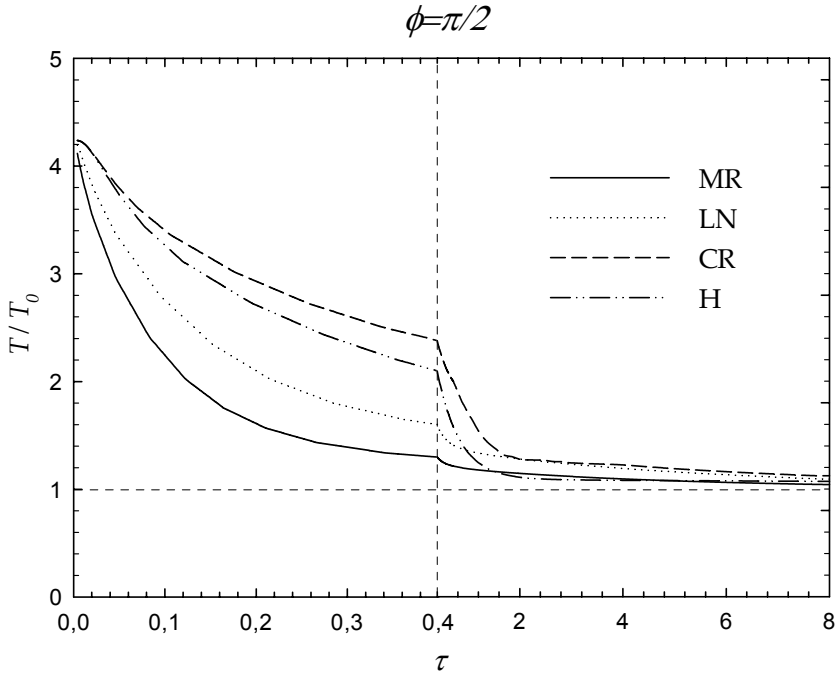

Figure 5.133 Normalized temperature at 90° crack front angle with respect to normalized time, a/t_1=0.4 and α=0°

5.4.16 Normalized SIFs and G Distributions with respect to Normalized Time for ϕ=90^o and α=15^o

Figure 5.134 shows normalized mode I stress intensity factor, K_{In} with respect to normalized time, τ for a/t_1=0.2. From this figure it can be seen that the maximum values of K_{In}, which are 0.199, 0.121, 0.111 and 0.088, are obtained at $\tau \cong 0.005$, 0.009, 0.041 and 0.029 for MR, LN, CR and H coatings, respectively. In Figure 5.135, K_{In} distributions with respect to τ are given for a/t_1=0.4. In this case, the maximum values of K_{In}, which are 0.005, 0.006, 0.022 and 0.003, are obtained at $\tau \cong 7{,}764$, 0.016, 7.764 and 7.764 for MR, LN, CR and H coatings, respectively.

Figure 5.136 depicts normalized mode II stress intensity factor, K_{IIn} with respect to normalized time, τ for a/t_1=0.2. From this figure it can be observed that the maximum values of K_{IIn}, which are -0.027, -0.016, 0.011 and 0.006, are obtained at $\tau \cong 0.261$, 0.381, 0.062 and 0.062 for MR, LN, CR and H coatings, respectively. In Figure 5.137, K_{IIn} distributions with respect to τ are given for a/t_1=0.4. In this case, the maximum values of K_{IIn}, which are 0.022, -0.018, -0.019 and -0.018, are obtained at $\tau \cong 0.424$, 0.012, 0.020 and 0.020 for MR, LN, CR and H coatings, respectively.

In Figure 5.138, normalized mode III stress intensity factor, K_{IIIn} with respect to normalized time, τ for a/t_1=0.2 is given. From this figure it can be seen that the maximum values of K_{IIIn}, which are -0.0011, -0.0010, -0.0008 and -0.0009, are obtained at $\tau \cong 0.221$, 0.301, 0.003 and 0.003 for MR, LN, CR and H coatings, respectively. In Figure 5.139, K_{IIIn} distributions with respect to τ are given for a/t_1=0.4. In this case, the maximum values of K_{IIIn}, which are -0.0017, -0.0015, -0.0015 and -0.0014, are obtained at $\tau \cong 0.008$, 0.012, 0.024 and 0.016 for MR, LN, CR and H coatings, respectively.

The normalized energy release rate, G_n distributions with respect to normalized time, τ for a/t_1=0.2 are presented in Figure 5.140. It can be observed from this

figure that the maximum values of G_n, which are 0.016, 0.008, 0.012 and 0.008, are obtained at $\tau \cong 0.261$, 0.009, 0.035 and 0.029 for MR, LN, CR and H coatings, respectively. In the case of a/t_1=0.4, as it can be seen in Figure 5.141, the maximum values of G_n, which are 0.0004, 0.0017, 0.0006 and 0.0009, are obtained at $\tau \cong 0.164$, 0.360, 0.012 and 0.012 for MR, LN, CR and H coatings, respectively. In Figure 5.142, the normalized temperature with respect to normalized time is shown.

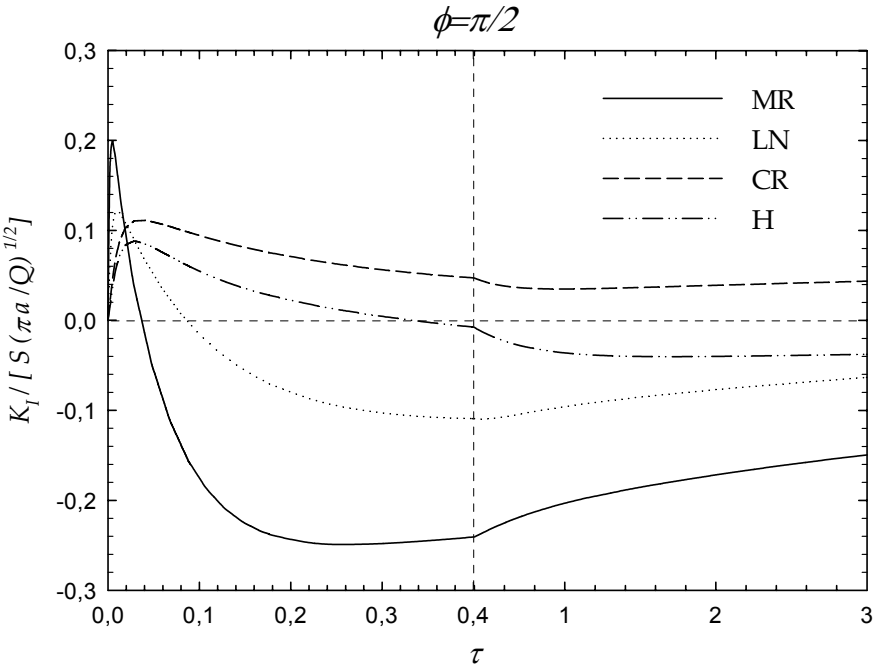

Figure 5.134 Normalized mode I stress intensity factors at 90° crack front angle with respect to normalized time, a/t_1=0.2 and α=15°

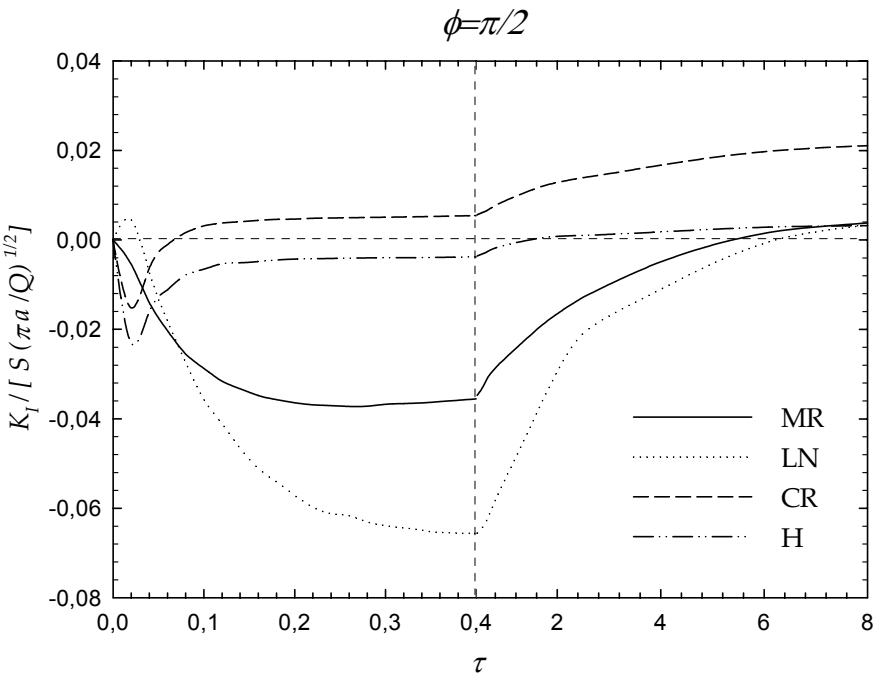

Figure 5.135 Normalized mode I stress intensity factors at 90° crack front angle with respect to normalized time, a/t_1=0.4 and α=15°

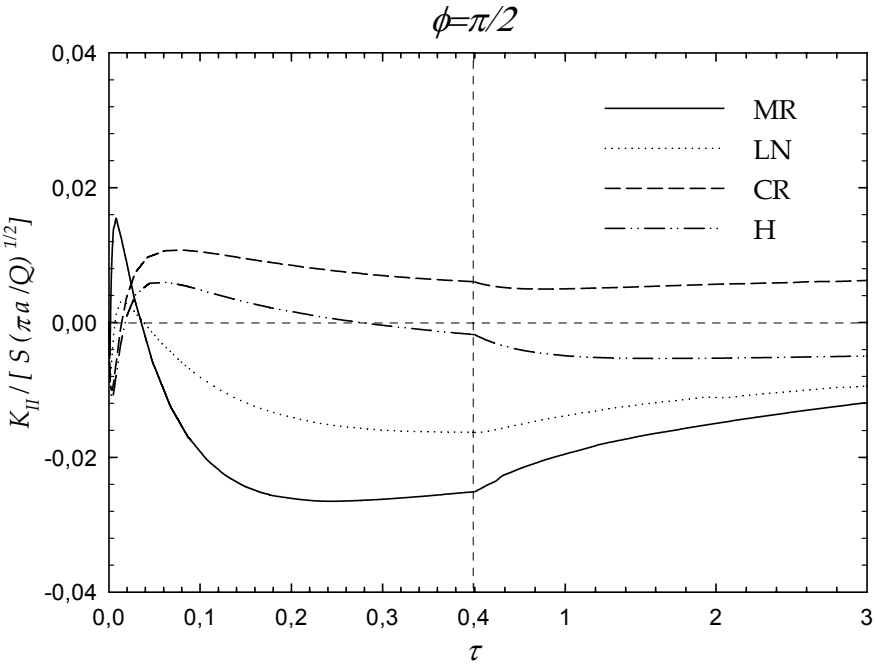

Figure 5.136 Normalized mode II stress intensity factors at 90° crack front angle with respect to normalized time, a/t_1=0.2 and α=15°

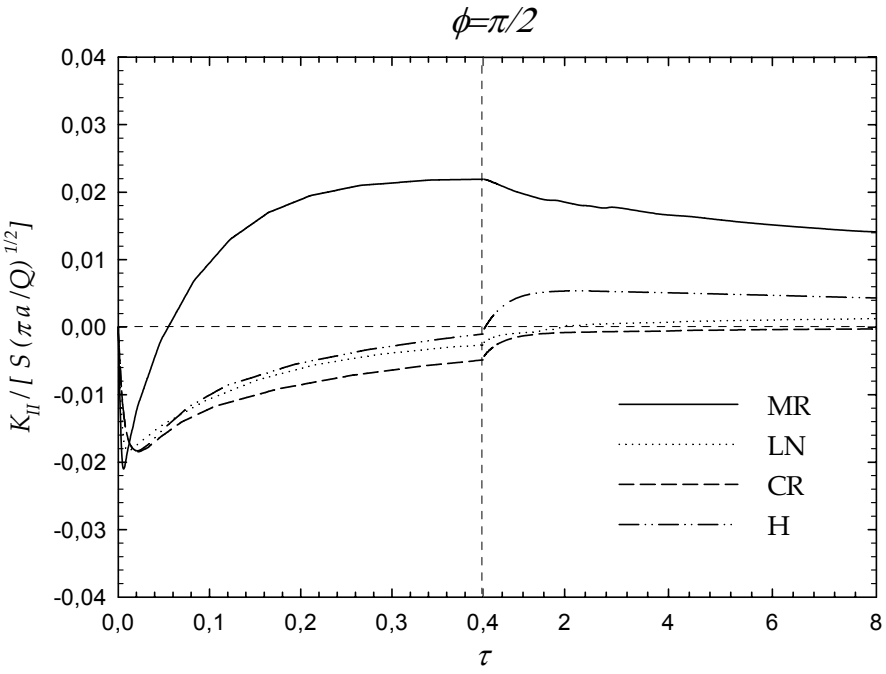

Figure 5.137 Normalized mode II stress intensity factors at 90° crack front angle with respect to normalized time, a/t_1=0.4 and α=15°

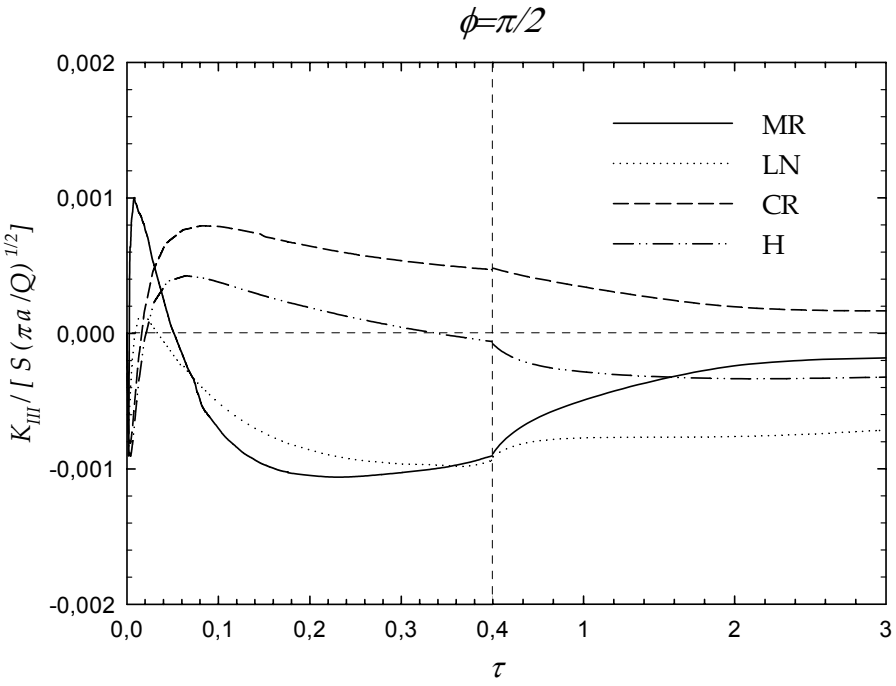

Figure 5.138 Normalized mode III stress intensity factors at 90° crack front angle with respect to normalized time, a/t_1=0.2 and α=15°

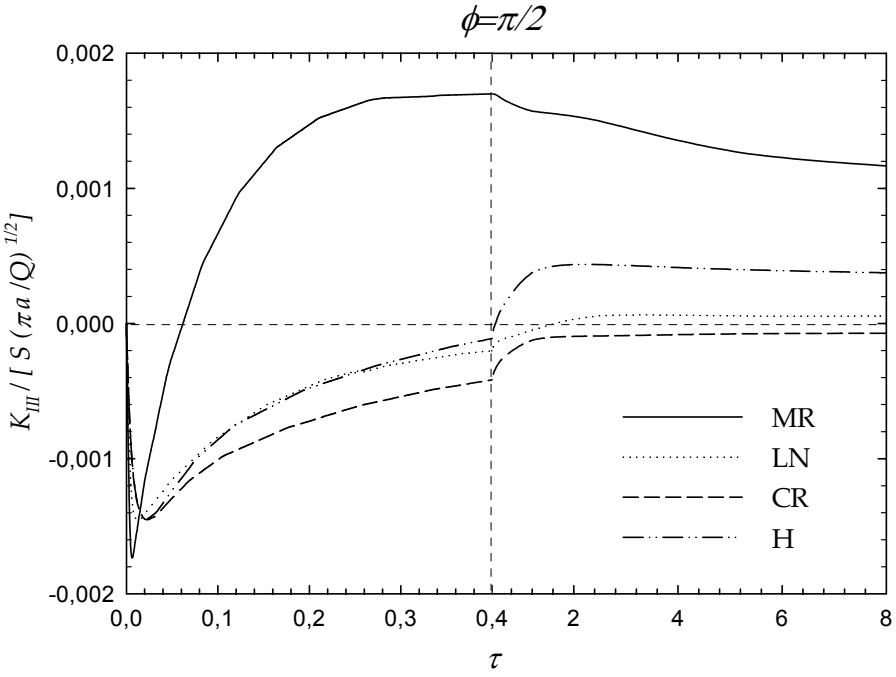

Figure 5.139 Normalized mode III stress intensity factors at 90° crack front angle with respect to normalized time, a/t_1=0.4 and α=15°

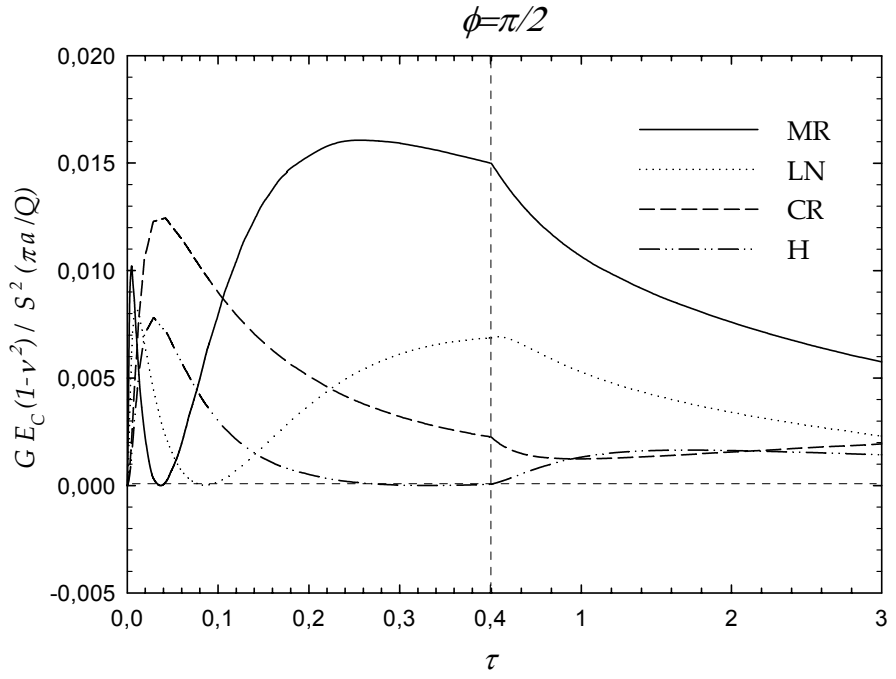

Figure 5.140 Normalized energy release rate at 90° crack front angle with respect to normalized time, a/t_1=0.2 and α=15°

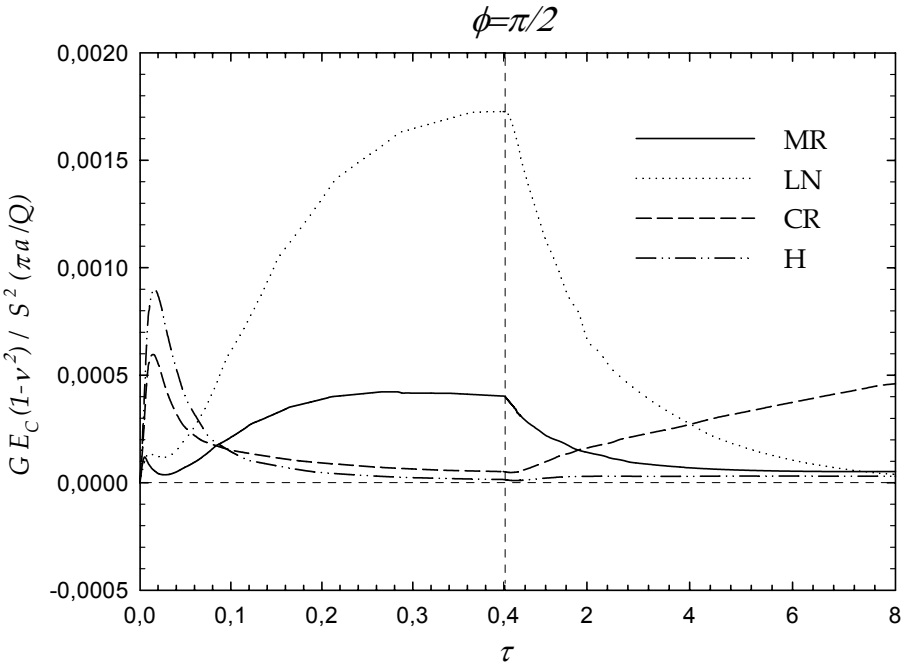

Figure 5.141 Normalized energy release rate at 90° crack front angle with respect to normalized time, a/t_1=0.4 and α=15°

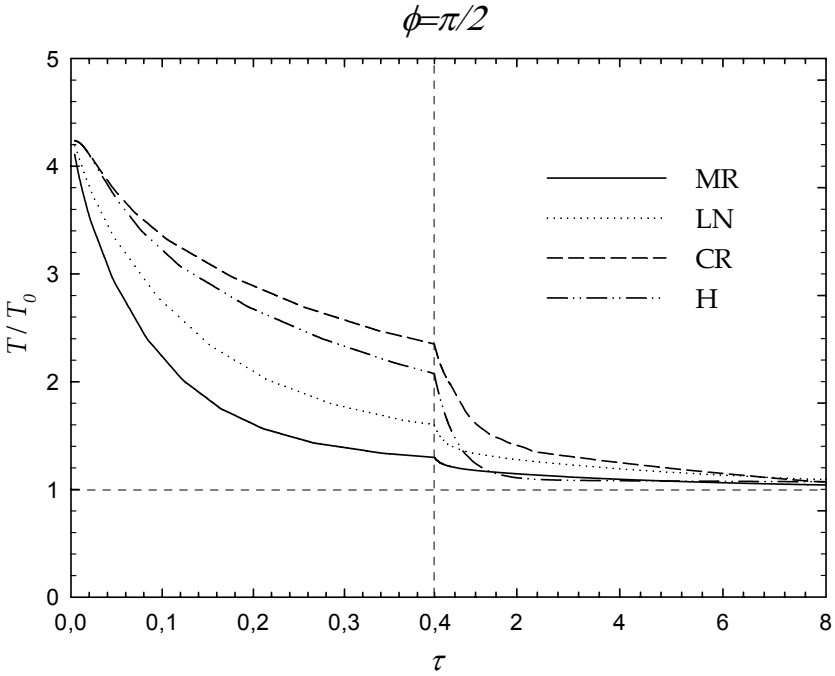

Figure 5.142 Normalized temperature at 90° crack front angle with respect to normalized time, a/t_1=0.4 and α=15°

5.4.17 Normalized SIFs and G Distributions with respect to Normalized Time for ϕ=90^o and α=30^o

Figure 5.143 shows normalized mode I stress intensity factor, K_{In} with respect to normalized time, τ for a/t_1=0.2. From this figure it can be seen that the maximum values of K_{In}, which are 0.203, 0.128, 0.117 and 0.096, are obtained at $\tau \cong 0.005$, 0.008, 0.029 and 0.029 for MR, LN, CR and H coatings, respectively. In Figure 5.144, K_{In} distributions with respect to τ are given for a/t_1=0.4. In this case, the maximum values of K_{In}, which are 0.017, 0.020, 0.027 and 0.005, are obtained at $\tau \cong 0.008$, 0.012, 7.764 and 0.080 for MR, LN, CR and H coatings, respectively.

Figure 5.145 depicts normalized mode II stress intensity factor, K_{IIn} with respect to normalized time, τ for a/t_1=0.2. From this figure it can be observed that the maximum values of K_{IIn}, which are -0.057, -0.032, 0.024 and 0.016, are obtained at $\tau \cong 0.261$, 0.421, 0.061 and 0.044 for MR, LN, CR and H coatings, respectively. In Figure 5.146, K_{IIn} distributions with respect to τ are given for a/t_1=0.4. In this case, the maximum values of K_{IIn}, which are -0.030, -0.030, -0.030 and -0.030, are obtained at $\tau \cong 0.008$, 0.008, 0.016 and 0.016 for MR, LN, CR and H coatings, respectively.

In Figure 5.147, normalized mode III stress intensity factor, K_{IIIn} with respect to normalized time, τ for a/t_1=0.2 is given. From this figure it can be seen that the maximum values of K_{IIIn}, which are -0.0093, -0.0055, 0.0015 and 0.0009, are obtained at $\tau \cong 0.341$, 0.501, 0.054 and 0.044 for MR, LN, CR and H coatings, respectively. In Figure 5.148, K_{IIIn} distributions with respect to τ are given for a/t_1=0.4. In this case, the maximum values of K_{IIIn}, which are -0.0029, -0.0024, -0.0023 and -0.0024, are obtained at $\tau \cong 0.008$, 0.008, 0.016 and 0.020 for MR, LN, CR and H coatings, respectively.

The normalized energy release rate, G_n distributions with respect to normalized time, τ for a/t_1=0.2 are presented in Figure 5.149. It can be observed from this

figure that the maximum values of G_n, which are 0.0174, 0.0097, 0.0141 and 0.0093, are obtained at $\tau \cong 0.261$, 0.008, 0.029 and 0.022 for MR, LN, CR and H coatings, respectively. In the case of a/t_1=0.4, as it can be seen in Figure 5.150, the maximum values of G_n, which are 0.0019, 0.0027, 0.0009 and 0.0009, are obtained at $\tau \cong 0.228$, 0.360, 0.016 and 0.016 for MR, LN, CR and H coatings, respectively. In Figure 5.151, the normalized temperature with respect to normalized time is shown.

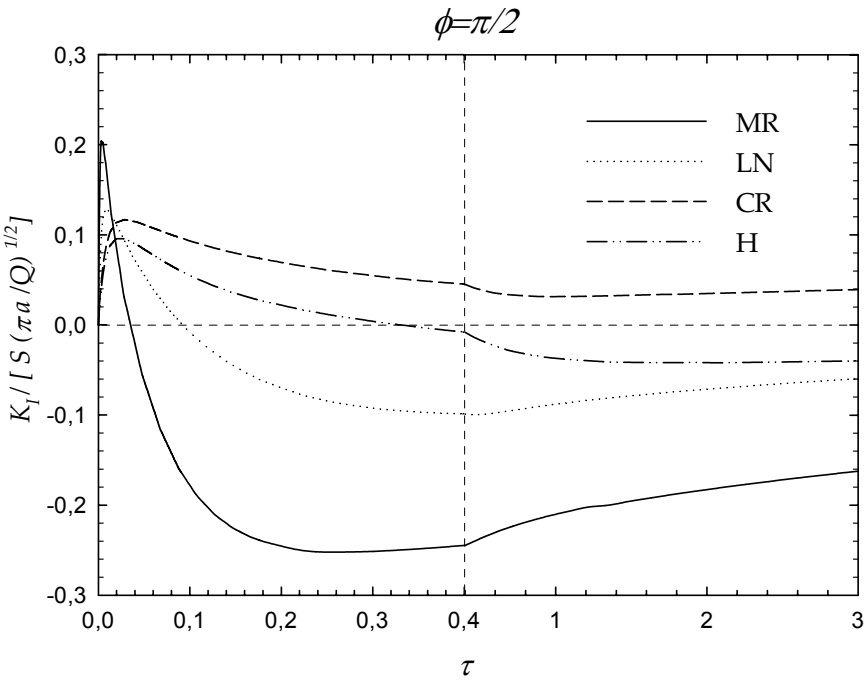

Figure 5.143 Normalized mode I stress intensity factors at 90° crack front angle with respect to normalized time, a/t_1=0.2 and α=30°

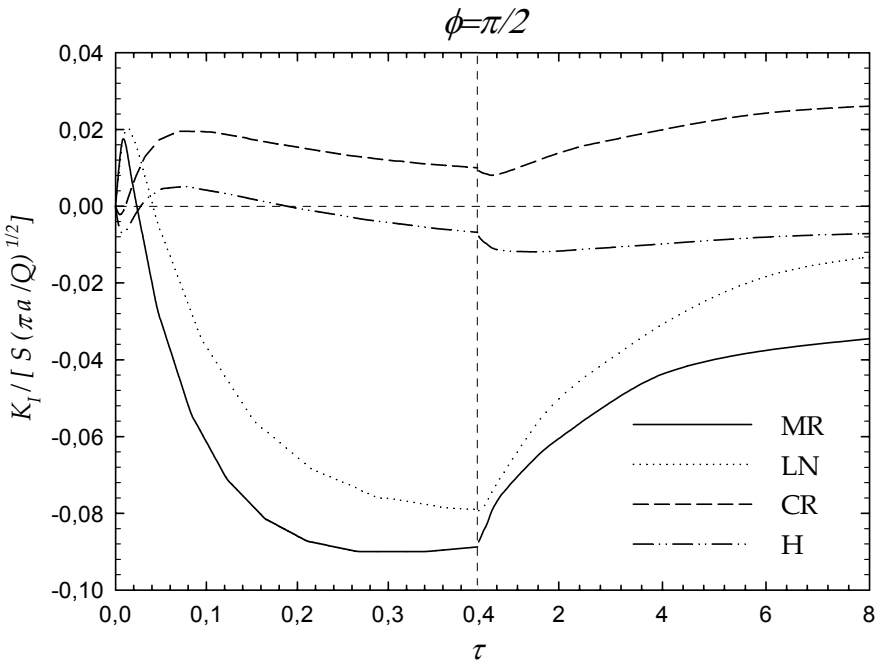

Figure 5.144 Normalized mode I stress intensity factors at 90° crack front angle with respect to normalized time, a/t_1=0.4 and α=30°

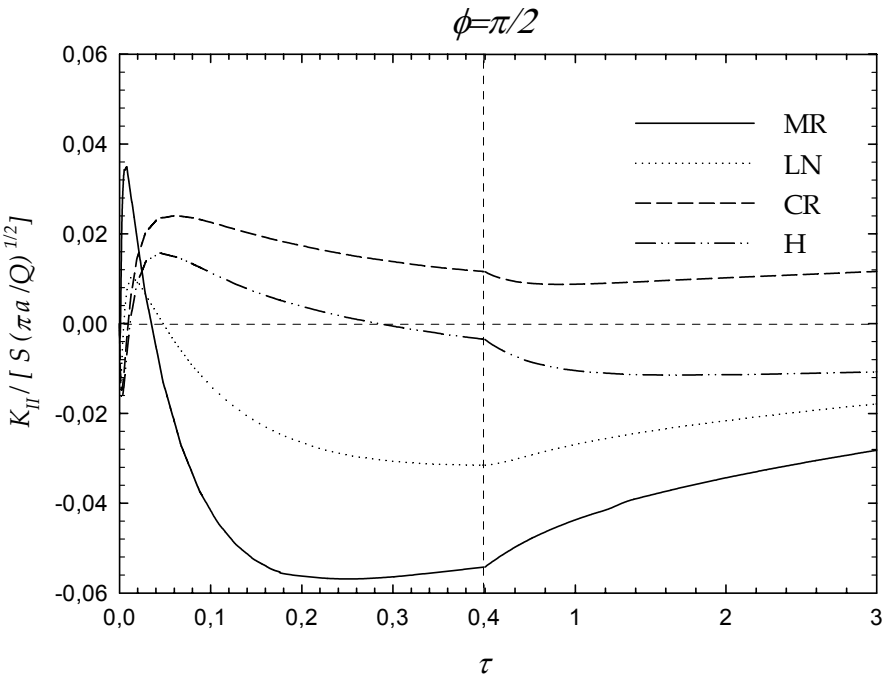

Figure 5.145 Normalized mode II stress intensity factors at 90° crack front angle with respect to normalized time, a/t_1=0.2 and α=30°

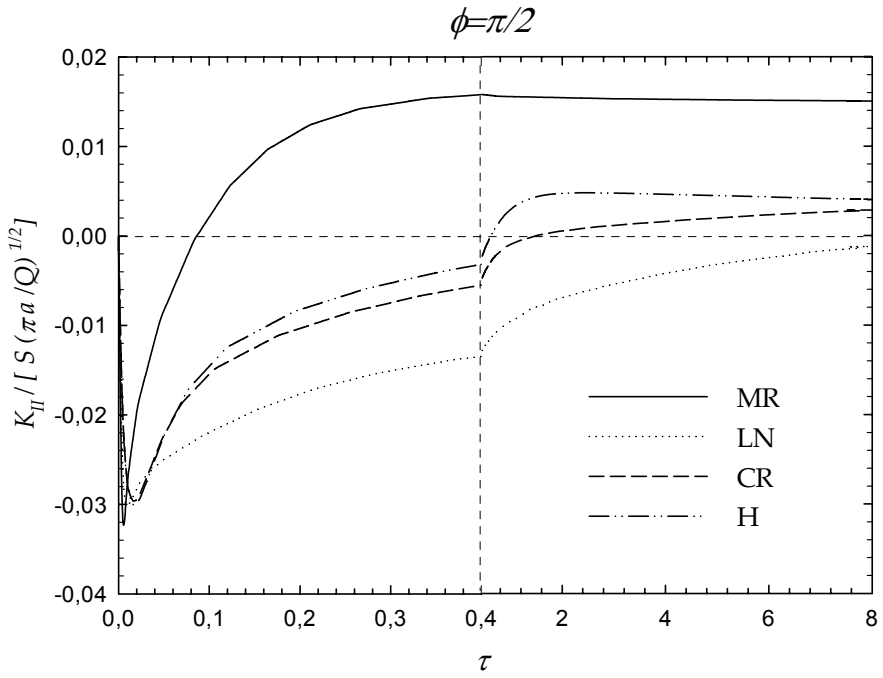

Figure 5.146 Normalized mode II stress intensity factors at 90° crack front angle with respect to normalized time, a/t_1=0.4 and α=30°

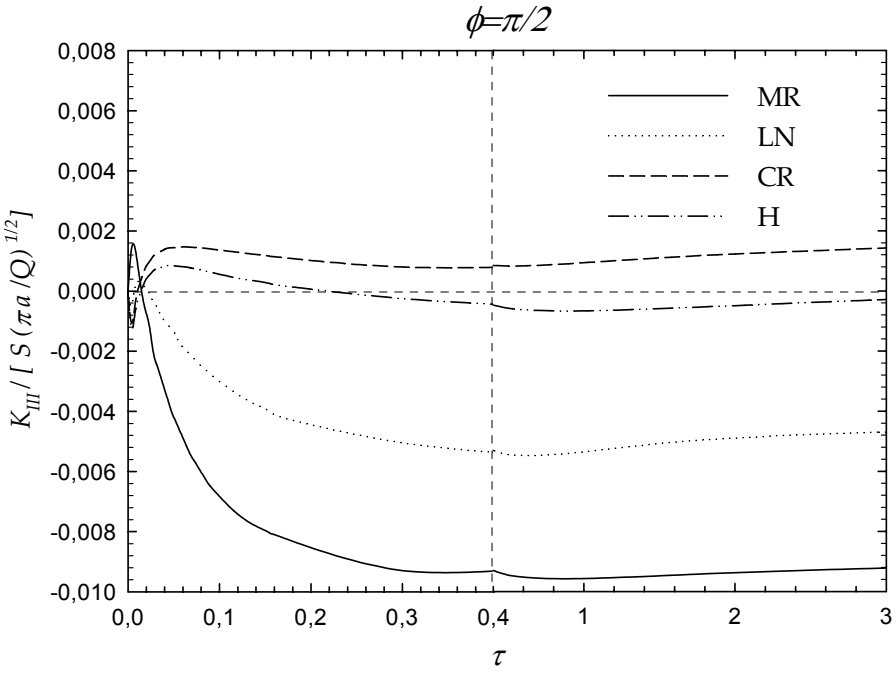

Figure 5.147 Normalized mode III stress intensity factors at 90° crack front angle with respect to normalized time, a/t_1=0.2 and α=30°

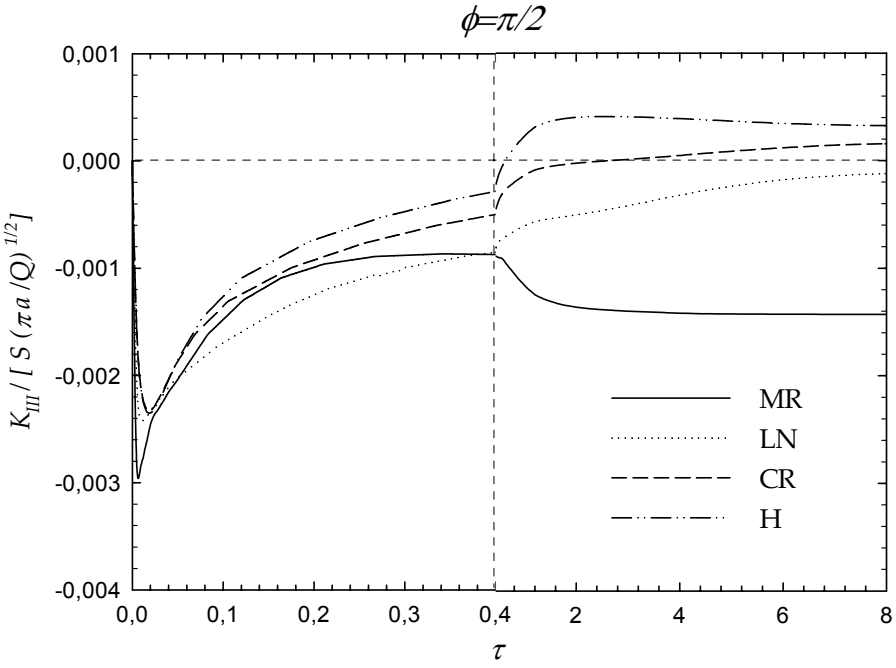

Figure 5.148 Normalized mode III stress intensity factors at 90^o crack front angle with respect to normalized time, a/t_1=0.4 and α=30^o

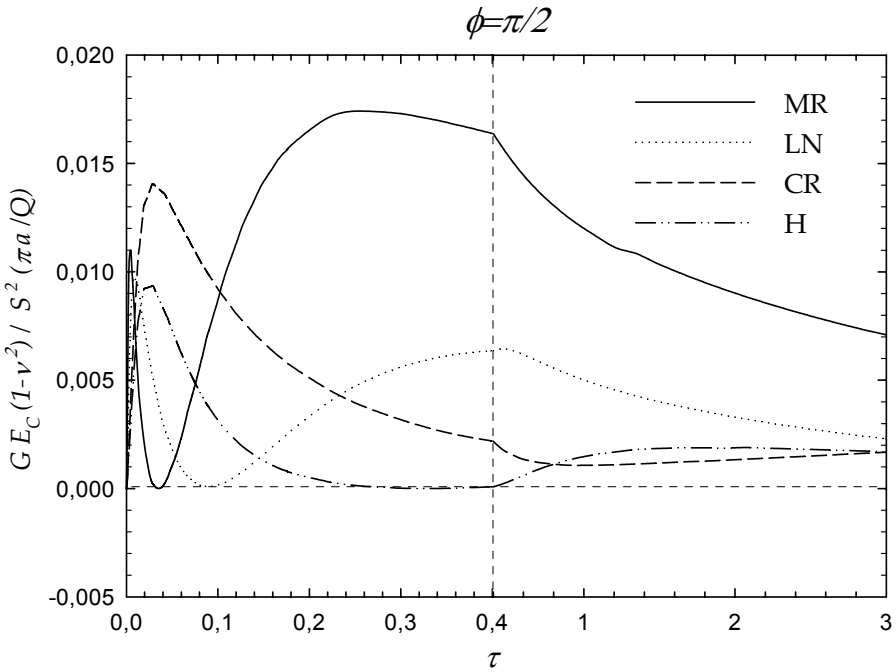

Figure 5.149 Normalized energy release rate at 90^o crack front angle with respect to normalized time, a/t_1=0.2 and α=30^o

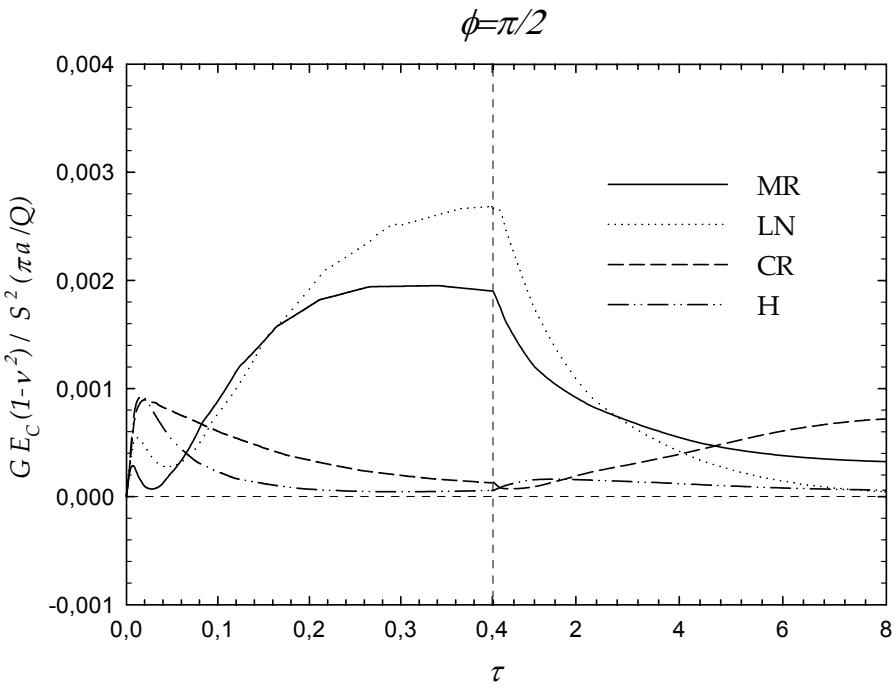

Figure 5.150 Normalized energy release rate at 90° crack front angle with respect to normalized time, a/t_1=0.4 and α=30°

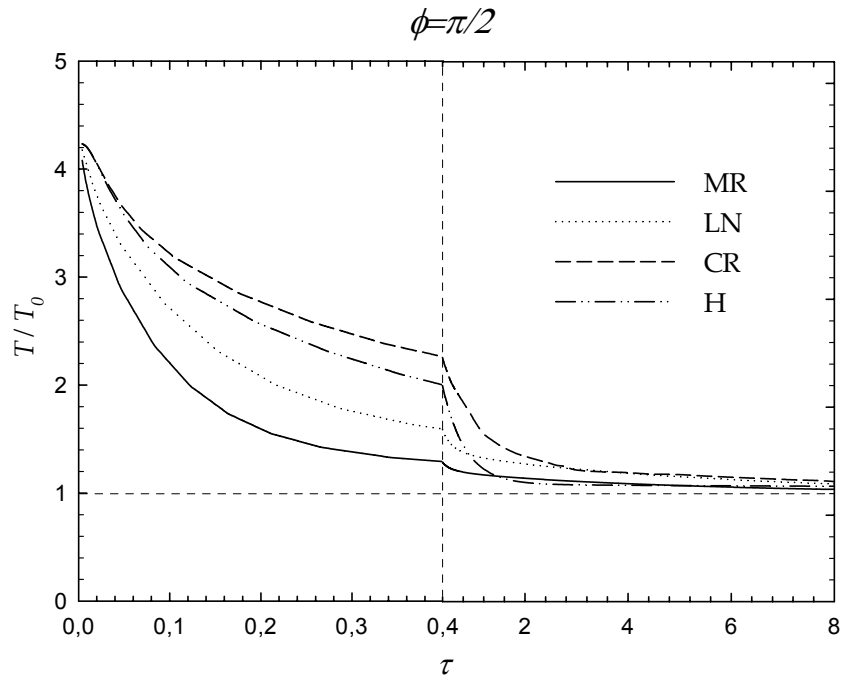

Figure 5.151 Normalized temperature at 90° crack front angle with respect to normalized time, a/t_1=0.4 and α=30°

5.4.18 Normalized SIFs and G Distributions with respect to Normalized Time for ϕ=90^o and α=45^o

Figure 5.152 shows normalized mode I stress intensity factor, K_{In} with respect to normalized time, τ for a/t_1=0.2. From this figure it can be seen that the maximum values of K_{In}, which are 0.209, 0.135, 0.118 and 0.103, are obtained at $\tau \cong 0.004$, 0.008, 0.019 and 0.019 for MR, LN, CR and H coatings, respectively. In Figure 5.153, K_{In} distributions with respect to τ are given for a/t_1=0.4. In this case, the maximum values of K_{In}, which are 0.048, 0.046, 0.040 and 0.027, are obtained at $\tau \cong 0.008$, 0.012, 0.048 and 0.032 for MR, LN, CR and H coatings, respectively.

Figure 5.154 depicts normalized mode II stress intensity factor, K_{IIn} with respect to normalized time, τ for a/t_1=0.2. From this figure it can be observed that the maximum values of K_{IIn}, which are -0.093, -0.040, 0.042 and 0.032, are obtained at $\tau \cong 0.261$, 0.421, 0.042 and 0.029 for MR, LN, CR and H coatings, respectively. In Figure 5.155, K_{IIn} distributions with respect to τ are given for a/t_1=0.4. In this case, the maximum values of K_{IIn}, which are -0.023, -0.032, -0.027 and -0.029, are obtained at $\tau \cong 0.164$, 0.288, 0.012 and 0.012 for MR, LN, CR and H coatings, respectively.

In Figure 5.156, normalized mode III stress intensity factor, K_{IIIn} with respect to normalized time, τ for a/t_1=0.2 is given. From this figure it can be seen that the maximum values of K_{IIIn}, which are -0.0069, -0.0031, 0.0029 and 0.0021, are obtained at $\tau \cong 0.221$, 0.381, 0.039 and 0.028 for MR, LN, CR and H coatings, respectively. In Figure 5.157, K_{IIIn} distributions with respect to τ are given for a/t_1=0.4. In this case, the maximum values of K_{IIIn}, which are -0.0021, -0.0023, -0.0022 and -0.0023, are obtained at $\tau \cong 0.004$, 0.088, 0.012 and 0.012 for MR, LN, CR and H coatings, respectively.

The normalized energy release rate, G_n distributions with respect to normalized time, τ for a/t_1=0.2 are presented in Figure 5.158. It can be observed from this

figure that the maximum values of G_n, which are 0.0152, 0.0121, 0.0151 and 0.0115, are obtained at $\tau \cong 0.261$, 0.008, 0.019 and 0.019 for MR, LN, CR and H coatings, respectively. In the case of a/t_1=0.4, as it can be seen in Figure 5.159, the maximum values of G_n, which are 0.0043, 0.0035, 0.0019 and 0.0013, are obtained at $\tau \cong 0.344$, 0.464, 0.032 and 0.020 for MR, LN, CR and H coatings, respectively. In Figure 5.160, the normalized temperature with respect to normalized time is shown.

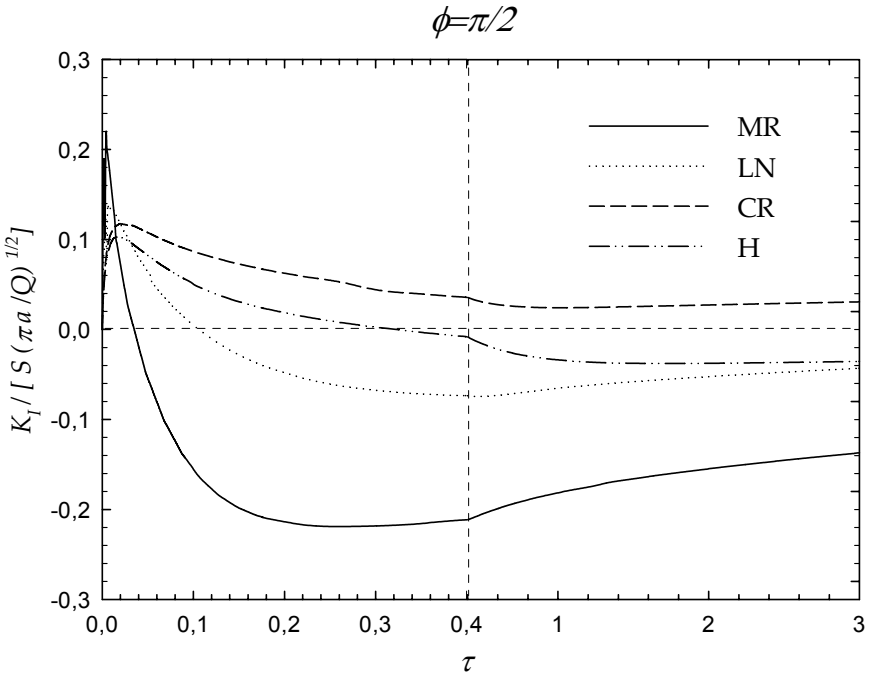

Figure 5.152 Normalized mode I stress intensity factors at 90° crack front angle with respect to normalized time, a/t_1=0.2 and α=45°

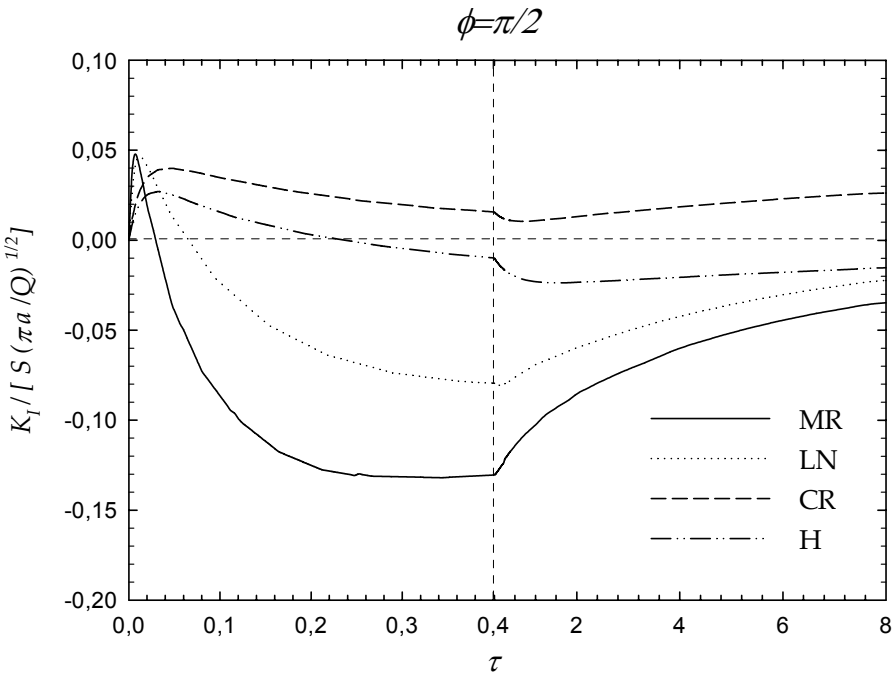

Figure 5.153 Normalized mode I stress intensity factors at 90° crack front angle with respect to normalized time, a/t_1=0.4 and α=45°

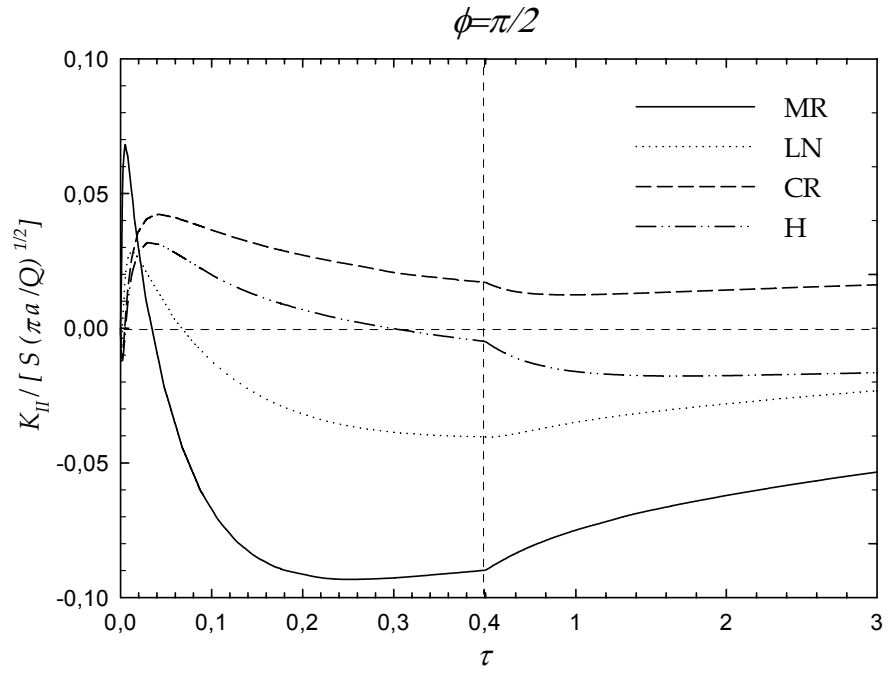

Figure 5.154 Normalized mode II stress intensity factors at 90° crack front angle with respect to normalized time, a/t_1=0.2 and α=45°

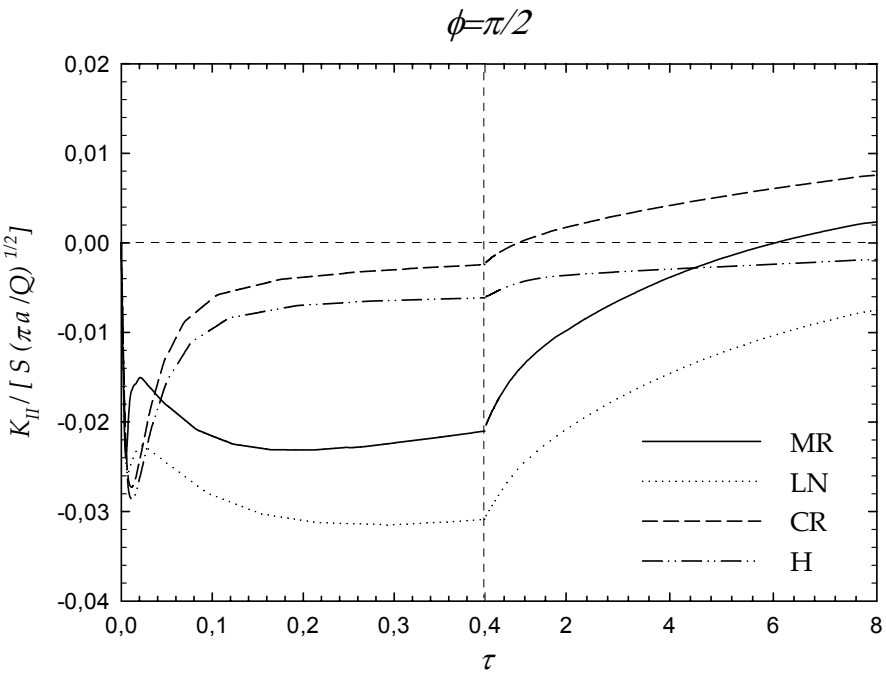

Figure 5.155 Normalized mode II stress intensity factors at 90° crack front angle with respect to normalized time, a/t_1=0.4 and α=45°

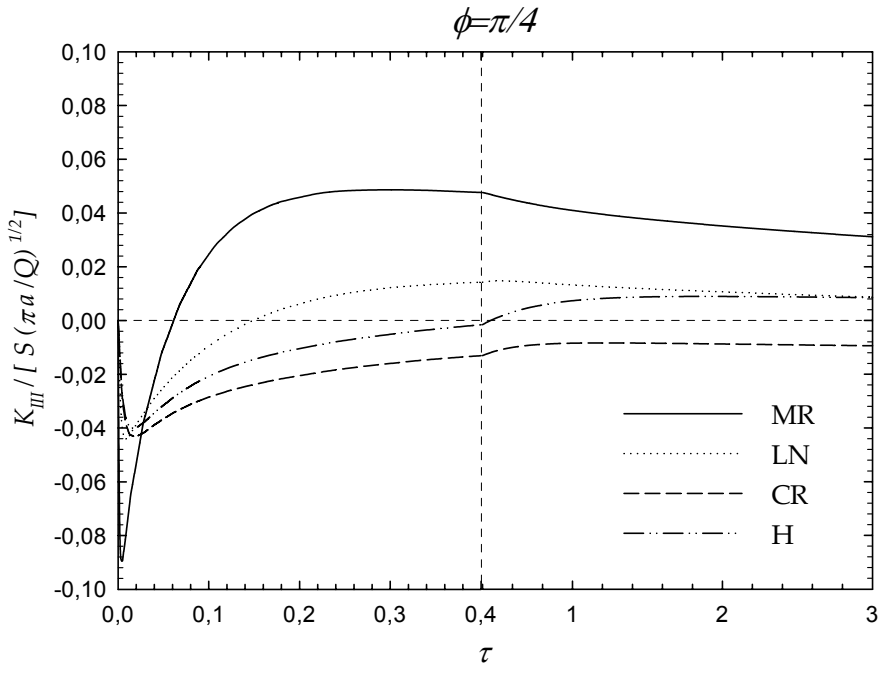

Figure 5.156 Normalized mode III stress intensity factors at 90° crack front angle with respect to normalized time, a/t_1=0.2 and α=45°

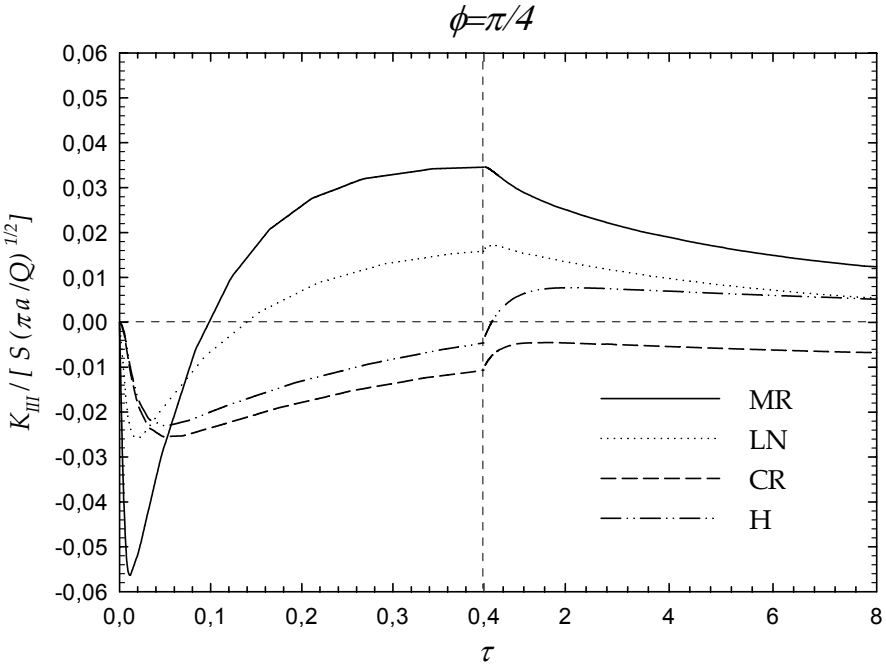

Figure 5.157 Normalized mode III stress intensity factors at 90° crack front angle with respect to normalized time, a/t_1=0.4 and α=45°

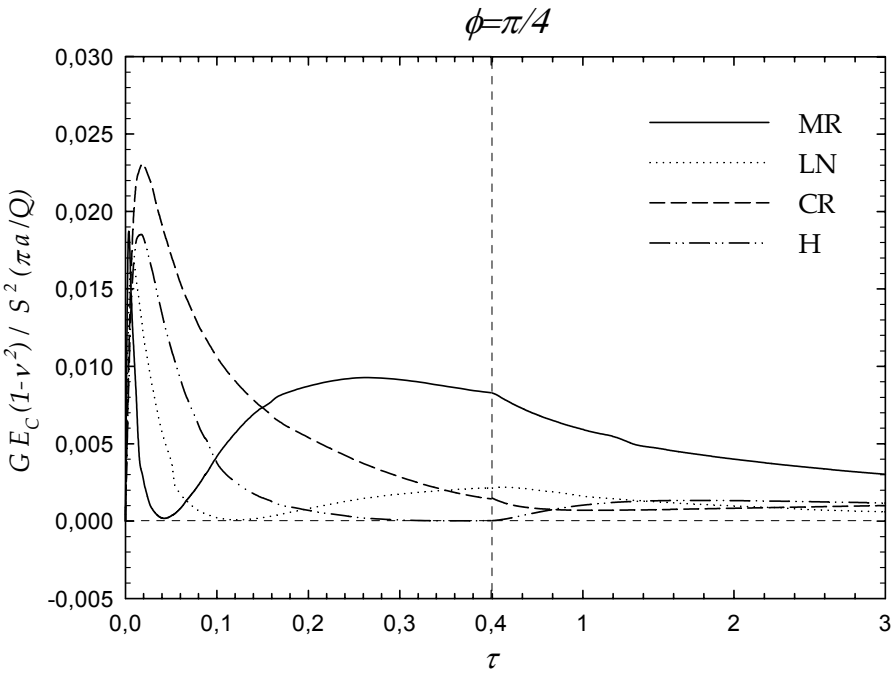

Figure 5.158 Normalized energy release rate at 90° crack front angle with respect to normalized time, a/t_1=0.2 and α=45°

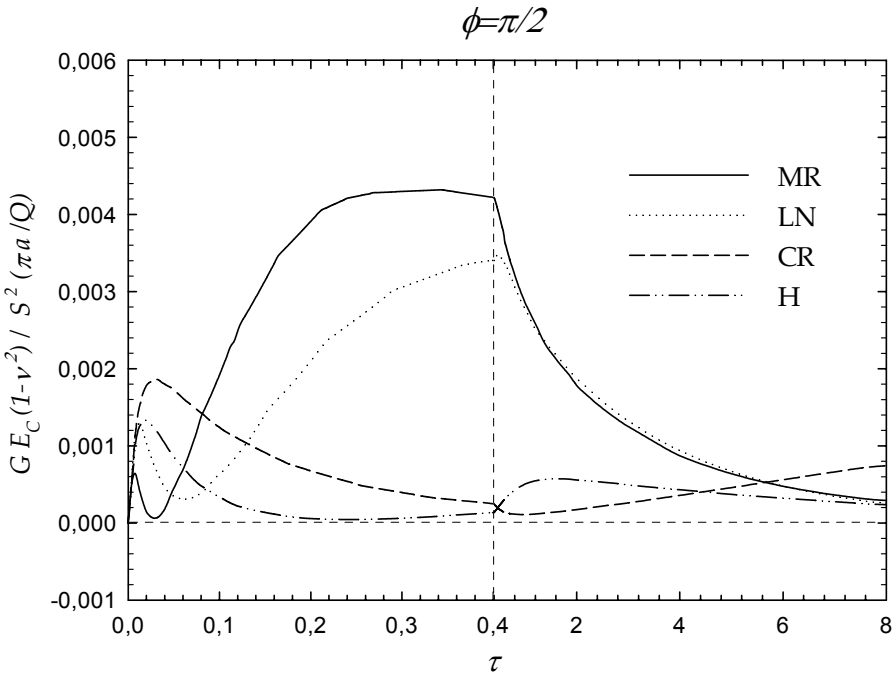

Figure 5.159 Normalized energy release rate at 90° crack front angle with respect to normalized time, a/t_1=0.4 and α=45°

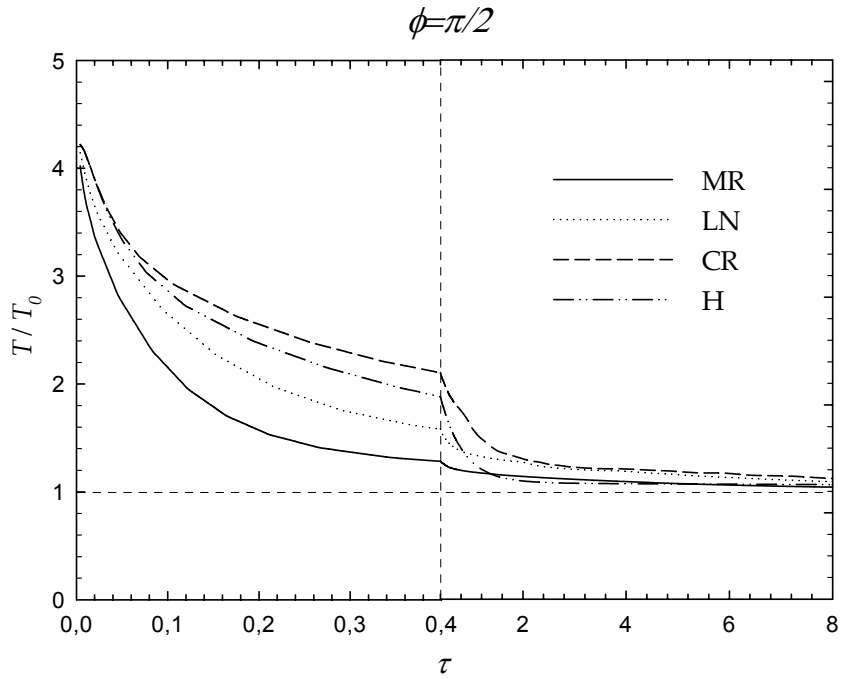

Figure 5.160 Normalized temperature at 90° crack front angle with respect to normalized time, a/t_1=0.4 and α=45°

5.4.19 Normalized SIFs and G Distributions with respect to Normalized Time for ϕ=90^o and α=60^o

Figure 5.161 shows normalized mode I stress intensity factor, K_{In} with respect to normalized time, τ for a/t_1=0.2. From this figure it can be seen that the maximum values of K_{In}, which are 0.172, 0.120, 0.107 and 0.097, are obtained at $\tau \cong 0.003$, 0.006, 0.013 and 0.012 for MR, LN, CR and H coatings, respectively. In Figure 5.162, K_{In} distributions with respect to τ are given for a/t_1=0.4. In this case, the maximum values of K_{In}, which are 0.058, 0.063, 0.056 and 0.048, are obtained at $\tau \cong 0.008$, 0.012, 0.020 and 0.020 for MR, LN, CR and H coatings, respectively.

Figure 5.163 depicts normalized mode II stress intensity factor, K_{IIn} with respect to normalized time, τ for a/t_1=0.2. From this figure it can be observed that the maximum values of K_{IIn}, which are -0.110, 0.046, 0.057 and 0.048, are obtained at $\tau \cong 0.261$, 0.009, 0.028 and 0.020 for MR, LN, CR and H coatings, respectively. In Figure 5.164, K_{IIn} distributions with respect to τ are given for a/t_1=0.4. In this case, the maximum values of K_{IIn}, which are -0.0678, -0.0397, 0.0138 and -0.0143, are obtained at $\tau \cong 0.268$, 0.384, 7.764 and 1.524 for MR, LN, CR and H coatings, respectively.

In Figure 5.165, normalized mode III stress intensity factor, K_{IIIn} with respect to normalized time, τ for a/t_1=0.2 is given. From this figure it can be seen that the maximum values of K_{IIIn}, which are -0.0138, -0.0050, 0.070 and 0.0058, are obtained at $\tau \cong 0.261$, 0.461, 0.028 and 0.020 for MR, LN, CR and H coatings, respectively. In Figure 5.166, K_{IIIn} distributions with respect to τ are given for a/t_1=0.4. In this case, the maximum values of K_{IIIn}, which are -0.0085, -0.0051, 0.0017 and -0.0018, are obtained at $\tau \cong 0.268$, 0.384, 7.764 and 1.564 for MR, LN, CR and H coatings, respectively.

The normalized energy release rate, G_n distributions with respect to normalized time, τ for a/t_1=0.2 are presented in Figure 5.167. It can be observed from this

figure that the maximum values of G_n, which are 0.0125, 0.0116, 0.0143 and 0.0114, are obtained at $\tau \cong 0.261$, 0.008, 0.019 and 0.013 for MR, LN, CR and H coatings, respectively. In the case of a/t_1=0.4, as it can be seen in Figure 5.168, the maximum values of G_n, which are 0.0072, 0.0026, 0.0032 and 0.0024, are obtained at $\tau \cong 0.344$, 0.524, 0.020 and 0.016 for MR, LN, CR and H coatings, respectively. In Figure 5.169, the normalized temperature with respect to normalized time is shown.

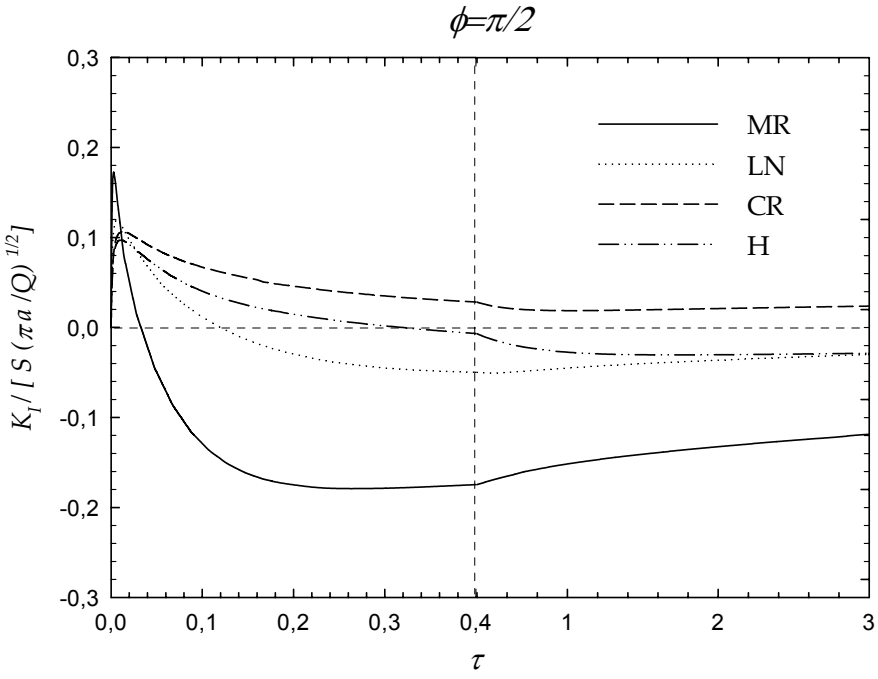

Figure 5.161 Normalized mode I stress intensity factors at 90° crack front angle with respect to normalized time, a/t_1=0.2 and α=60°

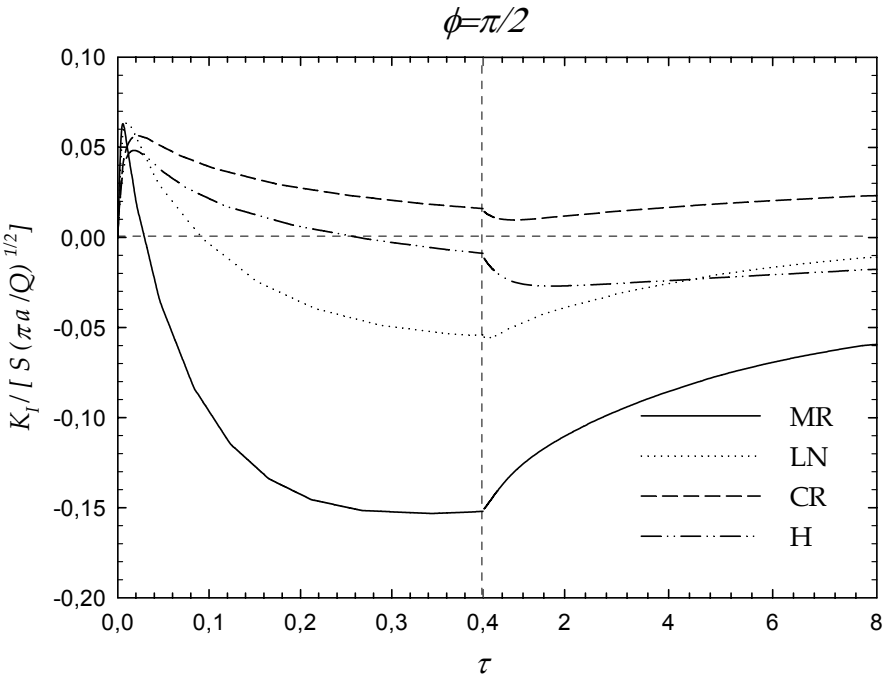

Figure 5.162 Normalized mode I stress intensity factors at 90° crack front angle with respect to normalized time, a/t_1=0.4 and α=60°

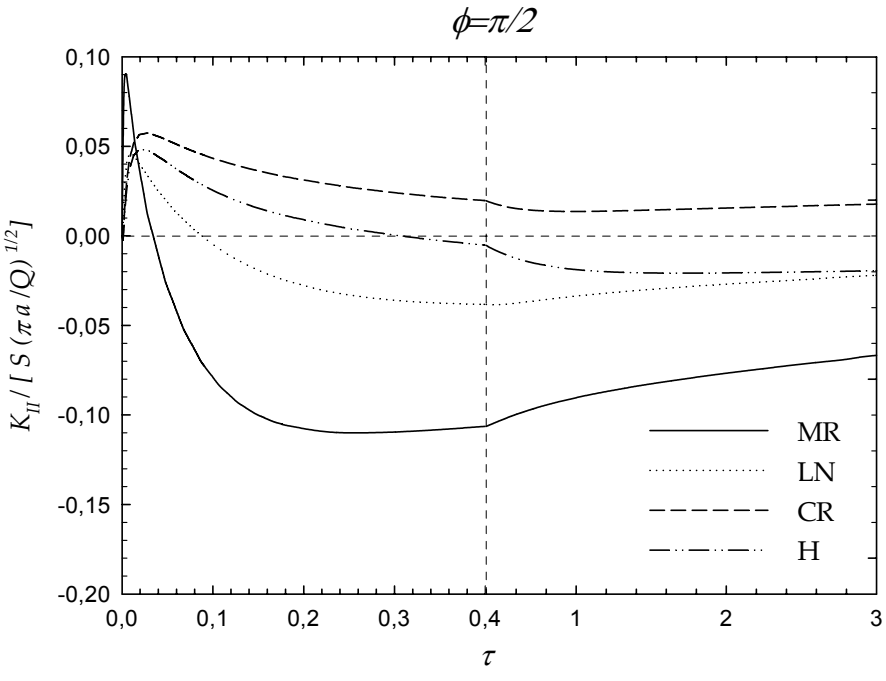

Figure 5.163 Normalized mode II stress intensity factors at 90° crack front angle with respect to normalized time, a/t_1=0.2 and α=60°

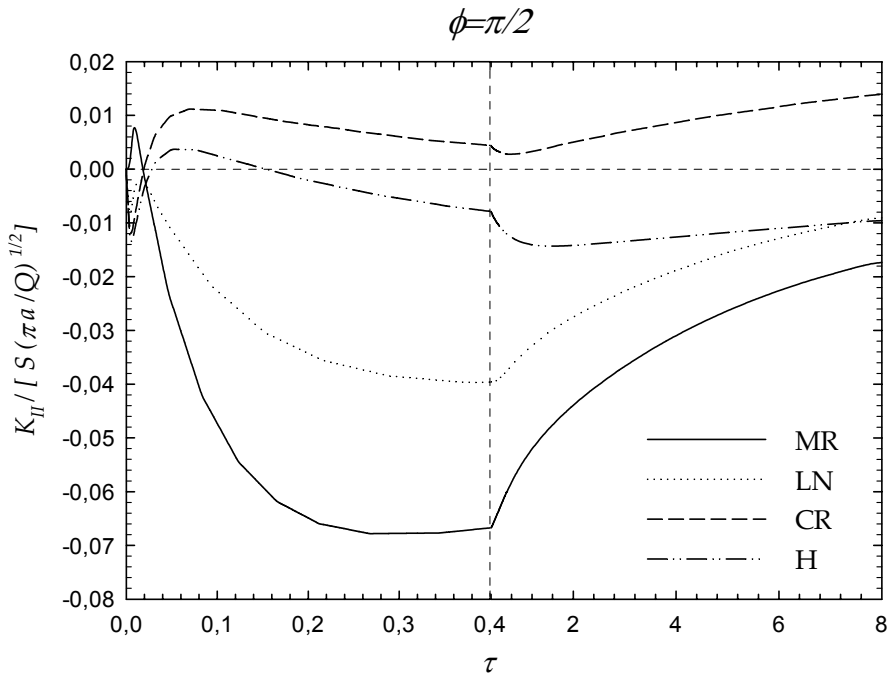

Figure 5.164 Normalized mode II stress intensity factors at 90° crack front angle with respect to normalized time, a/t_1=0.4 and α=60°

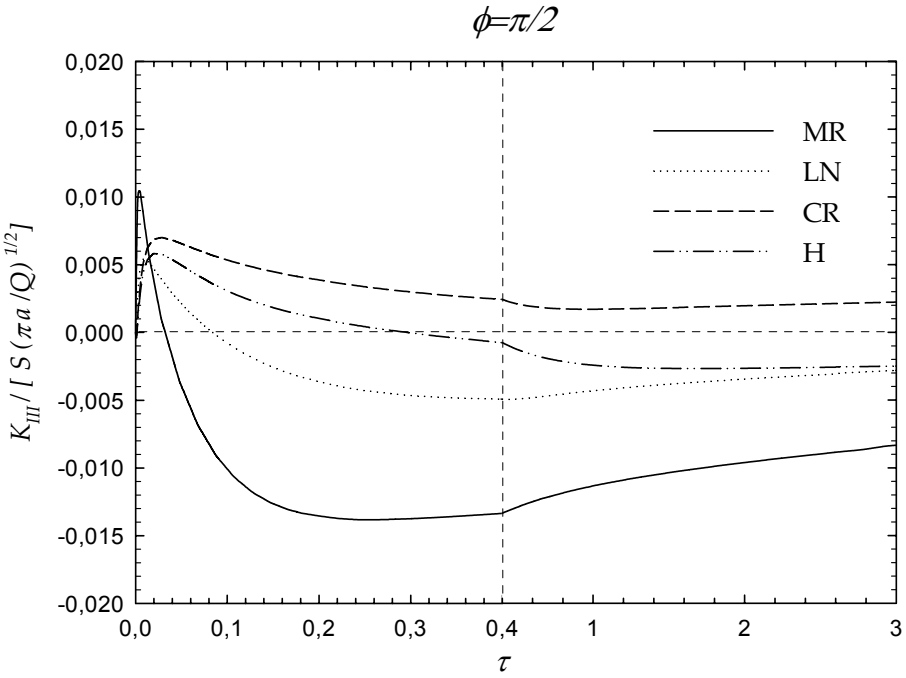

Figure 5.165 Normalized mode III stress intensity factors at 90° crack front angle with respect to normalized time, a/t_1=0.2 and α=60°

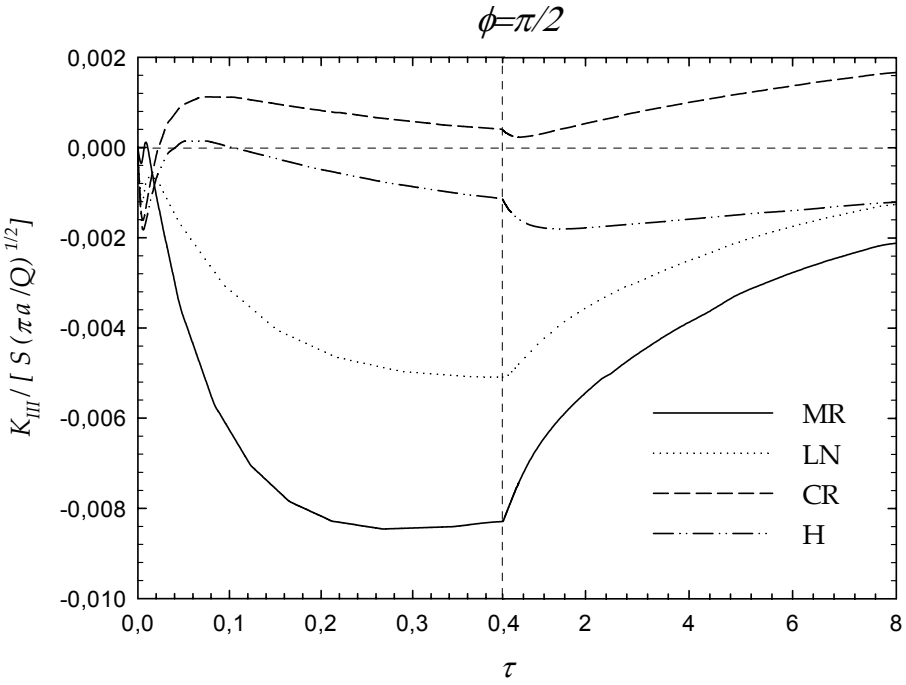

Figure 5.166 Normalized mode III stress intensity factors at 90° crack front angle with respect to normalized time, a/t_1=0.4 and α=60°

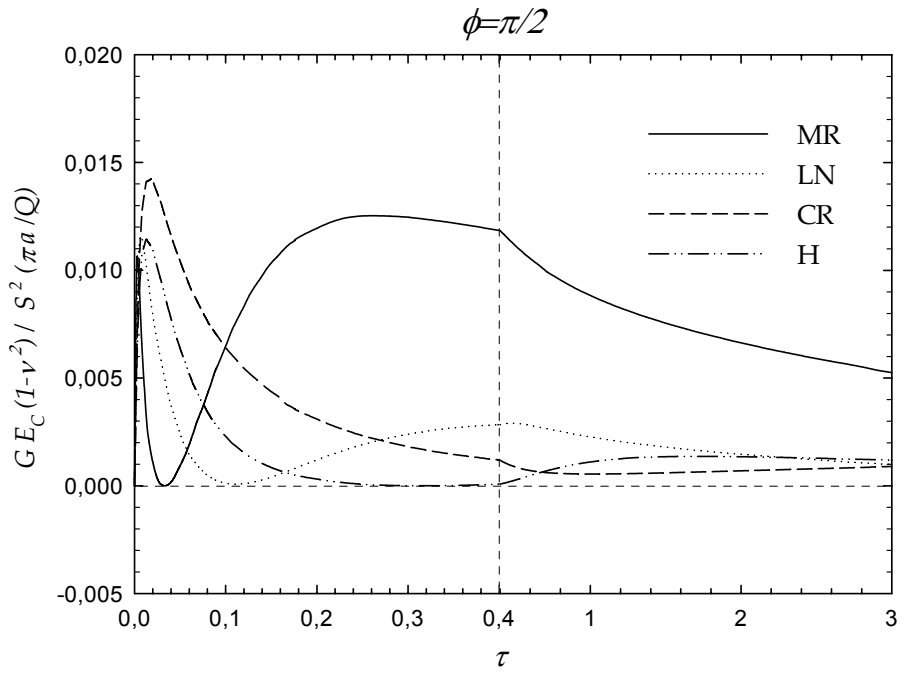

Figure 5.167 Normalized energy release rate at 90° crack front angle with respect to normalized time, a/t_1=0.2 and α=60°

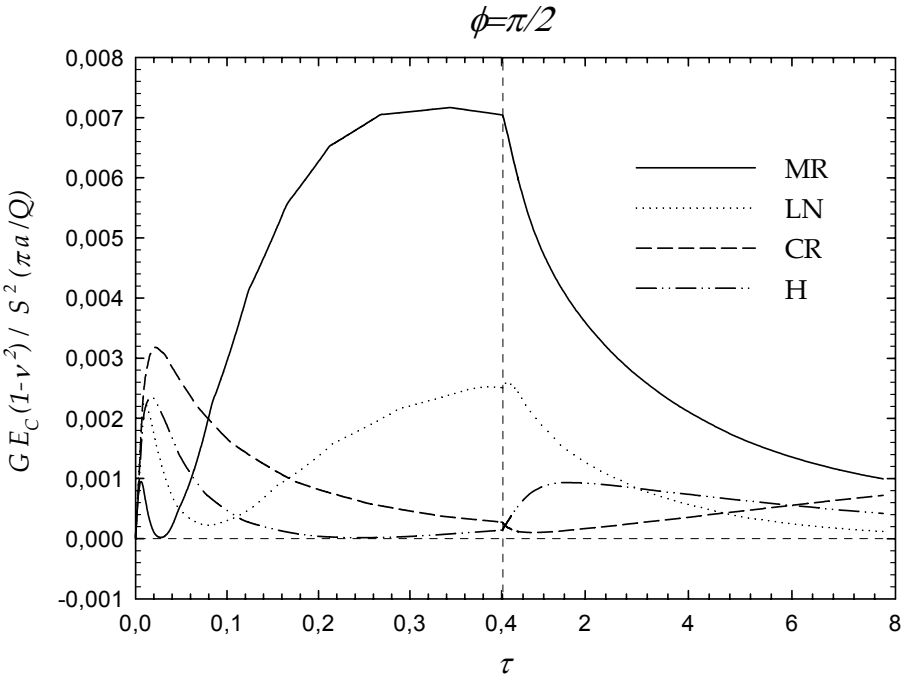

Figure 5.168 Normalized energy release rate at 90° crack front angle with respect to normalized time, a/t_1=0.4 and α=60°

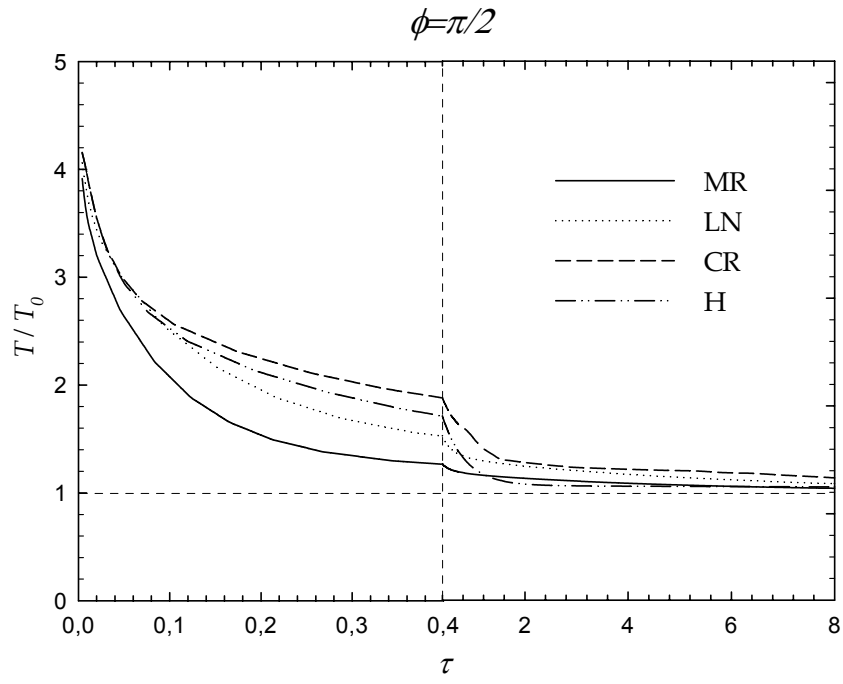

Figure 5.169 Normalized temperature at 90° crack front angle with respect to normalized time, a/t_1=0.4 and α=60°

CHAPTER 6

CONCLUDING REMARKS

In this study, an inclined semi-elliptical surface crack in an FGM coating-bond coat-substrate structure is modeled in three dimension and fracture analyses are carried out by implementing finite element technique. For the model generations and finite element analyses, the multi-purpose finite element code ANSYS is used. The behavior of three dimensional inclined semi-elliptical surface cracks is examined under transient thermal loading for different coating variations and crack depth/ FGM coating thicknesses. The mixed mode stress intensity factors and energy release rates around the crack front are calculated by utilizing displacement correlation technique. In order to evaluate mixed mode stress intensity factors and energy release rates, the commands existed in ANSYS are not preferred, rather APDL programming is highly used to make it possible to implement the displacement correlation technique for the calculations.

In order to verify the model and technique utilized in FGM coating-bond coat-substrate structure, first of all, a plate and a semi-infinite solid with homogeneous material properties are modeled and analyzed under uniform tension. Then, the results obtained are compared to those given by Ayhan et al. [11] and Isida et al. [9]. It is observed that the figures generated for comparisons are in good agreement and therefore, it is concluded that this model can also be used for the finite element analyses of the composite medium.

In the analyses, the first point on the crack front is not considered for two reasons. The first reason is that, the mixed mode stress intensity factors at the free surface can not be evaluated correctly since the singular behavior of the crack tip fields at this surface is different than that of the inner points on the crack front. This is known as free surface effect. The second and the main reason is that for the inclination angles except 0^o, due to the inclination of the crack, it is not possible to calculate mixed mode stress intensity factors correctly at the point which intersects the free surface. For the implementation of displacement correlation technique, the program calculates mixed mode SIFs by defining a new coordinate system perpendicular to the crack front. Since the plane containing the first point on the crack front is not perpendicular to the crack front, it is not possible to generate a perpendicular coordinate system and obtain the correct displacement values of the node at the first point on the crack front.

The transient thermal analyses of the FGM coating-bond coat- substrate structure are carried out for four different material types which are metal-rich (MR), linear variation (LN), ceramic-rich (CR) and homogeneous (H) coatings. It is assumed that the composite medium is initially at a high processing temperature. Then, this structure is left in an environment which is at a low temperature. Due to the high temperature difference, thermal stresses are induced at the composite structure containing an inclined semi-elliptical surface crack. For this reason, mixed mode SIFs and energy release rates are calculated along the crack front.

As expected, the temperature of the points on the crack front first decreases rapidly and then reaches to a steady-state value after a certain time. In the analyses, it is observed that for a/t_1=0.2, the steady-state values are obtained at $\tau \approx 3$, whereas for a/t_1=0.4 they are reached at $\tau \approx 8$.

The distribution of normalized SIFs and energy release rates are investigated around the crack front for the transient thermal analysis of composite medium. It is observed that as the inclination angle increases, the normalized mode I stress intensity factors decrease. For a/t_1=0.2, the maximum value of K_{In} around the

crack front is obtained by MR coating at the point closest to the free surface for $\alpha = 0^o$. Similarly, for a/t_1=0.4, the maximum value of K_{In} around the crack front is obtained by CR coating at the point closest to the free surface, again for $\alpha = 0^o$. On the other hand, the normalized mode II stress intensity factors increase as the inclination angle increases. It is seen that the maximum value of K_{IIn} around the crack front is obtained by MR coating for $\alpha = 45^o$ at the point closest to the free surface for a/t_1=0.2, whereas the maximum is attained by MR coating at $\alpha = 60^o$ at the point closest to the free surface for a/t_1=0.4. The normalized mode III stress intensity factors also increase as the inclination angle increases. It is found that the maximum value of K_{IIIn} around the crack front is obtained by MR coating for $\alpha = 60^o$ at the point closest to the free surface both for a/t_1=0.2 and a/t_1=0.4. As in the case of K_{In}, the normalized energy release rates also decrease as the inclination angle increases. The maximum value of G_n around the crack front is obtained by CR coating for $\alpha = 0^o$ at the point closest to the free surface both for a/t_1=0.2 and a/t_1=0.4. It is observed that for all normalized mixed mode SIFs and energy release rates, the values obtained for the case a/t_1=0.2 are greater than that of a/t_1=0.4. Additionally, it is seen that for all inclination angles and coating types, the normalized temperature increases as the crack front angle increases.

The distribution of peak values of normalized SIFs and energy release rates at specific crack front angles are also analyzed in this study for various inclination angles of semi-elliptical surface crack embedded in the FGM coating of composite structure under transient thermal loads. It is found that the peak values of normalized mode I stress intensity factor decrease as crack front angle, ϕ increases. The maximum peak of K_{In} is obtained for $\phi = 30^o$ by MR coating at $\alpha = 0^o$ and a/t_1=0.2. For a/t_1=0.4, the maximum peak of K_{In} is obtained for $\phi = 30^o$ by MR coating at $\alpha = 30^o$. On the other hand, it is seen that the peak values of normalized mode II stress intensity factor increase as crack front angle, ϕ increases for a/t_1=0.2. The maximum peak of K_{IIn} is attained by MR coating for $\phi = 90^o$ and at $\alpha = 60^o$ for a/t_1=0.2. For a/t_1=0.4, it is observed that the peak

values of K_{IIn} increases as ϕ increases. In this case, the maximum peak of K_{IIn} is reached by MR coating for $\phi = 45^o$ and at $\alpha = 60^o$. It is found that the peak values of normalized mode III stress intensity factor decreases as ϕ increases. Both for a/t_1=0.2 and a/t_1=0.4, the maximum peak of K_{IIIn} is obtained for $\phi = 30^o$ and at $\alpha = 60^o$. These maximums are attained by MR coating for both a/t_1=0.2 and a/t_1=0.4, respectively. As in the case of K_{In}, the peak values of energy release rates decrease as ϕ increases. It is seen that the maximum peak of G_n is attained by CR coating for $\phi = 30^o$ at $\alpha = 0^o$ for a/t_1=0.2. For a/t_1=0.4, this maximum is obtained by MR coating for $\phi = 30^o$ and at $\alpha = 30^o$.

The variations of the normalized mode I, II and III stress intensity factors, energy release rates and temperature at the crack fronts $\phi = 45^o$ and $\phi = 90^o$ with respect to normalized time is also examined in this study for 0^o, 15^o , 30^o , 45^o and 60^o inclination angles of semi-elliptic surface crack. In order to more clearly present the variations for small τ, double scales are used for normalized time.

It should be noted that, for the problems under mixed-mode conditions (like the one considered in this study), during the design and production of the FGMs, the energy release rate is the most critical parameter that must be taken into account. While selecting the coating type for the FGMs, the one with maximum energy release rate should not be preferred. As an example, in this study for $\phi = 45^o$ and a/t_1=0.2, it is observed that the maximum of G_n is reached by CR coating for all inclination angles. On the other hand, for a/t_1=0.4, the maximum of G_n is attained by MR coating again for all inclination angles of the crack. For $\phi = 90^o$ and a/t_1=0.2, the maximum of G_n is obtained by CR coating for $\alpha = 0^o$, 45^o and 60^o. For $\alpha = 15^o$ and 30^o, the maximum of G_n is reached by MR coating. For a/t_1=0.4, on the other hand, the maximum of G_n is obtained by LN coating for $\alpha = 0^o$, 15^o and 30^o and for $\alpha = 45^o$ and 60^o, the maximum value of G_n is attained by MR coating.

An immediate extension of the present study can be the modeling of the semi-elliptical surface crack, the plane of which is rotated with respect to the axis passing through the symmetry plane considered in this study, in an FGM coating-bond coat-substrate structure under thermomechanical loading. This problem requires a development of a full model since there does not exist any symmetry condition. Due to this drawback, this problem needs to be analyzed with very powerful workstations. In addition, for the transient thermal analyses, the radiation effect may also be taken into account. Moreover, a different solution technique like J-integral method can be utilized in order to calculate the mixed-mode stress intensity factors along the crack front.

REFERENCES

[1] Glaeser, A. M., 1997, "The Use of Transient FGM Interlayers for Joining Advanced Ceramics", *Composites Part B*, Vol. 28B, pp.71-84.

[2] Yamanouchi, M., Hirai, T. and Shiota, I., 1990, "Proceedings of First International Symposium on Functionally Gradient Materials", *FGM Forum, Tokyo, Japan*.

[3] Shabana, Y. M. and Noda, N., 2002, "Geometry Effects of Substrate and Coating Layers on the Thermal Stress Response of FGM Structure", *Acta Mechanica*, Vol. 159, pp.143-156.

[4] Liew, K. M., He, X. Q., Ng, T. Y. and Sivashanker, S. 2001, "Active Control of FGM Plates Subjected to a Temperature Gradient: Modeling via Finite Element Method Based on FSDT" *International Journal for Numerical Methods in Engineering*, Vol. 52, pp

[5] Long, X. and Delale, F., 2005, "The Mixed Mode Crack Problem in an FGM Layer Bonded to a Homogeneous Half-Plane", *International Journal of Solids and Structures*, Vol. 42, pp.3897-3917.

[6] Jeanine T. DeMasi-Marcin, J. T. and Gupta, D.K.,1994, "Protective Coatings in the Gas Turbine Engine", *Surface and Coatings Technology*, Vol. 68, pp.1-9

[7] Lee, Y.-D. and Erdoğan, F., 1998, "Interface Cracki*n*g of FGM Coatings Under Steady – State Heat Flow", *Engineering Fracture Mechanics*, Vol. 59, No. 3, pp. 361-380.

[8] Wang, B.-L. and Tian, Z.-H., 2005, "Application of finite element–finite difference method to the determination of transient temperature field in functionally graded materials", *Finite Elements in Analysis and Design*, Vol. 41, pp. 335-349.

[9] Isida, M., Tokumoto, A. and Noguchi, H., 1990, "Oblique Semi-Elliptical Surface Crack in Semi-Infinite Solid Subjected to Tension", *Engineering Fracture Mechanics*, Vol. 36, No. 6, pp. 889-892.

[10] Noda, N.-A., Kobayashi, K. and Yagishita, M., 1999, "Variation of Mixed Modes Stress Intensity Factors of an Inclined Semi-Elliptical Surface Crack", *International Journal of Fracture*, Vol. 100, No. 3, pp. 207-225.

[11] Ayhan, A.O., 2004, "Mixed Mode Stress Intensity Factors for Deflected and Inclined Surface Cracks in Finite-Thickness Plates", *Engineering Fracture Mechanics*, Vol. 71, pp. 1059-1079.

[12] Kadıoğlu, S., Dağ, S. and Yahşi, O.S., 1998, "Crack Problem for a Functionally Graded Layer on an Elastic Foundation", *International Journal of Fracture*, Vol. 94, pp. 63-77.

[13] Jin, Z.-H. and Paulino, G.H., 2001, "Transient Thermal Stress Analysis of an Edge Crack in a Functionally Graded Material", *International Journal of Fracture*, Vol. 107, pp. 73-98.

[14] Wang, B.L., Mai, Y.-W. and Noda, N., 2002, "Fracture Mechanics Analysis Model for Functionally Graded Materials with Arbitrarily

Distributed Properties", *International Journal of Fracture*, Vol. 116, pp. 161-177.

[15] Wang, B.L., Mai, Y.-W. and Noda, N., 2004, "Fracture Mechanics Analysis Model for Functionally Graded Materials with Arbitrarily Distributed Properties (Mode II and Mode III Problems)", *International Journal of Fracture,* Vol. 0, pp. 1-14.

[16] Guo, L.-C., Wu, L.-Z., Ma, L. and Zeng, T., 2004, "Fracture Analysis of a Functionally Graded Coating - Substrate Structure with a Crack Perpendicular to the Interface – Part I: Static Problem", *International Journal of Fracture*, Vol. 0, pp. 1-18.

[17] Guo, L.-C., Wu, L.-Z., Zeng, T. and Ma, L., 2004, "Fracture Analysis of a Functionally Graded Coating-Substrate Structure with a Crack Perpendicular to the Interface – Part II: Transient Problem", *International Journal of Fracture*, Vol. 0, pp. 1-22.

[18] Chi, S.-H. and Chung, Y.-L., 2003, "Crack*i*ng in Coating – Substrate Composites with Multi - Layered and FGM Coatings", *Engineering Fracture Mechanics*, Vol. 70, pp. 1227-1243.

[19] Lee, Y.-D. and Erdoğan, F., 1998, "Interface Crack*i*ng of FGM Coatings Under Steady – State Heat Flow", *Engineering Fracture Mechanics*, Vol. 59, No. 3, pp. 361-380.

[20] Yıldırım, B., Dağ, S. and Erdoğan, F., 2005, "Three Dimensional Fracture Analysis of FGM Coatings under Thermomechanical Loading", *International Journal of Fracture*, Vol. 132, pp.369-395.

[21] Yıldırım, B., 2006, "An Equivalent Domain Integral Method for Fracture Analysis of Functionally Graded Materials under Thermal Stresses", *Journal of Thermal Stresses*, Vol. 29, pp.371-397.

[22] Long, X. and Delale, F., 2005, "The Mixed Mode Crack Problem in an FGM Layer Bonded to a Homogeneous Half-Plane", *International Journal of Solids and Structures*, Vol. 42, pp.3897-3917.

[23] Shabana, Y. M. and Noda, N., 2002, "Geometry Effects of Substrate and Coating Layers on the Thermal Stress Response of FGM Structure", *Acta Mechanica*, Vol. 159, pp.143-156.

[24] Nemat-Alla, M. and Noda, N., 2000, "Edge Crack Problem in a Semi-Infinite FGM Plate with a Bi-Directional Coefficient of Thermal Expansion under Two Dimensional Thermal Loading", *Acta Mechanica*, Vol. 144, pp.211-229.

[25] Zehnder, A.T., 2007, "Modes of Fracture", *Lecture Notes on Fracture Mechanics*, pp.8.

[26] "Stresses and Displacement near Crack Tips", *http://www.efunda.com/formulae/solid_mechanics/fracture_mechanics/fm_lefm_stress.cfm*, last accessed 01.08.2007.

[27] Nusier, S. and Newaz, G., 1998, "Analysis of Interfacial Cracks in a TBC Superalloy System under Thermal Loading", *Engineering Fracture Mechanics*, Vol. 60, No. 3, pp. 577-581.

[28] Walters, M.C., Paulino, G.H. and Dodds Jr., R.H., 2004, "Stress-Intensity Factors for Surface Cracks in Functionally Graded Materials under mode-I Thermomechanical Loading", *International Journal of Solids and Structures* , Vol. 41, pp. 1081-1118.

[29] ANSYS, Inc. Southpointe 275 Technology Drive Canonsburg, PA 15317, USA.

[30] ANSYS Help-Release 10.0 Documentation for ANSYS.

[31] Koers, R.W.J., 1989, "Use of Modified 20-Node Isoparametric Brick Elements for Representing Stress/Strain Fields at a Crack Tip for Elastic and Perfectly Plastic Material", *International Journal of Fracture*, Vol. 40, pp. 79-110.

[32] Eischen, J.W., 1987, "Fracture of Nonhomogeneous Materials", *International Journal of Fracture*, Vol. 34, pp. 3-22.

[33] Jin, Z.-H. and Noda, N., 1994b, "Crack-tip Singular Fields in Nonhomogeneous Materials", *Journal of Applied Mechanics – Transactions of the ASME* , Vol. 61, pp. 738–740.